Imperial College London

Local rheology of lubricants in the elastohydrodynamic regime

By

Aleks Ponjavic

Thesis Submitted to Imperial College London

for the Degree of Doctor of Philosophy

and Diploma of Imperial College (DIC)

April 2014

Tribology Section

Department of Mechanical Engineering

Imperial College London

Acknowledgements

I could not have completed my doctoral studies without the support of a great number of amazing mentors, friends and relatives to which I dedicate my thesis.

I would like to thank my high school physics teacher Per Brantmark for fostering my love for physics, and for his inspiring work in facilitating Sweden's participation in the International Young Physicist' Tournament. I would also like to thank Dr. Tamer Zaki for his enthralling fluid mechanics lectures, and for giving me the opportunity of carrying out a research internship, which after being recommended by Tamer led to my PhD position working with Dr. Janet Wong.

A number of people have directly aided in carrying out the experimental work, and these people deserve my thanks. Dr. Mourad Chennaoui taught me most of what I know about optics and helped me design the optical setup which was used in this work. Johan Guegan provided great help with the interferometric film thickness measurements and Dr. Patrick Wong recommended using the Fusso coating to promote slip. Dr. Frank Beyrau lent us the high speed Guppy camera, while Dr. Amir Kadiric provided us with the ICCD camera used for FLIM measurements.

I would like to thank Prof. David Heyes, Prof. Hugh Spikes and Dr. Daniele Dini for all the fruitful discussions that took place over the past years, which helped me make sense of the abundance of experimental data collected. I would like to thank my supervisor Dr. Janet Wong, for believing in me and giving me the opportunity to carry out this research, which I most certainly could not have done alone. It has been a long and hard road and in the end we ended up with something exciting.

A massive shout-out goes to all my friends in and out of the Tribology group that have truly made my experience over the years great. I will never forget all the fun and drama we've had and I almost wish I could do it all again. I would also like to thank Arwen, who has been there for me through the highs and lows of my doctoral years, for all the good times.

Finally, I would like to thank the best family in the world. My lovely sisters have always been there for me, picking on me and letting me know my place as the middle child. There aren't many people I love to spend time with more than them. My parents have given me the best environment a child could want to grow up under safe, warm and nourishing conditions. I will never forget sitting with my dad at the kitchen table, as he taught me algebra as a young kid, while mom was cooking dinner. Thank you mom and dad for an amazing childhood, and for always being there for me.

Declaration of originality

The work presented in this thesis is that of the author, unless otherwise referenced.

Declaration of copyright

The copyright of this thesis rests with the author and is made available under a Creative Commons Attribution Non-Commercial No Derivatives licence. Researchers are free to copy, distribute or transmit the thesis on the condition that they attribute it, that they do not use it for commercial purposes and that they do not alter, transform or build upon it. For any reuse or redistribution, researchers must make clear to others the licence terms of this work.

Journal papers

[1] Ponjavic, A., Chennaoui, M., Wong, J. S. S.: Through-Thickness Velocity Profile Measurements in an Elastohydrodynamic Contact. Tribol. Lett. 50, 261–277 (2013)

[2] Ponjavic, A., di Mare, L., Wong, J. S. S.: Effect of pressure on the flow behaviour of polybutene. J. Polym. Sci. Part B: Polym. Phys. (2014) doi: 10.1002/polb.23472

[3] Ponjavic, A., Wong, J. S. S.: The effect of boundary slip on elastohydrodynamic lubrication. Submitted to RSC Advances

Abstract

Numerous models have been developed to describe the viscosity and rheology of lubricants in elastohydrodynamic (EHD) lubrication, but little experimental and theoretical work has been done on the flow of lubricants. Due to the high pressures in a tribological contact it is likely that lubricants may undergo structural changes, which would significantly affect their flow.

Photobleached-fluorescence imaging velocimetry was applied to a glass-glass EHD contact, lubricated with the oligomer polybutene, which was doped with fluorescent dye. The technique involved tagging a volume inside the contact, by making it dark compared to its surroundings. A model was developed to solve for the through-thickness velocity profile using the experimental data and the technique was validated experimentally using a parallel plate Couette setup.

Velocity profiles of polybutene in an EHD contact were measured under various conditions. Three distinct rheological responses could be observed. At low pressures, the velocity profile was mostly linear. At a critical pressure, a low shear rate plug formed in the centre of the film, possibly due to pressure-induced glass transition of the lubricant. The application of a low surface energy coating caused the lubricant to slip at the interface, depending on the applied pressure.

The velocimetry studies were supported by film thickness and friction measurements. Laser-induced fluorescence was used to measure the film thickness, showing that the plug flow of polybutene coincided with an anomalous increase in film thickness, while the occurrence of boundary slip resulted in reduced film thickness. Friction measurements showed that plug flow had negligible effects on friction. Boundary slip however caused a decrease in friction (up to 70 %).

Results suggest that lubricant flow in an elastohydrodynamic contact is non-trivial and deserves more consideration than is typically given. Direct flow measurements could be useful to elucidate the complex relationship between film thickness, friction and flow.

Table of contents

LIST OF FIGURES **12**

LIST OF EQUATIONS **18**

NOMENCLATURE **21**

1 INTRODUCTION **23**

1.1 Friction and rheology of lubricants 23

1.2 Experimental methods for lubricant rheometry 28

1.3 The velocity profile in EHD lubrication 32

1.4 Inhomogeneous shear flows 35

1.5 Experimental velocimetry for EHD lubrication 39

2 EXPERIMENTAL SETUP AND TECHNIQUE **45**

2.1 Photobleached-fluorescence imaging 45

2.1.1 Photobleaching *45*

2.1.2 Principle of photobleached-fluorescence imaging *46*

2.1.3 Optical setup *48*

2.1.4 Image acquisition *50*

2.1.5 Optical characteristics *53*

2.1.6 Photobleaching characteristics *55*

2.2 Fluid properties 57

2.2.1 Lubricant and fluorophore selection *57*

2.2.2 Properties of polybutene *61*

2.2.3 Diffusion coefficient of nile red *65*

2.2.4 Heating due to photobleaching process *68*

2.3 EHD Contact 71

2.3.1 Establishment of an EHD contact and its stability *71*

2.3.2 Pressure and size of the EHD contact *74*

2.3.3 Film thickness calculation *75*

2.3.4 Friction calculation *78*

2.3.5 Shear heating *80*

2.3.6 Squeeze film solidification *80*

2.3.7 Interference *83*

2.3.8 Low surface energy coating *85*

2.4 Summary 88

3 FILM THICKNESS MEASUREMENTS 90

3.1 Interferometry 90

3.2 Laser-induced fluorescence 93

3.2.1 Setup *93*

3.2.2 The effects of load and speed *95*

3.2.3 Calibration *98*

3.2.4 Classical EHD *99*

3.2.5 Dimple *100*

3.2.6 Slip coating *102*

3.3 Summary 107

4 ANALYSIS 109

4.1 Modelling 109

4.2 Velocity profile reconstruction 112

4.3 Evaluation of reconstruction scheme 115

4.3.1 Couette and Poiseuille flow *115*

4.3.2 Inhomogeneous shear flow *118*

4.3.3 Boundary slip flow *121*

4.4 Resolution 123

4.5 Validation using parallel plate geometry 126

4.6 Two-dimensional flow mapping 129

4.6.1 Velocity field *130*

4.7 Validation with Soft-EHD contact 132

4.8 Through-thickness velocity profile overview 137

4.9 Summary 139

5 THE LIQUID (LOW PRESSURE) REGIME 141

5.1 Typical result 141

5.2 The effect of normal pressure on EHD flow 145

5.3 Spatial variations 146

5.4 Summary 148

6 THE GLASSY (HIGH PRESSURE) REGIME 150

6.1 Typical result 150
6.2 The effect of load and speed 154
6.3 Spatial variations 158
6.4 Critical transition pressure 160
6.5 Summary 162

7 BOUNDARY SLIP 164

7.1 Typical result 164
7.2 Dependency on shear rate and load 167
7.3 Spatial variations 170
7.4 Summary 172

8 FRICTION MEASUREMENTS 173

8.1 Setup 173
8.2 PB in a Glass-glass contact 175
8.3 The effect of interfacial slip on friction 178
8.4 Summary 183

9 LOCAL RHEOMETRY IN PRACTICAL EHD LUBRICATION 185

9.1 Phosphorescence 185
9.2 Fluorescence-lifetime imaging microscopy 187
9.3 Proof of concept 189
9.4 FLIM for practical EHD lubrication 191
9.5 Summary 197

10 CONCLUSIONS 200

10.1 Summary of main findings 200
10.2 Limitations 204
10.3 Future work 206
10.4 Implications of results 207

REFERENCES 209

APPENDIX: COPYRIGHT PERMISSIONS 214

List of figures

Fig. 1: Stribeck curve: logarithmic plot of coefficient of friction (COF) against the lubrication parameter. Four lubrication regimes are identified. B: boundary, M: mixed, EHD: elastohydrodynamic, HD: hydrodynamic. 24
Fig. 2: Log-log plot of flow curves for four commonly used rheological models for lubricants. 26
Fig. 3: a) Ball impact apparatus of Höglund. (Adapted from [20]) b) Ball impact apparatus of Workel et al. (Adapted from [20]) 29
Fig. 4: a) Traction coefficient plotted against shear rate (effectively a flow curve) for mineral oil (triangles) and Santotrac 50 (circles) at various pressures. (Adapted from [15]) b) Shear stress variations in an EHD contact for various lubricants. (Adapted from [22]) 30
Fig. 5: a) Pressure-viscosity relationship for a mineral oil measured using a high pressure rheometer. (Adapted from [18]) b) Flow curves for a mineral oil at various pressures and temperatures measured using a high pressure rheometer. (Adapted from [18]) 31
Fig. 6: A linear velocity profile is shown for an EHD contact of film thickness hc and contact radius a, with the top surface moving at a velocity U. The position of minimum film thickness, the horseshoe, is indicated. (From [29] with kind permission from Springer Science and Business Media) 32
Fig. 7: Some possible velocity profiles for EHD lubrication. IS: inhomogeneous shear, SB: shear banding. 33
Fig. 8: a) Mean lubricant velocity as a function of position in the contact. (Adapted from [31]) b) Friction coefficient plotted against sliding speed for non-coated surface (black) and surface with low surface energy coating (white), at various loads. (Adapted from [36]) 34
Fig. 9: a) Schematic of the EHD contact and optical setup used for the dimple method. Interferograms (I) and (II) show that the entrapped dimple moves due to the flow of the lubricant. (Adapted from [38]) b) Stribeck curve (white) and film thicknesses (black) for polybutene, where U is a speed parameter. The friction drops at the transition from elastohydrodynamic lubrication (EHL) into the hydrodynamic lubrication (HL) region. (Adapted from [39]) 35
Fig. 10: a) Relative velocity profiles for shear flows of foams at various velocities. (Adapted from [41]) b) Velocity profile for a yield stress fluid. (Adapted from [43]) c) Velocity profile of a solidified model lubricant in an EHD contact. (Adapted from [45]) 36
Fig. 11: a) Adiabatic shear band in a high pressure rheometer. (Adapted from [17]) b) Velocity profile of wormlike micelle solution at various times after start-up of shear. Steady state is reached at 29 s. The inset shows the measured shear stress as a function of time. (Adapted from [51]) 38
Fig. 12: Non-monotonic flow curve. The line BC indicates the apparent shear stress which would be measured using rheometry. σSB is the critical shear rate for shear banding. $\gamma 1$ and $\gamma 2$ are the local shear rates of the solid and shear banding regions respectively. (Adapted from [52]) 39
Fig. 13: a) Particle image velocimetry in a T-junction. Acquired images (bottom) and constructed velocity field (top). (Adapted from [54]) b) Photobleached-fluorescence imaging of microfluidic flow in a turn geometry. (Adapted from [55]) 40
Fig. 14: Phosphorescent grid printed in the intake gas-phase flow of an internal combustion engine. Second image is at a delay of 50 µs where the grid has been distorted due to the flow. (Adapted from [56]) b) Combined pressure driven and electro-osmotic flow in a microchannel probed by the uncaging of fluorescent dye. (Adapted from [57]) 41
Fig. 15: a) Flow curves of molten polybutadiene at various gap heights. (Adapted from [9]) b) Drainage force for an aqueous solution as a function of distance at two velocities. The dotted line shows the theoretical force for no-slip. (Adapted from [61]) 42
Fig. 16: a) Penetration of an evanescent wave due to total internal reflection at a polymer-glass interface. (Adapted from [62]) b) Near surface velocity profile measured using double-focus fluorescence cross-correlation. Disagreement with theory due to hindered diffusion can be seen. (Adapted from [64]) 43
Fig. 17: a) Viscosity variation with nanochannel thickness for a polyacrylamide solution. (Adapted from [65]) b) Velocity profile of the pressure driven flow of water in a 360 nm capillary. (Adapted from [66]) 44
Fig. 18: a) A lubricant film in an EHD contact is depicted. Fluorescent lubricant is indicated by orange. The volume containing the photobleached molecules is shown in black. The intensity distribution is shown at three successive times after photobleaching; $t1$, $t2$ and $t3$. b) The intensity distributions in the top figure are shown in the x-y plane. The velocity of the glass ball is indicated by U and the slip velocity is indicated by ub. 47
Fig. 19: Beam path diagram with EHD contact setup on stage. Abbreviations: Shutter (S), beam expander (BE), dichroic mirrors (DM1 and DM2), objective (OB), long pass filter (LP), tube lens (TL), mirror (M) and electron multiplying charge coupled device (EM-CCD). The inset in the

dotted rectangle depicts the alternate parallel plates setup that can be placed on top of the microscope stage. The arrow indicates that the top slide can be translated at a velocity U 49
Fig. 20: Schematic of image acquisition sequence. The dotted lines indicate repetitions. The time between bleach and post bleach allows the camera shutter to open. 51
Fig. 21: Schematic of the geometry of a focused Gaussian laser beam. The red line indicates the intensity distribution across the beam waist and the green rectangle shows where the intensity is approximately constant in the z-direction. 53
Fig. 22: a) Colour map of the intensity distribution of the focused laser beam in the fluorophore-doped lubricant, which was sandwiched between two glass slides. White represents high intensity and black represents low intensity. The scale bar, which applies to both x- and y-direction, is 2.5 μm and the yellow rectangle indicates the region used for averaging. b) The intensity distribution averaged in the y-direction is shown. The red line indicates a Gaussian fit to the data. 54
Fig. 23: The simulated intensity distribution after 2 ms of photobleaching is shown at various bleaching laser beam power. The red lines indicate fits to a Gaussian distribution. 56
Fig. 24: Plot of the coefficient of determination, $R2$, against the non-dimensional parameter, B, at varying beam radii, bleaching times and velocities. This is used to determine an appropriate bleaching time for the creation of the photobleached spot. 57
Fig. 25: a) Colour map of the intensity distribution before and after photobleaching. White represents high intensity and black represents low intensity. The scale bar is 2.5 μm. b) Colour map of the IN distribution of the photobleached spot. Due to the definition of equation (3), photobleaching is represented as positive relative intensity. The scale bar is 2.5 μm and the yellow rectangle indicates the region used for averaging. c) The IN distribution averaged in y is shown. The red line indicates a Gaussian fit to the data. 61
Fig. 26: Rheology of PB2300 measured using flow (white circles) and oscillatory (grey circles) modes. 62
Fig. 27: Fluorescence recovery after photobleaching curves for the three polybutenes. The red lines indicate the fit to equation (11). The data for PB2300 extends to 10000 s. 67
Fig. 28: Mesh of the bounded lubricant film being heated by a cylindrical heat source. The scale bar is 0.5 μm. A Gaussian heat source is applied in the polybutene (PB) heat source rectangle. The geometry extends further in r than shown to simulate an infinite cylinder. The inset shows the result of the simulation indicating a steady state temperature rise of 5.5 K. The scale bar is 0.5 μm. 71
Fig. 29: EHD contact setup. a) The EHD contact, showing the glass ball (B), microscope slide (S), carriage (C) and motor (M). b) The loading mechanism and positioning stages, showing the load (L), linear bearing (LB) and micrometers (μ). 72
Fig. 30: a) White light microscopy image of the EHD contact. The arrow indicates the direction of flow. Features on the steel surface can be seen moving. The scale bar is 50 μm. Cavitation can be seen at the outlet. b) Plot of the ratio of the measured velocity UM and the set velocity US against time, indicating the stability of the velocity. 73
Fig. 31: a) Fluorescence image of the EHD contact. The arrow indicates the direction of flow. The scale bar is 100 μm. The horseshoe can be seen near the outlet followed by cavitation. b) Plot of the normalised intensity against time, indicating the stability of the load applied and the film thickness. 74
Fig. 32: Lubrication regime map constructed for a point contact with k=1. IV: isoviscous, PV: piezoviscous, R: rigid, E: elastic. The symbols represent the operating conditions for various experimental parameters detailed in the text. 77
Fig. 33: a) Decrease in relative squeeze film thickness over time for PB2300 after stopping the ball. The black lines are fits to equation (34). b) Non-dimensional squeeze film time constant as a function of pressure. 82
Fig. 34: a) Intensity variation with film thickness for a steel-glass EHD contact at 2 N. The red line shows a fit for the intensity due to interference. a) Intensity variation with film thickness for a glass-glass EHD contact at 5 N. The red line is a linear fit to the data. The lubricant was H-300. 84
Fig. 35: Water and PB920 on glass and on the Fusso coated glass slide. The green lines indicate the fitting done by the LBADSA plug-in, to determine the contact angle. 87
Fig. 36: Central film thickness for PB2300 and H-300 against ball surface speed. The normal load is 10 N (403 MPa). The red lines indicate fits to equation (27). The contact was created by loading a steel ball against a chromium and silica coated glass disc. 91
Fig. 37: Interference images of the contact for H-300 at various loads and speeds. A dimple, indicated by white arrows, can be seen to appear at high loads and high speeds. 92

FIG. 38: FLAT-FIELD CORRECTION FOR FILM THICKNESS MEASUREMENTS. A) FLAT FIELD IMAGE OF RHODAMINE 6G IN WATER. THE SCALE BAR IS 100 μM. B) 6.4 N (263 MPA) CALIBRATION IMAGE OF NILE RED DOPED PB. C) FLAT-FIELD CORRECTED CALIBRATION IMAGE. THE YELLOW RECTANGLE SHOWS THE AREA USED FOR AVERAGING. 94

FIG. 39: FLAT-FIELD CORRECTED INTENSITY DISTRIBUTIONS OF PB2300 FOR VARIOUS SPEEDS AND LOADS IN A GLASS-GLASS CONTACT WITHOUT CALIBRATION. THE RANGE OF INTENSITIES VARIES FOR EACH IMAGE TO HIGHLIGHT FEATURES OF THE FILM. THE MINIMUM FILM THICKNESS HORSESHOE IS INDICATED BY A RED H AND THE BLACK ARROW SHOWS THE DIRECTION OF THE FLOW. AN INCREASE OF THE FILM THICKNESS TOWARDS THE OUTLET OF THE CONTACT CAN BE SEEN FOR HIGHER LOADS, AS IDENTIFIED BY THE RED D (FOR DIMPLE). THE SCALE BAR IS 100 μM. 95

FIG. 40: FLAT-FIELD CORRECTED INTENSITY DISTRIBUTIONS OF PB2300 FOR VARIOUS SPEEDS AND LOADS IN A SAPPHIRE-GLASS CONTACT WITHOUT CALIBRATION. THE RANGE OF INTENSITIES VARIES FOR EACH IMAGE TO HIGHLIGHT FEATURES OF THE FILM. THE BLACK ARROW SHOWS THE DIRECTION OF THE FLOW. AN INCREASE OF THE FILM THICKNESS TOWARDS THE OUTLET OF THE CONTACT CAN BE SEEN FOR HIGHER LOADS, AS IDENTIFIED BY THE RED D (FOR DIMPLE). THE SCALE BAR IS 100 μM. 96

FIG. 41: A) INTENSITY AND FILM THICKNESS DISTRIBUTIONS ACROSS THE CENTRE OF THE GLASS-GLASS CONTACT FOR H-300 AT A LOAD OF 6.4 N (263 MPA). B) FILM THICKNESS PLOTTED AGAINST THE INTENSITY, YIELDING A CALIBRATION CURVE. THE BLACK LINE IS A LINEAR FIT TO THE DATA IN THE RANGE ($0 < h < 0.8$ μM). THE INSET SHOWS THE LINEARITY AT LARGER FILM THICKNESSES (UP TO 4 μM). 99

FIG. 42: A) TWO-DIMENSIONAL FILM THICKNESS DISTRIBUTION AT A SPEED OF 720 μM/S AND A LOAD OF 6.4 N (263 MPA) FOR PB2300. THE SCALE BAR IS 50 μM. THE WHITE BOX HIGHLIGHTS THE AREA USED FOR AVERAGING AND THE YELLOW AREA MARKS THE HORSESHOE. B) FILM THICKNESS DISTRIBUTION IN THE X-DIRECTION ALONG THE CENTRE OF THE CONTACT (Y = 0). 100

FIG. 43: A) TWO-DIMENSIONAL FILM THICKNESS DISTRIBUTION AT A SPEED OF 2400 μM/S AND A LOAD OF 35 N (463 MPA) FOR PB2300. THE SCALE BAR IS 50 μM. B) FILM THICKNESS DISTRIBUTION IN THE X-DIRECTION ALONG THE CENTRE OF THE CONTACT (Y = 0) FOR TWO SPEEDS. 101

FIG. 44: A) TWO-DIMENSIONAL FILM THICKNESS DISTRIBUTION AT A SPEED OF 720 μM/S AND A LOAD OF 6.4 N (263 MPA) FOR A GLASS-FUSSO EHD CONTACT LUBRICATED WITH H-300. THE SCALE BAR IS 50 μM. B) FILM THICKNESS DISTRIBUTION IN THE X-DIRECTION ALONG THE CENTRE OF THE CONTACT (Y = 0) FOR THE TWO VELOCITY BOUNDARY CONDITIONS. 103

FIG. 45: A) TWO-DIMENSIONAL FILM THICKNESS DISTRIBUTION AT A SPEED OF 720 μM/S AND A LOAD OF 0.9 N (137 MPA) FOR A GLASS-FUSSO EHD CONTACT LUBRICATED WITH H-300. THE SCALE BAR IS 50 μM. B) FILM THICKNESS DISTRIBUTION IN THE X-DIRECTION ALONG THE CENTRE OF THE CONTACT (Y = 0) FOR THE TWO VELOCITY BOUNDARY CONDITIONS. 104

FIG. 46: A) MINIMUM FILM THICKNESS AT 0.9 N (137 MPA) AS A FUNCTION OF SPEED FOR H-300. B) CENTRAL FILM THICKNESS AT 6.4 N (263 MPA) AS A FUNCTION OF SPEED. THE BLACK LINE INDICATES THE PREDICTION FOR THE FILM THICKNESS, WHILE THE DOTTED LINE SHOWS THE PREDICTION FOR THE FILM THICKNESS AT A RELATIVE SLIP VELOCITY OF 80 %. 105

FIG. 47: A) TWO-DIMENSIONAL FILM THICKNESS DISTRIBUTION AT A SPEED OF 2400 μM/S AND A LOAD OF 35 N (463 MPA) FOR A GLASS-FUSSO EHD CONTACT LUBRICATED WITH H-300. THE SCALE BAR IS 50 μM. B) FILM THICKNESS DISTRIBUTION IN THE X-DIRECTION ALONG THE CENTRE OF THE CONTACT (Y = 0) FOR THE TWO DIFFERENT SURFACES. 106

FIG. 48: A) A LINEAR VELOCITY PROFILE IS SHOWN FOR AN EHD CONTACT OF FILM THICKNESS, hc, AND CONTACT RADIUS, a, WITH THE TOP SURFACE MOVING AT A VELOCITY U. THE POSITION OF MINIMUM FILM THICKNESS, THE HORSESHOE, IS INDICATED. (FIG. 48A IS A DUPLICATE OF FIG. 6) B) THE FLUID IS MODELLED AS LAYERS OF INFINITESIMAL THICKNESS, MOVING AT A VELOCITY OF $u(z)$. HERE, A LINEAR PROFILE WITH SLIP AT THE INTERFACE IS SHOWN. THE POSITION OF THE PHOTOBLEACHED LAYERS IS SHOWN JUST AFTER PHOTOBLEACHING, $t0$, AND AFTER ADVECTION AT TIME tn. (FROM [29] WITH KIND PERMISSION FROM SPRINGER SCIENCE AND BUSINESS MEDIA) 109

FIG. 49: THREE SUCCESSIVE FITTING ATTEMPTS FOR THE VELOCITY PROFILE $u(z)$ ARE DEPICTED. TOP: THE POSITION OF THREE FLUID LAYERS AT TIMES $t0$ AND tn ARE SHOWN. BOTTOM: THE ONE-DIMENSIONAL INTENSITY DISTRIBUTION FOR IN FROM EXPERIMENTAL RESULTS (OPEN CIRCLE) AND $IN*$ (SOLID LINE), CALCULATED BY SUMMATION OF THE LAYERS IN THE TOP FIGURE. THE DISTRIBUTIONS ARE SHOWN AT TIMES $t0$ AND tn. IN THE FIRST ITERATION THERE IS A MISMATCH BETWEEN IN AND $IN*$ AT tn, SO $u(z)$ IS VARIED UNTIL THEY ARE EQUAL, AS SEEN IN THE LAST ITERATION. (FROM [29] WITH KIND PERMISSION FROM SPRINGER SCIENCE AND BUSINESS MEDIA) 113

FIG. 50: A) SIMULATED EXPERIMENTAL (Ix) AND RECONSTRUCTED ($IN*$) INTENSITY DISTRIBUTIONS AT FIVE TIMES. B) RELATIVE VELOCITY u/U AT RELATIVE POSITION z/h. u IS THE RECONSTRUCTED VELOCITY PROFILE AND uS IS THE INPUT PROFILE FOR THE SIMULATION. 116

FIG. 51: A) SIMULATED EXPERIMENTAL (Ix) AND RECONSTRUCTED ($IN*$) INTENSITY DISTRIBUTIONS AT FIVE TIMES. B) RELATIVE VELOCITY u/U AT RELATIVE POSITION z/h. u IS THE RECONSTRUCTED VELOCITY PROFILE AND uS IS THE INPUT PROFILE FOR THE SIMULATION. 117

FIG. 52: A) RECONSTRUCTED VELOCITY PROFILES FOR LOW (uL) AND HIGH (uH) CRITERION RATIO $\delta I/\delta u$ RESPECTIVELY. THE RED LINE INDICATES THE INPUT VELOCITY PROFILE. B) DEPENDENCY OF PRODUCT OF COEFFICIENTS OF DETERMINATION ON THE CRITERION RATIO. IN THE INSET, THE OPTIMAL REGION IS IDENTIFIED. 118

FIG. 53: A) VELOCITY PROFILES FOR THE CASE OF PLUG FLOW AS THE THICKNESS OF THE BOUNDARY LAYERS IS VARIED. CIRCLES REPRESENT THE PROFILES DETERMINED BY THE RECONSTRUCTION SCHEME AT VARIOUS BOUNDARY LAYER THICKNESSES WHILE THE BLACK LINES ARE THE INPUT VELOCITY PROFILES. B) RATIO OF THE MAXIMUM RECONSTRUCTED AND INPUT SHEAR RATES OF THE BOUNDARY LAYER FOR PLUG FLOW. THE VERTICAL LINE INDICATES THE CRITICAL HEIGHT FOR THE ACCEPTABLE DETERMINATION OF THE SHEAR RATE. 119

FIG. 54: A) RECONSTRUCTED VELOCITY PROFILES (CIRCLES) FOR THE CASE OF SHEAR BANDING AS THE POSITION OF THE SHEAR BAND OF THE INPUT PROFILES (SOLID LINES) IS VARIED. THESE RESULTS ARE FOR A SHEAR BAND WIDTH OF 0.6. B) RATIO OF THE MEASURED AND THE INPUT POSITION OF THE SHEAR BAND FOR THREE SHEAR BAND WIDTHS. THE VERTICAL BLACK LINE INDICATES THE MINIMUM POSITION AT WHICH THE BAND POSITION CAN BE IDENTIFIED FOR ALL WIDTHS. 120

FIG. 55: A) ACCURACY OF THE RECONSTRUCTED RELATIVE SLIP LENGTH AS A FUNCTION OF THE INPUT RELATIVE SLIP LENGTH FOR A PLANE COUETTE PROFILE. B) AS (A) FOR A POISEUILLE PROFILE. THE INSETS SHOW THE INPUT (SOLID LINE) AND RECONSTRUCTED (CIRCLES) PROFILES AT VARIOUS SLIP LENGTHS. 121

FIG. 56: A) SAMPLE VELOCITY PROFILES FOR AN INPUT SLIP VELOCITY OF 0.8, FOR THE 'FREE' AND POLYNOMIAL RECONSTRUCTION SCHEMES. B) ERROR IN RELATIVE SLIP, AS A FUNCTION OF THE SLIP VELOCITY FOR THE TWO RECONSTRUCTION SCHEMES. 122

FIG. 57: A) EXPERIMENTAL (EXP) AND NUMERICAL (NUM) SPATIOTEMPORAL NORMALISED RELATIVE INTENSITY DISTRIBUTIONS AT THREE TIMES FOR A 1 μM THICK FILM OF H-300 AT A SPEED OF 26.3 μM/S. THE ARROW INDICATES THE DIRECTION OF THE FLOW. THE DOTTED LINE A INDICATES THE POSITION OF THE BACK OF THE COLUMN. B) AVERAGED INTENSITY DISTRIBUTIONS FROM (A), WITH POINT A INDICATING THE BACK OF THE COLUMN. C) RECONSTRUCTED VELOCITY PROFILE AND THEORETICAL COUETTE VELOCITY PROFILE. (FROM [29] WITH KIND PERMISSION FROM SPRINGER SCIENCE AND BUSINESS MEDIA) 127

FIG. 58: FLUORESCENCE IMAGE OF THE STEEL-GLASS EHD CONTACT FOR H-300 AT SPEED 360 μM/S, LOAD 6.4 N (347 MPA) AND FILM THICKNESS ~190 NM. THE WHITE DASHED CIRCLE SHOWS THE PERIMETER OF THE CONTACT. THE HORSESHOE REGION IS MARKED BY A BLACK ARC. THE WHITE ARROW INDICATES THE DIRECTION OF THE FLOW. WHITE CROSSES SHOW THE LOCATIONS AT WHICH PHOTOBLEACHED-FLUORESCENCE IMAGING WAS APPLIED. THE CROSS-HATCHED REGION HIGHLIGHTS POSITIONS WHERE THE RECONSTRUCTION SCHEME COULD BE APPLIED SUCCESSFULLY. (FROM [29] WITH KIND PERMISSION FROM SPRINGER SCIENCE AND BUSINESS MEDIA) 129

FIG. 59: VECTOR PLOT OF THE VELOCITY FIELD (WHITE ARROWS) OVERLAID ONTO A FLUORESCENCE IMAGE OF THE CONTACT. THE VELOCITY IN THE Y-DIRECTION HAS BEEN MULTIPLIED BY TEN FOR CLARITY. THE LARGE WHITE ARROW INDICATES THE DIRECTION OF THE FLOW. FOR EXPERIMENTAL CONDITION, SEE CAPTION IN FIG. 58. (FROM [29] WITH KIND PERMISSION FROM SPRINGER SCIENCE AND BUSINESS MEDIA) 131

FIG. 60: FLUORESCENCE IMAGE OF THE SOFT-EHD CONTACT FOR H-300 BETWEEN A STEEL BALL AND A PMMA-COATED PDMS SURFACE, CAPTURED AT 2 N (0.30 MPA) AND 720 μM/S. THE ARROW INDICATES THE DIRECTION OF FLOW. THE SCALE BAR IS 100 μM. THE HORSESHOE CAN BE SEEN NEAR THE OUTLET FOLLOWED BY CAVITATION. 133

FIG. 61: A) EXPERIMENTAL (EXP) AND NUMERICAL (NUM) SPATIOTEMPORAL NORMALISED RELATIVE INTENSITY DISTRIBUTIONS AT THREE TIMES FOR H-300 AT SPEED 720 μM/S, LOAD 6.4 N (0.44 MPA) AND FILM THICKNESS 10 μM BETWEEN A STEEL BALL AND A PDMS SURFACE. THE ARROW INDICATES THE DIRECTION OF THE FLOW. THE DOTTED LINE A INDICATES THE POSITION OF THE BACK OF THE COLUMN. THE SCALE HAS BEEN STRETCHED BY A FACTOR OF THREE IN THE Y-DIRECTION, DUE TO THE NUMBER OF PIXELS MEASURED BEING SMALL. B) AVERAGED DISTRIBUTIONS FROM (A) WITH THE POINT A INDICATING THE BACK OF THE COLUMN. C) RECONSTRUCTED VELOCITY PROFILE AND THEORETICAL COUETTE VELOCITY PROFILE. 135

FIG. 62: A) EXPERIMENTAL (EXP) AND NUMERICAL (NUM) SPATIOTEMPORAL NORMALISED RELATIVE INTENSITY DISTRIBUTIONS AT THREE TIMES FOR H-300 AT SPEED 720 μM/S, LOAD 6.4 N (0.44 MPA) AND FILM THICKNESS 10 μM BETWEEN A STEEL BALL AND A PMMA-COATED PDMS SURFACE. THE ARROW INDICATES THE DIRECTION OF THE FLOW. THE DOTTED LINE A INDICATES THE POSITION OF THE BACK OF THE COLUMN. B) AVERAGED DISTRIBUTIONS FROM (A) WITH THE POINT A INDICATING THE BACK OF THE COLUMN. C) RECONSTRUCTED VELOCITY PROFILE AND THEORETICAL COUETTE VELOCITY PROFILE. 136

FIG. 63: NORMALISED RELATIVE INTENSITY, IN AT THREE TIMES FOR FOUR DIFFERENT EXPERIMENTAL CONDITIONS, AT THE CENTRE OF A POINT CONTACT. FOR THE CASES OF EHD, IS (INHOMOGENEOUS SHEAR) AND SLIP, THE SCALE BAR IS 20 μM. FOR THE CASE OF SOFT, THE SCALE BAR IS 40 μM. DOTTED WHITE LINE A INDICATES THE BACK OF THE PHOTOBLEACHED COLUMN IMMEDIATELY AFTER PHOTOBLEACHING. DOTTED WHITE LINE B INDICATES THE APPROXIMATE POSITION OF THE BACK OF THE COLUMN, FOR THE CASE WHERE THE LUBRICANT SLIPS AT THE LUBRICANT-GLASS INTERFACE. 137

FIG. 64: A) EXPERIMENTAL (EXP) AND NUMERICAL (NUM) SPATIOTEMPORAL NORMALISED RELATIVE INTENSITY DISTRIBUTIONS AT THREE TIMES FOR H-300 AT SPEED 720 μM/S, LOAD 13.3 N (335 MPA) AND FILM THICKNESS 263 NM. THE ARROW INDICATES THE DIRECTION OF THE FLOW. THE DOTTED LINE A INDICATES THE POSITION OF THE BACK OF THE COLUMN. B) AVERAGED DISTRIBUTIONS FROM (A) WITH POINT A INDICATING THE INITIAL BACK POSITION OF THE BACK OF THE COLUMN. C) RECONSTRUCTED VELOCITY PROFILE AND THEORETICAL COUETTE VELOCITY PROFILE. 142

Fig. 65: Variation of viscosity with molecular weight of PB. The black line shows a power law fit to the data. 143
Fig. 66: Velocity profiles for H-300 at loads 6.4 N (263 MPa) and 13.3 N (335 MPa). a) Relative velocity profiles at position x/a = 0 (centre). The central film thicknesses are given in the table inset. b) Relative velocity profiles at approximate position x/a = -0.5 (near inlet). 145
Fig. 67: a) Spatial variation of mean lubricant velocity of H-300 for various loads and speeds. Information on film thickness and pressure is given in Fig. 66. b) Fluorescence intensity map of a 13.3 N (335 MPa) EHD contact, indicating positions (red dots) where measurements are performed for the data in (a). The white circle shows the contact area. 147
Fig. 68: Spatial variation of the relative slip velocity for H-300 at the lubricant-glass ball (a) and lubricant-glass slide (b) interfaces. Information on pressure and film thickness is given in Fig. 66. 148
Fig. 69: a) Experimental (EXP) and numerical (NUM) spatiotemporal normalised relative intensity distributions at three times for PB2300 at speed 360 μm/s, load 28 N (430 MPa) and film thickness ~900 nm. The arrow indicates the direction of the flow. The dotted line A indicates the position of the back of the column. b) Averaged distributions from (a) with point A indicating the initial back position of the back of the column. c) Reconstructed velocity profile and theoretical Couette velocity profile. The red lines are a guide to the eyes, indicating three separate regions of varying shear rate. 151
Fig. 70: a) Velocity profiles at various applied loads for PB2300 at speed 360 μm/s. The film thickness at the lowest pressure is 654 nm. At the highest pressure the dimple causes the thickness to increase to 980 nm. The dotted line indicates a linear velocity profile. The red arrows show how the plug grows with load. b) Central relative shear rate and mean velocity as a function of load. The dotted line shows the apparent shear rate for Couette flow. (Adapted from [127]) 155
Fig. 71: a) Velocity profiles at various applied speeds for PB2300 at load 28 N (430 MPa). The approximate central film thicknesses in the dimple are 397, 829 and 1320 nm for the three speeds. b) Relative normalised intensity distributions for three speeds, at a fixed characteristic distance after photobleaching. The distributions have a significant Gaussian component with visible shoulders on either side of the peak intensity. The red dotted arrows indicate the decay of these shoulders with increased velocity. 157
Fig. 72: a) Spatial variation of central relative shear rate and mean lubricant velocity for H-300 at load 28 N (430 MPa) and speed 720 μm/s. The film thickness varies between 249-398 nm depending on position. b) Fluorescence intensity map of a 28 N (430 MPa) EHD contact, indicating positions (red dots) where measurements were performed for the data in (a). The white circle shows the contact area. 159
Fig. 73: Pressure-molecular weight phase diagram for polybutene. Black data points are in the liquid phase (nearly Couette flow) and red data points are glassy (sigmoidal velocity profile). Squares represent data for a glass-glass contact and stars represent data for a glass-sapphire contact. The coloured areas are a guide to the eye, indicating the author's interpretation of a possible glass transition boundary. Adapted from [127]. 161
Fig. 74: a) Experimental (EXP) and numerical (NUM) spatiotemporal normalised relative intensity distributions at three times for H-300 at speed 720 μm/s, load 6.4 N (263 MPa) and film thickness ~120 nm. The arrow indicates the direction of the flow. The dotted line A indicates the initial position of the back of the column. The dotted line B shows the approximate measured back of the column, indicating interfacial slip. b) Averaged distributions from (a) where points 'A' and 'B' maintain the same definitions. c) Reconstructed velocity profiles and theoretical Couette velocity profile. 165
Fig. 75: a) Relative slip velocity as a function of load for two speeds for H-300. The dotted line indicates the critical pressure for phase transition of H-300. Note that the error bars are barely visible. b) Film thickness map of a 6.4 N (263 MPa) glass-Fusso EHD contact, indicating the position (red dot) where measurements were performed for the data in (a). The white circle shows the contact area and the scale bar is 50 μm. 167
Fig. 76: a) Spatial variation of the relative slip velocity for various loads and speeds for H-300. The dotted line indicates the slip velocity predicted for 263 MPa by the power law fit in Fig. 75. The arrow shows the direction of the flow. b) Film thickness map of a 6.4 N (263 MPa) glass-Fusso EHD contact, indicating the positions (red dots) where measurements are performed with respect to the EHD contact for the data in (a). The white circle shows the contact area and the scale bar is 50 μm. 170
Fig. 77: a) UMT-2 tribometer setup. b) Schematic of thin film deposition using a wiper. c) Schematic of the setup used for the friction measurement. 174
Fig. 78: Sample speed ramp for coefficient of friction (COF) measurements. 175
Fig. 79: a) Coefficient of friction as a function of speed for various loads for H-300. b) Estimated flow curves of polybutene. The black lines indicate a fit to Johnson's constitutive relationship. 5, 10, 15, 20 and 25 N correspond to 242, 305, 349 384 and 414 MPa respectively. Pressure-induced glass transition occurs at 390 MPa. 176

Fig. 80: a) The estimated Eyring stress as a function of mean contact pressure. The dotted line shows the critical transition pressure and the red line indicates a linear fit to the data. b) Variation of estimated viscosity with mean contact pressure. The dotted line shows the critical transition pressure and the red line indicates a fit to the Barus equation. 176

Fig. 81: Coefficients of friction (COF) at a load of 0.5 N (112 MPa) (a) and 5 N (242 MPa) (b) for the glass-glass and glass-Fusso contacts lubricated by H-300. 179

Fig. 82: a) Ratio of glass-Fusso friction, FF, to glass-glass friction, FG. The coloured areas represent the uncertainty. b) Friction ratio at the fixed velocity of 400 μm/s as a function of load. The solid line indicates a calculated relative friction determined by applying the determined pressure-slip length relationship based on Fig. 75a. The dashed line shows the calculation when the rheology was determined assuming spatially varying properties (see text). The dotted line shows a fit to the friction data used to determine an alternative pressure-slip length relationship 180

Fig. 83: a) Schematic of the optical setup. b-f) Intensity distributions of the fluorophore excited in the cuvette with varying delay times. White represents high intensity and black represents low intensity. The length scale is given by the distance between the cuvette walls indicated in (b), which is 10 mm. 188

Fig. 84: a) Intensity distribution at various delay times, td, for phosphorescent solution between cover slip and glass slide. The scale bar is 20 μm in both directions. b) Mean intensity plotted against delay time for acquisition. The red line indicates a single component exponential fit to the data. 189

Fig. 85: a) Schematic of the system geometry. b) Intensity distribution of the phosphorescent volume at various delay times post excitation. The scale bar is 20 μm. c) Intensity distribution averaged in the y-direction for the three different delays. The red lines indicate Gaussian fits to the experimental data. 190

Fig. 86: a) Position of centre of the Gaussian fit plotted against delay time for three speeds. The red lines indicate linear fits to the data. b) The slope of the lines in (a) plotted against the theoretical value. 191

Fig. 87: a) Relative phosphorescence intensity distribution at three delay times. The scale bar is 20 μm in both directions. b) Intensity distributions averaged over 9 pixels in the y-direction (note that these are not the same times as in (a)). The solid lines indicate Gaussian fits to the data. Phosphorescent decay is not considered. The solution is 5 mM of Eu(DBM)3Phen dissolved in THF. The THF solution was then dissolved in polybutene H-300 at a volume ratio of 3:7. Load is 20 N (508 MPa). Speed is 360 mm/s. The film thickness is unknown. 193

Fig. 88: a) Central position of Gaussian fit to the intensity distribution as a function of delay time for three different velocities. b) Measured average velocity plotted against the applied average velocity. The dotted line is the Couette solution and the solid line is a fit for Couette flow with a relative slip length of 3.17. 194

Fig. 89: a) Experimental (EXP) and numerical (NUM) spatiotemporal normalised relative intensity distributions at three times using data from Fig. 87a. The arrow indicates the direction of the flow. The dotted line A indicates the position of the back of the column. b) Averaged distributions from (a) with the point A indicating the back of the column. c) Reconstructed velocity profile and theoretical isothermal Couette velocity profile. 195

List of equations

$$u(z) = \frac{1}{2\mu_p}\frac{\partial p}{\partial x}(z^2 - zh) + U\frac{z}{h} \tag{1}$$

$$I_p(t_b) = I_0 e^{-k_p t_b} \tag{2}$$

$$I_N(t) = 1 - I_{NORM} = \frac{I_0 - I(t)}{I_0} \tag{3}$$

$$I_N(t) = \frac{I_0 - I(t) - I_{ph}}{I_0} \tag{4}$$

$$d = \frac{\lambda n}{NA^2} \tag{5}$$

$$w_0 = \frac{\lambda}{\pi NA} \tag{6}$$

$$P_b = P_0 e^{\left(-\frac{(x-x_0)^2}{2{w_0}^2}\right)} \tag{7}$$

$$\frac{I}{I_0} = exp\left(-P_0 e^{\left(-\frac{(x-x_0)^2}{2{w_0}^2}\right)} k_z t\right) \tag{8}$$

$$\overline{B} = \frac{Ut_b}{w_0} \tag{9}$$

$$\mu_p = \mu e^{\alpha p} \tag{10}$$

$$I(t) = 1 - \frac{C_m}{1 - {}^{t}\!/_{\tau_r}} + C_i \tag{11}$$

$$I(t) = 1 - C_{m1} e^{-{}^{t}\!/_{\tau_{r1}}} - C_{m2} e^{-{}^{t}\!/_{\tau_{r2}}} + C_i \tag{12}$$

$$D = {w_0}^2/(4\tau_r) \tag{13}$$

$$I_{norm}(t) = \frac{I_{bg}(0)}{I_{spot}(0)}\frac{I_{spot}(t)}{I_0}\Big/\frac{I_{bg}(t)}{I_0} = \frac{I_{bg}(0)}{I_{spot}(0)}\frac{I_{spot}(t)}{I_{bg}(t)} \tag{14}$$

$$D_P = k_b T/(4\pi\mu R_H) \tag{15}$$

$$s_0 = \Delta I/(\rho C l) \tag{16}$$

$$\Delta T(0,t) = \frac{s_0 {w_0}^2}{8K} ln(1 + 8\kappa t_b/{w_0}^2) \tag{17}$$

$$s_0 = 4.6\epsilon c P_0/\pi {w_0}^2 e^{-2r^2/{w_0}^2} \tag{18}$$

$$a = \left(\frac{3}{4}\frac{WR}{E'}\right)^{1/3} \tag{19}$$

$$\frac{1}{R} = \frac{1}{R_1} + \frac{1}{R_2} \tag{20}$$

$$\frac{1}{E'} = \frac{1-{v_1}^2}{E_1} + \frac{1-{v_2}^2}{E_2} \tag{21}$$

$$p_{max} = \frac{1}{\pi}\left(\frac{6WE'^2}{R^2}\right)^{1/3} \tag{22}$$

$$\bar{p} = \frac{2}{3}p_{max} \tag{23}$$

$$g_E = \frac{\bar{G}\overline{W}^3}{\bar{U}^2} \tag{24}$$

$$g_V = \frac{\overline{W}^{8/3}}{\bar{U}^2} \tag{25}$$

$$\bar{U} = \frac{U_e \mu}{E'R}, \bar{G} = \alpha E', \overline{W} = \frac{W}{E'R^2} \tag{26}$$

$$h_c = 1.90\bar{U}^{0.67}\bar{G}^{0.53}\overline{W}^{-0.067}R \tag{27}$$

$$\mu_p\dot{\gamma} = D\frac{d\sigma}{d(x/l)} + \sigma_0\, sinh\frac{\sigma}{\sigma_0} \tag{28}$$

$$\sigma = \sigma_0 sinh^{-1}\frac{\mu_p\dot{\gamma}}{\sigma_0} \tag{29}$$

$$u(z) \approx U\frac{z}{h} \tag{30}$$

$$u(z) = U(z+b)/(h_c+b) \tag{31}$$

$$b_{rel} = \frac{u_{brel}}{1-u_{brel}} \tag{32}$$

$$\Delta T_L = \frac{\tau W U h_c}{8\pi a^2 k_l} \tag{33}$$

$$\frac{h_c}{h_0} = e^{-t/\tau_s} \tag{34}$$

$$\tau_s^* = \frac{Wh_0^2}{\mu_p R_1^4}\tau_s \tag{35}$$

$$A_i = 2A_0\, sin\left(2\pi n\frac{d_i}{\lambda}\right) \tag{36}$$

$$\Delta W = \gamma_{LV}(1+cos\,\theta) \tag{37}$$

$$I_{FG} = \frac{I-I_{bg}}{I_F-I_{bg}} \tag{38}$$

$$A = \varepsilon cl \tag{39}$$

$$h = \frac{ap_{max}}{E^*}\left(-\left(2-\frac{r^2}{a^2}\right)cos^{-1}\frac{a}{r} + \sqrt{\frac{r^2}{a^2}-1}\right) \tag{40}$$

$$\frac{h_b}{h_c} = \frac{U}{U+u_b} = \frac{1}{1+u_{brel}} = \frac{1}{1+b_{rel}/(1+b_{rel})} \tag{41}$$

$$\frac{\partial c}{\partial t} = D\nabla^2 c - \vec{u} \cdot \nabla c \tag{42}$$

$$Pe_z = \frac{h_c U}{D} \tag{43}$$

$$\frac{\partial c}{\partial t} + u\frac{\partial c}{\partial x} = 0 \tag{44}$$

$$c(x, z, t) = c_0(x - ut) \tag{45}$$

$$\frac{c_0(x)}{c_i} = 1 - A_p e^{-\frac{(x-x_0)^2}{2{w_0}^2}} \tag{46}$$

$$\frac{c(x, z, t)}{c_i} = 1 - A_p e^{-\frac{(x-(ut+x_0))^2}{2{w_0}^2}} \tag{47}$$

$$I_N^* = \frac{I^*(x,t)}{I_0} = \int_0^{h_c} \frac{c(x,z,t)}{c_i} dz \tag{48}$$

$$I_x(i,n) = \sum_{j=-w}^{w} I_N(i,j,n)\,/(2w) \tag{49}$$

$$\sum_{i=1}^{128}\sum_{n=5}^{N} \|I_N^* - I_x\|^2 \tag{50}$$

$$\sum_{k=2}^{K-1} \|u(k+1) - 2*u(k) + u(k-1)\| \tag{51}$$

$$\sum_{i=1}^{128}\sum_{n=1}^{N} \|I_N^* - I_x\|^2 + \frac{\delta_I}{\delta_U}\sum_{k=2}^{K-1} \|u(k+1) - 2*u(k) + u(k-1)\| \tag{52}$$

$$\vec{u}_{xy}(x,y) = \frac{1}{h_c}\int_0^{h_c} \vec{u}(x,y,z)dz \tag{53}$$

$$\int_{y=0}^{H} \left(y \int_{x=0}^{L} I_N(x,y,t)dx \right) dy = (y_{CM} + y_0) \int_{y=0}^{H}\int_{x=0}^{L} I_N(x,y,t)\,dxdy \tag{54}$$

$$I_N(x,y,0) = A_P e^{-\left(\frac{(x-x_0)^2}{2{w_x}^2} + \frac{(y-y_0)^2}{2{w_y}^2}\right)} \tag{55}$$

$$h_c = 3.34\bar{U}^{0.64}\overline{W}^{-0.22}R \tag{56}$$

$$I_{ph}(t) = I_0 e^{-k_{ph}t} \tag{57}$$

$$I_N(i,j,n) = {I_{ph}/I_{bg}}\Big/{\overline{I_{ph}/I_{bg}}} \tag{58}$$

Nomenclature

A = Absorbance

A_0 = Amplitude

A_i = Interference amplitude

A_p = Peak bleach proportion

a = Contact radius (m)

a_b = Power law exponent

b = Slip length (m)

$\bar{B}$ = Non-dimensional photobleaching distortion

b_{rel} = Relative slip length

b_S = Input slip length

c = Concentration (mol/l)

C = Specific heat capacity ($J/(kg \cdot K)$)

c_0 = Post bleach concentration

C_m = Mobile population constant

c_i = Initial concentration

C_i = Immobile population constant

d = Depth of field (m)

d_i = Distance from reflective surface (m)

D = Diffusion coefficient (m^2/s)

D_P = Stokes-Einstein diffusion coefficient (m^2/s)

dz = Layer thickness (m)

E = Young's modulus (Pa)

E' = Contact modulus (Pa)

E^* = $2E'$

F = Frictional force (N)

$\bar{G}$ = Non-dimensional material parameter

g_E = Non-dimensional elasticity parameter

g_V = Non-dimensional viscosity parameter

H = Observation area height (m)

h = Film thickness (m)

h_0 = Initial film thickness (m)

h_b = Film thickness with slip u_b (m)

h_c = Central film thickness (m)

h_{coat} = Coating thickness (m)

I = Intensity (AU)

I^* = Theoretical intensity (AU)

I_0 = Initial intensity (AU)

I_{bg} = Background intensity (AU)

I_c = Central intensity (W/m^2)

I_F = Flat-field intensity (AU)

I_{FG} = Flat-field corrected intensity (AU)

I_N = Normalised relative intensity

I_N^* = Theoretical normalised relative intensity

I_{NORM} = Normalised intensity (AU)

I_p = Photobleaching intensity (AU)

I_{ph} = Phosphorescence intensity (AU)

I_{spot} = Average central intensity (AU)

I_x = y-averaged mean intensity (AU)

K = Number of fluid layers

k_b = Boltzmann constant ($m^2k \cdot kg/(s^2 \cdot K)$)

k_l = Thermal conductivity ($W/(m \cdot K)$)

k_p = Overall photobleaching rate (s^{-1})

k_{ph} = Phosphorescence rate constant (s^{-1})

k_z = Power independent photobleaching rate (s^{-1})

l = Thickness (m)

L = Observation area length (m)

L_c = Characteristic length (m)

M_n = Number average molecular weight rate (g/mol)

n = Refractive index

n_b = Flow behaviour index

N = Number of frames

NA = Numerical aperture

p = Pressure (Pa)

P = Power (W)

$\bar{p}$ = Mean pressure (Pa)

P = Photobleaching power distribution (W)

Pe = Péclet number

p_{max} = Maximum pressure (Pa)

p_R = Roelands reference pressure (Pa)

R = Radius of relative curvature (m)

R^2 = Coefficient of determination

R_1, R_2 = Sphere radii (m)

R_a = Arithmetic mean roughness (m)

R_H = Hydrodynamic radius (m)

r = Distance from contact centre (m)

s_0 = Source strength (K/s)

T = Temperature (K)

t_0 = Time of photobleaching (s)

t_b = Photobleaching duration (s)

t_{cycle} = Cycle time (s)

t_d = Acquisition delay time (s)

t_{exp} = Exposure time (s)

T_g = Glass transition temperature (K)

u = Velocity in the x-direction (m/s)

U = Sliding velocity (m/s)

$\vec{u}$ = Velocity field (m/s)

$\overline{U}$ = Non-dimensional speed parameter

u_b = Slip velocity (m/s)

u_{brel} = Relative slip velocity

U_c = Characteristic velocity (m/s)

U_e = Entrainment velocity (U/2) (m/s)

u_S = Input velocity profile (m/s)

$\vec{u}_{xy}$ = Two-dimensional flow field (m/s)

v = Poisson's ratio

w = Numer of pixels for averaging

w_0 = Diffraction limited radius (m)

W = Load (N)

$\overline{W}$ = Non-dimensional load parameter

x_0 = x-centre of Gaussian distribution (m)

y_0 = y-centre of Gaussian distribution (m)

Z = Roelands exponent

ΔI = Absorption rate (W/m^2)

ΔT = Temperature rise (K)

ΔW = Interfacial work of adhesion (J/m^2)

α = Pressure-viscosity coefficient (Pa^{-1})

δ_I = Intensity convergence criterion

δ_u = Continuity convergence criterion

ϵ = Molar extinction coefficient (m^2/mol)

θ = Contact angle (°)

γ = Interfacial energy (N/m)

$\dot{\gamma}$ = Shear rate (s^{-1})

$\dot{\gamma}_A$ = Apparent shear rate (s^{-1})

$\dot{\gamma}_S$ = Input shear rate (s^{-1})

κ = Thermal diffusivity (m^2/s)

λ = Wavelength (m)

λ_b = Time constant (s)

μ = Low shear dynamic viscosity at ambient pressure ($Pa \cdot s$)

μ_g = Glass transition viscosity ($Pa \cdot s$)

μ_p = Pressure corrected low shear dynamic viscosity ($Pa \cdot s$)

μ_R = Roelands reference viscosity ($Pa \cdot s$)

μ^* = Complex viscosity ($Pa \cdot s$)

ρ = Density (kg/m^3)

σ = Shear stress (Pa)

σ_0 = Eyring stress (Pa)

τ = Friction coefficient

τ_{ph} = Phosphorescence lifetime (s)

τ_r = Diffusion time constant (s)

τ_s = Squeeze film time constant (s)

τ_s^* = Non-dimensional squeeze film time constant

ω = Angular velocity (rad/s)

1 Introduction

In this chapter methods of friction prediction in tribological contacts are described. The importance of lubricant rheology, and popular constitutive relations describing the flow curve of shear stress as a function of shear strain, are overviewed. Experimental methods for probing the rheology of lubricants are listed and the limitations of these methods, as well as the need for alternative experimental techniques, are highlighted.

The significance of the velocity profile in an elastohydrodynamic (EHD) contact is discussed. Current theory commonly assumes that the velocity profile is linear, but experimental evidence contradicting such an assumption is shown. Theoretical descriptions of other possible profiles and how they may be related to the rheology of the lubricant are detailed. The measurement of the velocity profile in an EHD contact, which has not been performed experimentally until recently by the author, is therefore suggested as a novel tool for probing the local rheology of lubricants under extreme conditions.

Finally, contemporary experimental methods of measuring velocity profiles are summarised. The potential of applying nanoscopic velocimetry in EHD lubrication and its implementations are discussed in detail. The ultimate choice of the molecular tagging velocimetry technique, photobleached-fluorescence imaging, is justified.

1.1 Friction and rheology of lubricants

When two rubbing surfaces are loaded against each other in the presence of a lubricant, the two surfaces can be separated by the entrained lubricant. This is an example of a tribological contact where the lubrication provides protection from wear while reducing the friction. The thickness of the lubricating film between the rubbing surfaces depends on many parameters including: the load exerted on the rubbing surfaces, W, the velocity at which lubricant is entrained (the average velocity of the two surfaces), U_e, the viscosity of the lubricant, µ, and the material properties of the surfaces. Based on the thickness of the protective film, relative to the roughness of the surfaces, multiple lubrication regimes exist. This was first shown by

Stribeck [1], who measured the friction coefficient for various combinations of these parameters, identifying four lubrication regimes. A typical Stribeck curve is presented in Fig. 1. It shows the variation of the coefficient of friction (COF) as a function of the lubrication parameter, $\mu U_e/W$, where μ is the low shear dynamic viscosity of the lubricant at ambient pressure. At very low speeds lubricant is not entrained quickly enough to prevent it from being squeezed out, such that there is no significant protective film. Hence the rubbing surfaces are in contact. This is the boundary lubrication regime, yielding the highest COF in Fig. 1. As the speed increases, a protective film of increasing thickness is created. However, due to the roughness of the rubbing surfaces, some asperities still rub against each other directly. This region is referred to as mixed lubrication, and the coefficient of friction is still relatively large, but drops as the entrainment speed, and hence film thickness, increases. When the film thickness becomes larger than the roughness of the surfaces, the surfaces are fully separated by a lubricating film. This is the elastohydrodynamic (EHD) region, which is usually characterised by the elastic deformation of the rubbing surfaces, facilitating a constant film thickness, and the lowest friction in the Stribeck curve. As the film grows even larger, at some point, no elastic deformation takes place at the surfaces. This is the hydrodynamic (HD) regime, where the lubricant flow can be described using classical fluid mechanics.

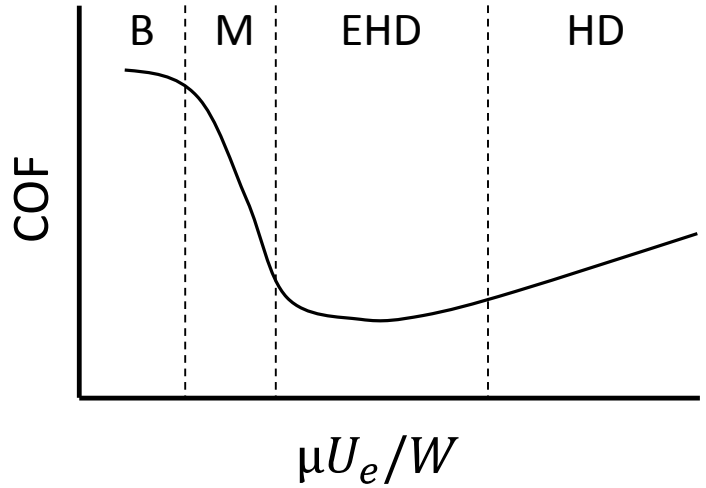


Fig. 1: Stribeck curve: logarithmic plot of coefficient of friction (COF) against the lubrication parameter. Four lubrication regimes are identified. B: boundary, M: mixed, EHD: elastohydrodynamic, HD: hydrodynamic.

The rheology of lubricant in a tribological contact is of great importance as it controls the friction exerted by the contact. The flow curve, which is in the form of $\sigma = f(\mu_p, \dot{\gamma})$, defines the relationship between the shear stress, σ, the pressure corrected low shear dynamic viscosity, μ_p, and the shear rate, $\dot{\gamma}$. The normal pressure distribution in an EHD contact can be determined using Hertzian contact mechanics [2]. The pressure enhanced viscosity of lubricant can be calculated using models such as the commonly used Barus equation [3] and Roelands equation [4]. Other models are available and the appropriate model depends on the particular lubricant [5]. Given the viscosity, the shear rate and the flow curve, the shear stress distribution in the contact is known. The integration of the shear stress over the area of the contact yields the frictional force. Thus, if the rheology of a lubricant is known, the friction coefficient, which is what tribologists commonly endeavour to control, can be predicted [6]. This prediction assumes average values for various properties in the contact, such as normal pressure and temperature. While this may not be the case, it has been shown that despite this assumption the method can be used to make a prediction which agrees well with experimental results [7]. One major assumption for performing this prediction is that the velocity profile of the lubricant is linear. For typical lubricants in plane Couette flow (with parallel plate geometry) at ambient pressures, the solution is indeed a linear velocity profile. However, under the high pressures and shear rates in an EHD contact, the accuracy of this assumption becomes questionable. This does not affect the applicability and accuracy of contemporary methods for friction calculations. However, an inaccurate description of the flow limits the understanding of lubricant rheology which impacts the ability to theorize novel ways of controlling friction, such as by using low friction coatings. Furthermore, the descriptions of transport phenomena like heat transfer are dependent on the flow of the lubricant. Currently, only rheometric measurements of the flow curve of lubricant at pressures and shear rates similar to EHD conditions exist [8]. These results have shown significant non-Newtonian behaviour of lubricants [9,10]. If these effects exist in an EHD contact, the Couette flow assumption may become inappropriate in an EHD contact. It is therefore important to directly investigate the flow of lubricant in an EHD contact to further our understanding of rheology in EHD lubrication.

The normal pressures in EHD contacts are often very high, reaching values of up to 5 GPa in ball bearings [11]. The high pressure increases the viscosity of the lubricant, and can lead to extremely large shear stresses, of the order of 10 MPa [12]. Since the thickness of the film is in the range of a few hundred nanometres, the typical shear rate reaches values of 10^8 s^{-1}. How the rheology of a lubricant is affected by the shear rate the lubricant experiences can vary significantly. For a Newtonian fluid the stress is related to the shear rate by $\sigma = \mu_p \dot{\gamma}$ (see Fig. 2). Under the severe conditions in an EHD contact, the relationship is more complicated and is a subject of continuous controversy.

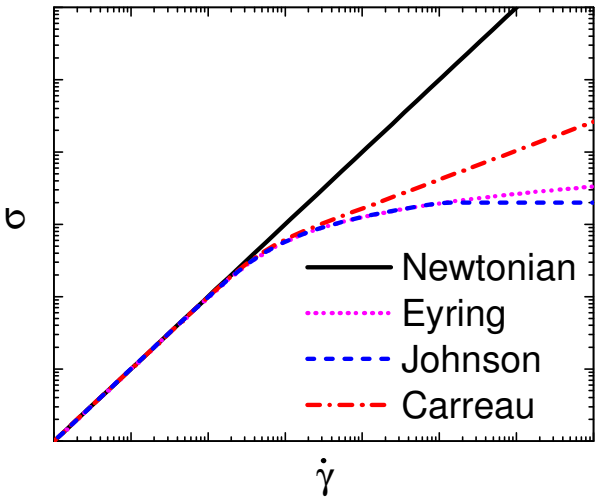


Fig. 2: Log-log plot of flow curves for four commonly used rheological models for lubricants.

Many constitutive relationships describing the rheology of lubricants have been developed, but the validity of these models is not easily assessed [13]. Firstly, measuring the rheology of lubricants under high pressures is a difficult task, as is described later in this section. Secondly, the extreme conditions exerted on the lubricant in a contact can cause the lubricant to become viscoelastic and behave as a pseudo-solid [14]. Common viscosity and rheology models are listed in Table 1. There are two main models, namely the Eyring adaptation by Johnson [15] and the power law implementations of Bair [12]. They are commonly used to relate the shear stress with the viscosity and the shear rate of a viscoelastic fluid.

Viscosity	Rheology	Flow profile
Barus law $\mu_p = \mu e^{\alpha p}$	Johnson $\sigma = \sigma_0 sinh^{-1} \frac{\mu_p \dot{\gamma}}{\sigma_0}$	Linear
Roelands $\mu_p = \mu e^{ln(\frac{\mu}{\mu_R})\left[(1+\frac{p}{p_R})^Z - 1\right]}$	Bair $\sigma = \mu_p \dot{\gamma}[1 + (\lambda_b \dot{\gamma})^{a_b}]^{(n_b-1)/a_b}$	

Table 1: List of models used for EHD lubrication (see nomenclature for parameter descriptions)

Johnson and co-workers developed a limiting shear stress constitutive model [15] (see Fig. 2) which is the most widely adopted model for the study of EHD lubrication. The model is based on Eyring's (see Fig. 2) description of viscosity [16], combined with the Maxwell model for viscoelasticity. The Eyring model describes the activation energy required for a molecule to displace another. Application of an external force will cause molecules to move at a speed which is related to the activation energy. This enables the establishment of the relationship between shear stress and shear rate, which can be shown to be hyperbolic. The Johnson model also imposes a limiting shear stress (see Fig. 2), which limits the greatest value the shear stress can assume. As the shear rate increases beyond the critical shear rate value for the limiting shear stress, the stress remains constant. The limiting shear stress has been attributed to yielding within the liquid in the form of shear banding [15]. Such yielding has been observed experimentally in a high pressure rheometer [17].

Bair opts for the use of a power law relationship for the flow curves of lubricants. The most general form of such a relationship is the Carreau-Yasuda model [18]. This is an empirical model that facilitates a transition between the low shear rate Newtonian region and the high shear rate power law region (see Fig. 2). A main reason the power law relationship has been adopted stems from flow curve results from high pressure rheometers, to which the Eyring model cannot be fitted. Power laws are also typically used to model flow curves for polymers which Bair's models are commonly applied to. It should be noted that both the Eyring and the Carreau-Yasuda models have been fitted to the same experimental traction data successfully [19], highlighting a common issue concerning the application of statistical

regression of rheological models to traction data. The large number of independent parameters in these models allows successful fits to the experimental data. Without independent validation of the models this can ultimately result in the misinterpretation of the physical mechanisms at work. Therefore alternative experimental methods are necessary for improving our understanding of lubricant rheology in EHD contacts.

1.2 Experimental methods for lubricant rheometry

There are generally three main methods of studying lubricant rheology, namely: the impact method, the regression to EHD traction data and high pressure rheometry. In the impact method an object, typically a ball, is dropped onto a thin lubricant film which has been placed on a force transducer. Many variations of the setup have been used as shown in [20]. The method by Jacobson measures the rotational velocity of the ball after impact with the lubricant and relates it to the limiting shear stress. This method was later improved by Höglund [21], who used an optical method of measuring the rotational velocity of the ball (see Fig. 3a). Another technique was developed by Workel *et al.* [20], where the impact and frictional forces were measured using strain gauges (see Fig. 3b). These forces could be used to determine the coefficient of friction during impact. The main advantages of ball impact techniques are the large range of pressures (0-7 GPa) that can be generated and the simplicity of the implementation. High pressures are difficult to achieve using other experimental methods, especially with high pressure rheometry. These pressures are similar to pressures in typical EHD applications such as ball bearings [11], and the impact of the ball mimics the transient loading of a lubricated ball bearing supporting a loaded shaft. However this method cannot measure the low shear viscosity, such that no flow curve can be produced. The impact occurs over a small timescale, which means that the lubricant film may not be equilibrated and steady. It is also difficult to control and measure the temperature during the experiment.

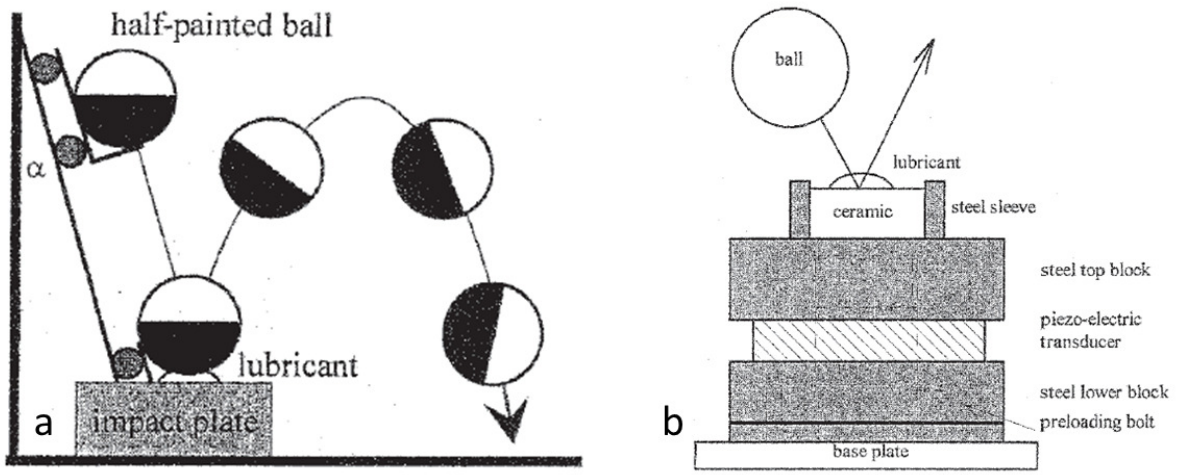


Fig. 3: a) Ball impact apparatus of Höglund. (Adapted from [20]**) b) Ball impact apparatus of Workel *et al.* (Adapted from** [20]**)**

For the EHD traction regression method, traction curves are measured experimentally for a particular lubricant at various temperatures, loads, slide-roll ratios and entrainment velocities. Spatial averages of properties are considered and statistical regression to the experimental data is applied to determine the parameters for the chosen constitutive relationship [15], such as the Johnson model. The film thickness can be measured simultaneously using interferometry, to further constrain the regression. The experimental traction data can be plotted as a flow curve (see Fig. 4a) to which the regression can be applied, enabling the determination of the Eyring stress and the limiting shear stress. The main advantage of the technique is the fact that an actual EHD contact is being studied and many parameters related to EHD contacts can be varied, such as the slide-roll ratio and the geometry of the contact. The main limitation is the use of averaged parameters. Unfortunately the traction cannot be measured locally. This has been somewhat alleviated with the recent development of temperature mapping of EHD contacts, which has been used to study lubricant rheology [13,22] by calculating local shear stresses (see Fig. 4b) from the local temperature rise. The temperature mapping technique requires relatively large temperature rises (order of tens of degrees), which restricts it to high speed contacts with high slide-roll ratios. As the infrared temperature measurement technique and equipment improves, the usefulness of the technique should improve significantly.

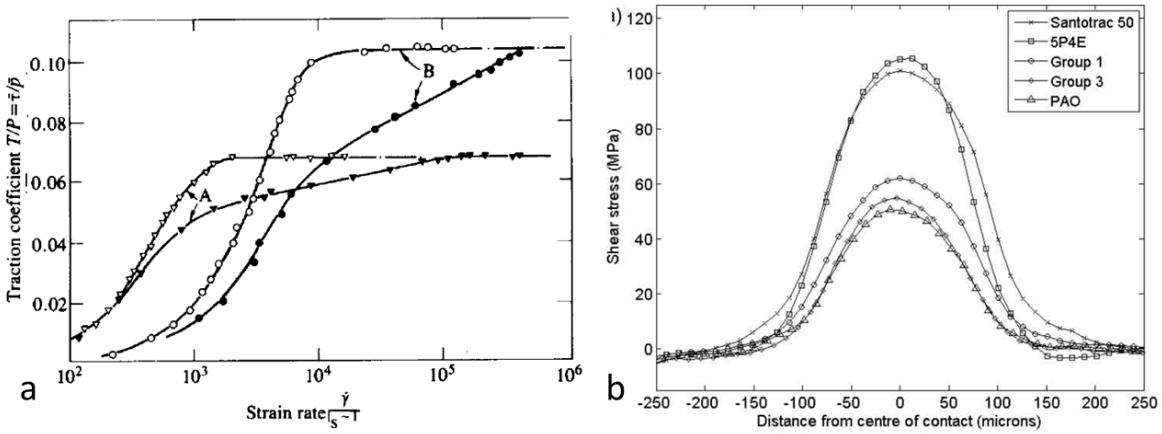


Fig. 4: a) Traction coefficient plotted against shear rate (effectively a flow curve) for mineral oil (triangles) and Santotrac 50 (circles) at various pressures. (Adapted from [15]**) b) Shear stress variations in an EHD contact for various lubricants. (Adapted from** [22]**)**

High pressure rheometers have been developed to study the rheology of a variety of lubricants at high pressure [18,19]. Again, multiple geometries and methods of measuring or inferring the shear stress exist [18]. There is typically a cell with a fixed geometry through which lubricant flows. The cell is pressurised uniformly, and the shear stress is determined by the deformation of some stressed component, which can be measured optically or through the use of a strain gauge. The pressure and temperature can be accurately controlled to determine the low shear pressure-viscosity relationship (see Fig. 5a), given the shear stress and the shear rate in the Newtonian region. This also allows the flow curve of the lubricant to be measured at various pressures and temperatures (see Fig. 5b). An advantage of the technique is that there is optical access to the lubricant through windows, such that the flow of the lubricant can be directly studied. This has enabled the observation of shear bands within the lubricant [14], which have been suggested to be related to lubricant solidification and the existence of a limiting shear stress. A second advantage is the direct measurement of a shear stress in a uniform lubricant. No spatial averaging of the shear stress or the properties of the lubricant are required, which results in the most accurate description of the flow curve among the described rheometric methods. The main limitation is that an EHD contact is not being studied. Effects due to spatial variations in geometry and properties cannot be modelled and confinement induced changes in the rheology are not taken into account [23,24]. The larger gap and the structure of the high pressure rheometer also

restricts the ranges of applicable pressures (up to about 1 GPa) and shear rates (up to about 10^5 s^{-1}) [8], which are significantly lower than those in a typical EHD contact.

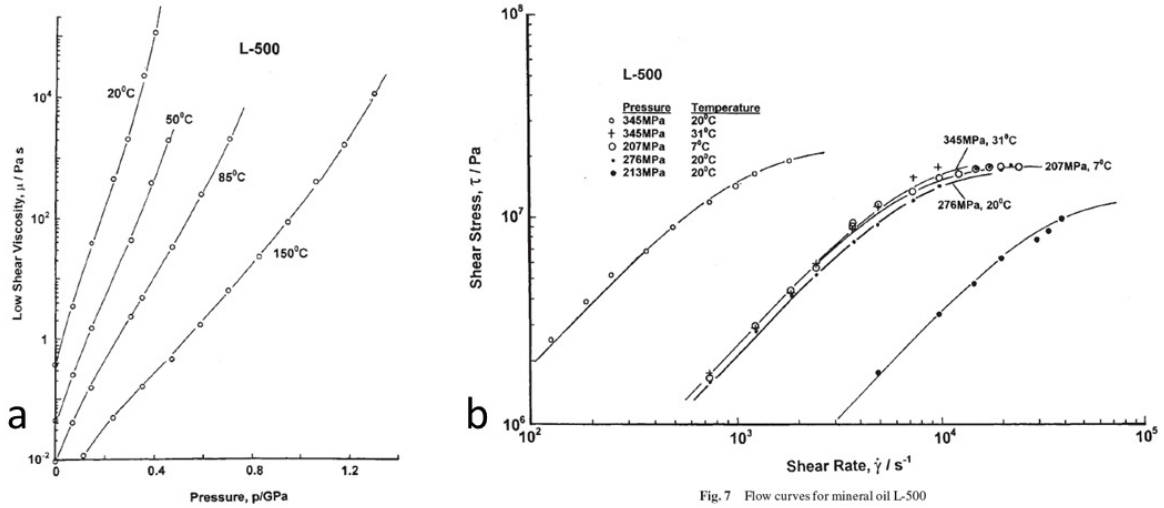


Fig. 5: a) Pressure-viscosity relationship for a mineral oil measured using a high pressure rheometer. (Adapted from [18]**) b) Flow curves for a mineral oil at various pressures and temperatures measured using a high pressure rheometer. (Adapted from** [18]**)**

The techniques described in this section have enabled the study of the rheology of lubricants under extreme conditions. The main findings are (1) the non-Newtonian behaviour of lubricant at high pressures and shear rates, and (2) the existence of a limiting shear stress. The origins of these phenomena remain unknown however. It has been shown that the limiting shear stress can be related to yielding of the lubricant in the form of shear bands [14], when examined by a high pressure rheometer. There is also experimental evidence for slip at the interface between the lubricant and the surfaces [25]. In rheometry, effects of slip [9] and inhomogeneous shear [26] can be investigated by obtaining the velocity profile of the fluid, and comparing this to measured flow curves. By accounting for effects such as slip and inhomogeneous shear, true constitutive relationships can be developed [27,28]. This would aid in the progress towards true prediction of friction in EHD contacts.

In light of the need for an understanding of the rheology of EHD lubricants and limitations of current available methods in this field, a new experimental technique, which is capable of locally measuring the velocity profile in an EHD contact, is proposed. Such a technique would also provide a tool aiding in the explanation of recently observed non-classical behaviour in EHD lubrication, thought to be related to changes in the flow of lubricant.

Prior to detailing the suggested experimental method, current knowledge on the flow of lubricants in EHD lubrication is presented.

1.3 The velocity profile in EHD lubrication

A pure sliding EHD contact for a sphere on flat geometry is shown in Fig. 6. The pressure-induced high viscosity of the lubricant enables the separation of the elastically deformed sphere and the flat by a lubricating film of submicron thickness. The enhanced viscosity of the lubricant causes the rate at which lubricant is squeezed out from the contact to be slower than the rate at which it is being entrained. Mass continuity then requires that the film thickness is mostly constant over the area of the contact. Near the outlet of the contact, there is a horseshoe region of minimum thickness, which is related to the drastic reduction of pressure combined with the pressure driven flow out of the contact, as the viscosity of the lubricant drops.

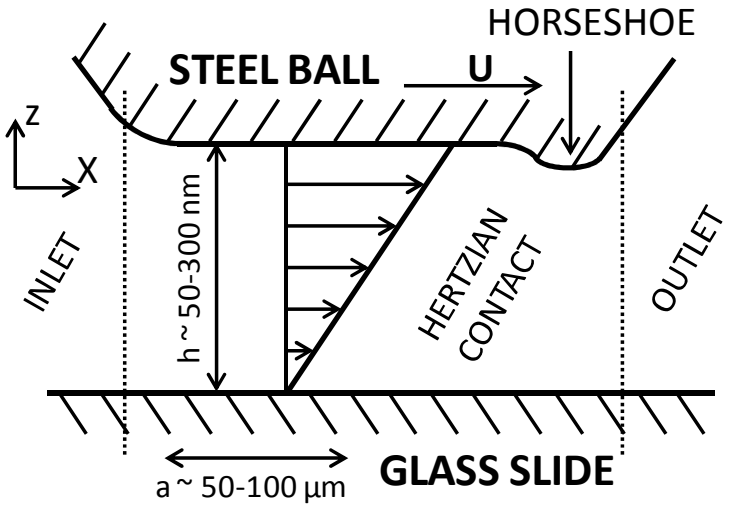


Fig. 6: A linear velocity profile is shown for an EHD contact of film thickness h_c and contact radius a, with the top surface moving at a velocity U. The position of minimum film thickness, the horseshoe, is indicated. (From [29] **with kind permission from Springer Science and Business Media)**

The velocity profile, $u(z)$, in a pure sliding EHD contact (the variation of velocity through the thickness, h, of the film) can be derived from the Reynolds equation [6,30].

$$u(z) = \frac{1}{2\mu_p}\frac{\partial p}{\partial x}(z^2 - zh) + U\frac{z}{h} \tag{1}$$

The solution consists of a quadratic Poiseuille term and a linear Couette term. The pressure driven Poiseuille term is inversely proportional to the viscosity of the lubricant and hence is commonly disregarded for the pure sliding condition [31], when the viscosity of the lubricant is large (as in EHD conditions). This has been shown to be appropriate using computational fluid dynamics [32]. The linear Couette profile means that the shear rate, $\dot{\gamma}$, in the contact is $\dot{\gamma} = 2U_e/h_c$, where h_c is the central thickness of the lubricant film separating the rubbing surfaces. The shear rate can be used for predicting shear stresses in the contact, and thus the friction, using the rheological models discussed in Table 1, section 1.1.

Given the existence of a limiting shear stress described in the previous section, as well as experimental evidence for solidification [33,34] and glass transition [35] of lubricants in EHD conditions, the validity of the linear velocity profile typically used for friction prediction [6] becomes questionable. Some possible velocity profiles that might occur in an EHD contact are depicted in Fig. 7. These include the typically assumed linear Couette flow, slip at the lubricant-solid interface and non-linear profiles such as inhomogeneous shear and shear banding. In the subsequent paragraphs, experimental evidence and theory for these possible velocity profiles are presented.

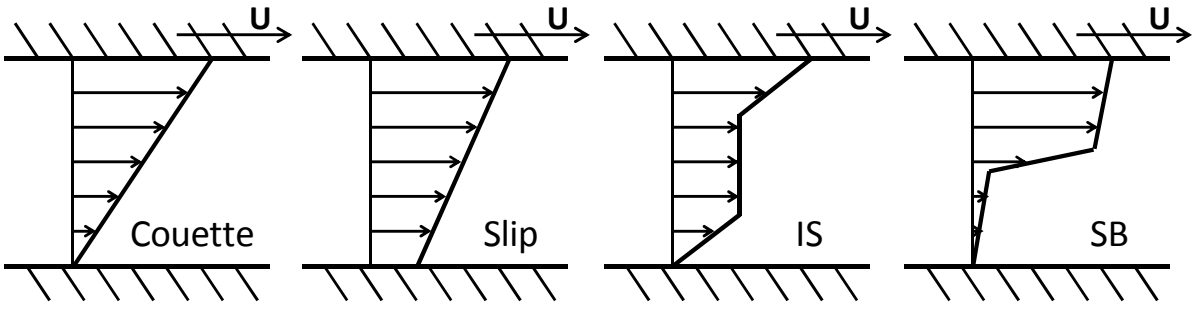


Fig. 7: Some possible velocity profiles for EHD lubrication. IS: inhomogeneous shear, SB: shear banding.

The velocity profile in an EHD contact has never been measured experimentally. Due to the submicron thin films, it is difficult to probe variations of the velocity through the thickness of the film with sufficient resolution. Nevertheless some measurements which can be related to the velocity profile have been made. Reddyhoff *et al.* [31] studied the flow of glycerol in a

pure rolling EHD contact using fluorescence imaging. The EHD contact was maintained at steady state conditions and dye solution was injected near the inlet of the contact. The spatiotemporal fluorescence intensity recorded was related to the average velocity of the lubricant. It was shown that the velocity was mostly constant within the contact and equal to the entrainment velocity, but at the outlet there was a drastic increase in the velocity (see Fig. 8a). This increase was argued not to be due to pressure driven flow by calculating the expected pressure driven velocity, and noting that the side leakage of the lubricant was small.

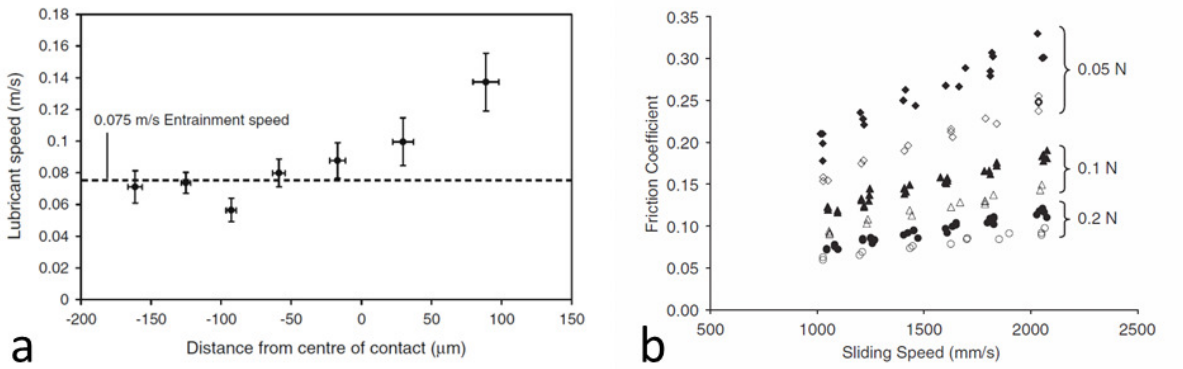


Fig. 8: a) Mean lubricant velocity as a function of position in the contact. (Adapted from [31]**) b) Friction coefficient plotted against sliding speed for non-coated surface (black) and surface with low surface energy coating (white), at various loads. (Adapted from** [36]**)**

Boundary slip has been shown to occur for polymer melts in plane Couette flow [9]. A general observation, as shown in [9], has been that a critical shear stress exists after which the slip velocity increases rapidly. Below this critical value of the shear stress, the no-slip condition holds. Choo *et al.* showed that the friction in a hydrodynamic contact, lubricated with aqueous solutions of glycerol, could be significantly reduced by treating one of the surfaces with a low surface energy coating [36]. The reduction in friction (see Fig. 8b) was explained by the lubricant slipping (second profile in Fig. 7) at the lubricant-solid interface, as described theoretically in [37]. It is also possible that a lubricant that does not slip under ambient conditions may slip in an EHD contact even without a low surface tension coating, due to the high stresses and shear rates. This was observed in a highly viscous lubricant, polybutene, by Guo *et al.* [38]. A dimple was created by dropping a rotating steel ball onto a lubricated glass disc, entrapping the high viscosity lubricant at the centre of the contact.

The motion of the dimple (see Fig. 9a) was then related to the slip velocity of the lubricant. Work from the same group [39] also showed a significant drop in friction coefficient while transitioning from EHD to the hydrodynamic regime (see Fig. 9b). This contradicts a typical Stribeck curve seen in Fig. 1 and has been attributed to the lubricant slipping at the lubricant-glass interface in [25]. Not only does the slip cause a reduction in the friction of the lubricant, it also causes the appearance of a stationary steady state dimple [40]. For the conservation of mass to apply, assuming that the density remains constant, the film thickness can only change by the acceleration or deceleration of the fluid. This indicates that the velocity profile in the contact is spatially non-uniform. This would be the case if slip only occurred in locations with high shear stress, which unfortunately cannot be ascertained in [25,38,39]. Due to the thickness of the dimple only low shear rates (order of 10 s^{-1}) were resolvable.

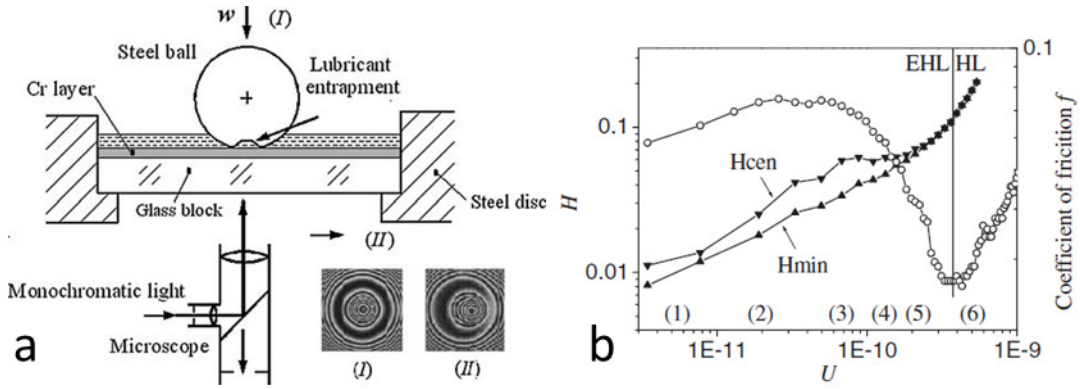


Fig. 9: a) Schematic of the EHD contact and optical setup used for the dimple method. Interferograms (I) and (II) show that the entrapped dimple moves due to the flow of the lubricant. (Adapted from [38]**) b) Stribeck curve (white) and film thicknesses (black) for polybutene, where *U* is a speed parameter. The friction drops at the transition from elastohydrodynamic lubrication (EHL) into the hydrodynamic lubrication (HL) region. (Adapted from** [39]**)**

While slip may potentially explain the anomalous film thicknesses and friction reductions observed in EHD lubrication, there are other explanations available. These explanations deviate from the assumption of a linear Couette velocity profile.

1.4 Inhomogeneous shear flows

The occurrence of dimples as well as shear and load dependent reductions in friction highlight that many questions remain in the field of EHD lubrication. Without proper

experimental techniques to directly probe the flow of lubricant, only conjectures can be made to explain the observed effects. This section showcases some abnormal flows which are thought to be related to these unexplained phenomena.

Parallel plate flows of inhomogeneous material, such as foams [41] (see Fig. 10a) and entangled polymers [42], have been shown to display non-linear velocity profiles due to the viscoelastic behaviour of the materials. Theoretical descriptions of yield stress fluids [43] (see Fig. 10b) and molecular dynamic simulations of amorphous flows [44] have also shown similar results. Although the stress field is effectively constant, inhomogeneity divides the fluid in [44] into three regions of varying shear, referred to as inhomogeneous shear (see Fig. 7). Such behaviour has also been predicted for lubricants at high pressures [45] (see Fig. 10c). It was conjectured that the lubricant solidifies and yields near the surfaces, due to the high shear stresses, creating shear zones of low viscosity. This forces the lubricant at the centre of the thickness to flow as a solidified plug. This description was used to explain the occurrence of a dimple in certain EHD contacts [45]. Both slip and inhomogeneous shear, and possibly a combination of the two, could theoretically cause the existence of the dimple. Another possible cause of the dimple formation stems from adhesion between the lubricant and the solid on a molecular scale [46]. Such adhesion is argued to occur over a region where the viscosity of the lubricant is different to bulk properties, causing inhomogeneous shear.

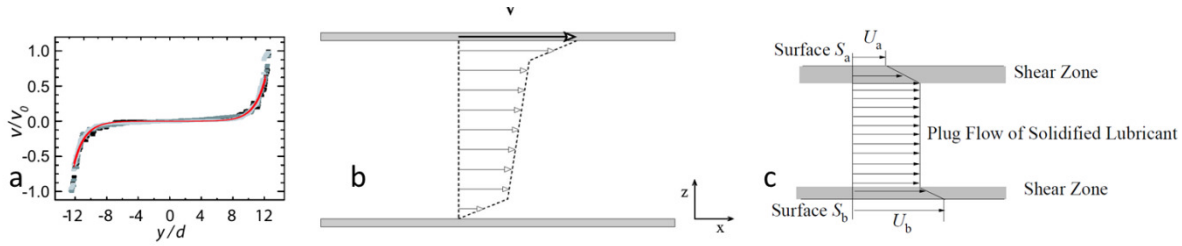


Fig. 10: a) Relative velocity profiles for shear flows of foams at various velocities. (Adapted from [41]**) b) Velocity profile for a yield stress fluid. (Adapted from** [43]**) c) Velocity profile of a solidified model lubricant in an EHD contact. (Adapted from** [45]**)**

There are two types of inhomogeneous shear [47]. Thermal inhomogeneity occurs when shear heating in an EHD contact induces a thermal gradient through the thickness of the lubricant film. This gradient appears due to the transportation of thermal energy from the heat generating lubricant to the solid surfaces. As the viscosity of the lubricant is sensitive to temperature, the thermal gradient causes the local viscosity of the lubricant to vary. This

leads to a variation of the local shear rate and thus results in a non-linear velocity profile [48]. Mechanical or adiabatic inhomogeneous shear can occur due to the viscoelasticity of lubricants. Because of the high shear stresses in the contact it is possible for lubricants to deform plastically. Such yielding typically occurs in a localized band [17], where the viscosity of the lubricant is relatively low, causing the velocity profile to be non-linear.

Molecular dynamics simulations of a simple Leonard-Jones fluid [49] have shown that inhomogeneous shear can occur for lubricants at pressures typical for EHD contacts. After reaching a critical shear rate or shear stress, a region of high shear rate appears at in the centre of the film. In this case the lubricant is solid near the surfaces, and the two solid regions are separated by a central region referred to as shear localization or shear banding (see Fig. 7). Both the cases of inhomogeneous shear and shear banding in [49] showed a significant effect on the friction coefficient. There was also significant heating present in the simulations, which would also cause a reduction in the friction coefficient.

Shear banding has previously been observed experimentally in a high pressure rheometer [17] (see Fig. 11a), where visible bands appeared chaotically above some critical pressure. It was shown that the shear bands nucleate at a particular angle related to the stress state of the lubricant. Shear banding has also been seen at ambient pressure in plane Couette flows of colloidal glasses [50] and wormlike micelles [51] (see Fig. 11b). It is typically not a stable phenomenon as the fluid yields locally. Thus any velocity profile representation of shear banding is merely an average which incorporates the flow due to banding.

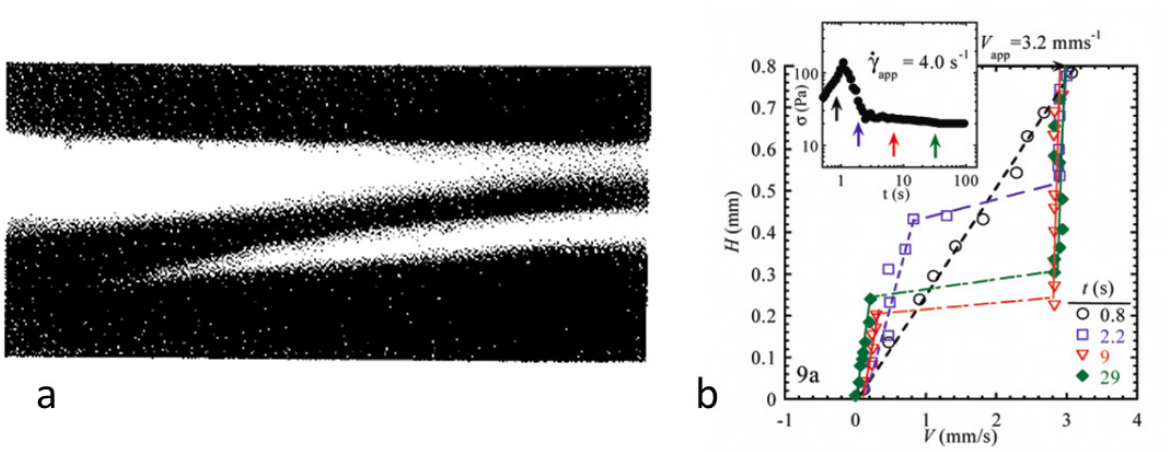


Fig. 11: a) Adiabatic shear band in a high pressure rheometer. (Adapted from [17]**) b) Velocity profile of wormlike micelle solution at various times after start-up of shear. Steady state is reached at 29 s. The inset shows the measured shear stress as a function of time. (Adapted from** [51]**)**

It is commonly assumed that shear stress is constant through the film in a plane Couette flow. Thus, for the cases of inhomogeneous shear and shear banding, there is an existence of multiple shear rates for a constant stress. This could either imply that the flow curve is flat (such as for a limiting shear stress) or that the assumption of a constant shear stress is incorrect. The latter can be explained by a non-monotonic flow curve, which has been suggested to be the cause of inhomogeneous shear and shear banding [52]. As shown in Fig. 12, any rheometric measurement of a non-monotonic flow curve would simply convey an average stress of the two phases, which would appear constant. Otherwise the rheological state of the lubricant would be unstable. One should note that simulations have shown that a non-monotonic flow curve is not a requirement [53] for the existence of inhomogeneous shear and shear banding, although there is no indication that non-monotonic flow curves cannot exist, and the topic is very much still under debate.

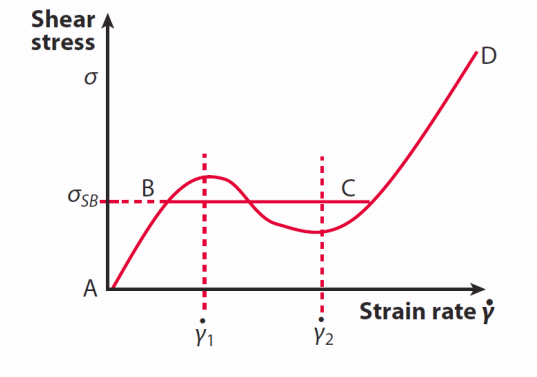


Fig. 12: Non-monotonic flow curve. The line BC indicates the apparent shear stress which would be measured using rheometry. σ_{SB} is the critical shear rate for shear banding. $\dot{\gamma}_1$ and $\dot{\gamma}_2$ are the local shear rates of the solid and shear banding regions respectively. (Adapted from [52])

It is clear that useful information, related to the rheological state of the lubricant, can be extracted from the velocity profile of the lubricant in an EHD contact. Slip would result in an overestimation of the shear rate in the contact and thus errors in any flow curve constructions. The same applies to systems where inhomogeneous shear and shear banding would be present. If the lubricant were to experience local variations in inhomogeneous shear, spatial averaging of properties would be inappropriate. For these reasons it would be extremely useful to probe the velocity profile, to study the local rheology of lubricants in EHD lubrication. Possible techniques for performing such an experiment are discussed section 1.5.

1.5 Experimental velocimetry for EHD lubrication

The difficulty in measuring the velocity profile in an EHD contact is the thin film present, making the application of most contemporary velocimetry techniques unsuitable. Many velocimetry techniques require direct optical observation of the flow being studied. When a collimated laser beam is focused, the light is not focused into an infinitely small point due to the diffraction limit (see subsection 2.1.5). This means that the flow of objects cannot be visualised at resolutions smaller than about 200 nm, which is the approximate thickness of an EHD film. In this section an overview is given on experimental velocimetry techniques. Based on this overview, a technique suitable for velocity profile measurements in EHD lubrication is detailed.

Fluid flow is commonly measured by seeding the fluid with particles that flow with the fluid. As the flow of these particles can be visualised, so can the flow of the fluid. Depending on the concentration of particles they can either be tracked individually using particle tracking velocimetry, or the mean displacement of the particles can be related to the velocity of the fluid using particle image velocimetry (see Fig. 13a). There are also methods which do not require seeding of the fluid. In hot wire anemometry for example, the convection of heat from a probe to the fluid is related to the fluid velocity.

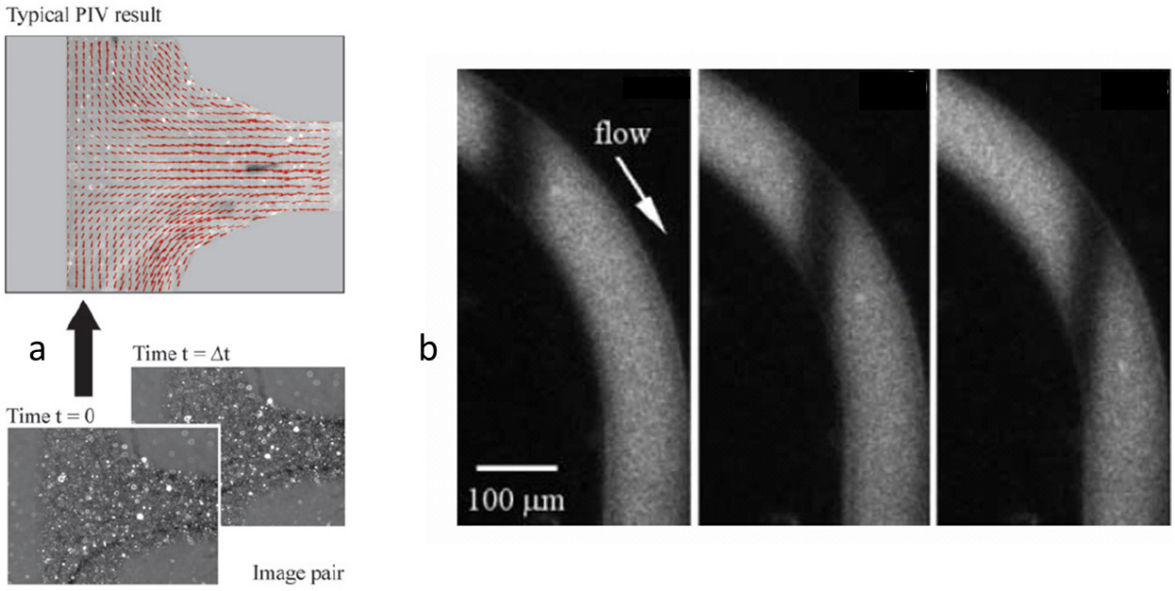


Fig. 13: a) Particle image velocimetry in a T-junction. Acquired images (bottom) and constructed velocity field (top). (Adapted from [54]**) b) Photobleached-fluorescence imaging of microfluidic flow in a turn geometry. (Adapted from** [55]**)**

Molecular tagging velocimetry (MTV) is another set of techniques which have proved very useful for microscopic flows. Fluids consist of molecules. Typically a laser beam is directed to the fluids to initiate some chemical process so that molecules along the path of the beam become tagged, highlighting a volume of fluid distinctly from the rest of the fluid. The chemical process can either be inherent to the fluid being probed, or it can be introduced by seeding the fluid, for example with a fluorescent dye. The subsequent flow of the tagged molecules can then be related to the flow of the fluid. There are many options of initiation processes. Molecules can be tagged by photobleaching [55], where there is a loss in fluorescence within the tagged volume (see Fig. 13b). They can also be tagged by phosphorescence [56], where tagged molecules phosphoresce for a duration, and during this

time they can be imaged (see Fig. 14a). Another option involves using caged fluorescent dye [57], which only fluoresces once it has been uncaged (see Fig. 14b), usually initiated using an ultraviolet laser beam. Finally, nuclear magnetic resonance imaging can also be used to probe flow. Molecules can be tagged by altering the nuclear spin, and the tagged molecules can be imaged as they flow. The technique has for example been used to show the existence of shear bands in wormlike micelles [58].

It is clear that numerous velocimetry techniques exist, all of which could potentially be used for EHD velocimetry. The main limitations of many of these techniques are the size of the probes used and the resolution that can be achieved. A number of techniques have been developed recently to study the existence of slip at the liquid-solid interface as well as the effects of nanoscopic confinement on flow. Some of these techniques could potentially be useful in EHD lubrication. Following, a short background of experimental methods for slip measurements is given. Subsequently, emphasis is placed on techniques related to nanoscopic velocimetry, which would be applicable to the flow of lubricant in an EHD contact.

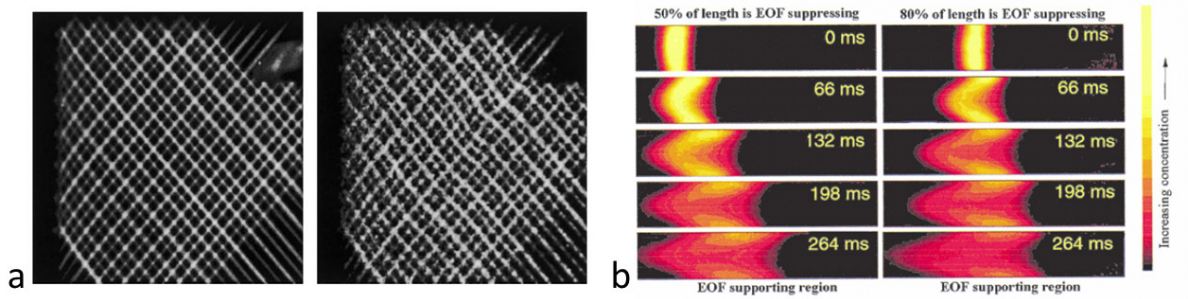


Fig. 14: Phosphorescent grid printed in the intake gas-phase flow of an internal combustion engine. Second image is at a delay of 50 µs where the grid has been distorted due to the flow. (Adapted from [56]**) b) Combined pressure driven and electro-osmotic flow in a microchannel probed by the uncaging of fluorescent dye. (Adapted from** [57]**)**

The breakdown of the no-slip boundary condition has been of great interest in recent years [59]. Interfacial slip can be inferred in a number of ways, without the need of directly measuring the velocity profile. In rheometric measurements the gap between the moving surfaces can be altered. In some cases with polymer melts, the flow curve changes with the gap size [9] (see Fig. 15a). These flow curves are then fitted to a constant slip length model, indicating the existence of slip. Furthermore, this slip can be suppressed by roughening the

surfaces. For substances less prone to slip, such as water on glass, the slip length is typically very small (order of 10 nm), such that no change with gap size would be seen in rheometric measurements. The drainage force due to fluid flow, as two surfaces approach each other, can be measured using a surface forces apparatus [60] or colloidal probe microscopy [61]. It has been shown that there is a reduction of the drainage force compared to the no-slip theoretical prediction in some cases [61] (see Fig. 15b), indicating slip at the interface.

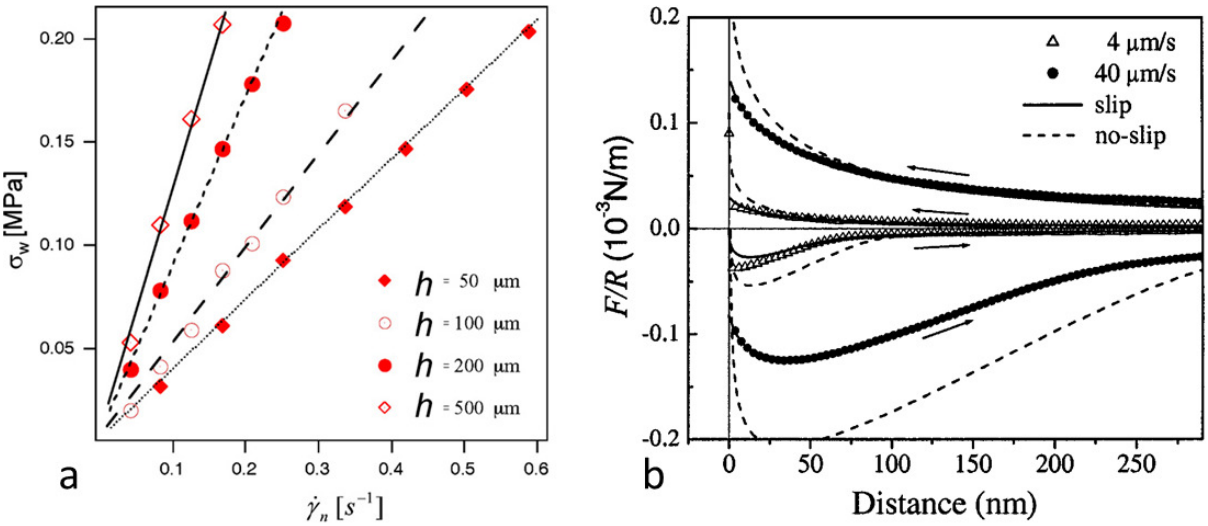


Fig. 15: a) Flow curves of molten polybutadiene at various gap heights. (Adapted from [9]**) b) Drainage force for an aqueous solution as a function of distance at two velocities. The dotted line shows the theoretical force for no-slip. (Adapted from** [61]**)**

Various techniques have been developed for the direct measurement of the flow of fluids at nanoscopic scales to provide evidence for and characterize the existence of slip. One such technique requires the fluid to be illuminated with a laser beam in a total internal reflection (TIR) geometry, such that an evanescent wave is generated and penetrates the substrate (see Fig. 16a). The magnitude of the evanescent wave decays exponentially with distance from the surface, and the characteristic length of this decay is of the order of the wavelength of the beam (hundreds of nm for visible lasers). A region within this characteristic decay length can be examined with this technique. This allows the study of near surface flow. TIR has been used in combination with fluorescence recovery after photobleaching (FRAP) to measure slip lengths of polymers [62] and hydrocarbons [63]. While this has been used to successfully measure slip lengths in microscopic geometries, the technique would not be applicable to the thin film in an EHD contact. TIR can also be combined with PIV to

construct the velocity profile near the surface [64] (see Fig. 15b), as the fluorescence intensity of the particle can be related to its distance from the surface. The size of the particles used for the experiment was 20 nm, which is relatively large compared to common EHD film thicknesses. It was also stated that hindered diffusion of the particles may take place, causing them to slow down. This limited accurate measurements to a distance of 600 nm from the wall. For these reasons, the technique could not be used for EHD lubrication.

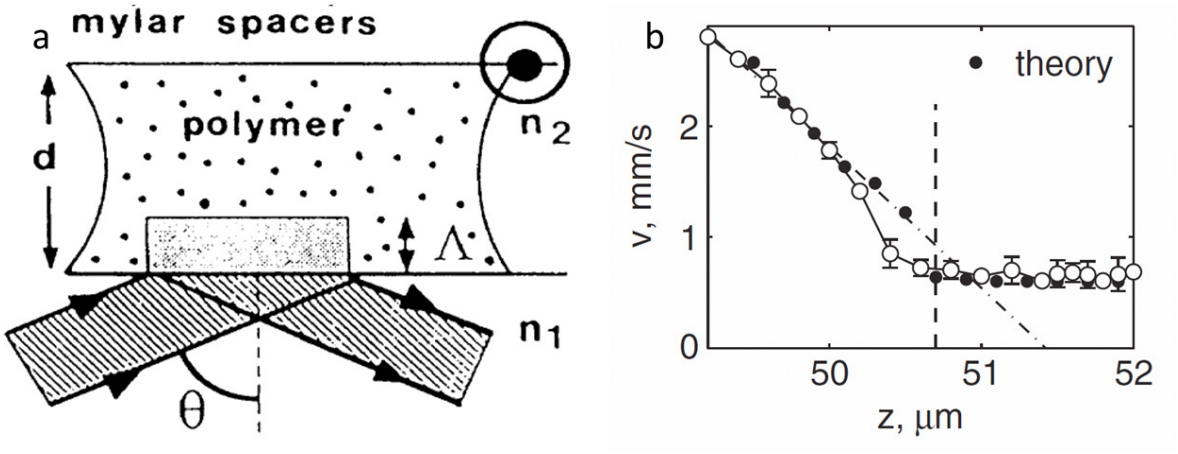


Fig. 16: a) Penetration of an evanescent wave due to total internal reflection at a polymer-glass interface. (Adapted from [62]**) b) Near surface velocity profile measured using double-focus fluorescence cross-correlation. Disagreement with theory due to hindered diffusion can be seen. (Adapted from** [64]**)**

Single-molecule tracking or image velocimetry has not been accurately implemented for small molecules ($\leq$ 10 nm) in conditions applicable to EHD lubrication to this date. Molecular tagging velocimetry (MTV), on the other hand, has already been utilized in an EHD contact to measure the average velocity profile [31]. MTV has also been implemented to measure flow in submicron geometries. Photobleached-fluorescence imaging was recently used in nanochannels as small as 266 nm, to study the flow of confined fluids [65]. This is similar to the application shown in Fig. 13b, although in [65] the thickness of the channels was much smaller. Due to the fast diffusion of the fluorescent probe through the height of the nanochannel, only an average velocity could be determined. The technique was however capable of measuring the local viscosity, based on the diffusion coefficient of the probe, and it was shown that the viscosity decreases as the fluid becomes confined (see Fig. 17a). Stimulated emission depletion microscopy has been combined with photobleaching to measure submicron velocity profiles in nanocapillaries [66] (see Fig. 17b). By using the

optical phenomenon of stimulated emission depletion, the diffraction limit can somewhat be surpassed, enabling a radial resolution of approximately 70 nm. This technique could potentially be applied to an EHD contact, although the z-resolution is still somewhat preventive. The option was not explored in this work due to the complexity of stimulated emission depletion microscopy and the prohibitive resolution.

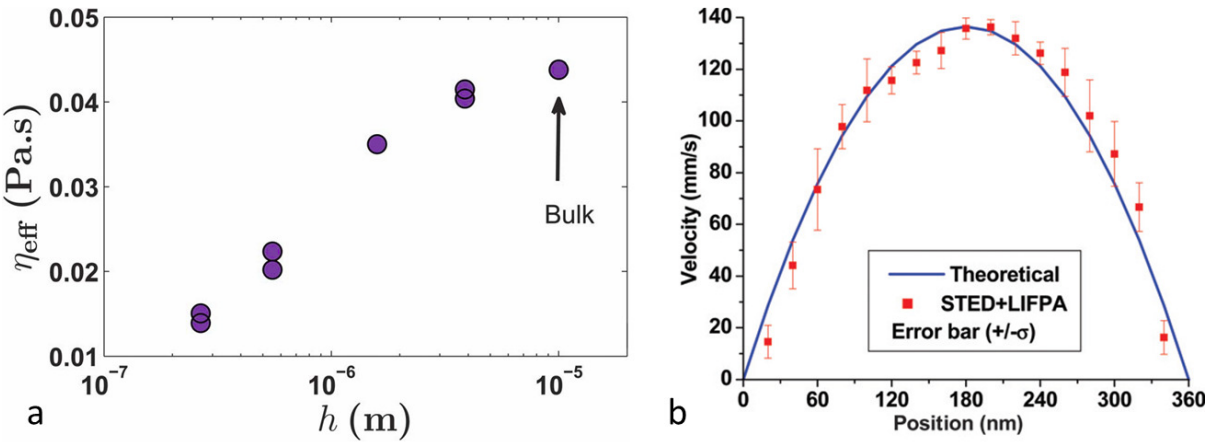


Fig. 17: a) Viscosity variation with nanochannel thickness for a polyacrylamide solution. (Adapted from [65]**) b) Velocity profile of the pressure driven flow of water in a 360 nm capillary. (Adapted from** [66]**)**

In this thesis a molecular tagging velocimetry technique is developed, which is capable of acquiring through-thickness velocity profiles in EHD films as small as 50 nm. Although phosphorescence and uncaging techniques could potentially be applied as well, the available equipment and possible dye-lubricant systems made photobleaching the more appropriate molecular tagging mechanism. Much information could be extracted from velocity profiles measured using such a technique, in terms of the rheological state of lubricants in real EHD conditions. This would be useful for the validation of present EHD theory and for the interpretation of experimental traction data, which was shown in section 1.1 to be far from conclusive. It would aid in the explanation of recently observed abnormal behaviour in EHD lubrication such as non-classical film thickness distributions and friction reduction, believed to be related to lubricant flow, and potentially the solidification of lubricant.

2 Experimental setup and technique

This chapter describes how photobleached-fluorescence imaging is implemented to measure the through-thickness velocity profile of lubricants in an elastohydrodynamic (EHD) contact. In this chapter, the phenomenon of photobleaching is explained. Common fluorophores used for photobleaching techniques are introduced and assessed on their suitability for this work. The chosen system of nile red in polybutene is justified and the dynamic properties of nile red in polybutene are determined. The EHD contact setup is described and evaluated based on capabilities and stability. Predictions for the film thickness and friction in an EHD contact are described. The effect of pressure on the dynamics of a squeeze film of polybutene is then studied to probe the possible solidification of lubricant. Finally, the effect of interference on laser-induced fluorescence is explored and related to the photobleached-fluorescence imaging technique. The preparation of a low surface energy coating facilitating slip is also described, serving as a benchmark example to which the developed technique can be applied.

2.1 Photobleached-fluorescence imaging

2.1.1 Photobleaching

Molecules can absorb light, causing electrons to assume an excited state. Once in the excited state the electrons can return to the ground state through competing mechanisms, for example: non-radiative relaxation by heat, quenching and fluorescence emission. Fluorescence emission involves the emission of a photon of a wavelength equivalent to the energy released by the electron as it returns to the ground state. This is not necessarily the same wavelength as the photon used to excite the molecule, due to the other competing relaxation mechanisms. For this reason fluorescence is often red shifted and spread over a range of wavelengths.

When a fluorescent solution is exposed to light, photobleaching can occur. Photobleaching involves the destruction of the fluorescence relaxation mechanism of a fluorophore. This can occur due to photo-induced damage or covalent bonding of the fluorophore. This results in a

reduction of the intensity of an excited fluorescent solution over time. The prediction of the photobleaching properties of a given compound is complicated. Many mechanisms of photobleaching are possible and they are affected by factors such as the molecular structure, the solvent, excitation intensity and quenching due to dissolved gases. However, the overall rate of photobleaching, k_p, can be described as a constant, by assuming that the fluorescence intensity decays exponentially with time [67]. The temporal intensity distribution during photobleaching, I_p, is then given by

$$I_p(t_b) = I_0 e^{-k_p t_b} \tag{2}$$

where I_0 is the intensity before the photobleaching process and t_b is the duration of photobleaching.

In photobleaching experiments, the quantity of interest is commonly the normalised intensity, I_{NORM}. This value is determined by comparing intensity measurements taken prior to photobleaching and after photobleaching. The normalised intensity can be used to define the relative normal intensity, I_N, (the percentage of photobleaching) according to

$$I_N(t) = 1 - I_{NORM} = \frac{I_0 - I(t)}{I_0} \tag{3}$$

where $I(t)$ is the post bleach intensity at a given time, t, after photobleaching.

2.1.2 Principle of photobleached-fluorescence imaging

In chapter 1, photobleached-fluorescence imaging is identified as an appropriate technique to investigate the rheology of lubricant in the EHD lubrication regime, due to its thickness independent resolution, chemical compatibility and temporal resolution. It is a molecular tagging velocimetry technique that utilises the fact that fluorescent molecules (fluorophores) cease to fluoresce due to photobleaching under strong illumination. If a strong laser beam is focused into a fluorophore-doped fluid, the intensity emitted by fluorophores at and near the focused beam will be lower than that emitted by fluorophores in the remaining fluid. This causes spatial variation in the fluorescence intensity. The technique developed in this work relies on the photobleaching of fluorophores to mark a volume of interest, which has lower fluorescent intensity, within a strongly fluorescent fluid. The evolution of the geometry of

this volume of interest, as the fluid flows, provides information about the dynamics of the photobleached fluorophores and hence the nature of the fluid flow. This is shown conceptually in Fig. 18a.

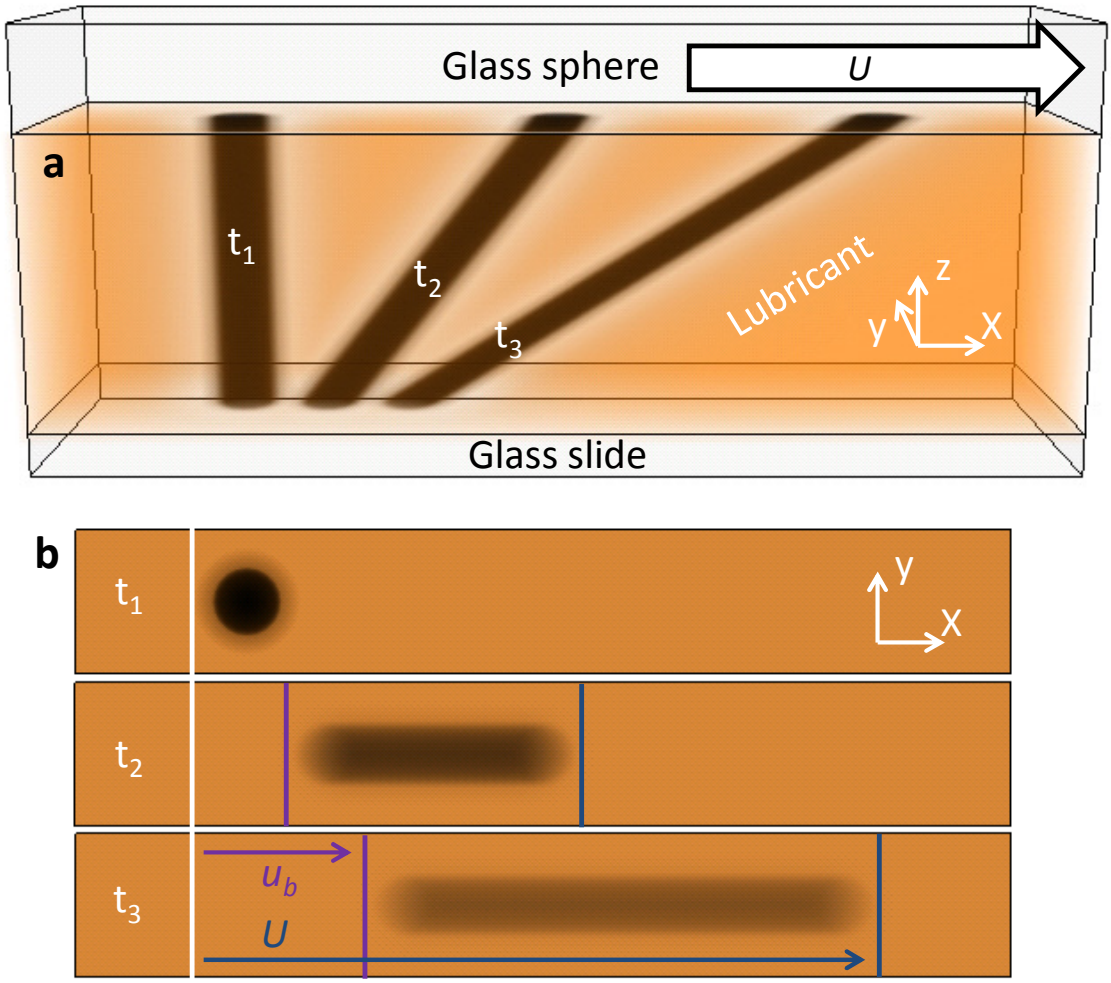


Fig. 18: a) A lubricant film in an EHD contact is depicted. Fluorescent lubricant is indicated by orange. The volume containing the photobleached molecules is shown in black. The intensity distribution is shown at three successive times after photobleaching; t_1, t_2 and t_3. b) The intensity distributions in the top figure are shown in the x-y plane. The velocity of the glass ball is indicated by U and the slip velocity is indicated by u_b.

In the schematic shown in Fig. 18a, a glass ball is loaded onto a microscope glass slide. A parallel plate geometry is depicted as the glass ball is elastically deformed in an EHD contact. The glass ball rotates at speed, U, while the glass slide is stationary. Due to the rotation of the ball, fluorescently doped lubricant is entrained between the solid surfaces, creating an EHD film of mostly constant thickness. At time, t_1, a volume containing photobleached fluorophores has been created in lubricant. This volume assumes the shape of a column, passing through the thickness of the film. As the lubricant flows, the column is

perturbed. One example of how the geometry of the column may have evolved, at later times t_2 and t_3, is also presented in Fig. 18a. In this example the column becomes skewed due to the shearing of the fluid. The projection of the column on the x-y plane, as shown in Fig. 18b, allows the determination of the interfacial slip velocity. Since the glass surface is stationary in this example, comparing the initial position (white line at t_1) and final position (purple lines at t_2 and t_3) of the back edge of the projection suggests that the lubricant slips at the lubricant-glass interface, with a slip velocity of u_b. The flow in this example is assumed to be advective and Brownian diffusion of the fluorophores is neglected. The diffusion of fluorophores in the lubricant can affect the geometry of the photobleached column over time due to exchange between fluorescent and photobleached fluorophores in the z-direction. This is addressed in subsection 2.2.3.

The response of the photobleached column to shear perturbation can be used to determine the through-thickness velocity profile of the lubricant in EHD lubrication. This could be examined most directly by observation in the x-z plane, as shown in Fig. 18a. However, this is not resolvable due to the small thickness of the film (of the order of 100 nm). While the projection of the photobleached column can be obtained in the x-y plane, as shown in Fig. 18b, no direct information about the intensity distribution in the z-direction is known. The intensity distribution in the x-y plane is however the sum of the distribution in the z-direction. Hence a scheme has been designed to extract through-thickness velocity profiles of lubricants in the EHD regime, based on images obtained in the x-y plane. Details of the scheme are discussed in chapter 4.

2.1.3 Optical setup

The optical setup for photobleached-fluorescence imaging employed in this work is shown schematically in Fig. 19.

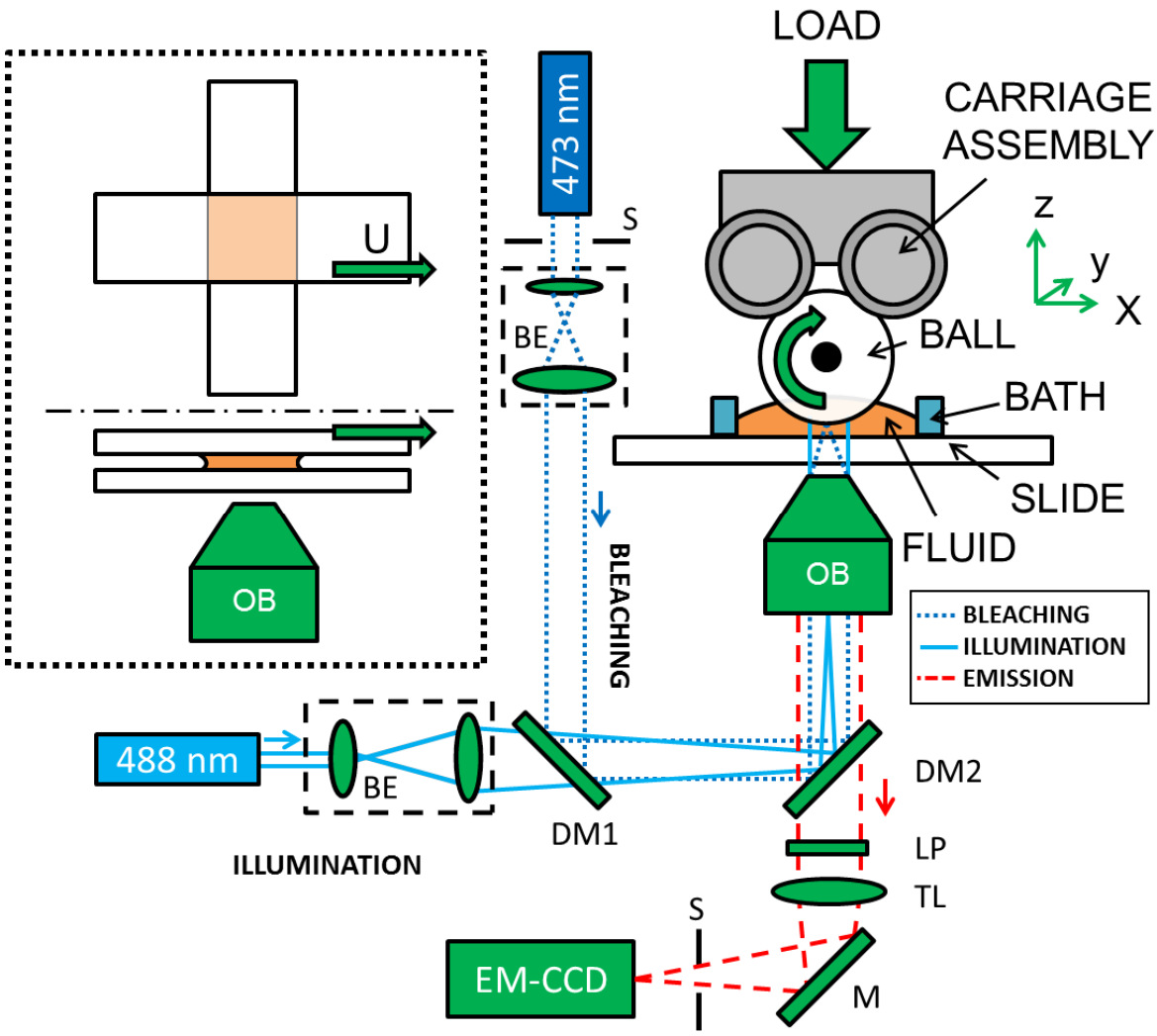


Fig. 19: Beam path diagram with EHD contact setup on stage. Abbreviations: Shutter (S), beam expander (BE), dichroic mirrors (DM1 and DM2), objective (OB), long pass filter (LP), tube lens (TL), mirror (M) and electron multiplying charge coupled device (EM-CCD). The inset in the dotted rectangle depicts the alternate parallel plates setup that can be placed on top of the microscope stage. The arrow indicates that the top slide can be translated at a velocity U.

A mechanical rig which creates an EHD contact using a sphere-on-flat geometry was built on top of a Zeiss Axiovert 200 M inverted microscope. The microscope is equipped with 10x (0.25 NA), 20x (0.4 NA) and 50x (0.7 NA) infinity corrected objectives. An Andor Ixon3 860 electron multiplying charge coupled device (EM-CCD) was used for acquiring images. A 100 mW cyan (488 nm) and a 100 mW blue (473 nm) solid state laser, operating in TEM_{00} mode (Gaussian beam), were used for epi-fluorescent illumination and for photobleaching respectively. The cyan beam was expanded by a beam expander, passed through a beam combining dichroic mirror, DM1, and was reflected into the objective by dichroic mirror

DM2. The blue beam was expanded by a beam expander with a pinhole (not shown), which was used as a spatial filter. It was then reflected by DM1 and directed into the objective by DM2. The fluorescence emission generated in the fluid was collected by the objective, passed through DM2 and a long pass filter (to remove the light of both the cyan and blue lasers), and was focused onto the sensor of the EM-CCD by a tube lens. A Stanford Research Systems shutter (SR 470), placed in the path of the blue laser, controlled the duration of photobleaching. A second shutter was placed in front of the EM-CCD sensor to protect the sensor during photobleaching. Density filters were placed in front of the laser beams to control the power directed into the lubricant. Depending on the speed applied to the ball or glass slide, the power for the bleaching laser was set to 20-40 mW (measured on stage) and the illumination laser was set to 10-20 mW (measured on stage).

2.1.4 Image acquisition

In this study, the model lubricant is doped with fluorophores. Throughout the duration of the experiment, the lubricant is illuminated by the cyan beam. The observation volume fluoresces homogeneously before the photobleaching process. At time t_0, the blue bleaching laser is directed into the lubricant for a predetermined duration, called the bleaching time. This creates a through-thickness photobleached column, which has lower fluorescent intensity compared to the rest of the lubricant, when illuminated by the cyan beam. Observation of the changes in the shape of the photobleached column is then carried out. Since the developed methodology is based on the monitoring of the evolution of the shape of the photobleached column with time, the duration of photobleaching, which governs the initial geometry of the column, needs to be controlled.

A sequence consisting of twenty images were acquired in the experiments. An example of the imaging sequence is given in Fig. 20. The first four frames were taken before the creation of the photobleached column. These are called pre bleach images and are used for normalisation purposes. The subsequent sixteen images under the illumination of the cyan laser, captured after the photobleaching process, recorded the post bleach temporal evolution of the photobleached spot. Images were acquired using the EM-CCD operating in external triggering mode, controlled by a LabJack U6 DAQ, enabling accurate timing to

approximately 200 µs. The period between each frame, the cycle time, t_{cycle}, was chosen such that the last frame was captured when the top surface has travelled a fixed characteristic distance, allowing direct comparison between experiments at different speeds. Depending on the speed, exposure times, t_{exp}, between 100 µs and 100 ms were used.

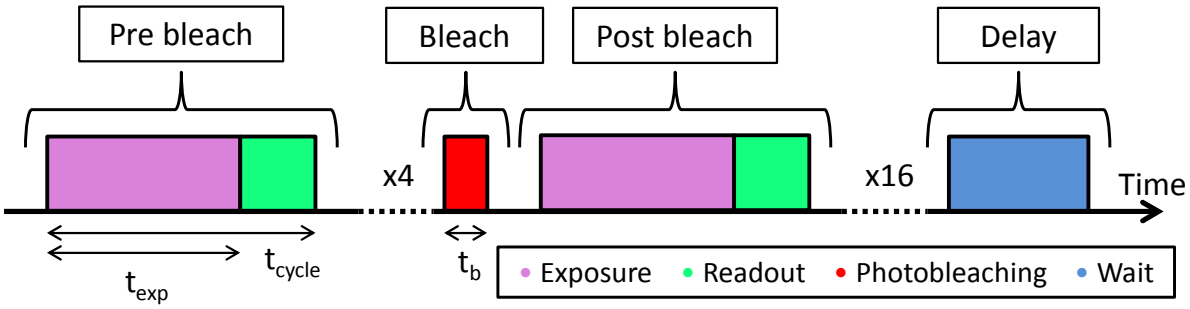


Fig. 20: Schematic of image acquisition sequence. The dotted lines indicate repetitions. The time between bleach and post bleach allows the camera shutter to open.

As the EHD films were very thin, the fluorescence emission, especially at short exposure times, was relatively weak. Hence any background phosphorescence from glass needs to be considered. The mechanism of phosphorescence is described in section 9.1. The main difference between fluorescence and phosphorescence that concerns this study is the emission decay time. Put simply, phosphorescence can occur over a long time (order of milliseconds [68]), as compared to nanoseconds for fluorescence. The phosphorescence from glass (both the glass sphere and the glass slide) can be accounted for by acquiring the sequence in Fig. 20 while blocking the illumination beam. Then only the intensity due to phosphorescence, I_{ph}, is acquired. The corrected relative normalised intensity distribution is then given by

$$I_N(t) = \frac{I_0 - I(t) - I_{ph}}{I_0} \tag{4}$$

Synchronous averaging [69] was also employed to adequately improve the signal for subsequent analysis. Synchronous averaging is typically applied to temporal measurements that can be repeated identically multiple times, such as the flow of light through static materials, or the motion of particles injected into a steady flow. After the event to be studied starts, measurements are made at various times after initiation. This is repeated many times, and the result can be averaged to reduce noise, as the response is expected to be identical every time. It is shown in subsection 2.3.1 that the fluorescence in the contact is

stable. Therefore the photobleached-fluorescence imaging sequence can be repeated to reduce stochastic noise. To apply synchronous averaging, 50-200 sequences were acquired successively in each experiment. A delay between each sequence was applied to ensure that the photobleached fluorophores created during the previous sequence have exited the observation volume, hence not affecting the results in the subsequent sequence. The final experimental result then consisted of twenty frames averaged 50-200 times. Due to relatively long exposure times and synchronous averaging, the technique is not able to resolve transient behaviour or instabilities at short timescales. Despite this limitation, the time averaged response is still useful for describing the rheology of the lubricant.

2.1.5 Optical characteristics

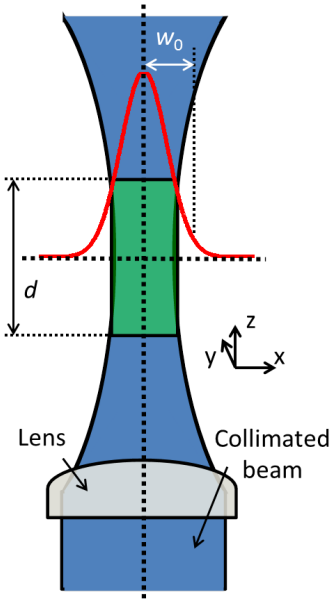


Fig. 21: Schematic of the geometry of a focused Gaussian laser beam. The red line indicates the intensity distribution across the beam waist and the green rectangle shows where the intensity is approximately constant in the z-direction.

A collimated laser beam, with a Gaussian intensity distribution, focused to form a diffraction limited spot, is shown in Fig. 21. The depth of field, d, describes the axial distance (along the beam), in the z-direction for the optical setup, over which the radius of the focused beam on the x-y plane is effectively constant. Hence the focal volume can be approximated by a cylinder and d is given by

$$d = \frac{\lambda n}{NA^2} \tag{5}$$

where λ is the wavelength of the beam, n is the refractive index of the medium (air ~ 1) and NA is the numerical aperture of the objective. This controls the geometry of the photobleached column used in this work. The thickness of the lubricant of interest being studied must be smaller than d for the cross-sectional intensity distribution of the photobleached column to be invariant along the z-direction. The size of the column in the x-y plane is also critical as it affects the spatial resolution of the technique. The radius of the diffraction limited spot, w_0, at the axial centre of the focal point, is the lateral distance at which the intensity drops to $1/e^2$ of the peak intensity. It is given by

$$w_0 = \frac{\lambda}{\pi NA} \tag{6}$$

Using the described setup the theoretical depths of field were $d = 7.57$ µm (10x), $d = 2.96$ µm (20x) and $d = 0.95$ µm (50x). As long as the EHD film is kept smaller than these values the photobleached column can be considered as a cylinder with uniform cross-sectional area and intensity. The theoretical radii were $w_0 = 602$ nm (10x), $w_0 = 376$ nm (20x) and $w_0 = 215$ nm (50x). In practice the spot can be slightly larger due to the laser beam passing a glass substrate and the lubricant as well as due to imperfect collimation and optical aberration. A focused spot created in a thin film of fluorophore-doped lubricant, between two microscope glass slides, is shown in Fig. 22. Fig. 22 was acquired using the 20x objective with 2.5x optovar, given an effective magnification of 50x. The colour map in Fig. 22a confirms the symmetric intensity distribution of the focused spot. Fig. 22b shows the intensity distribution in the x-direction, taken as the mean of five pixels in the y-direction, as highlighted by the yellow rectangle in Fig. 22a. It is clear that the intensity distribution was indeed Gaussian, as indicated by the red line. The radius w_0 was 3 µm, which is larger than the theoretical prediction. This result suggests that improvements are required in order to achieve optimal theoretical optical conditions. While this reduces the maximum spatial resolution of the technique, the assumption of a symmetric Gaussian beam used in the analysis presented in this work remains valid.

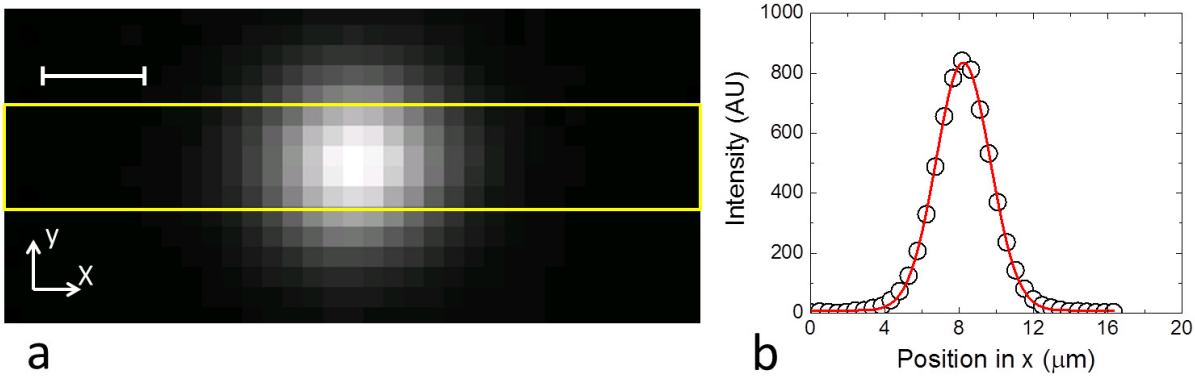


Fig. 22: a) Colour map of the intensity distribution of the focused laser beam in the fluorophore-doped lubricant, which was sandwiched between two glass slides. White represents high intensity and black represents low intensity. The scale bar, which applies to both x- and y-direction, is 2.5 µm and the yellow rectangle indicates the region used for averaging. b) The intensity distribution averaged in the y-direction is shown. The red line indicates a Gaussian fit to the data.

2.1.6 Photobleaching characteristics

For the photobleached spot to be distinguishable, some minimum percentage of photobleaching is necessary. Thus the fluorophore solution chosen must have a sufficient photobleaching rate. The intensity reduction due to photobleaching specified in equation (2) is an exponential decay. As the laser beam, hence the power distribution, is Gaussian, photobleaching will be faster near the centre. Therefore, the shape of the photobleached spot will be increasingly distorted with the amount of photobleaching that has occurred. Recall the temporal intensity distribution, I_p, during photobleaching, shown in equation (2), reproduced below

$$I_p(t_b) = I_0 e^{-k_p t_b}$$

The photobleaching power distribution, P_b, can be described by a Gaussian profile of peak power, defined as

$$P_b = P_0 e^{\left(-\frac{(x-x_0)^2}{2{w_0}^2}\right)} \tag{7}$$

The normalised photobleached intensity distribution of a photobleached spot in a fluorescent solution due to a Gaussian beam can then be found by combining equations (2) and (7)

$$\frac{I}{I_0} = exp\left(-P_0 e^{\left(-\frac{(x-x_0)^2}{2{w_0}^2}\right)} k_z t\right) \tag{8}$$

where k_z is the power independent photobelaching rate and $k_p = k_z P_b$. k_z was determined using the experimental result in Fig. 25b. This enables evaluation of the photobleached intensity profile at various powers, assuming that k_z does not vary with power. Simulated intensity profiles for a typical photobleaching duration of 2 ms, created using various values for P_0 in equation (8), is shown in figure Fig. 23. It is clear from the Gaussian fit (shown as red lines in Fig. 23) that the profile becomes distorted at higher powers. To reach a compromise between the criteria of sufficient photobleaching and negligible distortion a power of 20 mW is chosen, giving an approximate peak relative intensity reduction of 30 %.

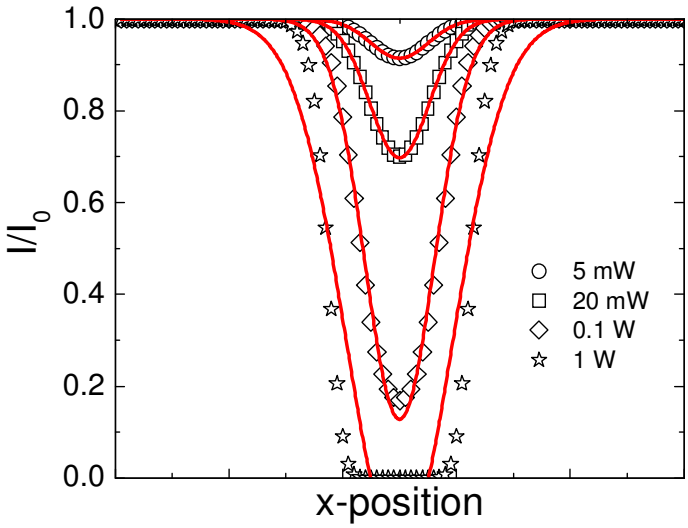


Fig. 23: The simulated intensity distribution after 2 ms of photobleaching is shown at various bleaching laser beam power. The red lines indicate fits to a Gaussian distribution.

To simplify the analysis of the evolution of the photobleached spot, it helps to assume that the initial intensity distribution after photobleaching is Gaussian. For this to occur, the photobleached must happen relatively instantaneously. Otherwise the assumed Gaussian profile of the photobleached spot will be distorted, due to the motion of photobleached fluorophores during the photobleaching process. The effect of the characteristic bleaching time, t_b, is thus studied to find an acceptable value for which distortion can be assumed to be negligible. The parameters affecting the distortion are the radius of the beam, the maximum velocity (the velocity profile also matters but for the purposes of this analysis the profile is assumed to be linear) and the bleach time. These can be used to formulate a non-dimensional number $\overline{B}$

$$\overline{B} = \frac{Ut_b}{w_0} \tag{9}$$

The analytical modelling of the lubricant flow is developed in chapter 4. The effect of $\overline{B}$ on the shape of the velocity profile can be evaluated by solving equation (44) numerically, with an additional source term defined by equation (47). Simulations of the intensity distribution created during the photobleaching process, at various conditions, i.e. different $\overline{B}$ values, were generated. They were then fitted with a Gaussian distribution. The coefficient of determination R^2 for the Gaussian fit was used to assess the amount of distortion. R^2 was evaluated at five beam radii, four velocities between 1-10 mm/s and five bleaching times in

the range 1-10 ms. This evaluation is shown in Fig. 24. At larger values of $\overline{B}$ the effect of the beam radius is significant, but at lower values of $\overline{B}$ the solution is independent of velocity, photobleaching time and beam size. A cut-off for R^2 is chosen as 0.99, giving a critical value for $\overline{B}$ of 4, ensuring that the photobleached spot created is virtually undistorted and thus approximately instantaneous. In this case, for a velocity of 1 mm/s and a photobleaching radius of 3 µm, as shown in Fig. 25, the photobleaching time is required to be less than 12 ms. To achieve a 30 % reduction in intensity, as chosen to result in an optimal shape (see subsection 2.1.6), in 12 ms at a power of 20 mW, a minimum photobleaching rate of 100 s^{-1} is found using equation (2), reproduced here: $I_p(t) = I_0 e^{-k_p t_b}$.

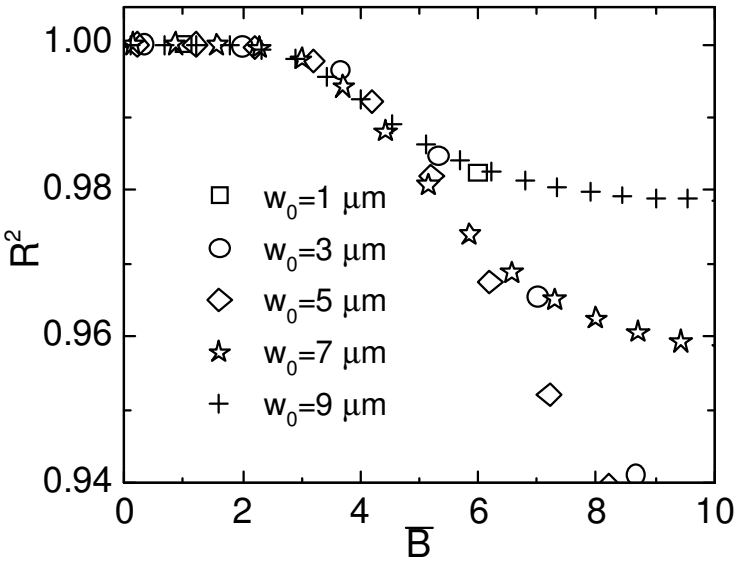


Fig. 24: Plot of the coefficient of determination, R^2, against the non-dimensional parameter, $\overline{B}$, at varying beam radii, bleaching times and velocities. This is used to determine an appropriate bleaching time for the creation of the photobleached spot.

2.2 Fluid properties

2.2.1 Lubricant and fluorophore selection

Since the developed technique is based on fluorescence imaging, an adequate signal to noise ratio, which is governed by various limitations of the EM-CCD used, is necessary for the successful application of the developed technique. With the current setup, the technique requires that the film thickness is of the order of 50 nm, such that a sufficient fluorescent signal is emitted. A second requirement is that the shearing velocity, U, as shown in Fig. 18a, is small enough so that multiple frames can be captured as the photobleached column

moves across the field of view. For this work 16 frames were captured after photobleaching, although a smaller number of frames could be used to enhance the temporal resolution of the technique. At 50x magnification, the field of view of the EM-CCD is 61 µm. The scale for all objectives was calibrated using a calibration slide. As the photobleached column is created in the centre of the field of view, the distance travelled by the photobleached spot in a sequence is approximately 30 µm. The minimum cycle time imposed by the EM-CCD is about 500 µs, totalling a period of 8 ms for the sixteen frames during which the spot is in motion. Thus, the maximum velocity of the top surface, given the acquisition conditions, is 3.7 mm/s. This is relatively low compared to commonly applied speeds for an EHD contact. To achieve an EHD lubricating film at low speeds a high viscosity lubricant is required. Based on the relationship between the viscosity of the lubricant and EHD film thickness, described in subsection 2.3.3, the model lubricants should have viscosities in the range of 10-1000 Pa s. Few lubricants exhibit such large viscosities at room temperature. Three possible candidates examined in this work were polybutenes, polyurethanes and silicone oils. The range of molecular weights available for these oligomers and polymers provided a wide selection of viscosities.

The photobleaching properties of various fluorophores in these lubricants determine their suitability for use in this work. Fluorophores vary greatly in chemistry. Their photo-physical properties and quantum efficiencies depend on: their molecular structures, their interaction with the surrounding solvent/matrix and the experimental conditions applied (such as pressure and temperature). The resolution of the developed technique partly depends on the photobleaching time necessary to create a suitable photobleached column. With shorter photobleaching time the temporal resolution improves. In subsection 2.1.6 it was shown that the minimum required photobleaching rate is 100 s^{-1}. Hence a fluorophore suitable for the developed technique should possess this rate in one of the three selected lubricants, when using the described setup in subsection 2.1.3. For aqueous solutions, coumarin- [67] and fluorescein-based [70] fluorophores are commonly used for photobleaching experiments due to their high photobleaching rate. Most lubricants are however carbon based and thus hydrophobic. Not only do coumarin and fluorescein show low solubility in hydrophobic

solvents but their photobleaching rate is also significantly reduced. Thus an alternative fluorophore must be found. Many fluorophores, including sulphorhodamine B, rhodamine B base, nile red, nile blue and variations of fluoresceins and coumarins, were dissolved in polybutene, polyurethane and silicone oil and tested to find an optimal candidate. Only one suitable combination of fluorophore and lubricant was identified to have an appropriate photobleaching rate constant, namely nile red in polybutene. This shows how important solvent effects are, as nile red is commonly accepted as a photostable fluorophore [71].

Solutions of 0.1-1 mM nile red (Sigma-Aldrich UK) in polybutenes PB920 (Sigma-Aldrich UK), PB2300 (Sigma-Aldrich UK) and Indopol H-300 (INEOS Oligomers) were prepared by magnetic stirring at 150 °C for 5 hours. The elevated temperature was necessary to reduce the viscosity of polybutene, and hence promote mixing. As nile red is hydrophobic, it dissolves well into the polybutene.

Since the adsorption of fluorophores onto the solid surfaces would cause an inhomogeneous intensity distribution in the z-direction of the photobleached column in the EHD contact, the adsorption of nile red in polybutene onto a glass slide was examined. A drop of nile red doped polybutene was placed on a glass slide overnight. This gave time for nile red to adsorb onto the glass surface if surface adsorption was thermodynamically favourable. The glass slide was then rinsed by replacing the bulk of the drop with undoped polybutene daily, over the course of a week. The fluorescence detected from the glass slide and that from a clean glass slide was then compared. No significant difference in intensity was observed, suggesting that the adsorption of nile red on glass is negligible. The suggestion is further supported by the observed stable intensity in the EHD contact, during experiments.

It should be noted that fluorescence emission can be affected by pressure [72]. In an EHD contact this could affect the application of the photobleached-fluorescence imaging velocimetry technique. As the pressure in a contact varies, this could cause problems when attempting to analyse experimental fluorescence results. It is shown later, using laser-induced fluorescence film thickness measurements, in subsection 3.2.6, that the effect of pressure on the fluorescence of the dye was negligible.

The photobleaching rate of a fluorophore depends on the molecular interaction between fluorophores and solvent, the concentration of fluorophores in the solution and the laser power used for photobleaching [67]. The photobleaching rate was therefore determined at a fixed power and a fixed concentration, similar to those used for the experiments. A small amount of 1 mM nile red in H-300 was squeezed between two microscope glass slides by heating the sample and loading the top slide with a weight for an hour. After being left to cool to room temperature the sample was used for testing the photobleaching properties of the solution, using the optical setup. The normalised relative intensity, I_N, was calculated using equation (3). The result for a photobleaching time of 2 ms and a bleaching power of 20 mW (measured on stage) is shown in Fig. 25. The photobleaching process resulted in a peak intensity reduction of 30 % in the photobleached spot. The shape of the spot was similar to that in Fig. 22 (shape of the intensity due to focused laser illumination), indicating that the Gaussian assumption remains appropriate for 30% photobleaching. Using equation (2) the overall rate of photobleaching for this system was determined to be 178 s^{-1}, which is sufficient given the required minimum rate of 100 s^{-1}.

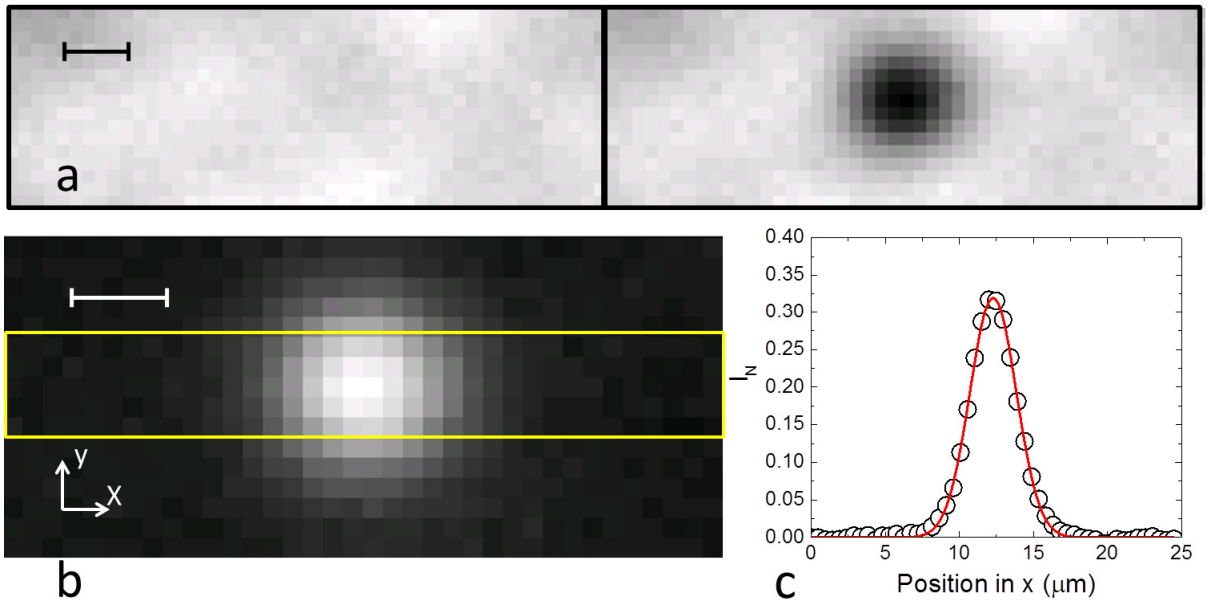


Fig. 25: a) Colour map of the intensity distribution before and after photobleaching. White represents high intensity and black represents low intensity. The scale bar is 2.5 µm. b) Colour map of the I_N distribution of the photobleached spot. Due to the definition of equation (3), photobleaching is represented as positive relative intensity. The scale bar is 2.5 µm and the yellow rectangle indicates the region used for averaging. c) The I_N distribution averaged in y is shown. The red line indicates a Gaussian fit to the data.

2.2.2 Properties of polybutene

Polybutene is an oligomer consisting mainly of repeating monomers of isobutylene (~ 90 %). There are also monomers of 1-butene and 2-butene which serve to reduce the reactivity of the lubricant. Polybutene is often used as a viscosity modifier or plasticizer in combination with base oils.

Some physical properties of the polybutenes used in this work are presented in Table 2. The dynamic viscosity, µ, at 25 °C for the three polybutenes was measured using a Discovery Hybrid Rheometer (TA Instruments), with parallel plates at a constant shear rate of 2 s^{-1} for PB2300 and at 10 s^{-1} for PB920 and H-300. The effect of shear rate on the viscosity of PB2300 at ambient pressure is shown in Fig. 26. In flow tests, the top plate rotates at a constant rotational velocity, which is incremented to determine the flow curve. Since polybutenes are highly viscous, the shear stress became too large for the rheometer, above shear rates of 10 s^{-1}. Oscillatory tests were thus used to measure the rheology at higher shear rate. In this test, the top plate oscillates at a given frequency for a constant rotational amplitude. The resulting parameters are the complex viscosity, μ^*, and the angular velocity,

ω. The Cox-Merz rule [73] shows that for certain polymers $\omega = \dot{\gamma}$ and $\mu = \mu^*$. Fig. 26 supports this relationship as the two measurements overlap, resulting in the full flow curve for PB2300.

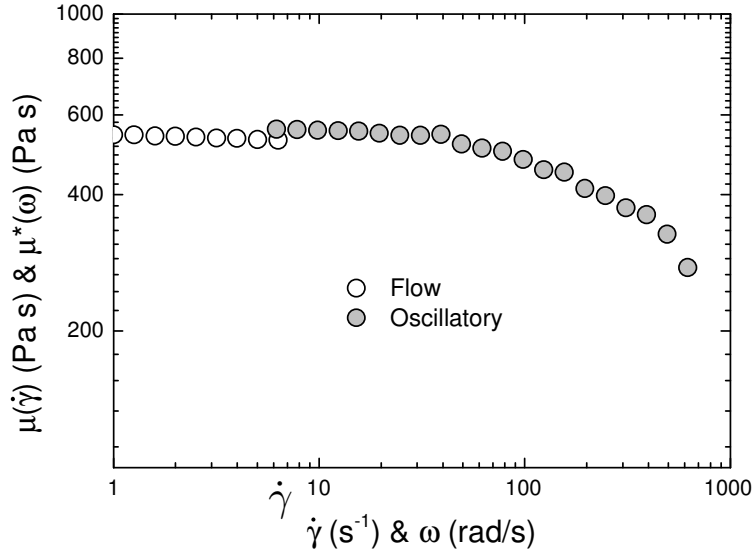


Fig. 26: Rheology of PB2300 measured using flow (white circles) and oscillatory (grey circles) modes.

The results in Fig. 26 confirm observations in [12], that the viscosity of polybutene remains constant up to a critical shear rate, at which point shearing thinning occurs. The value of the critical shear rate varies with molecular weight, temperature and pressure. While the rheology of polybutene was Newtonian below the critical shear rate at ambient condition, it should be stressed that the rheology of polybutene in an EHD contact can deviate from Newtonian behaviour as presented in this work. The viscosities at 100 °C, the molecular weights and the glass transition temperatures were sourced from the product data sheets supplied by the manufacturers. There is no data for the glass transition temperature of PB920. An estimate was made using linear interpolation between the values for PB460 and PB1290 (Sigma-Aldrich UK).

	μ @ 25 °C (Pa s)	μ @ 100 °C (Pa s)	M_n (g/mol)	T_g (°C)	R_H @ 25 °C (nm)
PB920	19.6	0.2-0.235	920	-68.1	0.71
H-300	66	0.65-0.7	1300	-66.9	0.85
PB2300	455	4-4.4	2300	-64.9	1.12

Table 2: Properties of polybutenes including dynamic viscosity μ, number average molecular weight M_n, glass transition temperature T_g and approximate (see text) hydrodynamic radius R_H.

The size of the molecules used in the system is important, as it affects the resolution of measurements in the z-direction. If very large molecules were used, for example with a radius of 20 nm, in a thin film of 50 nm the velocity would not be resolvable in through the thickness of the film. Fortunately polybutenes exhibit large viscosities at relatively low molecular weight. There is no known published data on the hydrodynamic radius, R_H, for polybutene. Attempts at determining R_H using dynamic light scattering failed due to insufficient resolution. Since polybutenes are mainly composed of isobutylene monomer, R_H of polybutenes were estimated using existing small-angle X-ray scattering data [74] for polyisobutylene. These are listed in Table 2. There will be slight differences between the hydrodynamic radii of polybutene and polyisobutylene, but their viscosities are similar for corresponding molecular weights (to about 5 %), such that the R_H should be comparable. The fluorophore, nile red, has a R_H of approximately 0.5 nm [75], which is smaller or comparable in size to the polybutene studied. The viscosity of nile red doped polybutene was measured and is comparable to that of neat polybutene.

The rheology of a low molecular weight polybutene (Mw = 510 g/mol) has been studied using high pressure rheometry [12]. At low shear rates and ambient pressures polybutene is a Newtonian fluid. As both increase, polybutene shows shear-thinning behaviour. The low shear viscosity dependency on pressure was measured in [12], and fitted using an empirical formula. The glass transition viscosity was found to be 10 MPa s. A simple comparison can be made between the expected viscosity for the polybutenes used in this work and the glass

transition viscosity of polybutene in [12]. The low shear viscosity at elevated pressures can be predicted using the Barus equation

$$\mu_p = \mu e^{\alpha p} \tag{10}$$

where μ_p is the pressure corrected low shear viscosity, μ is the low shear viscosity at ambient pressure, α is the pressure-viscosity coefficient and p is the pressure. The Barus equation is usually not valid at very large pressures but the pressure-viscosity results in [12] indicate that an exponential expression is a reasonable approximation for the purposes of the comparison. In this work interferometry (see section 3.1) was used to determine α giving a value of about 32 GPa^{-1} for PB2300. Common pressures in tribology applications are usually a few 100 MPa but they can reach up to GPa in rolling element bearings. For PB2300 at 300 MPa and 25 °C, which is within the range of pressure used in this work, equation (10) gives a viscosity of 6.7 MPa s. This value is close to the glass transition viscosity, μ_g, of 10 MPa s. Hence it is expected that polybutene is extremely viscous and is completely or partially solidified under the experimental conditions in this work. The fact that polybutene is likely to solidify allows a gauge of the effectiveness of the developed technique. If solidification occurs, the velocity profile would be expected to deviate from a linear profile, as argued by Ehret and Dowson [45].

Polybutene is much more viscous at ambient pressure than commonly used lubricants, such that solidification is more likely to occur in polybutene than in lubricants typically used in tribology applications. A comparison with the widely used lubricants mineral oil ($\mu_g = 10^7 Pa\ s,\ \alpha = 23.1\ GPa^{-1}$) [19] and polyalphaolefin ($\mu_g = 10^6\ Pa\ s,\ \alpha = 12.6\ GPa^{-1}$) [19] shows, however, that these lubricants would reach the glass transition viscosity at pressures of about 2 GPa, which are commonly encountered in bearings. Such enhanced viscosity has been observed by others, in the form of the limiting shear stress [33,76,77]. Hence observations made here are not necessarily unique to polybutene and they have important effects on the behaviour of lubricants at high pressure.

2.2.3 Diffusion coefficient of nile red

Since the developed technique employs fluorescent imaging to obtain information about the rheology of EHD lubricant, care should be exercised to ensure that the Brownian diffusion of the fluorophores is considered. The Péclet number describes the relative effects of advection and diffusion on fluid flow. It is shown in section 4.1 that a Péclet number of at least 100 is necessary for dispersion and diffusion effects to be negligible, allowing the flow to be modelled as pure advection. The diffusion coefficients of nile red in the three polybutenes were measured using fluorescence recovery after photobleaching. The average intensity of a photobleached spot in a stationary fluid increases over time due to the diffusion of bleached and unbleached fluorophores. Two possible relations describing the exponential recovery due to Brownian diffusion were attempted, which are defined as

$$I(t) = 1 - \frac{C_m}{1 - {}^{t}\!/_{\tau_r}} + C_i \tag{11}$$

$$I(t) = 1 - C_{m1} e^{-{}^{t}\!/_{\tau_{r1}}} - C_{m2} e^{-{}^{t}\!/_{\tau_{r2}}} + C_i \tag{12}$$

where C_m and C_i are population constants for the mobile and the immobile populations respectively and τ_r is a diffusion time constant. C_{m1} and C_{m2} are the population constant of two mobile populations which exhibit fast and slow diffusion dynamics. The difference between the time constant acquired using equation (11) and the slower time constant acquired using equation (12) was found to be negligible (within 20 %). The faster time constant in equation (12), although it was ten times faster than that obtained from equation (11), only constituted a small fraction (30 %) of the recovery. For these reasons equation (11) was used for all fits. The diffusion coefficient, D, assuming two-dimensional diffusion, can be determined by

$$D = {w_0}^2/(4\tau_r) \tag{13}$$

where again w_0 is the radius of the photobleached spot. A photobleached column (with uniform w_0 along z) was created in a polybutene film with 1 mM nile red, between two glass slides. The intensity recovery of the photobleached column was monitored by acquiring images every 10 s with the optical setup described in subsection 2.1.3, using an exposure and

excitation time of 100 ms. In this experiment an additional shutter was installed in front of the illumination beam to reduce background photobleaching, which cannot be completely avoided. To account for the background photobleaching the data was analysed in the following manner. For each frame the intensity of 4x4 pixels at the centre of the spot were averaged, denoted as I_{spot}, to track the intensity of the photobleached spot. I_o is the average intensity of the image before photobleaching has been carried out. Due to background photobleaching and fluctuations, a second intensity average was made over 4x4 pixels, far from the bleach spot, representing the background intensity, I_{bg}. The normalised intensity of the bleach spot, $I_{norm}(t)$, is then given by

$$I_{norm}(t) = \frac{I_{bg}(0)}{I_{spot}(0)} \frac{I_{spot}(t)}{I_0} \Big/ \frac{I_{bg}(t)}{I_0} = \frac{I_{bg}(0)}{I_{spot}(0)} \frac{I_{spot}(t)}{I_{bg}(t)} \tag{14}$$

where $t = 0$ is the time immediately after photobleaching. Typical intensity recovery curves for the three polybutenes can be seen in Fig. 27. Equation (11) is used to determine the diffusion time constant of nile red in the x and y dimensions. It fits the data for PB920 and H-300 well, as shown by the coefficients of determination, R^2, given in Table 3. The rates of recovery for PB920 and H-300 versus PB2300 differ significantly. This is partly because a longer bleach time was used for the PB2300, creating a larger photobleached spot (see table 2). The longer it takes to reach intensity equilibrium, the more data is needed for proper curve fitting. The lower quality of fit for PB2300 can also be partially attributed to the relative increase in drift associated with longer experiment durations.

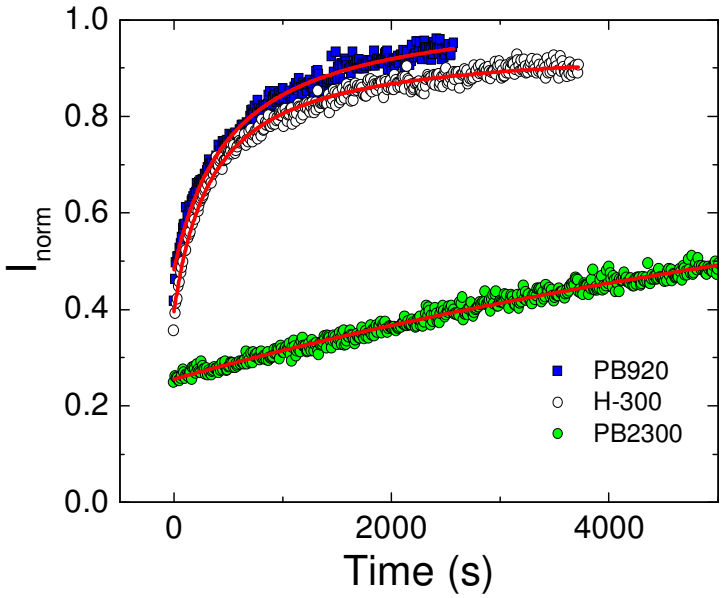


Fig. 27: Fluorescence recovery after photobleaching curves for the three polybutenes. The red lines indicate the fit to equation (11). The data for PB2300 extends to 10000 s.

The diffusion coefficients of nile red in polybutenes, D, based on equation (11), are shown in Table 3. A prediction for the diffusion coefficient, D_P, can also be made using the two-dimensional Stokes-Einstein equation

$$D_P = k_b T/(4\pi\mu R_H) \tag{15}$$

where k_b is the Boltzmann constant and T is the temperature (25 °C in this case). The hydrodynamic radius, R_H, of nile red of about 0.5 nm [75] is used and the predictions are given in Table 3. The experimental results for nile red in polybutene match the predictions well. This confirms that the use of equation (11), rather than a two-component fit, does not significantly affect the conclusions made about the diffusion of nile red in polybutene.

	w_0 (µm)	P (mW)	t_b (ms)	τ_r (s)	D (m²/s)	D_P (m²/s)	R^2
PB920	6	50	25	355	$2.5\text{x}10^{-14}$	$3.3\text{x}10^{-14}$	0.983
H-300	5	50	25	517	$7.7\text{x}10^{-15}$	$9.9\text{x}10^{-15}$	0.987
PB2300	11	10	1000	14800	$2.0\text{x}10^{-15}$	$1.4\text{x}10^{-15}$	0.919

Table 3: Diffusion properties of nile red in polybutenes. P and t_b denote the laser power at the sample and the bleaching time applied.

Using the experimental results in Table 3, for H-300 at a speed of 360 µm/s and a film thickness of 170 nm, the Péclet number is about 8000. Thus the Brownian diffusion of nile red in polybutene is negligible, on the timescale of the experiments. Hence the flow of nile red in polybutene, which is representative of the rheology of polybutene in the EHD contact, is driven by advection under all conditions in this work. This analysis does not take into account the pressure induced reduction of the diffusion coefficient [24], which would increase the Péclet number even more. This provides further confidence that the flow for all experiments conducted in an EHD contact is dominated by advection.

2.2.4 Heating due to photobleaching process

As fluorescent molecules are excited by light, energy is dissipated through multiple mechanisms, one of which is heating. In common fluorescence imaging setups such heating is negligible. Yet, for high power experiments such as photobleaching, it can be critical [78]. If there is significant heating during the photobleaching process the rheology of the lubricants would be altered and the analysis would need to take that into account.

The heating of cell surfaces during photobleaching experiments has been modelled by Axelrod [79]. It was shown that the temperature rise due to photobleaching was negligible under common experimental conditions for FRAP. In this work however the heat source is three-dimensional and thus potentially much larger. Hence the analysis by Simon *et al.* [80], where a cylindrical source was considered, is more appropriate for modelling the heat generated due to photobleaching in this work. Simon *et al.* consider a cylindrical Gaussian heat source, completely bounded by liquid, of source strength, s_0, given by

$$s_0 = \Delta I/(\rho C l) \tag{16}$$

where ΔI is the absorption rate of the fluorophore in the liquid, ρ is the density of the liquid, C is the specific heat capacity of the liquid and l is the thickness of the specimen. The absorption rate is defined as $\Delta I = I_c A \ln(10)$. Here $A = \epsilon c l$ is the absorbance, with ϵ being the molar extinction coefficient of the fluorophore and c being the concentration of fluorophores in the solution. $I_c = 2P/(\pi {w_0}^2)$ is the central intensity of the Gaussian beam, of radius w_0, and P is the power. This model heat source assumes that all energy absorbed by the fluorophore is converted into heat, which is a conservative assumption. Using this model heat source, the temperature rise of the lubricant at the centre of the heat source, ΔT, can be defined as

$$\Delta T(0,t) = \frac{s_0 {w_0}^2}{8K} ln(1 + 8\kappa t_b/{w_0}^2) \tag{17}$$

where κ is the thermal diffusivity of the liquid and t_b is the bleaching time. Using typical parameters of $w_0 = 1.5 \cdot 10^{-4}$ cm, $P_0 = 20$ mW, $\epsilon = 38000$ mol^{-1}cm^{-1}, $c = 0.001$ mol, $l = 1.8 \cdot 10^{-5}$ cm, $t_b = 8.5$ ms and parameters for polybutene found in [81], the predicted temperature rise is 1920 °K. The cause for the significant temperature rise in this work is the high concentration of fluorophores required, due to the small film thickness. At such high temperature polybutene would simply evaporate, which was not observed in the experiments. The presented analysis assumes an unbounded cylindrical heat source, which does not account for the heat dissipating effects of the glass rubbing surfaces used in this work. No analytical solution exists for the temperature rise of a bounded cylindrical heat source. Therefore simulations were carried out using the open source finite element software ElmerFEM (http://www.csc.fi/english/pages/elmer), to determine the temperature rise due to photobleaching.

A heat source, in units of W/kg, is required for the simulation. A suitable expression for the heat source in W/m^3 is given in [82] as

$$s_0 = 4.6\epsilon c P_0 / \pi {w_0}^2 e^{-2r^2/{w_0}^2} \tag{18}$$

where r is the radial distance from the centre of the beam. Division with the density yields the source in units W/kg.

A two-dimensional geometry was created in axisymmetric coordinates to model heat transfer from a cylindrical source within the lubricant film, bounded by a glass surfaces with outer boundaries set to 293 K. The source was defined using equation (18). The geometry of the bounded lubricant is shown in Fig. 28, with an inset of the result determined using the previously stated parameters and typical parameters for glass. A simulation was also carried out for an unbounded lubricant film with periodic boundary conditions in z. In the unbounded lubricant film the steady state temperature rise was approximately 1500 K, which is close to the analytical solution of 1920 K. The bounded simulation, as presented in Fig. 28, clearly shows that most of the heat is dissipated in the glass surfaces and only a maximum temperature rise of 5.5 K is reached with continuous photobleaching. Transient simulations were also carried out with t_b = 8 ms, resulting in a temperature rise of 3.5 K, and the heat generated dissipated within 1 ms after cessation of photobleaching. Considering that the time between the photobleaching and the first image is about 2 ms, and that a typical measurements occur over 100 ms after photobleaching, the heating effects of photobleaching are negligible. This conclusion is consistent with the observation that variations in laser power used for photobleaching and fluorophore concentration, other than changing the size of the photobleached spot, had negligible effects on the rheology of EHD lubricants investigated.

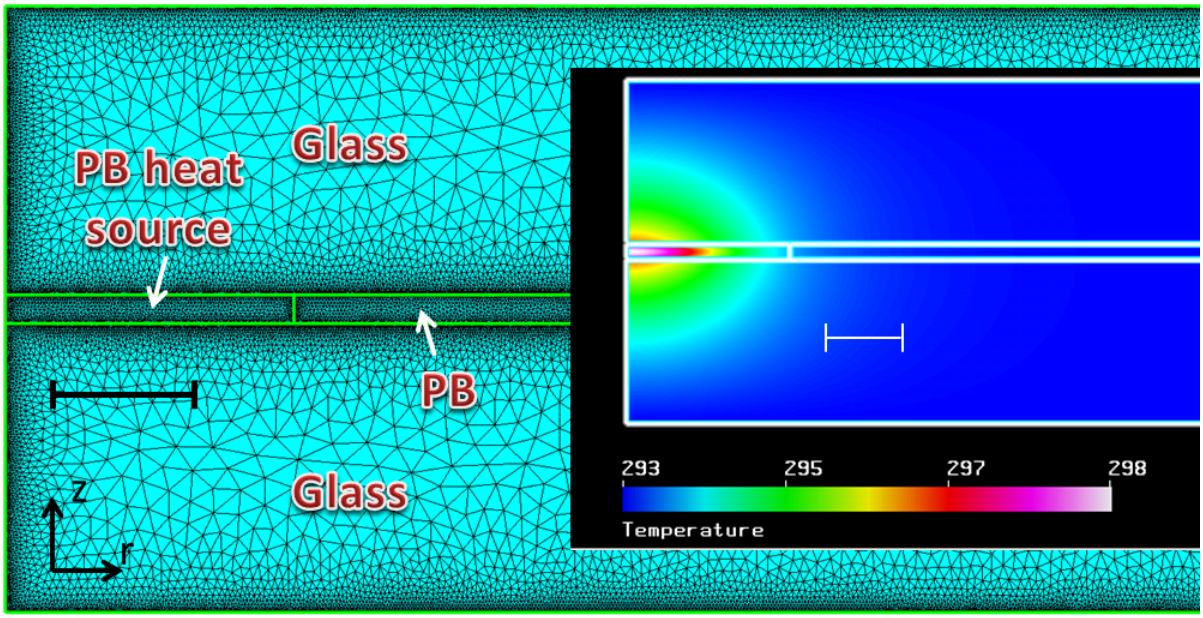


Fig. 28: Mesh of the bounded lubricant film being heated by a cylindrical heat source. The scale bar is 0.5 µm. A Gaussian heat source is applied in the polybutene (PB) heat source rectangle. The geometry extends further in r than shown to simulate an infinite cylinder. The inset shows the result of the simulation indicating a steady state temperature rise of 5.5 K. The scale bar is 0.5 µm.

2.3 EHD Contact

2.3.1 Establishment of an EHD contact and its stability

An EHD contact was created by a mechanical rig which loads a ¾" glass ball (PCS Instruments, borosilicate grade 25) against a microscope glass slide (VWR, borosilicate). Lubricant was entrained between the surfaces due to the rotation of the glass ball. A schematic of the contact is shown in Fig. 19, with the optics used for photobleached-fluorescence imaging velocimetry. The borosilicate glass slide was fixed to the optical stage. The substrate could be replaced by other transparent substrates, such as a sapphire window or a polydimethoxysilane (PDMS) coated glass slide to vary the elastic and interfacial properties of the stationary flat surface. A ¾" diameter steel ball (PCS Instruments, AISI 52100 grade 10) was also used to change the properties of the moving surface. The topography of the specimen was measured using a Veeco profilometer, operating in phase shifting interferometry mode. The arithmetic mean roughnesses R_a of the substrates were: steel ball (5 nm), glass ball (10 nm), sapphire window (0.8 nm), glass slide (0.5 nm) and PDMS coated glass slide (10 nm).

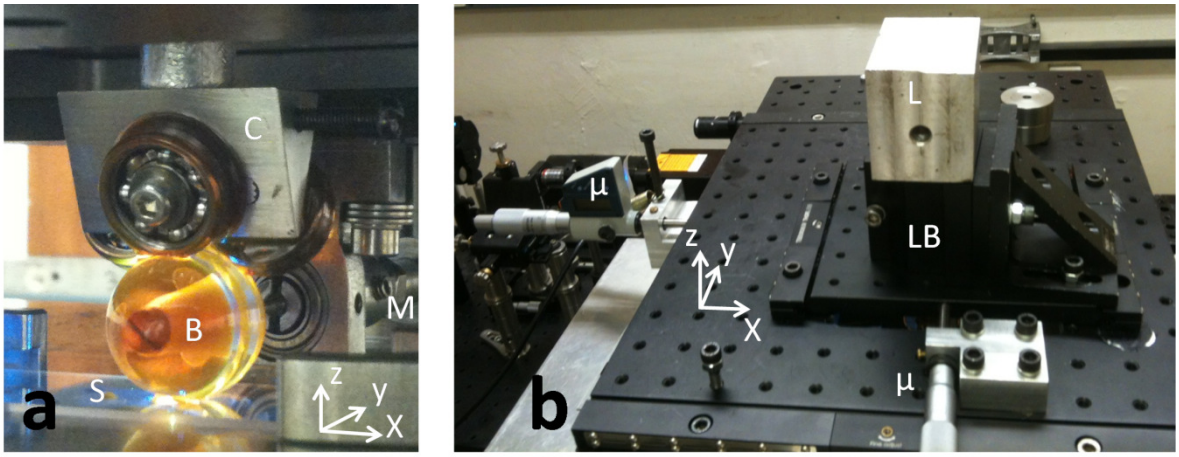


Fig. 29: EHD contact setup. a) The EHD contact, showing the glass ball (B), microscope slide (S), carriage (C) and motor (M). b) The loading mechanism and positioning stages, showing the load (L), linear bearing (LB) and micrometers (μ).

Fig. 29 shows the EHD contact setup placed on top of an inverted microscope. The ball was constrained in x-y by a ball carriage assembly, which was constrained in z through a pillar passing through a linear bearing, mounted on two positioning stages. The stages were controlled with micrometers, giving x-y positioning control over the position of the contact. The lubricant was contained on the slide by a PDMS bath (not shown in these images). The ball was rotated by a Cool Muscle 23L (Reliance Precision Mechatronics) precision stepper motor, with a maximum speed of 2000 rpm and an encoder resolution of 50000. A 100x reduction gear box was mounted to enable low speed precision, resulting in a surface velocity range of approximately 1-20000 μm/s. The load was applied by mounting free weights on top of the ball carriage holder. The natural load exerted by the system without a free weight was measured by placing a scale in place of the glass slide.

The stabilities of the speed of the ball, the loading mechanism and the position of the contact were determined to ensure that the assumptions used for the subsequent analysis were appropriate. The stability was tested for multiple speeds and loads, up to a maximum of 2.4 mm/s and 50 N. The speed of the ball was stable within the tested range. A typical result is included here. The speed (set to 120 μm/s at a load of 6.4 N with H-300 as the lubricant) of a steel ball was measured by tracking the speed of visible features on the surface with white light microscopy, as seen in Fig. 30a. The images were analysed using PIVlab (http://pivlab.blogspot.co.uk/) for Matlab. The surface velocity of the ball was

stable within 2.7 % of the set speed, as shown in Fig. 30b. The peak at 48 s is caused by the algorithm failing to identify any features in those particular frames.

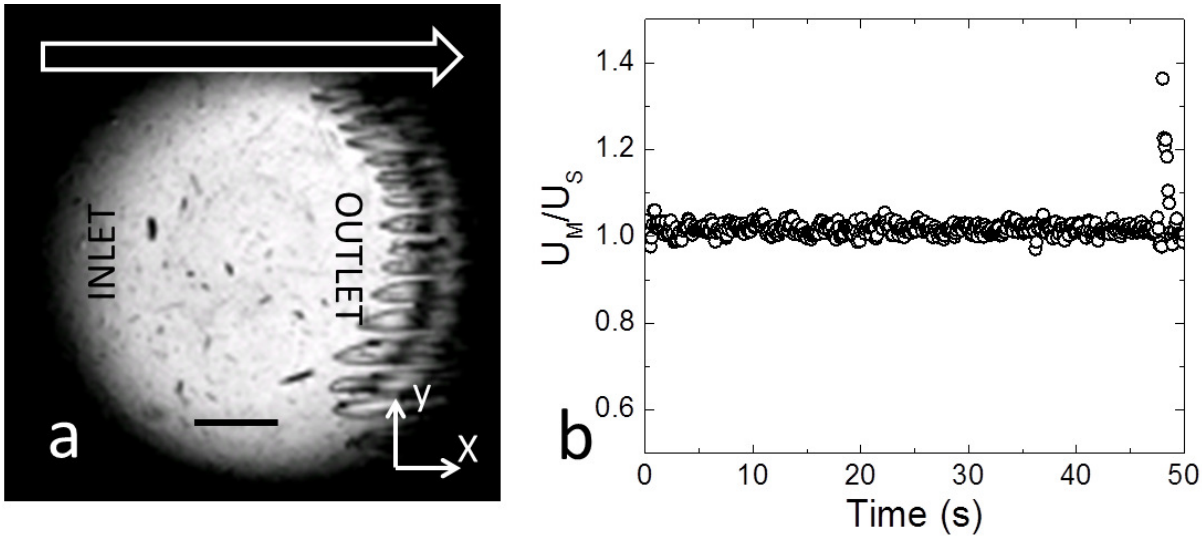


Fig. 30: a) White light microscopy image of the EHD contact. The arrow indicates the direction of flow. Features on the steel surface can be seen moving. The scale bar is 50 µm. Cavitation can be seen at the outlet. b) Plot of the ratio of the measured velocity U_M and the set velocity U_S against time, indicating the stability of the velocity.

The contact was also observed using fluorescence imaging, as shown in figure Fig. 31a. The drift of the position of the contact was examined by tracking the centre of the circular contact over the course of 1000 s. The maximum distance between extreme positions was determined to be approximately 5 µm, with oscillations occurring over tens of seconds depending on the load and speed. The relative speed of these oscillations is negligible compared to the speed of the flow being studied. Given the accuracy of the speed, the load stability was measured by monitoring fluorescence fluctuations at a load of 6.4 N. The standard deviation of the intensity, shown in Fig. 31b, is 0.8 %. Hence the load applied, and the thickness of entrained lubricant, are deemed to be stable.

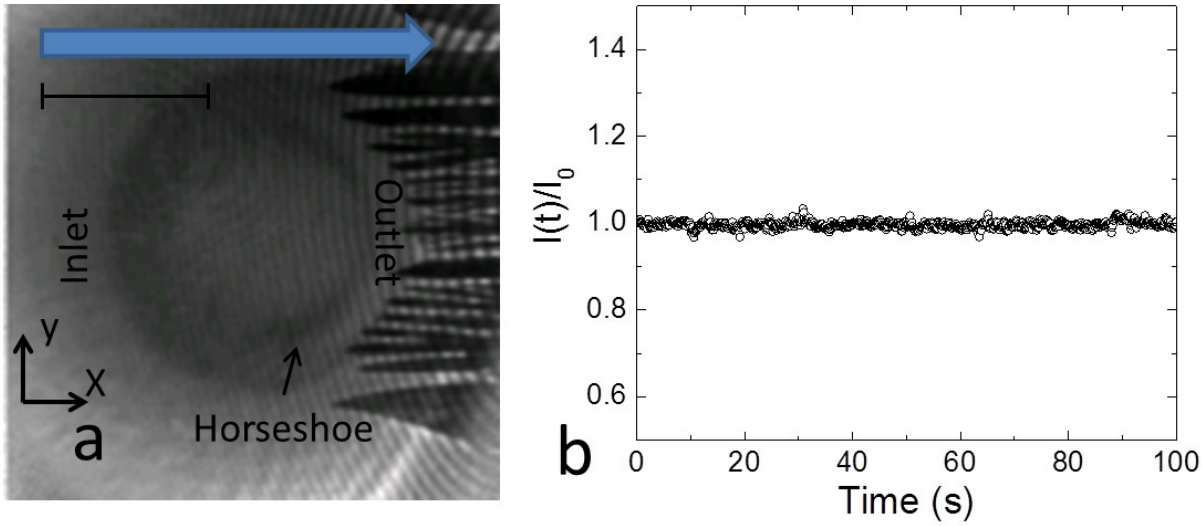


Fig. 31: a) Fluorescence image of the EHD contact. The arrow indicates the direction of flow. The scale bar is 100 µm. The horseshoe can be seen near the outlet followed by cavitation. b) Plot of the normalised intensity against time, indicating the stability of the load applied and the film thickness.

2.3.2 Pressure and size of the EHD contact

In an EHD point contact, two spheres, of radii R_1 and R_2, are elastically deformed against each other, forming a circular contact due to the external normal load applied. The resulting normal pressure distribution and the radius of the EHD contact can be approximated using Hertzian contact mechanics [30]. The contact area has a radius a given by

$$a = \left(\frac{3}{4}\frac{WR}{E'}\right)^{1/3} \tag{19}$$

where W is the load, R is the radius of relative curvature and E' is the contact modulus. R is defined as

$$\frac{1}{R} = \frac{1}{R_1} + \frac{1}{R_2} \tag{20}$$

For a sphere on flat, $R_2 = \infty$ and $R = R_1$. E' is given by

$$\frac{1}{E'} = \frac{1 - {v_1}^2}{E_1} + \frac{1 - {v_2}^2}{E_2} \tag{21}$$

where v_1 and v_2 are the Poisson's ratios and E_1 and E_2 are the Young's moduli for the two materials. The normal pressure distribution is parabolic, with the maximum pressure, p_{max}, and the average pressure, $\bar{p}$, defined as

$$p_{max} = \frac{1}{\pi}\left(\frac{6WE'^2}{R^2}\right)^{1/3} \tag{22}$$

$$\bar{p} = \frac{2}{3}p_{max} \tag{23}$$

The typical properties of four materials used in this work are given in Table 4.

	Steel	Glass	Sapphire	PDMS
v	0.3	0.2	0.27	0.45
E (GPa)	210	70	370	0.002

Table 4: Typical material properties for specimen used in this work

The resulting maximum pressure and contact area, at three typical loads used in this work are shown in Table 5. The selected loads and interfaces give a large range of pressures, at which different rheological responses would be expected.

Load (N)	Steel - Glass	Glass - glass	Glass - Sapphire	Steel - PDMS
1.1	193 MPa & 52 µm	146 MPa & 60 µm	207 MPa & 50 µm	246 kPa & 1.5 mm
6.4	347 MPa & 94 µm	263 MPa & 108 µm	373 MPa & 91 µm	441 kPa & 2.6 mm
23.7	537 MPa & 145 µm	407 MPa & 167 µm	577 MPa & 140 µm	682 kPa & 4.1 mm

Table 5: The maximum pressure and contact radius for different materials at three loads are listed.

2.3.3 Film thickness calculation

Knowledge of the film thickness in an EHD contact is required to calculate the friction. It is also necessary for assessing the assumptions, such as uniform photobleaching and pure advection, used for photobleached-fluorescence imaging velocimetry. It is also necessary to estimate the experimental condition required to generate an EHD lubricant film that allows application of the developed technique without wearing the rubbing surfaces. It was argued, in subsection 2.2.1, that a minimum film thickness of about 50 nm is required to produce a sufficient fluorescence signal. The film thickness in an isothermal EHD point contact cannot be directly calculated by solving the Reynolds equation, although analytical approximations are available.

Many empirical equations have been developed to enable the calculation of the film thickness. The appropriate equations depend on the regime the EHD contact is operating in. The rubbing surfaces can either remain rigid or deform elastically while the viscosity of the lubricant can change significantly due to the pressure or remain constant. Esfahanian and Hamrock [83] constructed regime maps for various elipticity parameters. Evaluation of the non-dimensional groups g_E and g_V enables the determination of the operating regime of a tribological contact. g_E and g_V are defined as

$$g_E = \frac{\bar{G}\overline{W}^3}{\bar{U}^2} \tag{24}$$

$$g_V = \frac{\overline{W}^{8/3}}{\bar{U}^2} \tag{25}$$

where $\bar{U}$, $\bar{G}$ and $\overline{W}$ are the non-dimensional speed, materials and load parameters respectively. The parameters are defined as

$$\bar{U} = \frac{U_e \eta}{E' R}, \bar{G} = \alpha E', \overline{W} = \frac{W}{E' R^2} \tag{26}$$

where U_e is the entrainment speed, which for a pure sliding contact is $U_e = U/2$. Using the equations provided in [83], the regime map for a sphere on flat (ellipticity k=1) contact was constructed, as shown in Fig. 32.

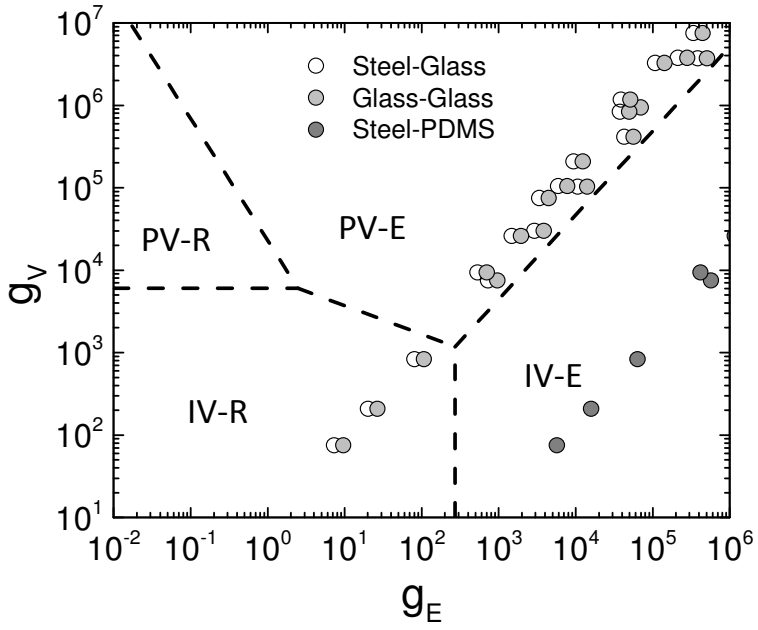


Fig. 32: Lubrication regime map constructed for a point contact with k=1. IV: isoviscous, PV: piezoviscous, R: rigid, E: elastic. The symbols represent the operating conditions for various experimental parameters detailed in the text.

It is clear from the definitions of g_E and g_V, that the slope of g_V/g_E is relatively constant, as long as the load does not vary significantly. Changing material parameters, $\bar{G}$, shifts the intercept with the y-axis. The parameters g_E and g_V are plotted in Fig. 32, for the loads, speeds, viscosities and three of the material combinations used in this work. Only the region of low values of g_E and g_V was plotted for clarity. g_E extends to about 10^{14}, but as the slope, g_V/g_E, is constant the operating regime does not change. The main regime of interest in this work is the piezoviscous-elastic (EHD) regime, where extreme pressures, viscosity and deformations are present. Fig. 32 shows that the steel-glass contact operates mostly in this regime. At combinations of high velocities and low loads the operating conditions are isoviscous-rigid (hydrodynamic lubrication). The conditions for the glass-glass contact are similar to the steel-glass contact. If the flat surface is PDMS, the contact is in the isoviscous-elastic (soft-EHD) regime under all operating conditions. Having identified the operating conditions of the EHD contact, the predicted film thickness can be determined. Part of the study is conducted with a low surface energy (Fusso) coated glass slide against a glass sphere. Since the coating is only 10 nm thick, it is likely that the condition of this contact will be similar to those for the glass-glass contact.

The Hamrock-Dowson equation [84] defines the central film thickness, h_c, for a piezoviscous-elastic EHD contact as

$$h_c = 1.90\bar{U}^{0.67}\bar{G}^{0.53}\overline{W}^{-0.067}R \tag{27}$$

The equation is commonly used to determine the pressure viscosity coefficient, α, of lubricants as all other parameters are usually known. Under typical experimental conditions of T = 25 °C, U = 20-1000 µm/s, W = 5 N, $\alpha \sim 30$ GPa^{-1} and µ = 66 Pa s (see Table 2), the central film thickness of H-300 is 25-349 nm in a glass-glass EHD contact. The definitions of $\bar{U}$ (equation (26)) and h_c (equation (27)), show that the range of appropriate speeds for a sufficient film thickness changes with the viscosity of the lubricant. However, they do not take into account that lubricants may shear thin under EHD conditions. Hence the actual film thickness in an EHD lubricant that shear thins will be smaller than predicted. Shear heating, which can reduce the viscosity of the EHD lubricant is also not considered in equation (21), but it can be shown that the effect is negligible for this study (see subsection 2.3.5). The film thickness of EHD lubricant for a range of speeds was measured with interferometry and α was obtained by equation (27) as shown in section 3.1. The friction in the contact can be predicted, as shown subsequently by using the rheology of polybutene, the pressure distribution in the contact and the film thickness.

2.3.4 Friction calculation

The friction in an EHD contact is generated through the interfacial shear stresses at the solid-lubricant boundaries. The shear stress, $\sigma = f(\dot{\gamma})$, at any point is a function of the shear rate, $\dot{\gamma}$. The flow curve can be determined by a number of methods, as listed in section 1.2. Here, the commonly applied constitutive relationship of Johnson and co-workers [15] is used, defined by

$$\mu_p\dot{\gamma} = D\frac{d\sigma}{d(x/l)} + \sigma_0\, sinh\frac{\sigma}{\sigma_0} \tag{28}$$

where μ_p is the pressure corrected viscosity, D is the Deborah number, l is the length of the contact and σ_0 is the Eyring stress. The Deborah number is defined as $D = \mu_p U/(Gl)$, where U is the sliding velocity and G is the shear modulus. Using typical experimental conditions

in this work (μ_p = 1e7 Pa s, U = 200 µm/s, l = 200 µm), and assuming that the shear modulus of polybutene is similar to that of polyisobutylene [85] ($G \sim 1$ GPa), the Deborah number is of the order of $D \sim 0.01$. Thus the elastic term in equation (28) is negligible, and the shear stress is given by

$$\sigma = \sigma_0 sinh^{-1} \frac{\mu_p \dot{\gamma}}{\sigma_0} \tag{29}$$

The parameters σ_0 and μ_p can be determined by fitting equation (29) to traction data, as is done in chapter 8. The shear rate is given by $\dot{\gamma}(z) = \frac{\partial(u(z))}{\partial z}$, where $u(z)$ is the velocity in the x-direction at position z through the film thickness. The Reynolds equation can be solved to determine $u(z)$ in an isothermal EHD contact (equation (1) reproduced here)

$$u(z) = \frac{1}{2\mu_p}\frac{\partial p}{\partial x}(z^2 - zh) + U\frac{z}{h}$$

This assumes a no-slip boundary condition, and that the lubricant is Newtonian, which does not apply to this work. A common assumption for pure sliding conditions is that the pressure gradient term (first term in equation (1)) is negligible [6], due to the high viscosity of the lubricant, such that

$$u(z) \approx U\frac{z}{h} \tag{30}$$

In this case, the shear rate becomes $\dot{\gamma} = \frac{U}{h_c}$. Then the friction in an isothermal EHD point contact can be determined by integrating the shear stress over the contact area. For the case where the lubricant slips at the bottom interface, the velocity profile becomes

$$u(z) = U(z + b)/(h_c + b) \tag{31}$$

which for a finite slip length, b, would clearly reduce the effective shear rate, and thus reduce friction as long as the flow curve $\sigma = f(\dot{\gamma})$ is monotonic.

The relationship between the slip length and the slip velocity can be constructed for a relative slip velocity, $u_{brel} = u_b/U$, and a relative slip length, $b_{rel} = b/U$, by setting $u(0) = u_b$ in equation (31) to give

$$b_{rel} = \frac{u_{brel}}{1 - u_{brel}} \tag{32}$$

It should be noted that the breakdown of the linear velocity profile significantly complicates friction prediction, as the shear rate within the film is unknown. Furthermore friction predictions typically do not include the possible effects of interfacial slip, shear banding and plug flow, which all may occur in an EHD contact. These phenomena cannot be ignored, as the formation of a dimple in an EHD contact would suggest. It is therefore necessary to directly measure the velocity profile to correctly identify the cause of friction.

2.3.5 Shear heating

Similar to heating due to fluorescence, heating due to traction could alter the local rheology of lubricant and complicate analysis of the flow. Temperature rises of tens of K can occur in high speed EHD contacts [86]. An analytical solution for heating in an EHD point contact due to traction has been developed by Olver *et al.* [6]. Taking into account heat removal by conduction and using average properties of the lubricant in the contact, the average temperature rise of the lubricant, ΔT_L, due to frictional heating is determined:

$$\Delta T_L = \frac{\tau W U h_c}{8\pi a^2 k_l} \tag{33}$$

where τ is the friction coefficient and k_l is the thermal conductivity of the lubricant found in [81]. The friction coefficient for an EHD point contact lubricated with polybutene is approximated as 0.1 [39]. For the harshest experimental conditions applied, consisting of a sliding speed of 1 mm/s, a normal load of 23.7 N and a film thickness of 2.25 µm, the temperature rise for PB2300 in a steel-glass contact is 0.013 K. This is a negligible amount, and the system can be assumed to be isothermal. The negligible temperature rise is caused by the very low velocities used in this work, as has been concluded previously [40].

2.3.6 Squeeze film solidification

It was stated, in section 1.4, that large pressures in EHD contacts have been known to cause phase transitions of lubricants, resulting in phenomena such as shear banding and the limiting shear stress. It is necessary to determine if such a transition occurs at the experimental conditions used in this work. The glass transition temperature and pressure of

polymers can be determined using a number of experimental techniques including: infrared spectrometry, differential scanning calorimetry and nuclear magnetic resonance. In this work the interest is the glass transition pressure at ambient temperature. The mentioned experimental techniques could not be applied in this work due to the lack of a pressure cell. While the effect of pressure could be investigated using an EHD contact, the resulting small sample volume makes the application of infrared spectrometry and nuclear magnetic resonance cumbersome. Instead, the dynamics of a squeeze film produced by a static loaded point contact was studied using laser-induced fluorescence to probe the possible event of a glass transition.

A squeeze film can be produced by the approach of a sphere onto a stationary flat surface, driven by an applied force. The lubricant separates the surfaces and the pressure caused by the Hertzian contact forces the lubricant outwards, causing the thickness of the film separating the surfaces to decrease over time. Pressure driven flow of lubricant in a point contact is relatively slow, resulting in low shear rates such that the flow of PB2300 can be approximated as Newtonian. For a Newtonian fluid, the central film thickness, h_c, as a function of time is given by [87]

$$\frac{h_c}{h_0} = e^{-t/\tau_s} \tag{34}$$

where h_0 is the initial central film thickness and τ_s is a time constant. A non-dimensional time constant, τ_s^*, can be described [88] as

$$\tau_s^* = \frac{W h_0^2}{\mu_p R_1^4} \tau_s \tag{35}$$

Given a Newtonian lubricant and an accurate value for the viscosity, the non-dimensional time constant should not vary with pressure. Polybutene is unfortunately non-Newtonian, and the Barus equation used for the viscosity is not necessarily correct. However, if the lubricant were to undergo a glass transition, the time constant would be expected to increase by a significant amount, such that this event could potentially be used to identify the transition despite the assumptions used being approximations.

The time dependent film thickness at the centre of a point contact was measured using the setup described in subsection 2.1.3. The blue collimated laser was focused with the 20x objective at the centre of the contact. An avalanche photodiode (APD) was used to collect the fluorescent emission. The power of the blue laser was 10 µW. It was necessary to keep the power low to avoid photobleaching. Results at a higher power (30 µW) were compared with the lower power results showing no significant difference, indicating that photobleaching was minimal.

An initial film of PB2300 was created by running the EHD contact at a given load and a ball speed of 720 µm/s, creating a film thickness of approximately 200 nm. The intensity was measured every second using the APD, for an exposure time of 10 ms. The acquisition was started with the ball running. After 10 seconds the ball was stopped, initiating the squeeze film.

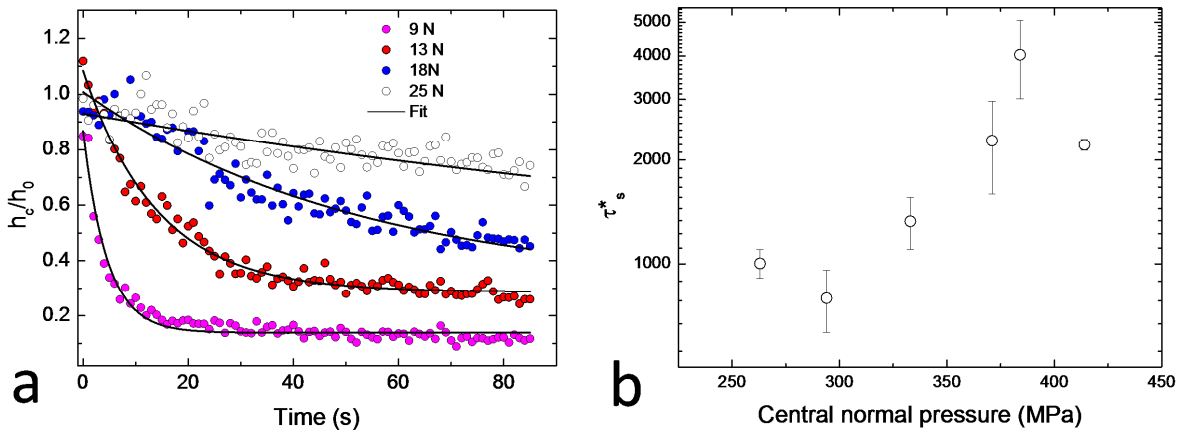


Fig. 33: a) Decrease in relative squeeze film thickness over time for PB2300 after stopping the ball. The black lines are fits to equation (34). b) Non-dimensional squeeze film time constant as a function of pressure.

Typical results for the decrease of the squeeze film thickness over time are shown in Fig. 33a. Tests were performed twice at each load. The intensity distribution was normalised by dividing it by the intensity before cessation of the glass ball. It was then representative of the relative film thickness, h_c/h_0. The intensity distributions were fitted to equation (34) (black lines) to determine the squeeze film time constant. The time constant varies with the applied pressure due to the pressure-induced increase of the viscosity, slowing down the pressure driven flow of the lubricant. The non-dimensional time constant, τ_s^*, is calculated to

account for changes in the viscosity. The effect of pressure on τ_s^* is presented in Fig. 33b. At an approximate transitional pressure of 330 MPa the non-dimensional time constant almost doubles. The squeezing out of the film has slowed down more than what is predicted by the calculated viscosity. A possible explanation for the observed behaviour is the glass transition of polybutene causing a sudden rise in the viscosity.

The performed squeeze film experiment is limited in that only a single lubricant is studied. It would be beneficial to compare the results to a lubricant which is not expected to show a glass transition, to show that the non-dimensional time constant remains fairly constant. The results do however show a distinguishable transition. Prior to, and after the transition, the value of the non-dimensional time constant seems mostly invariable, although more data would be necessary to prove this conclusively. In the scope of the project, this result is used as an independent indication of the likely glass transition of polybutene, which can be compared to other subsequent experimental results.

2.3.7 Interference

Steel is one of the most common materials used in EHD contacts. When steel is finely polished, as is typically done for research in EHD lubrication, it is highly reflective. In the case of interferometry, this is beneficial. If laser-induced fluorescence is to be used, the effect of interference due to a reflective surface must be taken into account [89].

Two different sources of light are typically incoherent such that they will not interfere with each other. However, if a mirror is used as the second source, interference can occur. When light is reflected by a mirror it goes through a $\lambda/2$ phase change, where λ is the wavelength. The amplitude of the interference pattern, A_i, at a distance, d_i, from the reflective surface, is given by

$$A_i = 2A_0 \, sin\left(2\pi n \frac{d_i}{\lambda}\right) \tag{36}$$

where A_0 is the amplitude of the incident wave and n is the refractive index. The intensity of the excitation field is given by the square of the amplitude, ${A_i}^2$. Consider an EHD thin film of lubricant doped with fluorescent molecules. Since the reflected beam would interfere

with the incoming beam, forming an interference pattern, the intensity available for exciting the fluorophores varies with distance from the reflective surface. This has two consequences for the proposed technique of photobleached-fluorescence imaging velocimetry. Firstly, the rate of photobleaching will vary through the thickness of the film, creating a non-uniform photobleached plug. Secondly the illumination field will also be non-uniform, further complicating the description of the intensity distribution within the photobleached plug. In thick films ($h_c > \lambda$), the effects of interference average out, but for thin films the effects clearly violate a main assumption used for the analysis developed in chapter 4.

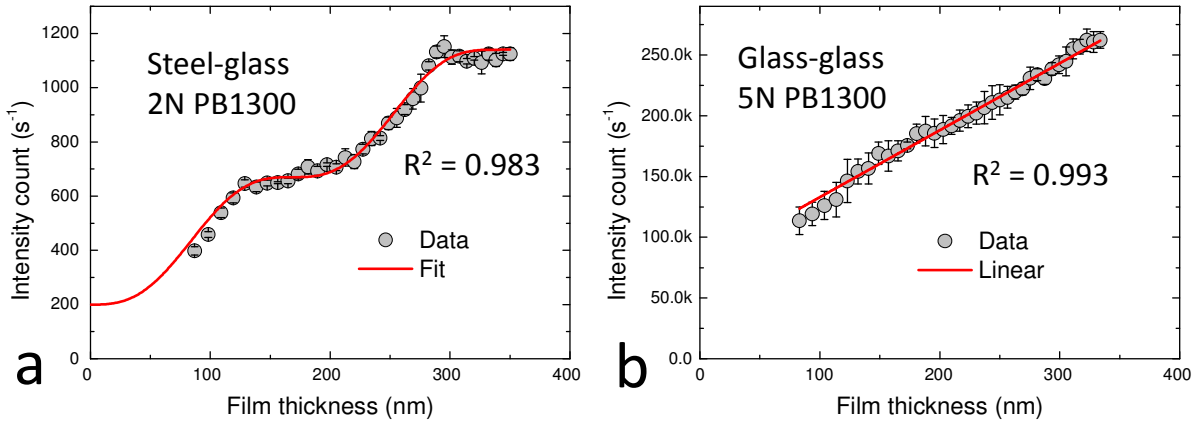


Fig. 34: a) Intensity variation with film thickness for a steel-glass EHD contact at 2 N. The red line shows a fit for the intensity due to interference. a) Intensity variation with film thickness for a glass-glass EHD contact at 5 N. The red line is a linear fit to the data. The lubricant was H-300.

The optical setup used to measure the squeeze film in subsection 2.3.6 was used to study the variation of intensity with film thickness. The photobleaching (blue) laser was used, and the power of the laser beam was set to 10 µW using a density filter, to reduce the likelihood of photobleaching. According to the law of absorbance, the emitted fluorescence intensity is expected to increase linearly with the film thickness [90]. Measurements were performed with H-300 for a range of speeds for both a reflective sphere (steel) and a transparent sphere (glass), and the experiments were repeated three times. The film thickness was calculated as described in 2.3.3. The result for the steel sphere is shown in Fig. 34a. It is clear that the intensity does not vary linearly with the film thickness. The fitting of the data to the integral of the square of equation (36), indicated by the red line in Fig. 34a, shows that the intensity variation can be explained by interference. For the case of the transparent sphere

(see Fig. 34b), it is evident that no interference occurs. The intensity varies linearly with film thickness, as shown by the red line. Since all polybutenes used in this study have similar refractive indices to glass, it is assumed that the interference effect is minimal at all conditions with transparent surfaces.

The effects of interference could be removed by using incoherent light sources. This would work for the illumination and it could be achieved using rotating diffusers for example. For the bleaching beam however the light is required to be coherent, to allow the focusing of the beam into a diffraction limited spot. The interference could potentially be advantageous. While destructive interference would always be present at the reflective surface, parameters could be tailored to ensure constructive interference at the stationary surface. This would provide enhanced sensitivity near the surface, which could be beneficial for studies of interfacial slip.

Due to interference caused by the use of reflective surfaces, only transparent substrates were used for the study of thin EHD films in this work. Reflective surfaces were only used for validation purposes with thicker films, for interferometric measurements of film thickness and to illustrate the effect of interference in fluorescence in thin films.

2.3.8 Low surface energy coating

It is postulated in the introduction that the load and shear rate may have an effect on the velocity profile in an EHD contact, and thus the friction. It is however not certain that such an effect would be significant. It would be beneficial to study a flow case where large effects are to be expected. The example response of the photobleached plug in Fig. 18 showcases such a case, caused by slipping of the lubricant at the lubricant-coating interface. If slip is present, the effective shear rate is reduced, lowering the shear stress and the friction. Significant slip should be identifiable using the photobleached-fluorescence imaging velocimetry technique as well as by friction and film thickness measurements. The observation of flow induced effects using three separate techniques aids in ensuring the validity of the developed method of photobleached-fluorescence imaging velocimetry. It also facilitates the direct study of the effect of slip on friction and film thickness, as well as the

effect of parameters such as load and shear rate on the degree of slip. Typically slip has to be inferred either by friction measurements [36,39], or surface deformation [25]. With photobleached-fluorescence imaging velocimetry, it can be measured directly using the flow of the lubricant.

To increase the likelihood of slip, the interfacial energy between the lubricant and interface should be minimized. Monolayers of hydrocarbon chains have been used previously to reduce the friction in hydrodynamic lubrication [36], achieving slip lengths of approximately 6 µm. Given an approximate film thickness of a micron, typical for an EHD contact, the effect of slip on the velocity profile would be significant. Such a slip length would be easily identifiable using the photobleached-fluorescence imaging velocimetry technique. The durability of a monolayer coating in an EHD contact is however questionable [91], given the large shear stresses present. Another option is to use diamond-like-carbon coatings (DLC). Such coatings have been shown to reduce the friction in both solid and liquid lubrication [92] while being extremely durable. Unfortunately DLC coatings affect the optical properties of the surfaces, typically resulting in reflective surfaces which would prohibit the use of the optical technique developed in this work. Optically compatible DLC coatings, commonly used with germanium for infrared applications, are however available and can also be applied to silica, although the fabrication of such coatings is not straightforward.

A commercially available alternative, Fusso Smartphone (Nippon Fusso), was chosen for this work, as recommended by P.L Wong. Fusso Smartphone is a fluoroalkyl polymer coating, similar to coatings typically used for touchscreen devices for anti-fingerprint protection. The fluoroalkyl polymer adheres to the silica surface, resulting in a durable and stable oleophobic coating. Silica slides were cleaned by sonication in toluene for 10 minutes followed by ultrasonication in isopropanol for 10 minutes. The slides were then plasma cleaned for another 10 minutes. The coating was applied to the clean slides, according to the included application instructions. 5 drops of the solution were deposited on each glass slide and the liquid was spread equally on the surface using paper tissue. The deposition was repeated three times after which the glass slides were left to rest for at least 8 hours. The

manufacturer quotes an approximate coating thickness of 10 nm. The roughness of the coating was determined to be approximately 0.5 nm, by phase shifting interferometry.

The interaction between PB and the coating was examined by performing contact angle measurements. The PB droplets were imaged using a camera, and the contact angle was determined using the LBASDA plug-in [93] for ImageJ (http://rsbweb.nih.gov/ij/), as shown in Fig. 35.

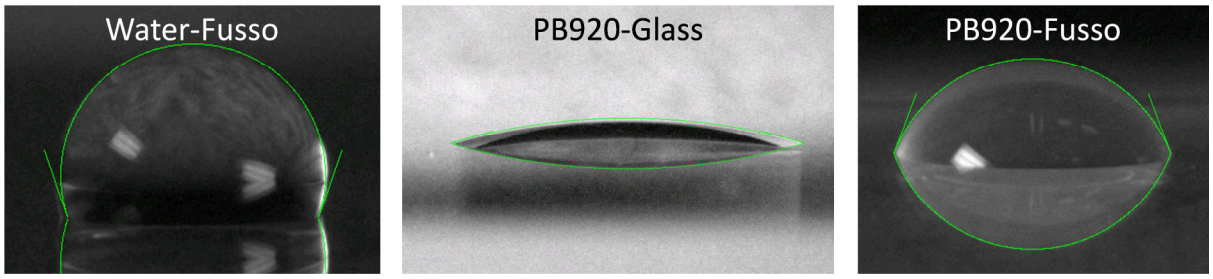


Fig. 35: Water and PB920 on glass and on the Fusso coated glass slide. The green lines indicate the fitting done by the LBADSA plug-in, to determine the contact angle.

The solid-liquid work of adhesion, ΔW, is related to the energy required to move a liquid molecule adhered to a solid substrate. It can be related to the liquid-vapour interfacial energy, γ_{LV}, and the contact angle, θ, by the Young-Dupré equation, defined as

$$\Delta W = \gamma_{LV}(1 + cos\,\theta) \tag{37}$$

The result for the work of adhesion at the solid-liquid interface is shown in Table 6. The surface tension of water is 0.075 N/m and that of polybutene is 0.025 N/m, which was provided by the supplier (INEOS oligomers). Water is well known to completely wet a clean glass substrate. The other contact angles were determined from Fig. 35. The results show that the low surface energy coating reduces the interfacial energy between the polybutene and the glass. This would decrease the energy required for the lubricant to flow at the interface, and thus promote slip.

	Water θ (°)	PB920 θ (°)	Water ΔW (J/m^2)	PB920 ΔW (J/m^2)
Glass	0	16	0.15	0.049
Fusso	109	69	0.05	0.034

Table 6: Surface energy properties of the liquid-solid combinations used in this work.

The coating was found to be susceptible to degradation at pure sliding EHD conditions, due to the high shear stresses involved. It was observed that the friction coefficient obtained at a constant speed on a stationary Fusso coated specimen increased after approximately five minutes. Therefore any experiments involving the Fusso coating were always performed on a fresh surface, to reduce the effects of wear.

The applied coating clearly reduces the interaction energy between PB and the glass substrate. This reduction would reduce the shear stress required to overcome the adhesive forces between the lubricant and the surface. Hence the likelihood and extent of slip, particularly under the extreme shear stresses in an EHD contact, increase.

2.4 Summary

The phenomenon of photobleaching, which involves the degradation in the ability of a fluorescent molecule to emit light, was introduced. This was suggested as a method to molecularly tag lubricant to study the flow of lubricants in an EHD contact. An optical setup, along with an acquisition system, which enables the use of the photobleached-fluorescence imaging velocimetry technique, was designed and characterised for this purpose. The ability of the proposed system to study flows in EHD lubrication was assessed in terms of limiting experimental conditions. These conditions mainly constituted the requirement of low entrainment velocities, requiring the use of a high viscosity lubricant to create a sufficiently large thin film.

Nile red in polybutenes was chosen as the model lubricant-fluorophore system to be used for photobleached-fluorescence imaging velocimetry. Using typical experimental conditions, the required photobleaching rate for producing a Gaussian photobleached spot was determined, and it was shown that the system of nile red-polybutene facilitated this rate. Results showed that photobleaching could be performed successfully using the designed optical and acquisition systems. The properties of the three chosen polybutenes, including viscosity, glass transition temperature and shear thinning behaviour were determined and discussed. It was noted that polybutene was likely to form a glass under the experimental conditions in an EHD contact due to the effect of pressure on the glass transition temperature. The dynamics

of squeeze films of polybutenes was studied to monitor the decay of film thickness with time. It was shown that the dynamics slowed down at a critical pressure, which is indicative of a possible phase transition of the lubricant. The diffusion coefficient of nile red in polybutene was determined using fluorescence recovery after photobleaching, and was found to be negligible within the range of experimental conditions used in this study. Heating induced by the photobleaching process was estimated, and it was found to be negligible under the experimental conditions due to conduction by the surfaces forming the contact. Hence the effect of heating on the viscosity of the polybutenes was neglected.

The experimental rig used to form the contact was described and its stability was investigated and found to be satisfactory. Commonly used methods for calculating pressure, film thickness and friction in tribological contacts were presented. It was shown that for the experimental conditions used in this work the lubrication regimes fall within either soft-EHD or EHD, depending on the substrates used. The velocity profile derived using the Reynolds equation was presented along with the concept of slip. Shear heating, which may occur in EHD contacts, was shown to be negligible in this work due to the low speeds used. The possibility of interference, when using the fluorescence techniques, was explored. It was determined that the use of transparent surfaces was necessary to completely avoid the phenomenon. Finally, the preparation of a low surface energy coating was described, which would be used to promote the occurrence of interfacial slip, a phenomenon which could be studied using the developed photobleached-fluorescence imaging velocimetry technique.

The next chapter (chapter 3) concerns the determination of PB film thicknesses at various experimental conditions. This is necessary to ensure the validity of assumptions used for analysis of the experimental results.

3 Film thickness measurements

In this chapter film thickness measurements for PB in an EHD contact are presented. These measurements are used to ensure the validity of assumptions used for the velocity profile reconstruction (chapter 4) and to find the pressure-viscosity coefficient, α, required to use the Hamrock-Dowson equation (equation (27)).

First, results obtained by interferometry for the steel-glass contact are shown. Then, the technique of laser-induced fluorescence for film thickness measurements is detailed. Laser-induced fluorescence is applied due to the necessity of using transparent surfaces for the photobleached-fluorescence imaging velocimetry technique. This enables the study of the effect of load and speed on the film thickness in a transparent EHD contact. Finally, the consequences of using a low surface energy coating are explored, to see if the coating had any effect on the film thickness, and thus on the flow of the lubricant.

3.1 Interferometry

The film thickness was measured for the lubricants to find the pressure-viscosity coefficient, α. It was also necessary to confirm that (1) the lubricant in the contact was of constant film thickness, so that the plane Couette assumption was valid for the analysis detailed in chapter 4, and that (2) the film thickness was small, so that the through-thickness intensity distribution of the photobleached column was uniform. The film thickness was measured with optical interferometry [94] using an EHL ultra-thin film measurement system (PCS Instruments). A glass disc was coated with a chromium layer of 20 nm and a silica spacer layer of 140 nm. A steel ball was loaded onto the glass disc with lubricant spread on the disc. The disc was spun at velocities of 10 – 2000 µm/s, while the ball remained stationary. Optical images for interferometric analysis were taken with a HV-F202GV (Hitachi) camera to observe the uniformity of the film at various loads and speeds.

Central film thickness measurements for PB2300 and H-300 at 25 °C and 10 N (403 MPa), in a steel-glass point contact, can be seen in Fig. 36. The Hamrock-Dowson equation (27) was detailed in subsection 2.3.3. By fitting the results in Fig. 36 to this equation, the

pressure-viscosity coefficients of 32 GPa^{-1} and 30 GPa^{-1} for PB2300 and H-300 respectively could be determined. This agrees quite well with previous results [12,95]. Measurements were not performed for PB920, due to the limitation of the equipment used to contain lower viscosity lubricant. The film thickness of PB920 was estimated by assuming that the pressure-viscosity coefficient determined with P2300 and H-300 does not vary significantly with molecular weight and hence, can be applied to PB920.

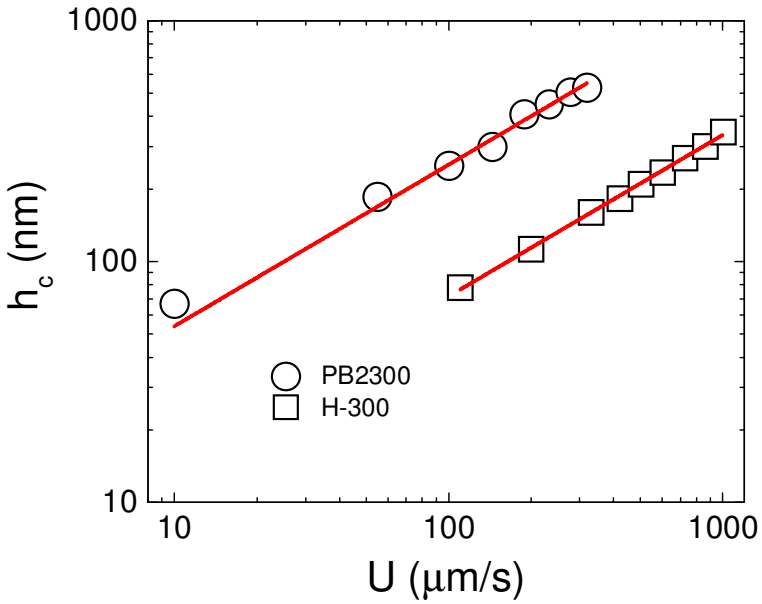


Fig. 36: Central film thickness for PB2300 and H-300 against ball surface speed. The normal load is 10 N (403 MPa). The red lines indicate fits to equation (27). The contact was created by loading a steel ball against a chromium and silica coated glass disc.

Optical interference images of the contact are shown for H-300 in Fig. 37. With optical interference, areas of constant thickness appear to have the same colour. At a load of 6.4 N (347 MPa), the central area of the contact appears uniform, up to speeds of about 600 µm/s. As the load increases, the uniformity is only maintained at low speeds. At higher speeds and higher loads, a dimple appears. The film thickness at the dimple is larger than that of the rest of the film. The dimple formation limits the range of accessible speeds and loads that create a parallel plate geometry, which is assumed in the EHD contact in this work. The dimple formation could also be observed for PB2300 at lower relative speeds, due to the increased viscosity.

The dimple effect has been studied in detail by Guo and Wong [95]. The authors in [95] suggest that the source of the dimple is a discontinuity in the velocity profile as the

lubricant passes through the contact. This discontinuity can be caused by slip between the lubricant and the glass surface [38]. To enable slip, the lubricant must accelerate, as the velocity profile outside the contact should be mostly linear. If the lubricant accelerates, the film thickness must drop towards the centre of the contact to ensure conservation of mass, causing the appearance of a dimple of thicker film thickness near the inlet. Ehret *et al.* [45] have shown that solidified lubricant, flowing as a solidified plug at the centre of the contact, can also cause the appearance of a dimple. The cause of the dimple is again a change in mean velocity of the lubricant, similar to boundary slip. The dimple formation may have a significant effect on friction, especially if it were to be caused by slip. This has been shown to be the case [39]. Directly measuring the velocity profile, as done in this work, enables the identification of the origin of dimple formation.

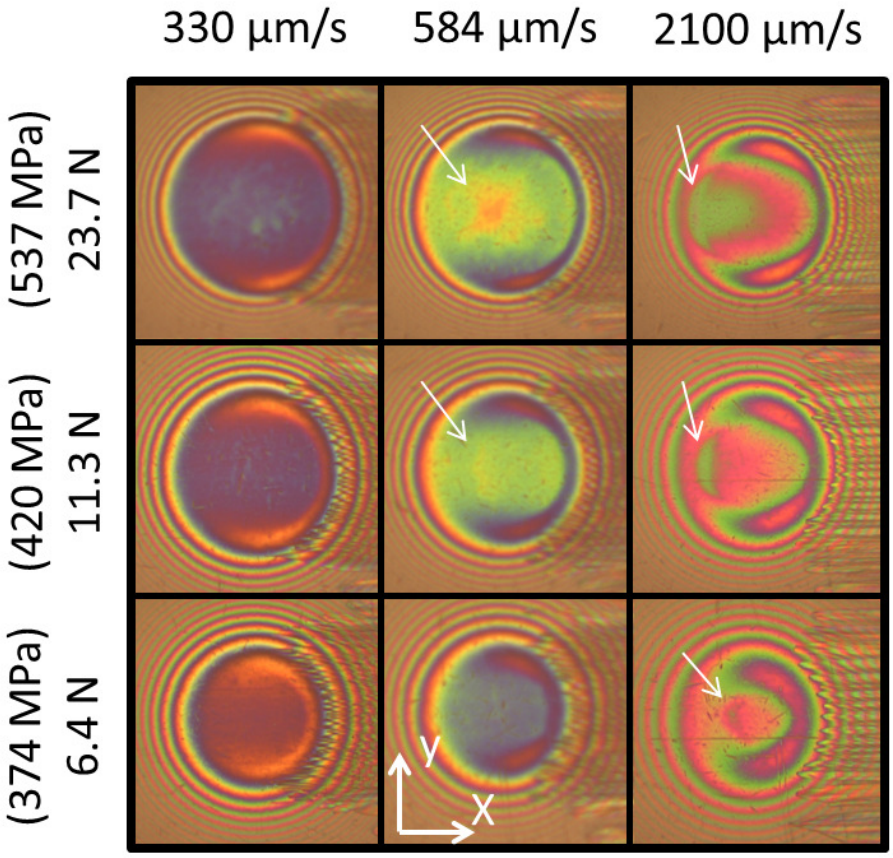


Fig. 37: Interference images of the contact for H-300 at various loads and speeds. A dimple, indicated by white arrows, can be seen to appear at high loads and high speeds.

It was noted in subsection 2.3.7 that the use of a reflective surface for one of the substrates would significantly complicate the interpretation of results acquired using the photobleached-

fluorescence imaging velocimetry technique. Therefore laser-induced fluorescence was applied for film thickness measurements in EHD films with non-reflective surfaces.

3.2 Laser-induced fluorescence

Laser-induced fluorescence was used to measure the film thickness in EHD contacts with transparent surfaces. Although Interferometry has a superior resolution to laser-induced fluorescence in terms of film thickness measurements [94], the latter has been used previously to measure film thicknesses as low as 300 nm [96].

3.2.1 Setup

A modified version of the optical setup described in subsection 2.1.3 was used with a 5x objective to capture the fluorescent intensity distribution of the EHD contact at various loads and speeds. Given the long beam path travelled by the cyan laser, the excitation beam profile was somewhat unstable over time, due to dust crossing the beam path and settling on the optics. While this was not an issue for the photobleached-fluorescence imaging velocimetry technique, due to the small experimental timescale, it can significantly affect film thickness measurements where flat-field correction is necessary. Therefore a blue light emitting diode (wavelength centred at 473 nm with a bandwidth of 20 nm) was mounted onto one of the ports of the inverted microscope. A short pass filter was used to ensure that no excitation light passed through the dichroic mirror. The light emitting diode produced an excitation field with a Gaussian distribution which was stable to within 2 % over the course of an hour.

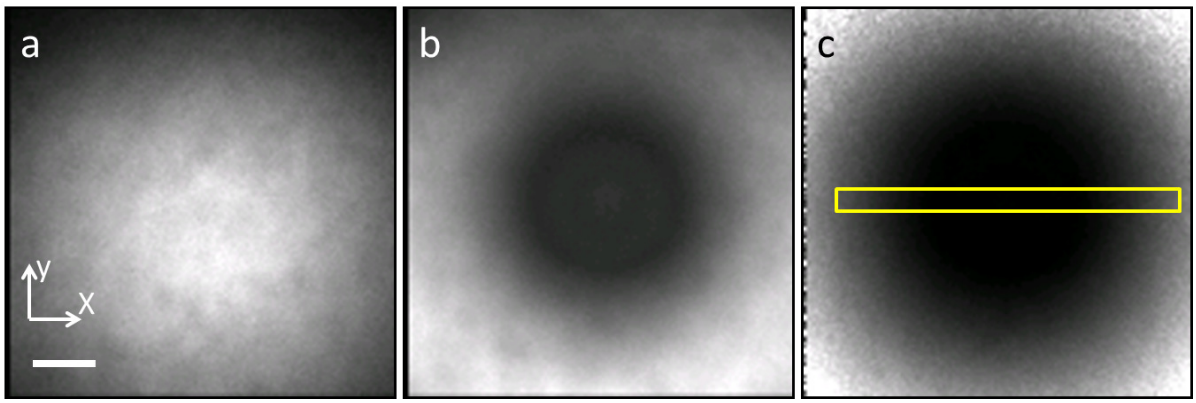


Fig. 38: Flat-field correction for film thickness measurements. a) Flat field image of rhodamine 6G in water. The scale bar is 100 µm. b) 6.4 N (263 MPa) calibration image of nile red doped PB. c) Flat-field corrected calibration image. The yellow rectangle shows the area used for averaging.

It is possible to correct for the non-uniform intensity distribution of the excitation field by using flat-field correction [96]. Typically, a specimen of constant thickness and uniform distribution of fluorophores is used to determine the intensity of the excitation field. In this study, Rhodamine 6G (Sigma-Aldrich) was dissolved in a 50 % w/w mixture of water and glycerol at a concentration of 100 µM. Rhodamine 6G was used as it is a photostable and efficient fluorophore. A mixture of water and glycerol was used to reduce the amount of evaporation while still retaining a relatively low viscosity. A small droplet of the solution was placed on a clean glass slide, and the uniform film was created by placing a cover slip on top of the solution, and allowing it to equilibrate overnight.

The distribution of the excitation with bulk Rhodamine 6G doped water-glycerol solution can be seen in Fig. 38a. This gives the flat-field intensity, I_F. Fig. 38b shows an image of a static Hertzian contact, flooded with a 1 mM solution of nile red in PB2300, using a load of 6.4 N (263 MPa). The flat-field corrected intensity, I_{FG}, is then given by

$$I_{FG} = \frac{I - I_{bg}}{I_F - I_{bg}} \tag{38}$$

where I_{bg} is the background intensity and I is the observed intensity. The flat field corrected intensity is used to produce intensity maps of EHD contacts where the intensity value is related to the film thickness. The relationship can be determined by performing a calibration, which is outlined in subsection 3.2.3.

3.2.2 The effects of load and speed

Initially intensity mapping was performed without calibration to assess the uniformity of the EHD films, and to explore if any unexpected phenomenon, such as dimple formation, would occur. Flat-field correction was performed as described in the previous subsection. Intensity distributions are shown in Fig. 39, for a pure sliding glass-glass contact at a temperature of 25 °C, lubricated by PB2300, at various loads and speeds.

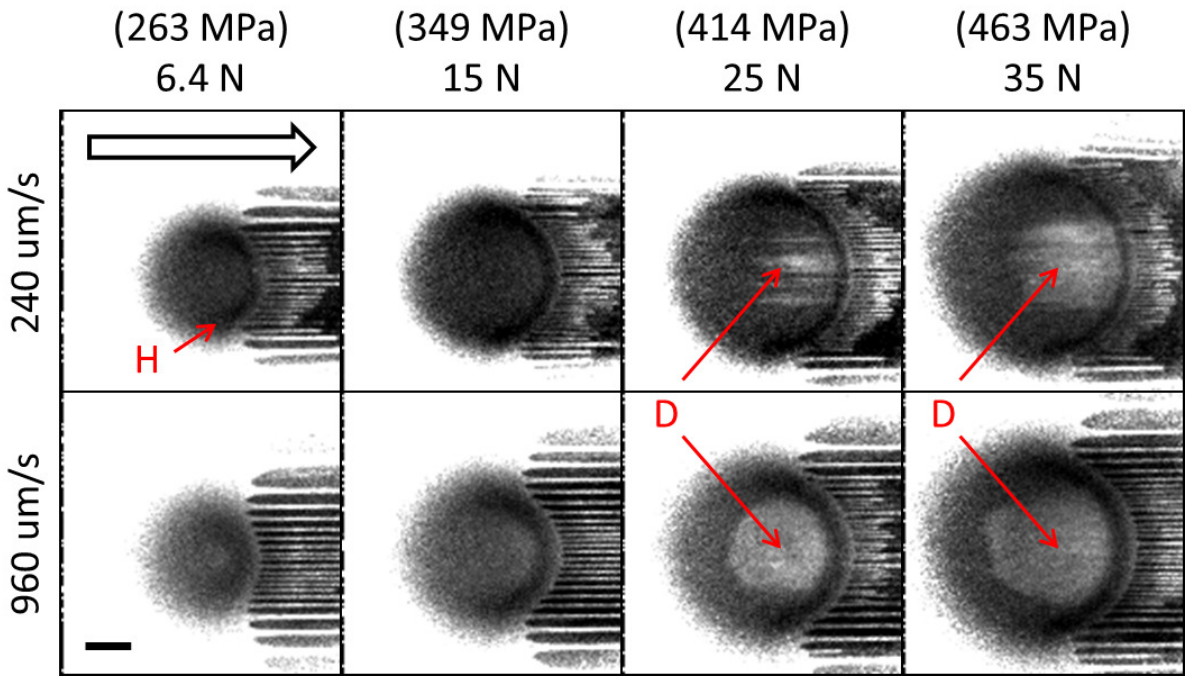


Fig. 39: Flat-field corrected intensity distributions of PB2300 for various speeds and loads in a glass-glass contact without calibration. The range of intensities varies for each image to highlight features of the film. The minimum film thickness horseshoe is indicated by a red H and the black arrow shows the direction of the flow. An increase of the film thickness towards the outlet of the contact can be seen for higher loads, as identified by the red D (for dimple). The scale bar is 100 µm.

The film thickness at low loads appears fairly uniform. At the lowest load the horseshoe (red H) can clearly be seen. As the speed increases the horseshoe becomes larger, as the operating regime of the contact approaches hydrodynamic conditions. When the load reaches approximately 25 N (414 MPa), a region of larger film thickness, a dimple, appears inside the contact near the outlet. The dimple grows as the load increases, but is mostly unaffected by the speed. The speed does however affect the intensity uniformity of the dimple, which improves with higher speed. The shape of the dimple is studied more in-depth in subsection 3.2.5, by measuring the film thickness.

A number of possibilities could be responsible for the dimple formation, as discussed in section 1.3, such as spatial variations of the velocity profile, due to interfacial slip [40], shear heating [97] or the plug flow of solidified lubricant [45]. The application of photobleached-fluorescence imaging velocimetry would therefore be useful to determine the cause of the dimple. The dimple can still however be studied by film thickness measurements. Either of the suggested mechanisms of slip, shear heating and plug flow would be expected to be pressure dependent [40]. Thus the dimple would be expected to appear at varying loads depending on the material properties of the surfaces. A sapphire-glass EHD contact was therefore investigated to see if the dimple appearance was related to pressure.

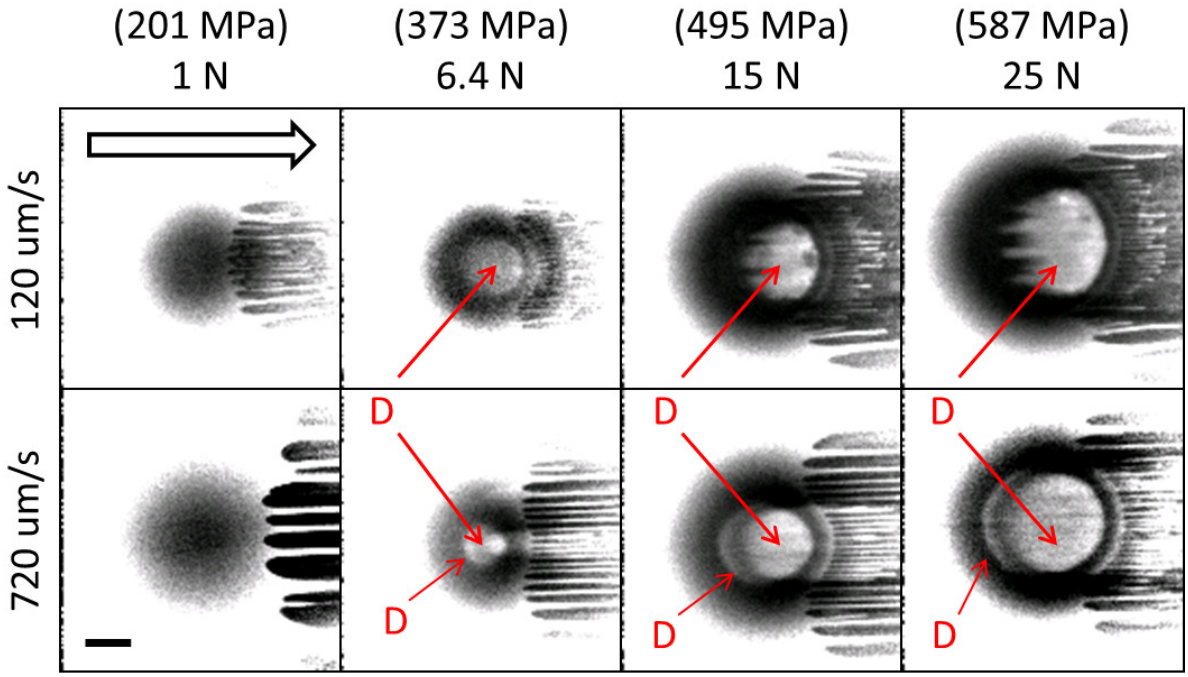


Fig. 40: Flat-field corrected intensity distributions of PB2300 for various speeds and loads in a sapphire-glass contact without calibration. The range of intensities varies for each image to highlight features of the film. The black arrow shows the direction of the flow. An increase of the film thickness towards the outlet of the contact can be seen for higher loads, as identified by the red D (for dimple). The scale bar is 100 µm.

Intensity distributions for the sapphire-glass EHD contact at various loads and speeds are shown in Fig. 40. The results are mostly similar to that of the glass-glass contact. There are however two differences. Firstly, as expected, the critical load (now 6.4 N) for the dimple to appear has reduced. The approximate pressure of 373 MPa at this load is fairly similar to the critical dimple pressure for the glass-glass contact. The second difference is the

occurrence of the secondary, crescent shaped dimple, near the inlet of the contact (observed at 263 MPa and 720 µ/s). This crescent shaped dimple is similar to the dimple found using interferometry in the steel-glass contact with H-300 in Fig. 37. Such a dimple was also observed in the glass-glass contact, although at much higher speeds (about 1400 µm/s). It should be mentioned that for the other polybutenes (PB920 and H-300), a larger pressure was required to cause the appearance of the primary dimple region. For PB920 the required pressure was about 520 MPa, although the dimple was not nearly as pronounced as for PB2300. The effect of molecular weight on the critical transition pressure is studied in further detail in subsection 6.4.

While the secondary crescent shaped dimple formation could potentially be studied using the sapphire-glass contact, the lower transmission of the sapphire surface complicates the application of the photobleached-fluorescence imaging velocimetry technique. For the glass-glass contact, the required speeds are prohibitively large. The crescent shaped dimple is also fairly small, causing the breakdown of the constant film thickness assumption, such that the velocity profile reconstruction scheme cannot be applied in the dimple. Therefore the crescent shaped dimple was not investigated further, and focus was placed on the dimple near the outlet of the contact.

There is a possibility that the fluorescence of nile red in polybutene is pressure sensitive, as other dyes have been shown to display such a sensitivity [72,98]. This could potentially cause the observed effects of increased intensity giving the appearance of a dimple, although typically emission decreases with pressure. A second dye was therefore used to discount this possibility. Few dyes are soluble in polybutene at the concentration required to produce sufficient fluorescence at small thicknesses. Bodipy-FL (Life Technologies) was however found to provide sufficient emission. Bodipy-FL was dissolved in PB2300 (similarly to the dissolution of nile red in polybutene) at a concentration of 100 µM. When acquisition using the new fluorophore-lubricant system was performed, it was noted that there was significant adsorption of Bodipy-FL on the glass surfaces. The intensity increased greatly with time. The effect of adsorption was countered by exposing the dye to high intensity illumination for a long time, effectively photobleaching the adsorbed fluorophores, while entraining

unbleached fluorophores. The imaging showed the appearance of a dimple at similar loads to those using nile red in polybutene, indicating that the observed effects are unlikely to be caused by the effect of pressure on the fluorescence of nile red.

Having identified the existence of a dimple, a calibration was performed to enable accurate film thickness measurements using laser-induced fluorescence.

3.2.3 Calibration

The fluorescence of a dye solution varies linearly with the path length, l, as described by the Beer-Lambert law of absorbance

$$A = \varepsilon c l \tag{39}$$

where A is absorbance, ε is the molar extinction coefficient and c is the concentration of the dye. This assumes that the absorbance remains relatively small. It is therefore possible to directly relate the path length to the fluorescence emission. The intensity of the flat-field corrected intensity distributions can thus be related to the film thickness, through a calibration detailed below.

A simple calibration, often used for interferometry film thickness measurements as well, involves a static Hertzian point contact, created by loading a sphere onto a flat surface. The separation between the sphere and the flat outside of the contact can be solved for using Hertzian contact mechanics. This can then be compared with the fluorescence intensity to relate the two quantities. For fluorescence calibration the contact is created within the PB-nile red solution. An approximate description of the separation, h, between the two surfaces [99] outside the contact is given by

$$h = \frac{a p_{max}}{E^*} \left(- \left(2 - \frac{r^2}{a^2} \right) cos^{-1} \frac{a}{r} + \sqrt{\frac{r^2}{a^2} - 1} \right) \tag{40}$$

where a is the contact radius, p_{max} is the peak pressure, $E^* = 2E'$ is the contact modulus and r is the distance from the centre of the contact. The flat-field corrected intensity distribution for a Hertzian contact used for calibration is shown in Fig. 38c. The distribution in the x-direction was calculated by averaging the intensity in the y-direction over five pixels as shown by the yellow rectangle.

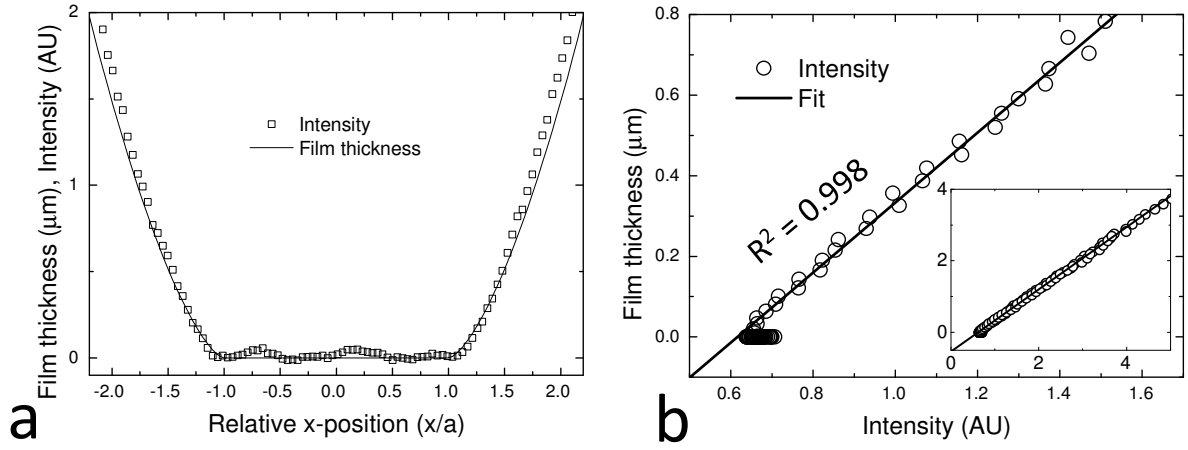


Fig. 41: a) Intensity and film thickness distributions across the centre of the glass-glass contact for H-300 at a load of 6.4 N (263 MPa). b) Film thickness plotted against the intensity, yielding a calibration curve. The black line is a linear fit to the data in the range ($0 < h < 0.8$ µm). The inset shows the linearity at larger film thicknesses (up to 4 µm).

The intensity distribution across the centre of the contact is compared to the theoretical film thickness (equation (40)) in Fig. 41a. The intensity has been rescaled to enable comparison. There is good agreement for the contact radius. The film thickness is plotted against the intensity in Fig. 41b, yielding a calibration curve. It is clear that the fluorescence is not constant inside the contact. This could be caused by an imperfect flat-field correction, fluorescence fluctuations as well as by a small amount of lubricant becoming trapped inside the contact. However, even if lubricant is trapped, the film thickness should be close to zero at the edges of the contact, due to lower viscosity, resulting in an accurate calibration.

A linear fit was made to the data, as indicated by the black line in Fig. 41b, yielding calibration constants, relating the intensity to the film thickness. The coefficient of determination indicates that the fit is accurate. Thus maps and plots of the film thickness for EHD lubrication at various conditions could be created. These results are presented in the subsequent sections.

3.2.4 Classical EHD

The calibration performed in the subsection 3.2.3 was used together with intensity maps in Fig. 39 to determine the film thickness distribution in pure sliding glass-glass EHD contacts lubricated with PB2300. A map of the film thickness for a load of 6.4 N (263 MPa) and a speed of 720 µm/s can be seen in Fig. 42a. The typical horseshoe region is visible

(highlighted in yellow) and near the centre of the contact, the film thickness appears to be mostly uniform. The film thickness distribution in the x-direction, for two speeds, across the centre of the contact (y = 0), taken as an average of 5 pixels in the y-direction (averaging area shown by a white rectangle), is shown in Fig. 42b. The result shows that the film thickness is indeed approximately uniform near the centre of the contact. It appears that the film thickness is slightly larger (order of 5 %) at the centre of the contact than the inlet. This could indicate spatial variations in the velocity profile, implied by conservation of mass.

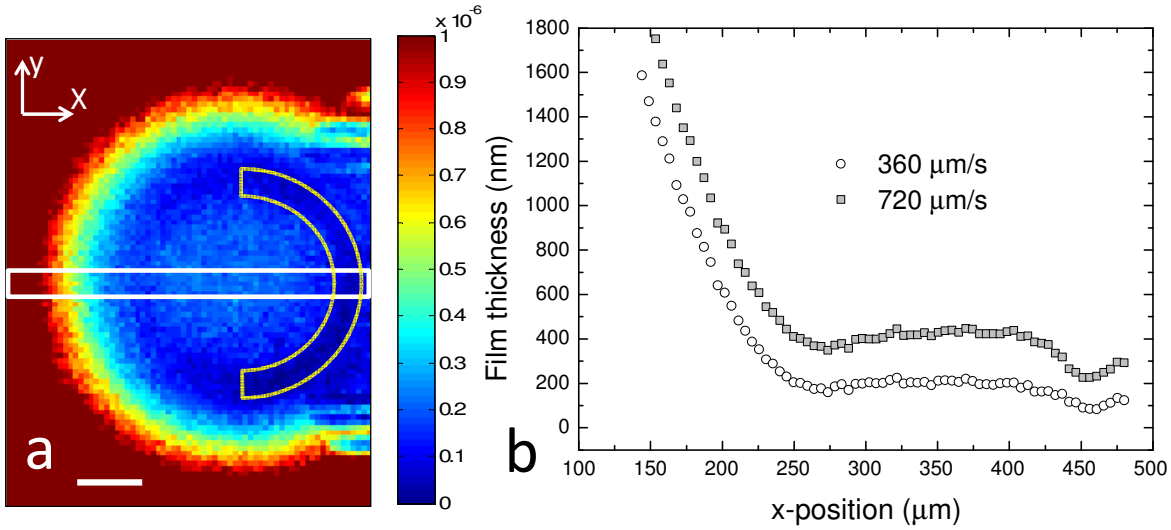


Fig. 42: a) Two-dimensional film thickness distribution at a speed of 720 µm/s and a load of 6.4 N (263 MPa) for PB2300. The scale bar is 50 µm. The white box highlights the area used for averaging and the yellow area marks the horseshoe. b) Film thickness distribution in the x-direction along the centre of the contact (y = 0).

3.2.5 Dimple

It was shown in subsection 3.2.2 that a dimple of increased film thickness appears inside the contact when the pressure reaches a critical value. Fig. 43a depicts a film thickness map for PB2300, at a load of 35 N (463 MPa) and a speed of 2400 µm/s. It is clear that the film thickness increases with the x-position in the contact. Furthermore a secondary crescent shaped dimple can also be observed.

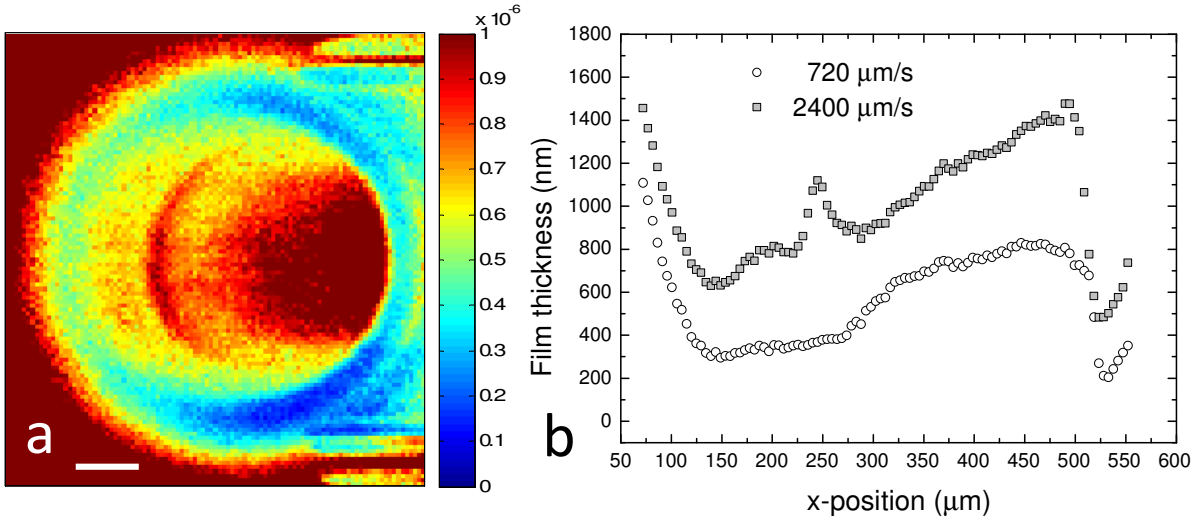


Fig. 43: a) Two-dimensional film thickness distribution at a speed of 2400 µm/s and a load of 35 N (463 MPa) for PB2300. The scale bar is 50 µm. b) Film thickness distribution in the x-direction along the centre of the contact (y = 0) for two speeds.

The average over 5 pixels in the y-direction is taken to plot the film thickness distribution in the x-direction, through the centre of the contact (y = 0), as shown in Fig. 43b. The crescent shaped dimple only appears if the speed is sufficiently large, as was concluded in subsection 3.2.2. For both speeds, the film thickness increases with x-position inside of the contact. At the lower speed of 720 µm/s two regions of approximately constant film thickness can be identified. It is possible that the flows in these two regions are substantially different, as some significant event must have taken place for the film thickness to suddenly almost double over a small distance of 50 µm. This could be investigated by application of the photobleached-fluorescence imaging velocimetry technique.

The crescent shape dimple has been observed for polybutene previously [40], and was also seen for the interferometric measurements performed in section 3.1. It was shown that the dimple appears at a critical load and a critical velocity. The results in [40] were measured for a pure sliding steel-chromium EHD contact. They showed that except for the occurrence of the crescent shape dimple, the film thickness decreases slightly with x-position inside the contact. This is significantly different from the results in Fig. 43 which show a large increase in the film thickness. The film thickness profile observed in Fig. 43b at 720 µm/s does however appear similar to some of the results presented for a pure sliding EHD contact lubricated by fatty alcohols [100], although those results were obtained at a lower slide-roll

ratio of 100 % (pure sliding is 200 %). The increase in the film thickness in [100] was proposed to be caused by plug flow due to the solidification of lubricant. A dimple was also shown to appear towards the back of the contact under certain conditions for Santotrac 70 in a steel-glass EHD contact [101], although this result was claimed to be caused by shear heating rather than wall slip, or plug flow.

The dimple is of interest for two reasons: (1) it presents a potential obstacle to the modelling developed in chapter 4.1 and (2) the anomalous film thickness is expected to be related to the rheology and flow of the lubricant. Since the film thickness of the dimples generated at low speed (i.e. the speed range used in this study) is mostly constant, the parallel plate assumption holds. Therefore photobleached-fluorescence imaging velocimetry can be applied to determine the cause of the observed anomalous film thickness.

The load and shear rate were shown to have significant effects on the film thickness distribution in glass-glass EHD contacts lubricated by polybutene. To study the effect of variations in the velocity boundary condition on the film thickness in EHD lubrication, laser-induced fluorescence was applied to an EHD contact with a low surface energy coating.

3.2.6 Slip coating

A low surface energy coating is used in this work to increase the likelihood of boundary slip in an EHD contact. The shear stress varies significantly with position in the contact (see Fig. 4b), due to the variation in normal pressure. It has been shown that the amount of slip experienced by a liquid is typically related to the shear stress experienced by the liquid [9]. Therefore the slip may vary with position in an EHD contact as well. If boundary slip is present and varies with position, the central film thickness would be expected to drop relative to the no-slip film thickness. This is because the fluid must accelerate or decelerate to accommodate this slip, requiring a change in the film thickness due to conservation of mass. Assuming a linear velocity profile, incompressible flow, and no-slip conditions at the inlet and outlet positions, the film thickness with a slip boundary condition, h_b, is given by the volume continuity equation

$$\frac{h_b}{h_c} = \frac{U}{U + u_b} = \frac{1}{1 + u_{brel}} = \frac{1}{1 + b_{rel}/(1 + b_{rel})} \tag{41}$$

where h_c is the film thickness for the no-slip boundary condition, U is the speed of the glass ball, u_b is the slip velocity at the coated surface, u_{brel} is the relative slip velocity and b_{rel} is the relative slip length given by equation (32). Film thickness measurements were performed for the EHD contact created by a glass sphere and a Fusso coated glass slide (see subsection 2.3.8), lubricated with H-300. A fresh Fusso surface was used for each measurement to minimize the effect of wear on the coating.

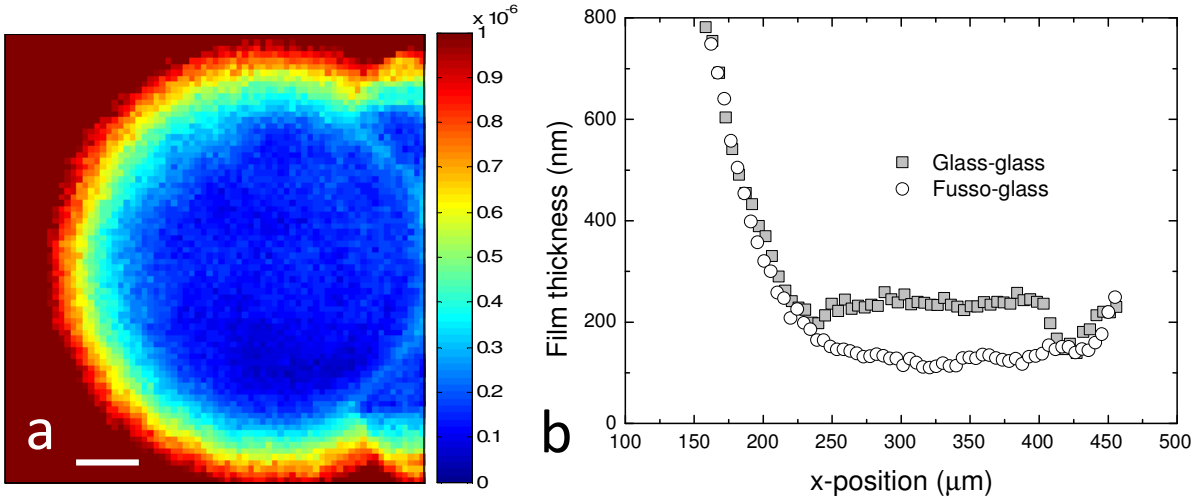


Fig. 44: a) Two-dimensional film thickness distribution at a speed of 720 µm/s and a load of 6.4 N (263 MPa) for a glass-Fusso EHD contact lubricated with H-300. The scale bar is 50 µm. b) Film thickness distribution in the x-direction along the centre of the contact (y = 0) for the two velocity boundary conditions.

The film thickness map for the glass-Fusso EHD contact, at a load of 6.4 N (263 MPa) and a speed of 720 µm/s, is presented in Fig. 44a. The horseshoe region is much less pronounced than it was for the glass-glass contact (see Fig. 42a). The mean film thickness in the x-direction, taken as an average over 5 pixels in the y-direction, along the centre of the contact (y = 0), is shown in Fig. 44b. Three distinct features can be observed. Firstly, the film thickness is significantly reduced in comparison to the glass-glass case. Secondly, although the effect is slight, the film thickness varies with x-position in the contact, decreasing towards the centre of the contact. Finally, the minimum film thickness now appears at the centre of the contact, rather than at the typical horseshoe position.

Outside of the contact the film thicknesses for glass-glass and glass-Fusso contacts, as shown in Fig. 44b are identical. The differences observed in the contact could be explained by the lubricant slipping at the lubricant-Fusso interface. It is conjectured that the lubricant accelerates due to the interfacial slip, causing a reduction in the film thickness, due to conservation of mass. The amount of slip would also be expected to vary with pressure such that the film thickness would vary with x-position, as was observed. At the typical position of minimal film thickness in a no-slip EHD contact, where the horseshoe is located, there is a rapid reduction of pressure. At the same position for a glass-Fusso contact, however, there would be a drastic reduction in the slip, and therefore an increase in the film thickness. It is possible that the reduction in slip counteracts the effect of the horseshoe; hence no horseshoe is observed when slip is present.

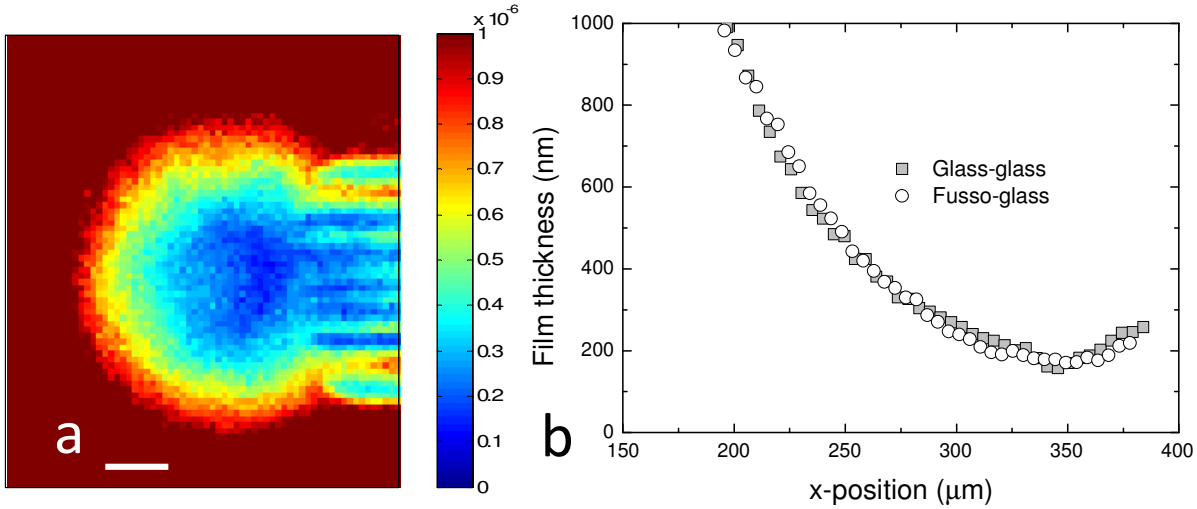


Fig. 45: a) Two-dimensional film thickness distribution at a speed of 720 µm/s and a load of 0.9 N (137 MPa) for a glass-Fusso EHD contact lubricated with H-300. The scale bar is 50 µm. b) Film thickness distribution in the x-direction along the centre of the contact (y = 0) for the two velocity boundary conditions.

As mentioned earlier the slip is expected to vary with pressure. Thus a change in the load should significantly alter the slip experienced by the lubricant. The load was therefore reduced to investigate if this assumption was accurate. Fig. 45a depicts the film thickness map for a glass-glass EHD contact at a load of 0.9 N (137 MPa) and a speed of 720 µm/s. It is clear that the operating regime is approaching hydrodynamic as the film thickness is far from uniform. The film thickness in the x-direction through the centre of the contact, taken as an average of 5 pixels in the y-direction, is shown in Fig. 45b for the two surfaces. The

low surface energy Fusso coating appears to have little effect on the film thickness in the contact. This indicates that the no-slip boundary condition holds at lower loads, suggesting that slip is indeed dependent pressure.

The entrainment speed would also be expected to affect interfacial slip. Slip is typically characterised by a slip length [9] which depends on the shear stress, causing the relative slip velocity to be a function of film thickness. Varying the speed of the sphere surface would affect the film thickness, shear rate and slip length which are all correlated.

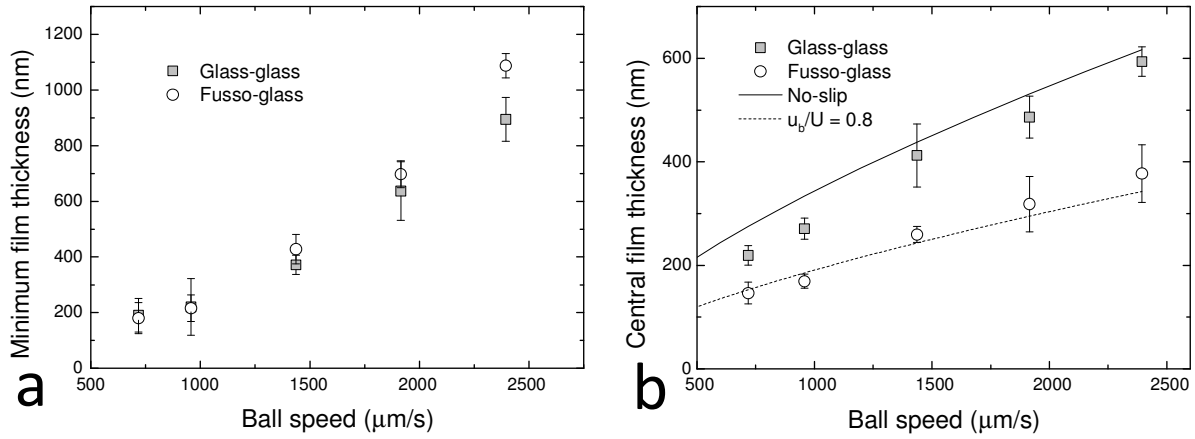


Fig. 46: a) Minimum film thickness at 0.9 N (137 MPa) as a function of speed for H-300. b) Central film thickness at 6.4 N (263 MPa) as a function of speed. The black line indicates the prediction for the film thickness, while the dotted line shows the prediction for the film thickness at a relative slip velocity of 80 %.

Film thickness measurements were performed for five different speeds at the loads of 0.9 N (137 MPa) and 6.4 N (263 MPa) for both velocity boundary conditions. Tests were performed twice. The results for the minimum film thickness, at a load of 0.9 N (137 MPa), are shown in Fig. 46a. There seems to be little differences between the two surfaces. At the highest speed the glass-Fusso contact minimum film thickness is slightly larger than that of the glass-glass contact. This is likely caused by uncertainty in the measurement of the minimum film thickness for the small contact, rather than an effect of the coating. At the higher load of 6.4 N (263 MPa, see Fig. 46b), there is a significant difference in the film thickness for the two surfaces. The Fusso coating causes the film thickness to reduce by approximately 40 %. The film thickness was calculated using equation (27), as shown by a black line in Fig. 46b, where the pressure-viscosity coefficient was determined in section 3.1. The film thickness is accurately predicted at high speeds, while at low speeds the prediction

is off by about 20 %. This is likely to be caused by the inaccuracy of the laser-induced fluorescence technique for film thickness measurements, which becomes apparent at low film thicknesses. The slip velocity was determined by fitting the glass-Fusso data to equation (41), as shown by the dotted line in Fig. 46b. This resulted in an approximate value of 0.8 for the relative slip velocity, giving a range of slip lengths of 500-1500 nm, as speed varies.

The final topic of this chapter focuses on the effect of slip on the existence of the dimple. Given that the dimple has been suggested to be caused by slip [39], a low surface energy coating should accelerate the appearance of the dimple. If the dimple is caused by solidification it may potentially be unaffected by slip, as the pressure distribution does not change drastically with the difference in boundary conditions.

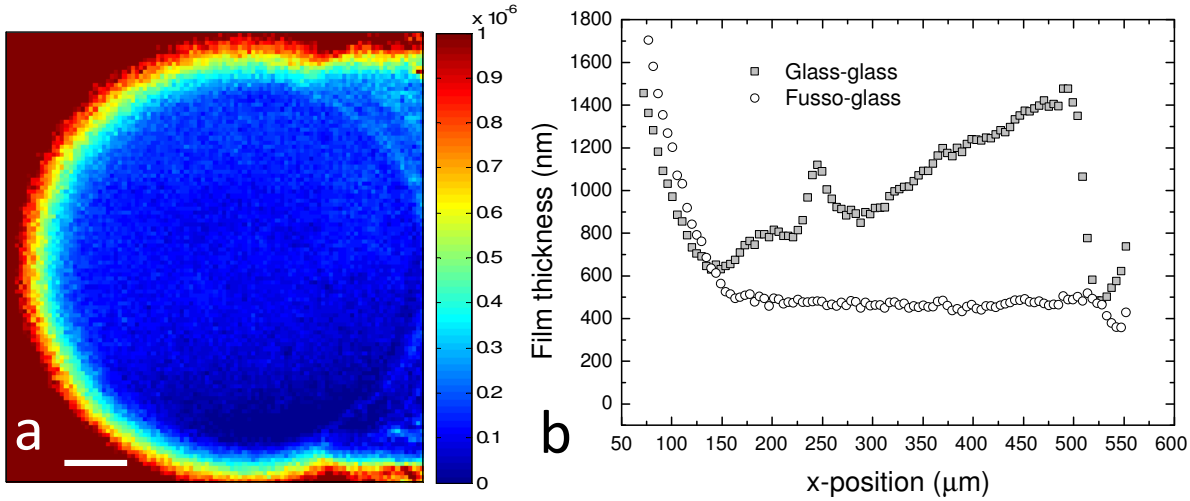


Fig. 47: a) Two-dimensional film thickness distribution at a speed of 2400 µm/s and a load of 35 N (463 MPa) for a glass-Fusso EHD contact lubricated with H-300. The scale bar is 50 µm. b) Film thickness distribution in the x-direction along the centre of the contact (y = 0) for the two different surfaces.

A map of the film thickness for the glass-Fusso contact, at a load of 35 N (463 MPa) and a speed of 2400 µm/s, is shown in Fig. 47a. At such a high pressure PB is expected to undergo a glass transition. No dimple is observed for the low surface energy coating. The mean film thickness, taken over 5 pixels in the y-direction, across the centre of the contact (y = 0), can be seen in Fig. 47b. It is clear that no dimple is formed in the glass-Fusso contact, as the film thickness is mostly uniform. The uniform film thickness for the slip boundary condition indicates that the dimple, observed for the no-slip case, is not caused by an effect of pressure on the fluorescence of nile red in polybutene, as the pressure distribution remains mostly

unaltered when a slip boundary condition is present. The disappearance of the dimple on the application of the coating suggests that severe shearing of the lubricant causes the dimple to form. If the coating enables significant boundary slip, the shear rate of the lubricant will be small. The requirement of sufficient shear rate for dimple formation agrees with results showing that the dimple disappears in pure rolling conditions [40], where the shear rate is negligible. Again the minimum film thickness, typically expected to appear near the outlet, is not very pronounced in Fig. 47b. If the amount of slip is large, as indicated by the drop in central film thickness in Fig. 46b, the amount of shear experienced by the lubricant is severely reduced. This suggests that both a critical shear rate, as well as a critical pressure, is required for the dimple to form.

3.3 Summary

Interferometry was used to measure the film thickness of polybutene in a steel-glass EHD contact. This was used to determine the pressure-viscosity coefficient for polybutene, which was found to be 32 GPa^{-1} for PB2300 and 30 GPa^{-1} for H-300. These values are similar to values found in literature. Laser-induced fluorescence (LIF) was used to acquire film thickness measurements in a glass-glass EHD contact. A calibration was performed using a static point contact, which related fluorescence intensity to film thickness. LIF results showed that anomalous film thicknesses appeared at large pressures for polybutene.

Glass-glass EHD contacts at relatively low pressures had films with the expected constant film thickness and horseshoe typically observed in EHD lubrication. Once a critical pressure was reached, a dimple appeared towards the outlet which had a film thickness of almost double the film thickness at the inlet. At high pressure and large speeds, a secondary dimple also formed near the inlet. Due to the small size of this secondary dimple it was decided that it could not be studied using velocimetry. The first dimple, however, formed a mostly constant film thickness over a sufficiently large area. Hence the rheology of lubricant in this first dimple could be investigated.

The low surface energy coating was applied to investigate the effect of interfacial slip on EHD contact tribology. It was found that at low pressure, there was no significant difference

in film thicknesses between a glass-glass EHD contact (no-slip) and a glass-Fusso contact (where the slip promoting coating was applied). At higher pressures however, the film thickness reduced by approximately 40 % when the coating was applied. Using the principle of conservation of mass it was shown that this reduction could be caused by the lubricant slipping at a relative velocity of 0.8, corresponding to a slip length in the range of 500-1500 nm.

To further shed light on the findings of this chapter it was necessary to directly measure the velocity profile. This would aid in explaining the observed effects revealed by film thickness measurements and answer the questions of whether the velocity profile in EHD lubrication varies locally, if dimple formation is related to slip or solidification and if the slip coating does indeed cause the lubricant to slip at the interface. The theory required for using photobleached-fluorescence imaging for velocimetry was developed in chapter 4 to accomplish this undertaking.

4 Analysis

In this chapter a model is developed, that describes the spatiotemporal intensity distribution for a photobleached-fluorescence imaging experiment. This model enables simulation of the intensity distribution, given a known velocity profile, which can then be compared with experimental data. A reconstruction scheme is developed to determine the velocity profile using this comparison. The scheme is then evaluated based on its accuracy in determining a set of typical profiles, inferring the resolution of the technique. The technique is then validated by application to a parallel plate setup and a soft-EHD contact with known velocity profiles. Finally, a brief overview is given of results for the velocity profile measured at various experimental conditions.

4.1 Modelling

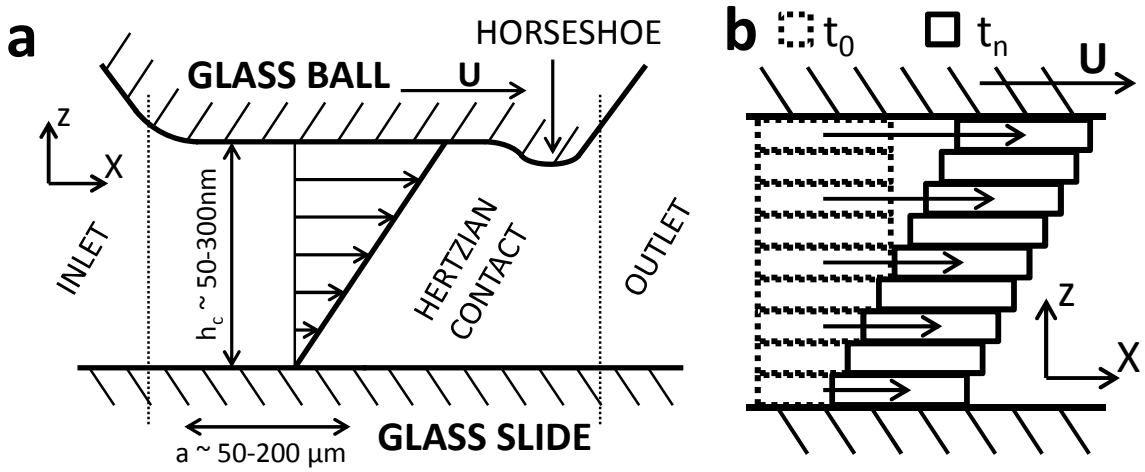


Fig. 48: a) A linear velocity profile is shown for an EHD contact of film thickness, h_c, and contact radius, a, with the top surface moving at a velocity U. The position of minimum film thickness, the horseshoe, is indicated. (Fig. 48a is a duplicate of Fig. 6) b) The fluid is modelled as layers of infinitesimal thickness, moving at a velocity of $u(z)$. Here, a linear profile with slip at the interface is shown. The position of the photobleached layers is shown just after photobleaching, t_0, and after advection at time t_n. (From [29] with kind permission from Springer Science and Business Media)

The geometry of a pure sliding EHD contact, pictured with the typically assumed linear velocity profile, can be seen in Fig. 48a. The contact is assumed to be mostly of constant thickness, with the minimum thickness occurring near the outlet. This allows the problem to be treated as plane Couette flow around the centre of the contact. As outlined in section 2.1,

a through-thickness photobleached column, within a fluorophore-doped lubricant in an EHD contact of lower intensity than its surroundings, is created by photobleaching at time $t = 0$. If the conditions of homogeneous diffusion, steady state and incompressible flow apply, the convection of scalar properties such as the concentration of excited unbleached fluorophores in the lubricant, c, at a particular location, is governed by the scalar transport equation

$$\frac{\partial c}{\partial t} = D\nabla^2 c - \vec{u} \cdot \nabla c \tag{42}$$

where ∇ is the gradient operator and $\vec{u}$ is the velocity field. The relative effects of diffusion and advection are quantified by the non-dimensional Péclet number, $Pe = L_c U_c / D$, where L_c is a characteristic length scale, U_c is a characteristic velocity and D is the diffusion coefficient. For diffusion in the z-direction, where diffusion would be most prominent in an EHD contact, the Péclet number is given by

$$Pe_z = \frac{h_c U}{D} \tag{43}$$

If diffusion is relatively fast, any variation of intensity in the z-direction will vanish over time as layers mix. On the other hand, if advection is fast, variations of intensity in the z-direction will persist. It has been shown that the effect of diffusion in flows is negligible for Péclet numbers larger than 100 [102]. Using the value of D determined in subsection 2.2.3 and a typical film thickness of 170 nm for H-300 at 360 µm/s, the Péclet number is 8000. If the fast component of diffusion is used (see subsection 2.2.3) $Pe_z = 500$ remains above 100. Under the conditions in this work, diffusion effects can therefore be assumed to be negligible. This allows the problem to be treated as a case of pure advection as shown in Fig. 48b, for a particular velocity field flowing only in the x-direction.

The fluid can be modelled as layers of infinitesimal thickness, moving independently, without mixing, at velocity, $u(z)$. For the case of the EHD contact, if the area being probed is relatively small compared to the contact area, the velocity profile can be assumed to be invariant in the x-y plane such that the velocity in the x-direction is given by $u = u(z)$. In this work the probing area is approximately 30x30 µm while the contact has a diameter of ~ 100 - 200 µm. Since the film thickness in an EHD contact is roughly constant, incompressible

flow can be assumed. By applying continuity, it can be shown that velocities in the z-direction are zero. Due to symmetry, along the centre-line of the contact, velocities in the y-direction are zero (supported experimentally in subsection 4.6.1). Using $\vec{u} = (u(z), 0, 0)^T$ and assuming negligible diffusion, equation (42) reduces to

$$\frac{\partial c}{\partial t} + u\frac{\partial c}{\partial x} = 0 \tag{44}$$

This is a hyperbolic partial differential equation which has the solution

$$c(x, z, t) = c_0(x - ut) \tag{45}$$

where c_0 is the concentration of unbleached fluorophores immediately after photobleaching (at $t = 0$). Assuming a Gaussian laser bleaching beam, instantaneous and uniform photobleaching in the z-direction, and a constant photobleaching rate, the initial distribution is invariant in z and c_0 can be defined as

$$\frac{c_0(x)}{c_i} = 1 - A_p e^{-\frac{(x-x_0)^2}{2{w_0}^2}} \tag{46}$$

where c_i is the fluorophore concentration, A_p is the ratio of bleached fluorophores at the centre of the photobleaching beam, x_0 is the central position of the photobleaching beam and w_0 is the beam radius. The appropriateness of the instantaneous photobleaching assumption can be evaluated experimentally by studying the shape of the initial post-bleach intensity distribution, which would be non-Gaussian for a finite photobleaching duration, when the lubricant is in motion, as is shown in subsection 2.1.6. Using equation (46), equation (45) can then be written as

$$\frac{c(x, z, t)}{c_i} = 1 - A_p e^{-\frac{(x-(ut+x_0))^2}{2{w_0}^2}} \tag{47}$$

Assuming homogenous illumination, the theoretical intensity distribution, I^*, that can be compared to the experimental results, is then the sum of the intensity in each layer, and the relative theoretical intensity distribution, I_N^*, is given by

$$I_N^* = \frac{I^*(x,t)}{I_0} = \int_0^{h_c} \frac{c(x,z,t)}{c_i} dz \tag{48}$$

where I_0 is the intensity without photobleaching. Hence the relative theoretical intensity distribution is related to the through-thickness velocity profile, $u(z)$, through equations (47) (48). This analysis differs from similar submicron photobleached-fluorescence imaging velocimetry implementations [65,103], where the low Péclet number causes the intensity to homogenize in the z-direction. In this work the system chosen allows the technique to resolve variations in the intensity through the thickness of the film, enabling identification of effects such as slip and inhomogeneous shear. Similar uses of molecular tagging velocimetry have been applied previously to high Péclet number flows of much larger geometry [104,105], where the variation of the intensity over time was used to determine the velocity profile. Here, a similar approach is taken to find the unknown velocity profile, $u(z)$, of lubricant in an EHD contact.

4.2 Velocity profile reconstruction

The local rheology of a lubricant in an EHD contact is probed in this work, by determining the velocity profile, $u(z)$. An experimental setup and technique (see section 2.1) have been developed to measure the spatiotemporal normalised relative intensity distribution, I_N. In section 4.1 it was shown that the distribution is a function of the initial distribution, $I_N = f(I_0, u(z))$, as the fluorophore concentration is constant and the flow is driven by advection. This relationship can however not be solved analytically. It has previously been solved by assuming a particular shape for the velocity profile [106], for which parameters can be determined through fitting. Another approach has also been taken, which requires no assumption of the velocity profile [105]. A similar scheme to [105] is developed here, where non-linear regression is used to relate I_N to the theoretical distribution I_N^*, by determining the unknown velocity profile $u(z)$.

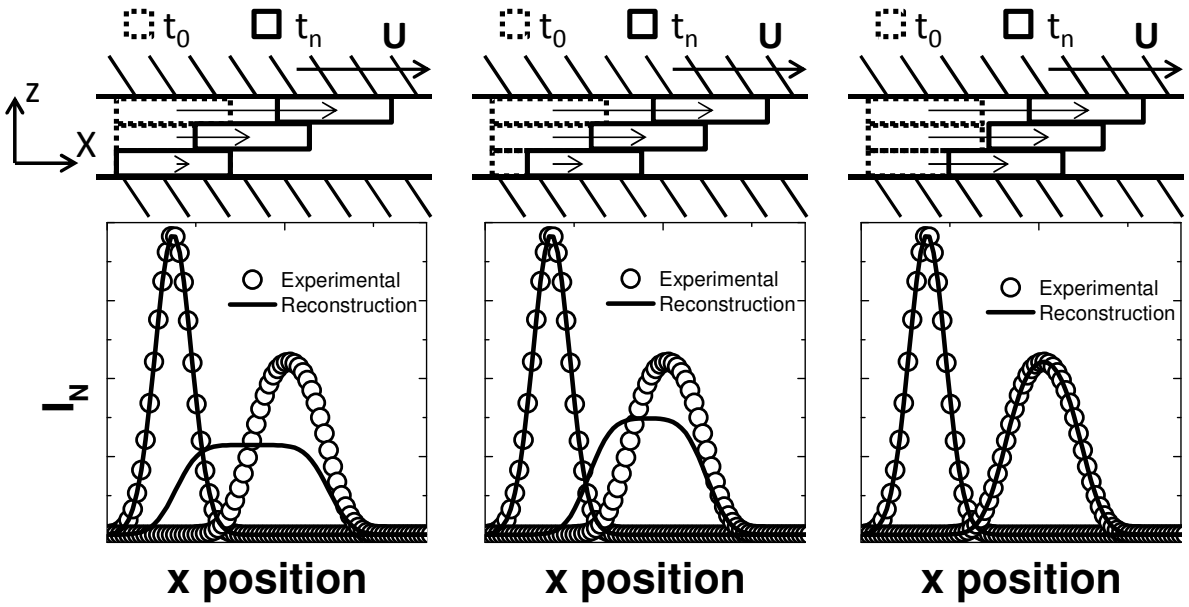


Fig. 49: Three successive fitting attempts for the velocity profile $u(z)$ are depicted. Top: The position of three fluid layers at times t_0 and t_n are shown. Bottom: The one-dimensional intensity distribution for I_N from experimental results (open circle) and I_N^* (solid line), calculated by summation of the layers in the top figure. The distributions are shown at times t_0 and t_n. In the first iteration there is a mismatch between I_N and I_N^* at t_n, so $u(z)$ is varied until they are equal, as seen in the last iteration. (From [29] **with kind permission from Springer Science and Business Media)**

A schematic depicting the velocity profile reconstruction scheme is shown in Fig. 49. It shows how a solution for the velocity profile can be found by varying $u(z)$ until the difference between the experimental and theoretical intensity distributions is minimized. From here on the discrete axes i, j, k are used for the continuous axes x, y, z, and the discrete frame number n is used for the continuous time t. To simplify the problem, and to improve the signal to noise ratio, the experimental distribution is averaged in the y-direction over $2w$ pixels using

$$I_x(i,n) = \sum_{j=-w}^{w} I_N(i,j,n)\,/(2w) \tag{49}$$

where I_x is the averaged intensity distribution in the x-direction from experimental results. To determine the unknown velocity profile, a simulated profile is varied until the experimental and theoretical distribution match. This can be done using a non-linear least squares minimization given by

$$\sum_{i=1}^{128}\sum_{n=5}^{N}\|I_N^* - I_x\|^2 \tag{50}$$

where N is the total number of frames. Convergence was achieved when the iterative change expression (50) was smaller than δ_I, which is the convergence criterion for the intensity. The minimization was performed using the function 'lsqnonlin' in Matlab. The solution obtained from the minimization in expression (50) is not unique. If the position of any two fluid layers in Fig. 49 were switched, the resulting intensity distribution would remain unchanged. Thus, multiple solutions for $u(z)$ are possible. A monotonic velocity profile constraint is thus applied ($du/dz \geq 0$), by setting a large penalty on negative strain rates.

A further constraint is applied to reduce step changes in the velocity profile. This simulates continuity and makes the minimization unique. This is done by minimizing the second differential of the velocity profile

$$\sum_{k=2}^{K-1}\|u(k+1) - 2*u(k) + u(k-1)\| \tag{51}$$

where K is the number of discrete fluid layers. Convergence was achieved when the iterative change of expression (51) was smaller than δ_u, which is the convergence criterion for continuity. Combining expressions (50) and (51) , the final minimization is given by

$$\sum_{i=1}^{128}\sum_{n=1}^{N}\|I_N^* - I_x\|^2 + \frac{\delta_I}{\delta_U}\sum_{k=2}^{K-1}\|u(k+1) - 2*u(k) + u(k-1)\| \tag{52}$$

In all cases, the convergence criterion for the iterative change in expression (52) was 10^{-8}. While this makes the solution of $u(z)$ unique, it is still defined by the ratio of the convergence criteria δ_I/δ_u. In [105] a ratio is effectively chosen. In this work an optimal ratio is found by comparing the effects of the value of δ_I/δ_u on the quality of the fit. The coefficient of determination, R_I^2, can be used to describe the goodness of fit between I_x and I_N^*. In the case where the profile is known, a coefficient, R_U^2, can be calculated for the correlation between the reconstructed velocity profile, u, and the input profile, u_s. R^2 should be maximised for both cases. By varying the ratio of the convergence criteria, the optimal product of $R_I^2 R_U^2$ can be found. Determination of this ratio can be found in section 4.3 and

the ratio was found to be approximately $\delta_I/\delta_u = 3 \cdot 10^{-4}$. As the profile is uniquely defined by this ratio, the solution for the velocity profile is independent of the number of layers K.

The boundary conditions for the minimization were $u(1) \geq 0$ and $u(K) \leq U$. The velocity profile was initialized as a linear profile from 0.3U to U. Parameters t_0, w_0 and A_p were initialised to typical values and then determined by the minimization, along with the velocity profile. x_0 was measured experimentally. The reconstruction scheme described in this section was implemented using a custom Matlab script, to reconstruct the velocity profile, $u(z)$, based on the experimental intensity distribution, I_N. It should be noted that two-dimensional minimizations, without the averaging used in equation (49), were also carried out, yielding similar results to the one-dimensional minimization, but with much longer computation times. Considering the large amount of data in this project (hundreds of profiles to be fitted), the one-dimensional minimization was used.

Having developed a method of determining a velocity profile from a comparison between a simulated and experimental spatiotemporal intensity distribution, it is possible to determine the accuracy of the reconstruction scheme in terms of resolving the correct velocity profile under various conditions.

4.3 Evaluation of reconstruction scheme

The success in reconstructing the velocity profile with the scheme outlined in section 4.2 is assessed for a variety of profiles and cases using simulated data.

4.3.1 Couette and Poiseuille flow

First, plane Couette flow is considered as it is the profile commonly assumed for an EHD contact. The velocity profile is given by equation (30), reproduced here: $u(z) \approx U\frac{z}{h}$. A simulated intensity profile was calculated by numerical solution of equation (48), using: velocity $U = 360$ µm/s, layers $K = 30$, bleaching time $t_b = 1$ ms and beam radius $w_0 = 3$ µm. The result for the intensity distribution over time is shown in Fig. 50a. There is a good correlation between the reconstructed and theoretical intensity distributions for all times. The reconstructed and input velocity profiles are compared in Fig. 50b. The coefficient of

determination is $R^2 = 1.0000$, indicating a good fit. This shows that for a simple velocity profile, the technique is capable of reconstructing the correct velocity profile.

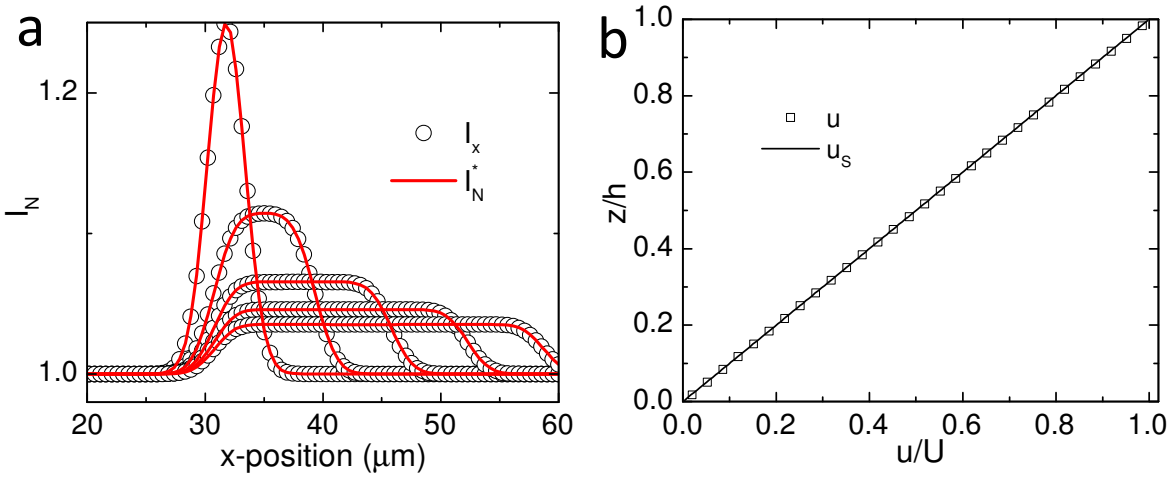


Fig. 50: a) Simulated experimental (I_x) and reconstructed (I_N^*) intensity distributions at five times. b) Relative velocity u/U at relative position z/h. u is the reconstructed velocity profile and u_S is the input profile for the simulation.

Pressure driven flow was also considered, specified as the first term in equation (1). The intensity distribution was constructed using the same conditions as for the Couette flow. The velocity profile reconstruction scheme was then applied to find the best fit for $u(z)$. The intensity distributions at various times are shown in Fig. 51a. The scheme was able to find a profile for which the intensity profiles match at all times. The result for the velocity profile is shown in Fig. 51b. Comparing the reconstructed velocity profile u to the theoretical profile u_S, the reconstruction is not successful. The developed reconstruction scheme requires that the reconstructed profile is monotonic. As the pressure driven profile is symmetric, the correct solution is found for half of the profile, as shown by comparing u and $2u_S$. The coefficient of determination for u and $2u_S$ is 0.9999, indicating a successful reconstruction. Due to the monotonic nature of the scheme, asymmetric profiles, such as pressure driven flow with slip on one surface, cannot be solved accurately. However, non-monotonic velocity profiles are not expected in this work, due to pure sliding conditions, which minimizes the Poiseuille component of the flow.

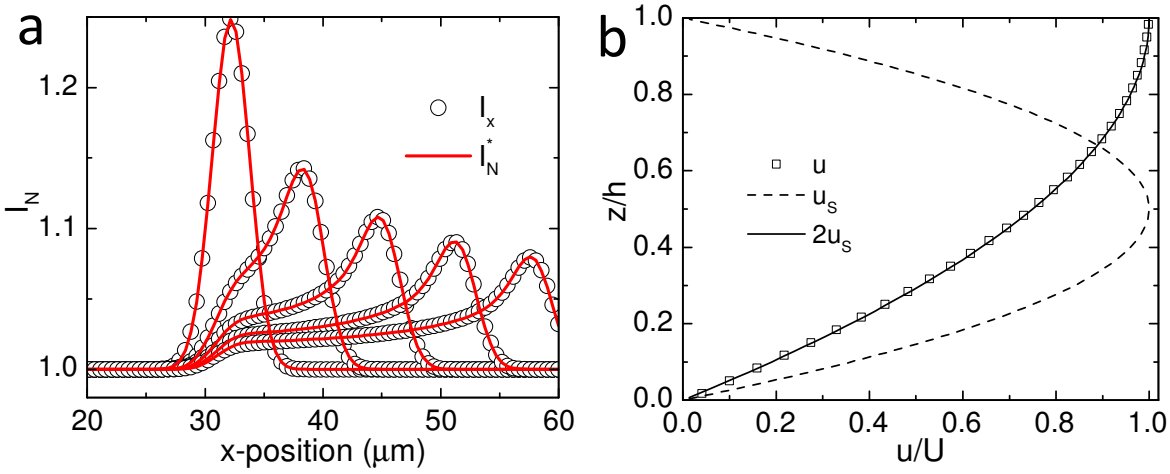


Fig. 51: a) Simulated experimental (I_x) and Reconstructed (I_N^*) intensity distributions at five times. b) Relative velocity u/U at relative position z/h. u is the reconstructed velocity profile and u_S is the input profile for the simulation.

As discussed in section 4.2, a value for the criterion ratio, δ_I/δ_u, needs to be chosen to provide a unique solution for the velocity profile reconstruction scheme. The optimal δ_I/δ_u ratio is determined for a given profile, to optimize the quality of the intensity fit and the shape of the reconstructed velocity profile. This is done by maximising the product of the coefficients of determination, $R^2{}_I R^2{}_u$, where $R^2{}_I$ and $R^2{}_u$ are the coefficients of determination for the intensity distributions and velocity profiles respectively. Note that the determination of the optimal ratio cannot be done for the plane Couette velocity profile as the optimal solution would have been $\delta_I/\delta_u \to \infty$. The Poiseuille profile can be used however as the velocity gradient is not constant. For an unperturbed distribution the limit is $\lim_{\delta_I/\delta_u \to 0}(R^2{}_I R^2{}_u) \to 1$, which is not realistic for experimental data. Hence, the intensity of each frame was perturbed by 5 % randomly to simulate noise which might be encountered in experiments. Solutions for low and high values of δ_I/δ_u are shown in Fig. 52a. At low values of δ_I/δ_u (u_L with open square), the profile deviates from the correct solution (red line). There is some waviness present, although a good fit for the intensity distribution is achieved ($R^2 = 0.992$). At high values of δ_I/δ_u the profile approaches a linear velocity profile and there is a lower correlation for the intensity fit ($R^2 = 0.98$). This shows how varying δ_I/δ_u represents a trade-off between the fits for the intensity and the velocity profile. The optimal criterion ratio occurs over a range of values, as seen in Fig. 52b, where the value does not significantly affect the reconstructed velocity profile. An approximate central value for this

range of $\delta_I/\delta_u = 3 \cdot 10^{-4}$ was chosen for all velocity profile reconstructions, resulting in the profile seen in Fig. 51b. Although the results here are specifically for a Poiseuille velocity profile, other profiles were tested, showing that the optimal value of the criterion ratio did not depend significantly on the shape of the profile as long as some non-linearity was present.

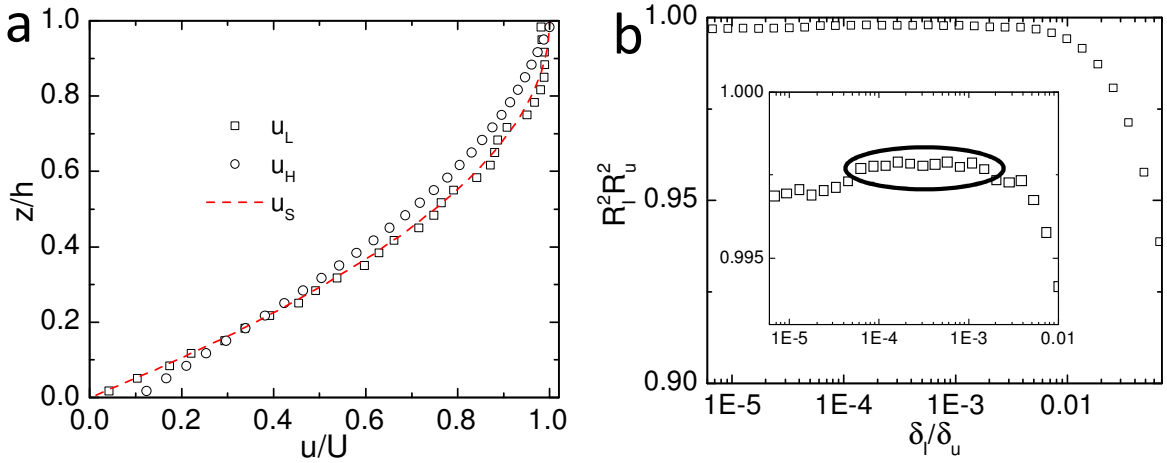


Fig. 52: a) Reconstructed velocity profiles for low (u_L) and high (u_H) criterion ratio δ_I/δ_u respectively. The red line indicates the input velocity profile. b) Dependency of product of coefficients of determination on the criterion ratio. In the inset, the optimal region is identified.

4.3.2 Inhomogeneous shear flow

One limitation that the continuity minimization imposes on the velocity profile reconstruction is the resolvable step change in shear rate. If the lubricant flows as a solid plug (as has been proposed previously [45]), there is a sharp gradient in the profile towards the surfaces. In the case of partial plug flow, the shear rate close to the wall is the highest in the flow profile. To assess the resolution of the reconstruction scheme in obtaining profiles with sharp gradient changes, the simulated intensity distribution corresponding to velocity profiles with varying boundary layer thicknesses, h_L, were created. Reconstructions, using these stimulated intensity distributions as input, were then performed to assess the accuracy of the reconstruction scheme, and how the accuracy depended on the input profiles. A comparison between input and reconstructed velocity profiles (with $\delta_I/\delta_u = 3 \cdot 10^{-4}$) can be seen in Fig. 53a for the scenario of plug flow. The number of layers is $K = 30$. Three profiles are presented with various degrees of plug flow, manifested as a change in the thickness of

the boundary layers, h_L. An increase in h_L corresponds to a reduction in relative shear rate. The maximum resolvable relative shear rate (close to the wall), $\dot{\gamma}_{max}$, can be found by calculating the maximum normalised shear rate at which the reconstructed velocity profile does not deviate significantly from the theoretical profile. The ratio of the reconstructed boundary layer shear rate, $\dot{\gamma}$, and the input boundary layer shear rate, $\dot{\gamma}_S$, is shown in Fig. 53b, where both shear rates are normalised by the apparent shear rate $\dot{\gamma}_A = U/h$. The shear rates for the plug flow case were determined using a linear fit to the first three points, k = 1-3. The maximum relative shear rate where the fit is acceptable occurs at h_L = 0.15, as indicated by the vertical line in Fig. 53b, which corresponds to a value of 3.5 for plug flow. Other profiles produce slightly different results but the maximum relative shear rate that can be successfully reconstructed is in the range of 3. Any shear rate above the threshold will result in an underestimation of shear rate by the reconstruction scheme.

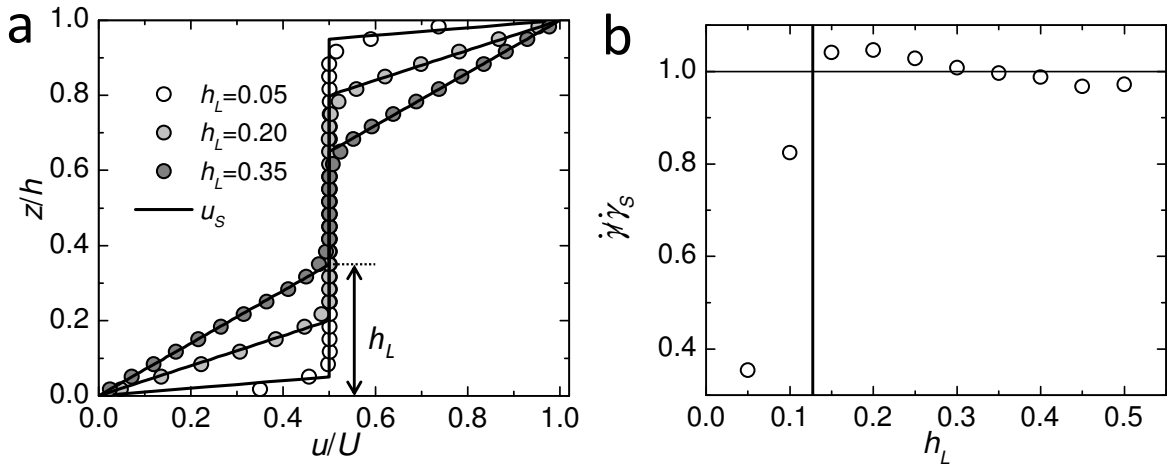


Fig. 53: a) Velocity profiles for the case of plug flow as the thickness of the boundary layers is varied. Circles represent the profiles determined by the reconstruction scheme at various boundary layer thicknesses while the black lines are the input velocity profiles. b) Ratio of the maximum reconstructed and input shear rates of the boundary layer for plug flow. The vertical line indicates the critical height for the acceptable determination of the shear rate.

Shear banding may be present in EHD lubrication, which can be described as a step increase in the velocity over a small height. Shear bands do not always necessarily take place in the centre of a plane Couette flow [107]. If the shear band occurs near the surfaces, it is possible that the band may not be detected, and it might be resolved as either slip or it may be neglected due to the low relative intensity of the stagnant portion of the lubricant. To

evaluate the ability to detect the band the same analysis performed for plug flow was applied to shear banding for varying shear band widths, h_W, and positions, h_P (see Fig. 54). The reconstruction for three example velocity profiles can be seen in Fig. 54a. For $h_P = 0.5$ and $h_P = 0.3$, where the band positions are close to the centre, it can be seen that the velocity profile is reconstructed relatively accurately, and the position of the shear band can be identified. For the case where the shear band is close to the surface, i.e. $h_P = 0.1$, the shear band cannot be identified. This is caused by the relatively low intensity of the small amount of slowly moving lubricant at the bottom surface.

The position of the shear band can be found from the reconstructed velocity profiles by locating the position where the derivative of the velocity profile is maximum. The determined location, h_{PM}, is compared to the input position, h_P, as the input position is varied, as shown in Fig. 54b. Another parameter is introduced, h_W, which describes extent of shear banding and is defined as the increase in velocity occurring in the shear band. h_W has a noticeable effect on the success of the reconstruction. It reduces the likelihood of identifying the shear band when it is close to the surface. Ultimately a minimum value of about $h_P = 0.15$ for the relative position of the shear band can be found, where the position can be accurately determined for all shear band widths.

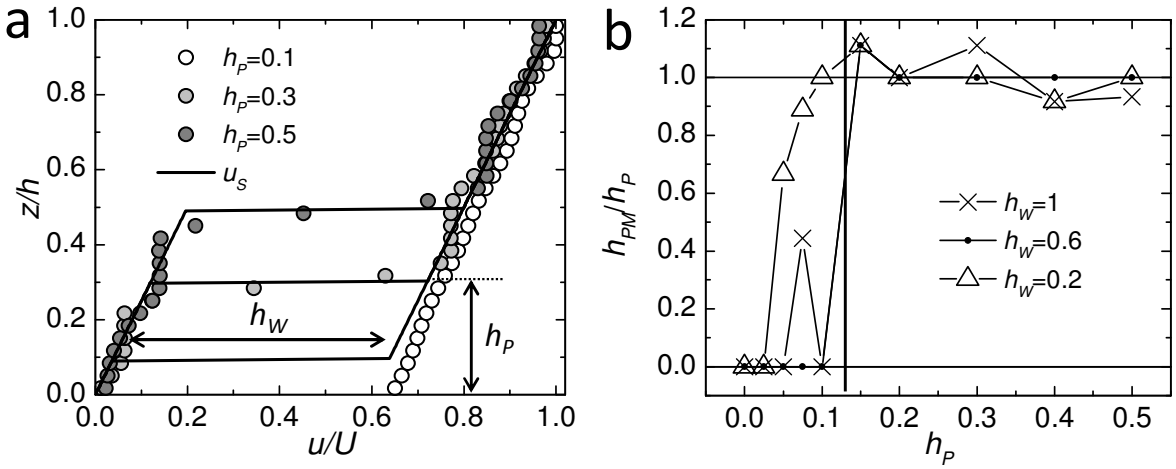


Fig. 54: a) Reconstructed velocity profiles (circles) for the case of shear banding as the position of the shear band of the input profiles (solid lines) is varied. These results are for a shear band width of 0.6. b) Ratio of the measured and the input position of the shear band for three shear band widths. The vertical black line indicates the minimum position at which the band position can be identified for all widths.

4.3.3 Boundary slip flow

One advantage of the developed technique, mentioned in subsection 2.1.2, is its ability to identify interfacial slip in very thin films. The reconstruction scheme is therefore assessed on its accuracy of slip length determination. For simplicity, the case of plane Couette flow, with interfacial slip at the bottom surface (equation (31)), is considered. Velocity profiles were reconstructed for input profiles with various relative slip lengths, $b_{rel} = b/h$. The slip length was determined by a linear fit to points k = 1-5 and extrapolation to $z = 0$. A comparison between the determined slip length, b, and the input slip length, b_S, is shown in Fig. 55a. The result shows that the difference between b and b_S is small and hence the slip length can be determined accurately over a range of slip lengths for a plane Couette velocity profile.

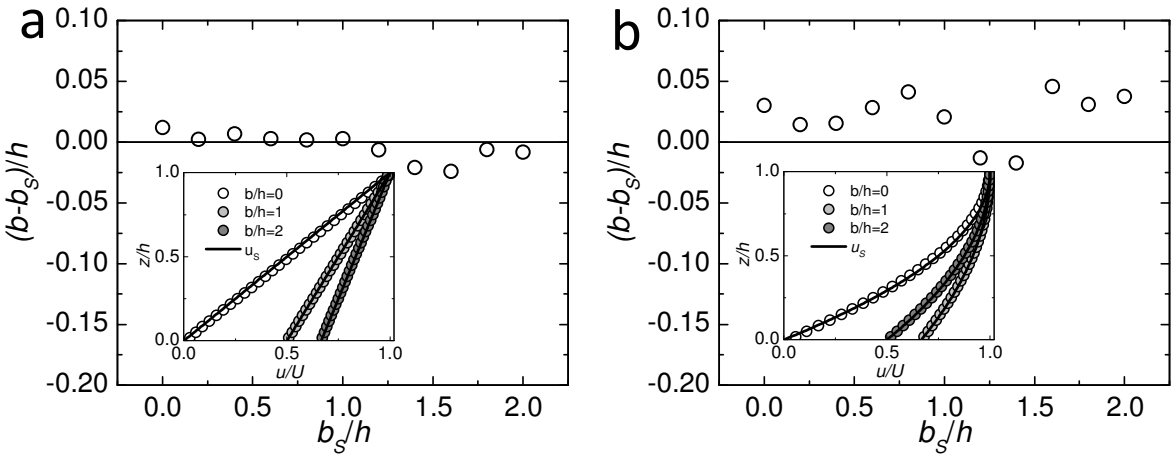


Fig. 55: a) Accuracy of the reconstructed relative slip length as a function of the input relative slip length for a plane Couette profile. b) As (a) for a Poiseuille profile. The insets show the input (solid line) and reconstructed (circles) profiles at various slip lengths.

In cases where shear banding or plug flow is present, the accuracy of the slip length determination reduces, due to the presence of high relative shear rates. The profiles for shear banding and plug flow are difficult to define as they can take on many forms. Pressure driven flow with slip at both interfaces is however well defined [108], and allows the effect of a gradient shear rate to be taken into account. The result of slip length determination accuracy with a Poiseuille flow profile is presented in Fig. 55b, showing that the reconstruction scheme can determine the slip length to within 5 %, even for a non-linear velocity profile. For cases with high shear rates (plug flow and shear banding) this accuracy would be diminished as is evident in Fig. 53a and Fig. 54a.

The results for the accuracy of the slip length determination shown in Fig. 55 do not take effects of noise into account. When noise is present in combination with a high relative shear rate, the result of the reconstruction scheme becomes extremely dependent on δ_I/δ_u. This becomes relevant when reconstructing experimental data where there is a significant amount of interfacial slip. The accuracy of the reconstruction scheme for a combined Couette and Poiseuille velocity profile, which may occur in an EHD contact with interfacial slip, was therefore studied. The slip length was varied for a Couette velocity profile with slip, which had a Poiseuille component of 30 %. Noise was simulated by applying a random fluctuation of $\pm$2.5 % to the intensity of all pixels. The initial intensity profile was also modified, to simulate slight deviations from a Gaussian shape which were typically observed for measurements in the EHD contact, by adding a secondary small broad Gaussian distribution of peak proportion, $A_0/3$, and radius, $3w_0$. As the applied noise was randomly generated, the intensity distributions were simulated twice, and the reconstruction scheme was applied to the two sets of distributions. The result of applying the reconstruction scheme, detailed in section 4.2, which has been applied for all previously presented analysis, subsequently labelled as 'free', is presented in Fig. 56. Note that the fit is particularly bad due the input profile having relative velocities above 1, which the reconstruction scheme does not permit. However, the analysis still enables the evaluation of the ability of the scheme to accurately determine the slip velocity.

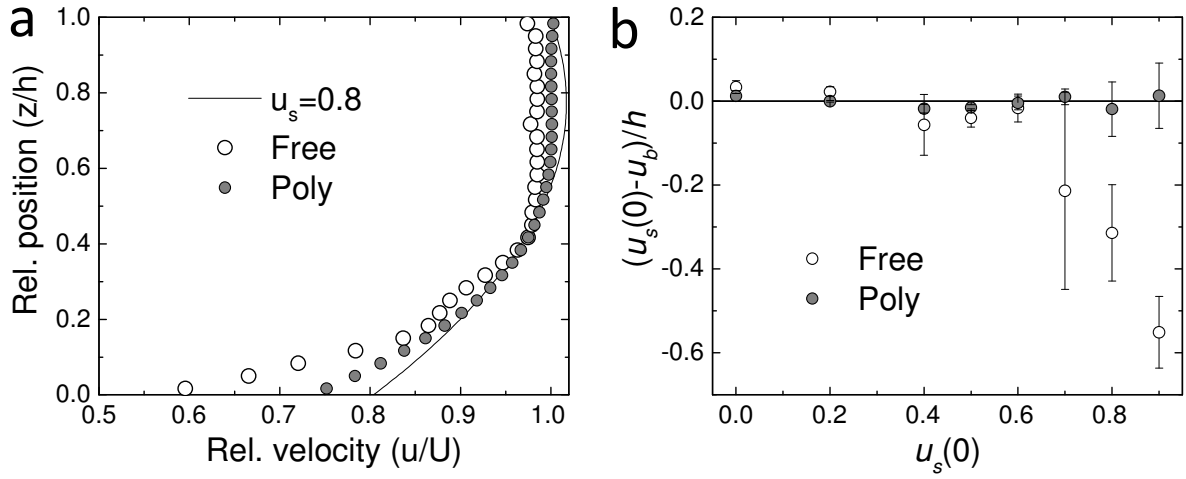


Fig. 56: a) Sample velocity profiles for an input slip velocity of 0.8, for the 'free' and polynomial reconstruction schemes. b) Error in relative slip, as a function of the slip velocity for the two reconstruction schemes.

It is clear that the 'free' scheme fails at large relative slip lengths under these conditions. While the reconstructed velocity profile is fairly representative of the input profile, there is a large error near the surface, due to the high relative shear rate. This leads to a significant uncertainty in the determined slip length, as shown in Fig. 56b, resulting in a significant underestimation. To solve the issue, the method of assuming a shape for the velocity profile is adopted [106]. The velocity profile is described by a polynomial of fourth order. The order was chosen to resolve more complex profiles than just parabolic pressure driven flow. The minimization used for the reconstruction remains similar, but now the coefficients for the polynomial are the free parameters, rather than the velocity of each individual layer. The velocity is calculated using the polynomial coefficients, and the profile is constrained to be monotonic. The result for the slip velocity determination using a polynomial profile is shown in Fig. 56. It is clear that the result for the slip length determination is greatly improved compared to the previous scheme. Whenever large amounts of slip are identified it is thus necessary to assume the shape of the velocity profile to adequately determine the slip velocity.

Having evaluated the effectiveness of the reconstruction scheme, showing that it is capable of being applied to the study of flow in EHD contacts, the potential resolution of the proposed technique is explored.

4.4 Resolution

The photobleached-fluorescence imaging technique developed in this work is a variant of molecular tagging velocimetry. The developed technique, with the accompanying reconstruction scheme, enables the determination of the velocity profile independent of the thickness in which the profile varies, and without the requirement of nanoscopic z-positioning. Other techniques, that are possibly capable of solving the same problem studied in this work, are listed in section 1.5. It is discussed here that photobleached-fluorescence imaging is an optimal candidate for the determination of the velocity profile in an EHD lubricant.

The spatial (x-y) resolution is governed by the minimum distance the photobleached column has to travel to determine the velocity profile accurately (where accuracy is based on R^2). In most cases in this work, this was approximately 30 µm. For measurements along the x-direction in the EHD contact, the column did not deform in the y-direction such that the resolution in the y-direction was governed by the column size, which had a radius of about 3 µm.

The developed technique has limitations in determining the velocity of each molecular layer, as shown in section 4.3. There are five factors that limit the z-resolution of the technique. They are: the roughness of the surfaces, the structure of polybutene, the fluorescence emitted by a molecularly small layer of fluorophore doped polybutene, the noise of the acquired intensity and finally the limitations of the reconstruction scheme.

The surfaces are rough. For the glass slide, the roughness is relatively negligible but for the glass ball there will be pits and asperities which are of the order of the size of polybutene. This makes it difficult to distinguish lubricant flow due to shear from lubricant trapped in pockets. This limits the minimum film thickness studied in this work, which is of the order of 50 nm. Due to the polymeric nature of the lubricant, it may not flow as layers, making the continuum assumption in the analysis valid only for an average of molecules. This sets the z-resolution at a minimum of a few molecular layers, which given the size of polybutene (see Table 3) is of the order of 4 nm.

The expected signal that would be acquired by the optical setup used can be predicted based on the concentration and spectral properties of nile red. Due to the high concentration, and the efficient fluorescent of the fluorophore, calculations show that even a monolayer of nile red would produce a signal sufficient for analysis.

In the case of the z-resolution the noise of individual pixels matter. The averaged intensity fluctuation in the contact was about 0.8 %. The noise of the intensity for a single pixel outside of the photobleached column is about 5 % over time. However when synchronous averaging is applied this reduces to approximately 0.4 %. Given a typical film thickness of 200 nm, a signal from a 2 nm layer would indicate the presence of lubricant. The final limit

for the z-resolution is the limitation of the reconstruction scheme. Based on Fig. 53 and Fig. 54, the velocity profile can only be determined accurately within approximately 10 % of the height, due to the limitation of resolvable relative shear rates. Then the through-thickness resolution (z-direction) depends on the film thickness, which for the lower speeds gives a resolution of about 10-20 nm, making the reconstruction scheme the dominant limitation for the z-resolution. The actual resolution cannot be determined accurately as no velocity profile within a 100 nm film or channel has been measured experimentally.

The temporal resolution of the technique is relatively limited, mainly due to shortcomings of the acquisition system. Fig. 20 depicts a single acquisition sequence. At the faster speeds, a sequence of 16 images is acquired within about 20 ms, such that the result would be sensitive to fluctuations of this frequency. Due to emission limitations and the requirement for synchronous averaging, the time required for a complete measurement to determine a single velocity profile increased to approximately 30 s, even at faster speeds, making the technique insensitive to rapid transients within the flow. The technique is best suited for the determination of an average velocity profile, which provides information about the rheology of the lubricant. There are ways of significantly improving the temporal resolution through the use of lifetime imaging and optical choppers as explained in chapter 9.

For typical velocity profiles (Couette and Poiseuille), the technique has an accuracy of ~ 5 % in the relative slip length measurements. It is difficult to compare slip length measurements between different techniques when dimensions vary greatly. Using a typical relative slip length of 1, depending on the velocity, the slip length range is approximately 50-300 nm. Using the accuracy for the slip length of approximately 5 % (see Fig. 55), the slip length can theoretically be determined within 2-12 nm. Compared to the fluorescence recovery after photobleaching technique [109] and double-focus cross correlation [64], the resolution here is higher. This is partially caused by the small thickness which is typically only encountered using techniques such as surface forces apparatus, atomic force microscope and colloidal probe. In comparison to the dimple technique [38] there are two significant differences. Firstly, in this work the measurements are local, enabling the determination of spatial variations in the velocity profile. Secondly, a stable and steady EHD contact is studied here,

whereas the dimple technique requires a transient dimple to be created, and to be transported out of the contact. The dimple technique does have the advantage that no lasers are required and there is no requirement for a specific fluorophore-lubricant system, greatly increasing the applicability of that technique.

The x-y spatial resolution of this technique is lower than that of stimulated emission depletion photobleached-fluorescence imaging velocimetry [66]. Due to the acquisition method and the system studied, the temporal resolution is also significantly lower in this work. The z-resolution however, is higher in this work, due to the diffraction limited point measurement used in stimulated emission depletion photobleached-fluorescence imaging velocimetry, making the method developed in this work more appropriate for the study of steady thin films.

The ability of the reconstruction scheme to accurately determine velocity profile based on simulated spatiotemporal intensity distributions has been confirmed. It is however necessary to validate that this can be performed using experimental data. To achieve this, a model setup with a known velocity profile was used.

4.5 Validation using parallel plate geometry

The photobleached-fluorescence imaging velocimetry technique and the velocity profile reconstruction scheme were validated, by comparing the experimental result to the theoretical solution for a standard system. To enable a suitable comparison to an EHD contact, it was necessary to use a setup with a known velocity profile and a small thickness. Nanofluidic channels could not be used due to the high pressure necessary to drive the high viscosity fluid required for advective flow. Thus a parallel plate setup was chosen, with the nile red doped PB confined between two glass slides. The preparation of the model lubricant is detailed in subsection 2.2.1. One end of a fishing line was attached to the shaft of a Cool Muscle 23L (Reliance Precision Mechatronics) precision stepper motor, and the other end was glued to the top glass slide. Fishing line was chosen for its stiffness, ensuring steady and responsive control of the velocity of the top slide. Velocity calibration was carried out by placing a metal piece on the top glass slide, and then tracking the motion of features on the

surface. The confined high viscosity lubricant ensured the preferential lateral motion of the top glass slide, due to the high torque required to alter the plate separation, effectively creating a plane Couette flow.

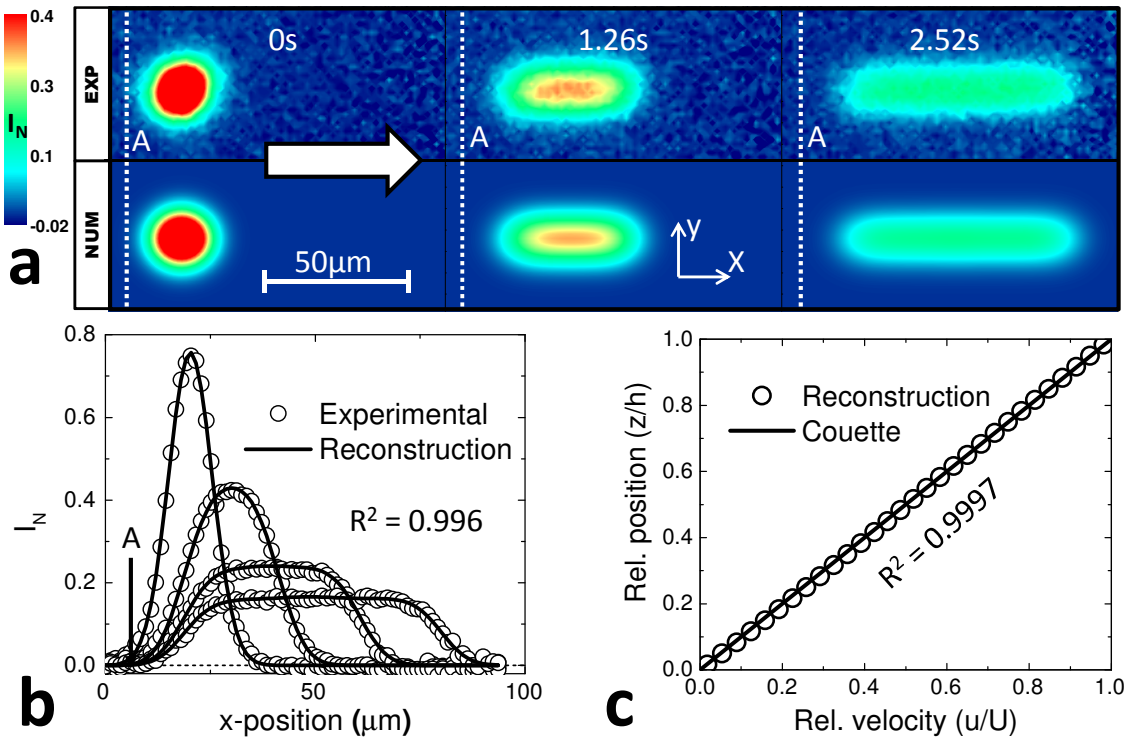


Fig. 57: a) Experimental (EXP) and numerical (NUM) spatiotemporal normalised relative intensity distributions at three times for a 1 µm thick film of H-300 at a speed of 26.3 µm/s. The arrow indicates the direction of the flow. The dotted line A indicates the position of the back of the column. b) Averaged intensity distributions from (a), with point A indicating the back of the column. c) Reconstructed velocity profile and theoretical Couette velocity profile. (From [29] with kind permission from Springer Science and Business Media)

The experimental setup, described in subsection 2.1.3, was used to study the parallel plate system. Images were acquired as detailed in subsection 2.1.4. The evolution of the photobleached column for a Couette flow was imaged using a bleach time of 25 ms, an exposure time of 180 ms and 10x synchronous averaging. Due to the relatively long exposure time in this experiment, it was also possible to analyse individual sequences, yielding similar results to that determined using synchronous averaging, showing that the averaging did not affect the result for the plane Couette flow setup. The experimental spatiotemporal normalised relative intensity distribution is shown in the top of Fig. 57a, for a micron thick film of H-300 at a speed of 26.3 µm/s, where the Péclet number is 3400. In the bottom of

Fig. 57a, the reconstructed intensity distribution is shown, which was created using the reconstructed velocity profile. The standard deviation of the average intensity over time is approximately 2 % for the experimental results. The dotted line (A) indicates the back of the photobleached column, which remains stationary due to the no-slip boundary condition. The result shows that the correct velocity of the top plate is determined (see Fig. 57c with relative velocity = 1 when relative position = 1). There is a good agreement between the two intensity distributions (Fig. 57b), indicating a successful reconstruction of the velocity profile (Fig. 57c) with high R^2. The shape of the photobleached spot is initially Gaussian, satisfying the assumption of instantaneous photobleaching. At longer times the intensity distribution flattens out, as is expected by a linear velocity profile.

The correlation between the experimental and reconstructed intensity distributions was studied further by taking the mean intensity of five pixels in the y-direction. The averaged one-dimensional distribution in the x-direction can be seen in Fig. 57b. The agreement between the two intensity distributions is evident as shown by the coefficient of determination R^2. The theoretical Couette velocity profile and the reconstructed velocity profile are shown in Fig. 57c, plotted using the relative position in the z-direction, z/h, and the relative velocity, u/U. The two match, showing that the developed technique is capable of accurately determining the velocity profile for the case of a linear velocity profile in a microscopic fluid film. The above experiment was also carried out for PB920 and PB2300, achieving similar results. At lower speeds (about 1 µm/s), especially for PB920, effects of dispersion (diffusion in the z-direction) could be seen by the incomplete extension of the bleached spot. No such dispersion was seen at higher speeds, as in Fig. 57, when the speed was comparable to those encountered for the EHD contact.

Having validated the application of photobleached-fluorescence imaging velocimetry to a model system in a parallel plate setup, the applicability of the assumption of one-dimensional flow at the centreline of the contact is explored.

4.6 Two-dimensional flow mapping

The pressure in an EHD contact varies with position. Although pure sliding contact conditions are applied in this work, there is still a non-negligible pressure gradient, causing a small pressure driven component of flow. The pressure driven flow can easily be visualised in the y-direction, as it solely contributes to flow in that direction. Photobleached-fluorescence imaging was applied to a steel-glass EHD contact (details in section 2.3), within a 7x7 grid, at a speed of 360 µm/s, a load of 6.4 N (347 MPa) and a temperature of 20 °C, to determine the spatial variation in the velocity profile. Measurements were repeated six times. At these conditions the film thickness is approximately 190 nm. The positions were located using the micrometers mounted on the stage. A fluorescence image of the contact, acquired using the 10x objective, is shown in Fig. 58. The locations, at which photobleached-fluorescence imaging was applied, are indicated by white crosses.

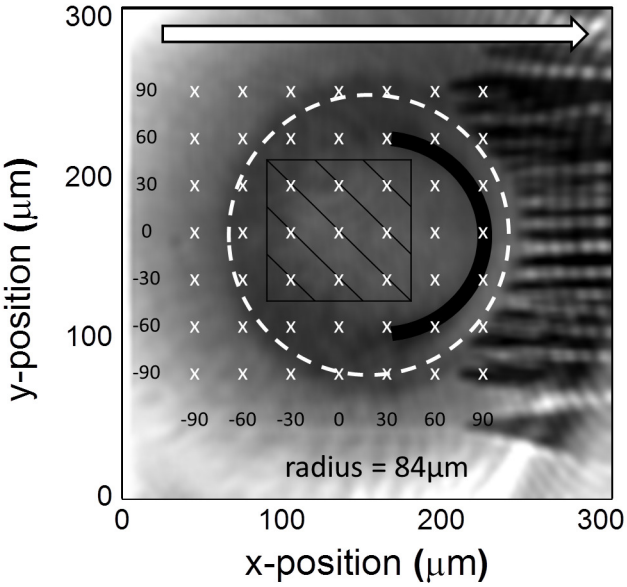


Fig. 58: Fluorescence image of the steel-glass EHD contact for H-300 at speed 360 µm/s, load 6.4 N (347 MPa) and film thickness ~190 nm. The white dashed circle shows the perimeter of the contact. The horseshoe region is marked by a black arc. The white arrow indicates the direction of the flow. White crosses show the locations at which photobleached-fluorescence imaging was applied. The cross-hatched region highlights positions where the reconstruction scheme could be applied successfully. (From [29] **with kind permission from Springer Science and Business Media)**

It should be noted that these results were acquired using a steel-glass EHD contact, and therefore interference complicates the application of the velocity profile reconstruction.

However, since only the two-dimensional average velocity is extracted in this exercise, the measurements can still be used to study the pressure driven flow of the lubricant, both inside and outside of the contact.

4.6.1 Velocity field

The analysis presented in this chapter is applicable along the central x-axis at y = 0. Away from the centre of the contact, in the y-direction, as well as outside of the contact, the pressure gradient, $\partial P/\partial y$, is non-zero. This creates a y-component of the flow. The spatiotemporal intensity distribution of the photobleached column can be used to determine the average velocity vector. This can be used to measure the averaged two-dimensional velocity field, $\vec{u}_{xy}$, described as

$$\vec{u}_{xy}(x,y) = \frac{1}{h_c}\int_0^{h_c} \vec{u}(x,y,z)dz \tag{53}$$

where h_c is the central film thickness, and $\vec{u}$ is the velocity field. $\vec{u}_{xy}$ can be found by calculating the position of the centre of mass of the intensity distribution, y_{CM}, given by

$$\int_{y=0}^{H}\left(y\int_{x=0}^{L} I_N(x,y,t)dx\right)dy = (y_{CM}+y_0)\int_{y=0}^{H}\int_{x=0}^{L} I_N(x,y,t)\,dxdy \tag{54}$$

where H is the height of the observation area in the y-direction, L is the length of the observation area in the x-direction, y_0 is the initial central position of the photobleached column at time $t = 0$ and I_N is the spatiotemporal normalised relative intensity distribution. The average y-component of velocity is then given by y_{CM}/t. The average velocity in the x-direction can be determined similarly. The central position of the initial intensity distribution can be found by fitting the distribution to a two-dimensional Gaussian distribution, defined as

$$I_N(x,y,0) = A_P e^{-\left(\frac{(x-x_0)^2}{2{w_x}^2}+\frac{(y-y_0)^2}{2{w_y}^2}\right)} \tag{55}$$

where A_p is the peak intensity, x_0 is the central position of the intensity distribution in the x-direction and w_x and w_y are the standard deviations of the intensity distribution in the x- and y-direction respectively. Equations (54) and (55) were discretized, enabling comparison

with the photobleached-fluorescence imaging data. The position of the centre of mass of intensity was determined at the positions indicated by white crosses in Fig. 58. The average result of the six repeats for each position gave the two-dimensional velocity field as shown in Fig. 59.

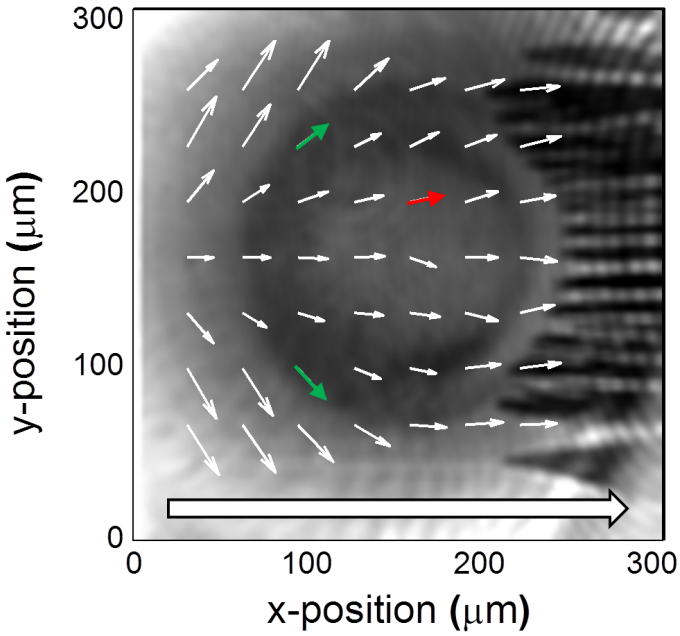


Fig. 59: Vector plot of the velocity field (white arrows) overlaid onto a fluorescence image of the contact. The velocity in the y-direction has been multiplied by ten for clarity. The large white arrow indicates the direction of the flow. For experimental condition, see caption in Fig. 58. (From [29] **with kind permission from Springer Science and Business Media)**

The average y-component of velocity was much smaller than that of the x-component. Inside the contact, the y-component reached at most 5 % of the x-component (green arrows in Fig. 59). This shows that the pressure driven flow, left part in equation (1), is effectively negligible. Results near the outlet were distorted due to cavitation. At the inlet in Fig. 59, it is shown that the lubricant is forced to travel around the contact, due to the obstruction of the steel ball.

The flow of the lubricant around the EHD contact, as shown experimentally in this section, can be described using the Navier-Stokes equations, as no pressure-induced rheological effects are present outside of the contact. The main use of the result for the averaged two-dimensional velocity field is the experimental verification of the negligible magnitude of the

pressure driven flow in pure sliding. This is a common assumption [6,31], which has previously been shown to be accurate using simulations [32,48].

By extending the two-dimensional mapping, and by either using transparent surfaces or taking interference into account, it would be possible to determine the viscosity by relating it to the y-component of flow. The pressure distribution could be determined either by Raman spectroscopy [110] or by reconstruction from the film thickness measurement [111], enabling the calculation of the viscosity from equation (1) (with x replaced by y and the Couette component being zero). A brief estimate is made here based on a Hertzian pressure distribution, where the pressure gradient is found by differentiating the parabolic pressure distribution. The mean speed in the y-direction for the red arrow in Fig. 59 is 7.2 µm/s, and the pressure gradient, dp/dy, is approximately -1.5 $\cdot 10^{12}$ Pa/m, resulting in a viscosity of 1.4 $\cdot 10^{5}$ Pa s. The estimate using the Barus equation is 1.2 $\cdot 10^{6}$ Pa s. While the two viscosity estimates differ by one order of magnitude, it is unclear if the viscosity of PB in an EHD contact can be accurately presented by the Barus equation. In addition, the through-thickness viscosity of PB, as shown in Chapter 6, may not be homogeneous. A more rigorous method of estimating the viscosity using alternate methods is required to validate the measurement. This also highlights the potential use of the application of the photobleached-fluorescence imaging velocimetry technique for local viscosity measurements in EHD lubrication.

4.7 Validation with Soft-EHD contact

In section 4.5, it was shown that photobleached-fluorescence imaging velocimetry and the reconstruction scheme are capable of obtaining a Couette velocity profile of PB confined by a parallel plate geometry. However, its applicability to an EHD contact could not be assumed *a priori*. As section 4.6 shows that the assumption of one-dimensional flow in an EHD contact at the centreline along the flow direction (y = 0) holds, verification of the developed technique was carried out by obtaining the through-thickness velocity profile in a soft-EHD contact at y = 0, where the y-component of velocity is minimal. The pressure induced effects are expected to be negligible, such that a Couette velocity profile is expected.

For the soft-EHD condition, the contact was imaged using the optical setup described in subsection 2.1.3, using the 10x objective (with 2.5x optovar) and 10x synchronous averaging, to reduce noise. A soft-EHD (or compliant) point contact was created by loading the ¾" steel ball onto a glass slide, coated with a 2 mm layer of Sylgard 184 (Dow Corning) PDMS. The Hertzian properties of contact are given in Table 5. The PDMS was mixed at a ratio of 5:1 of elastomer to curing agent and was degassed using a desiccator, to remove dissolved air bubbles. Scotch tape was used on the edges of the glass slide, to create a mould into which the PDMS was poured. It was then cured in an oven for one hour, at a temperature of 60 °C. The topography of the surface was measured using a Veeco profilometer, operating in phase shifting interferometry mode. A roughness of approximately 5 nm was measured, which is negligible given the large film thickness created in the soft-EHD contact. This larger film thickness is also why the steel ball could be used, despite its reflective surface causing interference (see subsection 2.3.7).

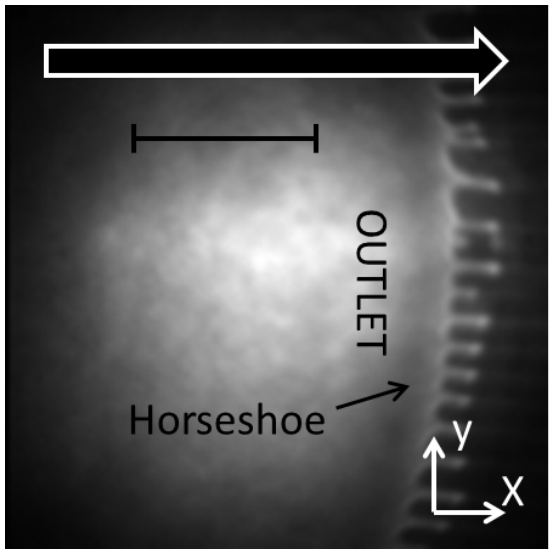


Fig. 60: Fluorescence image of the soft-EHD contact for H-300 between a steel ball and a PMMA-coated PDMS surface, captured at 2 N (0.30 MPa) and 720 µm/s. The arrow indicates the direction of flow. The scale bar is 100 µm. The horseshoe can be seen near the outlet followed by cavitation.

A raw fluorescence image of the soft-EHD contact (without flat-field correction) is shown in Fig. 60. It is clear that the contact size is now much larger than for the steel-glass EHD contact (see Fig. 31). The horseshoe region, a distinct feature for an EHD contact, is clearly visible, and the fluorescence is mostly constant, indicating the formation of a constant film

thickness due to the elastic deformation of the PDMS film. The PDMS film in Fig. 60 was coated with poly(methyl methacrylate) (PMMA) to prevent the absorption of dye.

The photobleached-fluorescence imaging technique was applied to the centre of the contact. The centre was located by finding the distance over which the fluorescence was approximately constant, and then moving the focal point to the centre using the micrometers on the stage. The normalized relative intensity distribution, I_N, for H-300 is shown in Fig. 61a, measured at a speed of 360 µm/s and a load of 6.4 N (0.44 MPa). The central film-thickness, h_c, for the soft-EHD contact can be calculated using the Hamrock-Dowson equation for isoviscous elastic lubrication [112], given by

$$h_c = 3.34\bar{U}^{0.64}\overline{W}^{-0.22}R \tag{56}$$

where $\bar{U}$ and $\overline{W}$ are non-dimensional parameters defined in subsection 2.3.3 and R is the radius. This results in a film thickness of 10 µm. While this value may seem large for an EHD contact, elastic deformation of soft materials can take place for much larger film thicknesses, maintaining the assumption of constant film thickness in the contact.

The result in Fig. 61a is different from the previous measurements for Couette flow (section 4.5). The coefficients of determination in both Fig. 61b and Fig. 61c are much lower than previously. While the intensity distributions in Fig. 61a did show some levelling at its rightmost part, suggesting Couette flow, the intensity close to point A does not change much over time, indicating that there might be some part of the lubricant or fluorophore sticking to the PDMS surface. This is confirmed by observing the intensity distribution averaged in the y-direction Fig. 61b, and the reconstructed velocity profile in Fig. 61c. The average intensity for t = 86 ms (red) in Fig. 61b shows a small peak at x = 30 µm. This may be due to the formation of PDMS transfer film on the steel ball and dye absorption into that film.

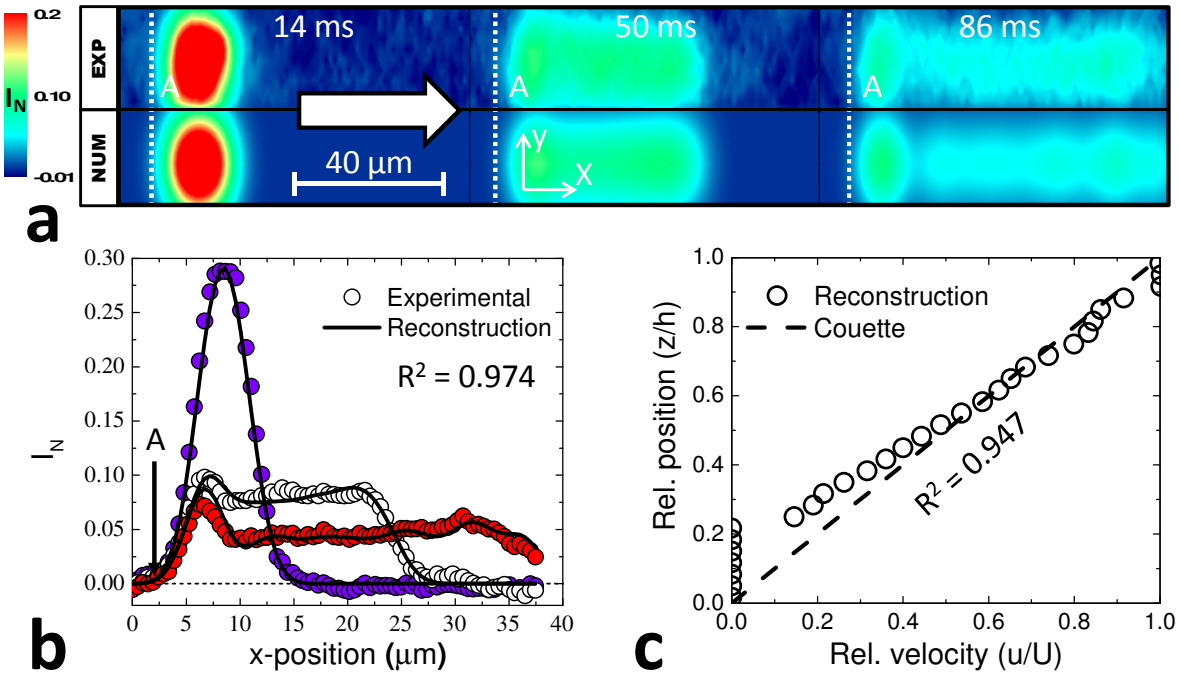


Fig. 61: a) Experimental (EXP) and numerical (NUM) spatiotemporal normalised relative intensity distributions at three times for H-300 at speed 720 µm/s, load 6.4 N (0.44 MPa) and film thickness 10 µm between a steel ball and a PDMS surface. The arrow indicates the direction of the flow. The dotted line A indicates the position of the back of the column. The scale has been stretched by a factor of three in the y-direction, due to the number of pixels measured being small. b) Averaged distributions from (a) with the point A indicating the back of the column. c) Reconstructed velocity profile and theoretical Couette velocity profile.

Nile red is a hydrophobic fluorophore. It has been shown that small hydrophobic molecules can absorb into PDMS [113]. This absorption into the coating, would explain the appearance of a fixed layer in the intensity distribution. When the steel-PDMS contact was observed using fluorescence, the intensity would increase over time. This confirms that the nile red does indeed diffuse into the PDMS. Thus, this system is not representative of the lubricant flow in soft-EHD, as the fluorophores do not strictly flow with the lubricant.

The issue of nile red absorption was resolved by spin coating a protective layer of PMMA, onto the PDMS coated glass slide. If the protective layer, h_{coat}, is small enough, the influence of the coated layer on the elastic properties of the contact is small [114] (for values of $a/h_{coat} \gg 1$), where a is the radius of the contact. Hence a coating thickness of $h_{coat} = 2$ µm was chosen. The thickness of the coated layer can be controlled by varying the spin coating speed and duration, the molecular weight of the polymer and the concentration of

PMMA in the solvent used [115]. PMMA (Sigma Aldrich, Mw = 130kg/mol) was dissolved in toluene, at a concentration of 10 % by mass. A homemade spin coater was used to create the coating. The spin coater was spun at 100 rpm for 10 s, while the solution was deposited until the PDMS coated glass slide was fully submerged. The speed was then raised to 1000 rpm, for 60 s, and the PMMA-PDMS coated glass slide was finally cured in an oven, at 80 °C, for one hour, facilitating the evaporation of toluene. The topography of the surface was measured using a Veeco profilometer, operating in phase shifting interferometry mode, which showed that the roughness was approximately 10 nm.

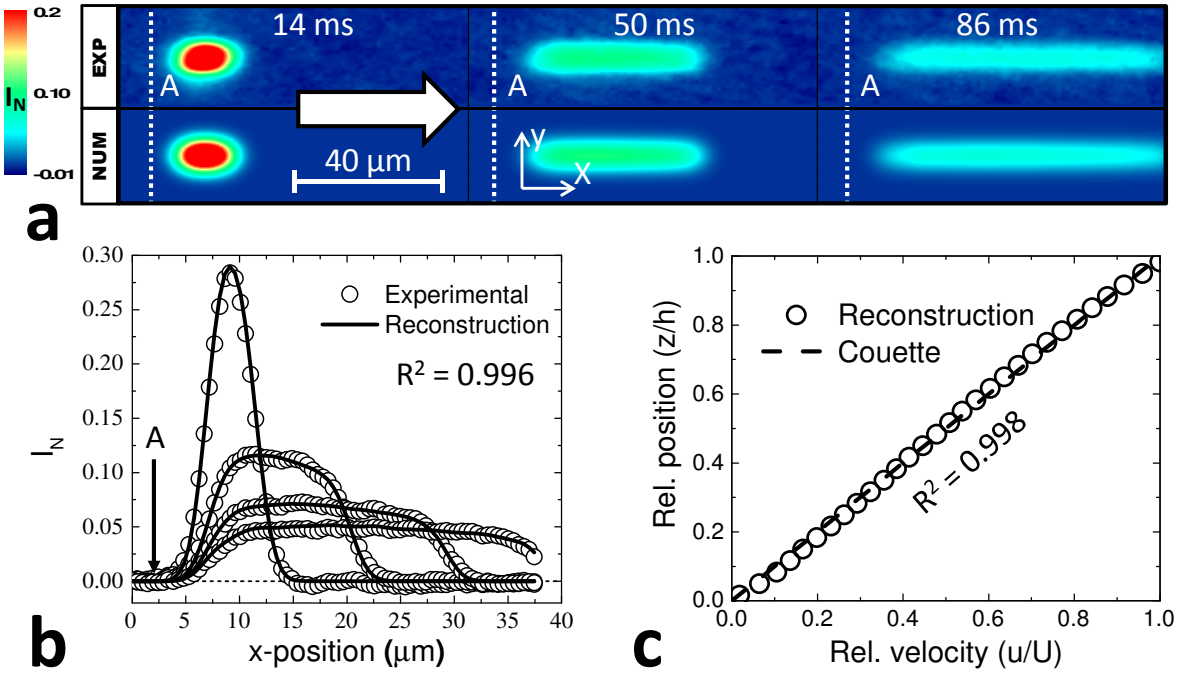


Fig. 62: a) Experimental (EXP) and numerical (NUM) spatiotemporal normalised relative intensity distributions at three times for H-300 at speed 720 µm/s, load 6.4 N (0.44 MPa) and film thickness 10 µm between a steel ball and a PMMA-coated PDMS surface. The arrow indicates the direction of the flow. The dotted line A indicates the position of the back of the column. b) Averaged distributions from (a) with the point A indicating the back of the column. c) Reconstructed velocity profile and theoretical Couette velocity profile.

Photobleached-fluorescence imaging was applied to the centre of the steel ball-PMMA coated PDMS contact. The result for the normalised relative intensity distribution, I_N, is shown in Fig. 62a, for a speed of 720 µm/s and a load of 6.4 N (0.44 MPa). The averaged intensity distribution in the y-direction is shown in Fig. 62b, and the reconstructed velocity profile is shown in Fig. 62c. The coefficient of determination is high, indicating a good fit between the

theoretical prediction and the experimental data. This result shows that the velocity profile is linear, i.e. Couette flow, in the centre of a soft-EHD contact, as predicted by the Reynolds equation. This further validates the use of photobleached-fluorescence imaging velocimetry to measure velocity profiles in EHD contacts.

4.8 Through-thickness velocity profile overview

Before proceeding to the detailed study of the velocity profile and hence rheology of PB in EHD lubrication, a brief overview of flow phenomena observed by application of the photobleached-fluorescence imaging velocimetry technique, at a variety of experimental conditions, is presented in this section. The first measurement is made for a soft-EHD contact (as shown in section 4.7), where pressure-induced effects on the lubricant rheology are expected to be small. The technique is then applied to an EHD contact. Two distinct types of flows (Chapters 5 and 6) are observed, as parameters such as load, speed and molecular weight are varied. These flows are studied in detail, and the origins of their nature are discussed, in terms of pressure and shear induced effects. Finally, the interfacial properties are altered using a low surface energy coating, enabling the direct study of slip in an EHD contact (Chapter 7).

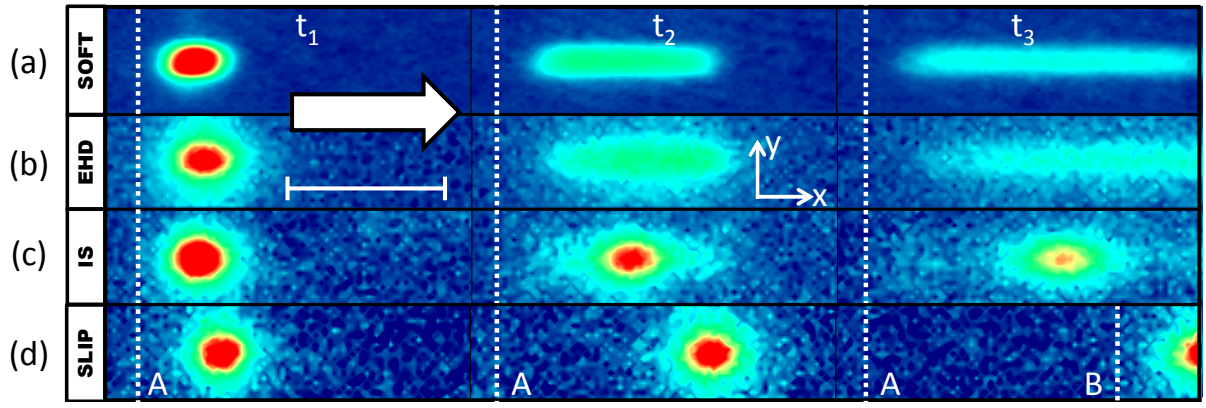


Fig. 63: Normalised relative intensity, I_N at three times for four different experimental conditions, at the centre of a point contact. For the cases of EHD, IS (inhomogeneous shear) and SLIP, the scale bar is 20 µm. For the case of SOFT, the scale bar is 40 µm. Dotted white line A indicates the back of the photobleached column immediately after photobleaching. Dotted white line B indicates the approximate position of the back of the column, for the case where the lubricant slips at the lubricant-glass interface.

The two-dimensional normalised relative intensity distribution, I_N, for polybutene H-300, is presented in Fig. 63, for four different experimental conditions, at three times, t_1, t_2 and t_3.

Experiments were carried out at a room temperature of 25±0.5 °C. Four distinct responses were identified. Some of these responses were significantly different from Couette flow.

A soft-EHD contact was created with a steel ball and a layer of PMMA coated PDMS on a glass slide (details in subsection 2.3.1 and section 4.8). The normal pressure in this condition is low enough not to cause any significant increase in the viscosity of the lubricant in the contact. The result for soft-EHD in Fig. 63a, measured at a speed of 720 µm/s and a load of 6.4 N (0.44 MPa), was similar to that observed for the parallel plate setup, seen in section 4.5, suggesting Couette flow.

The EHD response in Fig. 63b was measured for a glass-glass contact, at a speed of 720 µm/s and a load of 6.4 N (263 MPa). The result is very similar to Couette flow, or that of soft-EHD.

Once a lubricant in an EHD contact reaches the glass transition viscosity, driven by effects such as pressure and confinement, the Couette flow assumption may no longer be valid. This is shown in Fig. 63c (labelled as 'IS'), which is obtained at a speed of 360 µm/s and a load of 28 N (430 MPa). In this case the photobleached column deformed much less over time, indicating a reduction in the shearing of the lubricant. This is a case of inhomogeneous shear and the observed reduction could potentially be explained by a pressure induced glass transition of the lubricant.

SLIP, shown in Fig. 63d was achieved by modifying the stationary glass slide with a low surface energy coating. The result was acquired at a speed of 720 µm/s and a load of 6.4 N (263 MPa). The white lines 'A' and 'B' in Fig. 63d, clearly show how the back of the photobleached column moves over time, indicating slip at the lubricant-solid interface.

In the subsequent chapters, the acquisition and experimental conditions for each distinct response are detailed. The intensity distributions are studied further by applying the velocity profile reconstruction scheme, and the implications and causes for the observed results are discussed.

4.9 Summary

The flow of the lubricant was modelled as layers of infinitesimal thickness flowing parallel to each other. In this case the distribution of fluorophores could be described by the scalar transport equation without diffusion. The assumption of negligible diffusion was ascertained by evaluating the Péclet number, which relates advective and diffusive flow components, and it was shown that the number was large, supporting the assumption of purely advective flow. An expression was then derived which describes the spatiotemporal intensity distribution, assuming an initially Gaussian intensity distribution, a constant film thickness and a known velocity profile.

The expression for the spatiotemporal intensity distribution could be used to simulate intensity distributions for various velocity profiles. As the velocity profile was unknown, a reconstruction scheme was developed that would take a spatiotemporal intensity distribution as input and solve for the velocity profile. This was done by performing a nonlinear least squares minimization, where the unknown velocity profile would effectively be guessed. The reconstructed intensity distribution would be compared to the known intensity distribution until the two distribution matched, while applying a constraint for the continuity of the profile, ultimately obtaining the unknown velocity profile.

The developed reconstruction scheme was evaluated in terms of the ability to accurately reconstruct a variety of velocity profiles including Couette, Poiseuille, inhomogeneous shear (plug), shear banding and slip flows. The reconstruction scheme was successful in reconstructing the Couette velocity profile. For the Poiseuille profile it was necessary to tune the continuity constraint to successfully reconstruct the velocity profile. For the shear banding and inhomogeneous shear flows it was shown that the developed scheme could only determine relative shear rates up to about 3.5. Furthermore, the velocity profile could only be accurately reconstructed within 10 % of the film thickness. For the case of interfacial slip, it was shown that the developed reconstruction scheme was inaccurate in determining slip velocities at large relative slip lengths. An alternative polynomial scheme was developed which was shown to be accurate for the full range of relative slip velocities.

The resolution of the experimental technique was discussed in light of the evaluation performed and the optical characteristics of the experimental setup were compared to other contemporary velocimetry techniques. The spatial x- and y-resolution was determined to be 30 µm and 3 µm respectively, while the through-thickness resolution was found to be approximately 10 % of the film thickness. The temporal resolution was 30 s, making the technique more suitable for the study of steady flows. For slip measurements, it was shown that the polynomial reconstruction scheme was able to determine the slip velocity with an accuracy of 5 %.

The model and the reconstruction scheme were validated experimentally using a Couette flow setup. A micron thin film was sandwiched between two glass slides, creating a parallel plate setup. The photobleached-fluorescence imaging velocimetry technique was applied as the top slide was moved at a fixed velocity. A linear velocity profile was found, agreeing with the theoretical prediction. The developed technique was applied a soft-EHD contact was studied, where pressure-induced effects were expected to be negligible. Using the glass-PDMS contact, it was shown that the dye adsorbed into the PDMS, obstructing the use of photobleached-fluorescence imaging. The PDMS coating was then protected using a thin layer of PMMA. The velocity profile determined for the soft-EHD contact was shown to be linear.

Finally a brief overview of photobleached-fluorescence imaging velocimetry results was presented for the various conditions explored in this work. In the soft-EHD regime, a linear velocity profile was observed. In an EHD contact at low pressures, the intensity distribution response appeared mostly similar to the soft-EHD contact. As the pressure was increased spreading of the intensity distribution due to Couette flow no longer occurred, indicating reduced shearing of the lubricant which could be related to a potential phase transition. Finally, the application of the low surface energy coating caused most of the lubricant to move with the top surface, indicating the existence of interfacial slip. In the subsequent chapters the three unique responses for polybutene at low pressure, high pressure and using a low surface energy coating are studied in detailed, and hypotheses are made for causes behind the observed phenomena.

5 The liquid (low pressure) regime

In this chapter the velocity profile in an EHD contact at low pressures (p = 250-350 MPa) is studied using the photobleached-fluorescence imaging velocimetry technique. It is hypothesised that the large pressure in an EHD contact may induce a deviation from the expected Couette flow. Such a deviation would be likely to depend on parameters such as shear rate and pressure. The effect of pressure and shear rate on the velocity profile are therefore examined in this section. The possibility of spatial variations in the velocity profile, caused by the pressure distribution in an EHD contact, is then investigated.

5.1 Typical result

Photobleached-fluorescence imaging velocimetry was applied to obtain the velocity profile of H-300 at the centre of a glass-glass EHD contact at a speed of 720 µm/s and a load of 13.3 N (335 MPa). The Hertzian properties of contact are given in Table 5. For the EHD condition, the contacts were imaged using the optical setup described in subsection 2.1.3, using the 20x objective (with 2.5x optovar) and 100x synchronous averaging, to reduce noise. The effects of phosphorescence were also accounted for (see subsection 2.1.4). The spatiotemporal normalised relative intensity distribution, I_N, is shown in Fig. 64a.

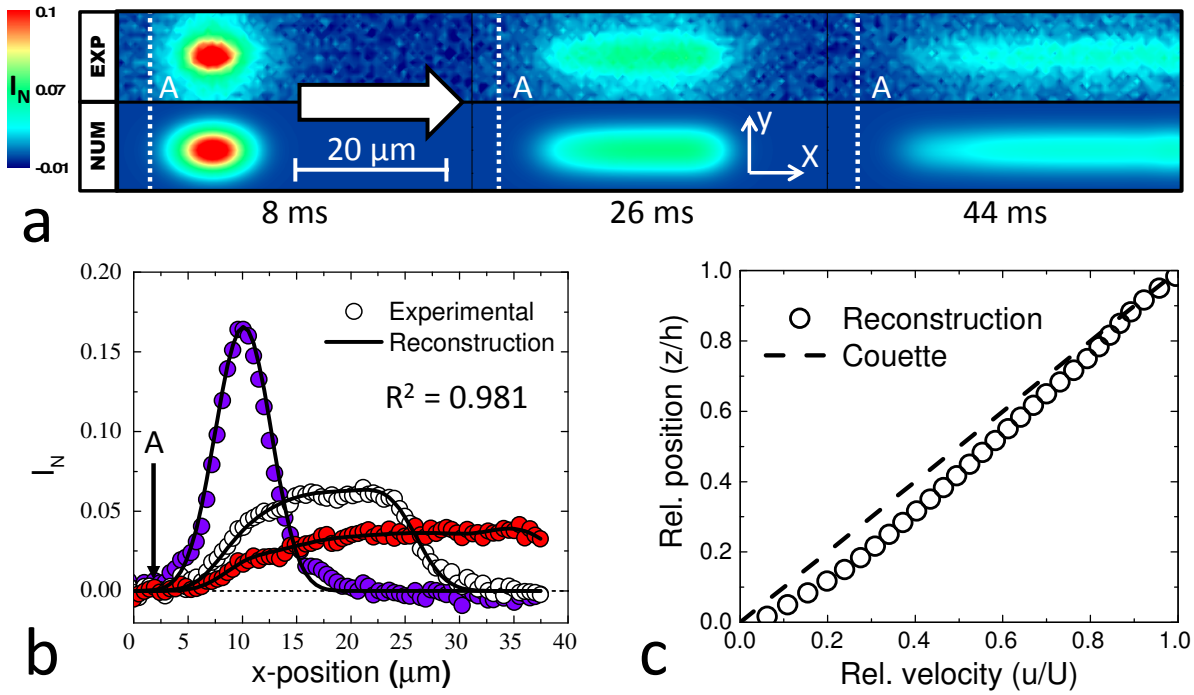


Fig. 64: a) Experimental (EXP) and numerical (NUM) spatiotemporal normalised relative intensity distributions at three times for H-300 at speed 720 µm/s, load 13.3 N (335 MPa) and film thickness 263 nm. The arrow indicates the direction of the flow. The dotted line A indicates the position of the back of the column. b) Averaged distributions from (a) with point A indicating the initial back position of the back of the column. c) Reconstructed velocity profile and theoretical Couette velocity profile.

The reconstructed intensity distributions, in Fig. 64a and Fig. 64b, match the experimental data well as shown by the coefficient of determination. The intensity distribution is no longer symmetric, as it was for the Couette flow case, but is now slightly shifted to the right. This response can be further investigated by studying the reconstructed velocity profile shown in Fig. 64c. It appears as though the lubricant accelerates in the EHD contact, assuming that the velocity profile is linear outside of the contact. If there is spatial variation in the flow of the lubricant, the film thickness would be expected to vary with position in the contact, although the effect would be expected to be minimal given the small increase in the average velocity. This observation agrees with the film thickness measurement in 3.2.4, which shows that the film thickness at these conditions is mostly uniform. One should note that this curvature effect on the velocity profile was not observed for the soft-EHD contact. Since the pressure and shear rate applied in a soft-EHD contact are lower than those resulted in Fig. 64b, the relatively higher applied pressure and shear rate in a glass-glass contact may be responsible for the observed deviation from Couette flow.

One may also argue that the observed velocity profile in Fig. 64 resembles combined Couette-Poiseuille flow [116] or Couette flow with a thermal gradient [48]. A pressure driven component of the flow is improbable given: the pure sliding condition, the high viscosity of the lubricant and that the probed volume is in the centre of the contact, where the pressure gradient is negligible. It was also shown in subsections 2.2.4 and 2.3.5 that a temperature increase is unlikely at the applied experimental conditions. There is therefore some other cause for the larger than expected mean velocity of the lubricant.

A possible cause for the observed profile is the entanglement of chains in the polybutene. By studying the power law relationship between viscosity and molecular weight, the entanglement of a polymer may be inferred. An exponent of 1 indicates untangled polymer, while an exponent of 3.4 indicates entangled polymer [117]. The viscosity of polybutene (at 100 °C) as a function of molecular weight is plotted in Fig. 65. The data was sourced from INEOS oligomers product data sheets for polybutene. The value for the exponent clearly indicates that the polybutene is entangled at the conditions in this work.

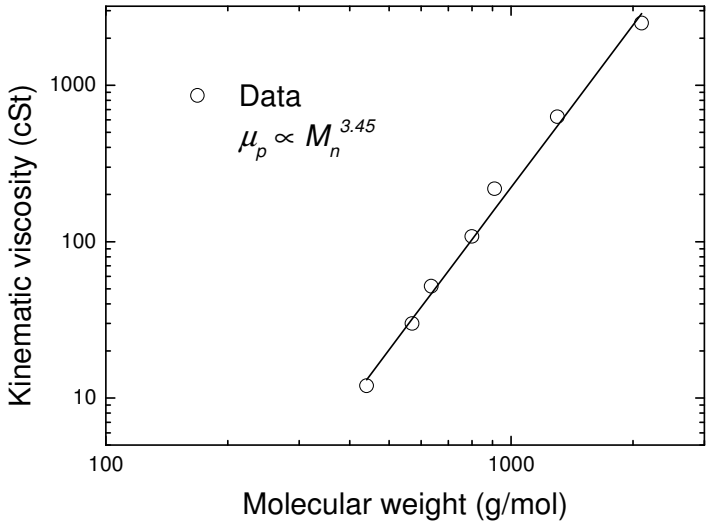


Fig. 65: Variation of viscosity with molecular weight of PB. The black line shows a power law fit to the data.

While the polymer entanglement could give rise to the atypical velocity profile in the EHD contact, shear flows of entangled polymers typically display a retardation of the velocity profile compared to Couette flow [42,118], rather than an acceleration as shown in this work. Shear thinning and polymer chain alignment due to the combined effect of applied shear rate

(~2000/s) and rubbing surfaces may allow PB to flow faster. Yet, it is unclear how these counter-acting factors interact. Hence it remains unclear if polymer entanglement is the cause of the observed velocity profile.

Apart from the slight deviation from Couette flow, another important feature of the velocity profile presented in Fig. 64c is that no significant slip is observed at either of the interfaces. It is well known that polymers in shear flows can slip against interfaces [9] under certain conditions. Given that slip is commonly considered to be initiated by a critical shear rate, or shear stress [9], both of which are relatively large in an EHD contact, slip may occur. In fact, slip in an steel-glass EHD contact for polybutene has been reported previously [38], using a transient dimple technique. It was suggested that the slip occurs at the lubricant-steel interface. Unfortunately that system cannot be accurately studied using fluorescence, due to the effect of interference (see subsection 2.3.7). It would still be possible to use the photobleached-fluorescence imaging velocimetry technique to measure the mean velocity, especially for large film thicknesses where the effects of interference diminish. Yet, no slip of PB was identified for the glass-glass EHD contact at the particular conditions used in this work. The steel and chromium interfaces that were used to identify slip using film thickness measurements have lower surface energies [119] than that of the glass surface. Indeed, no significant effects of slip was observed for the glass interface in [119]. Slip may still be possible for the glass-glass contact, but higher pressures and shear rates would most likely be required, at which point the photobleached-fluorescence imaging velocimetry technique is no longer applicable or peculiar pressure-induced effects on the velocity profile are observed.

The findings presented in the current section do not affect current theoretical methods remarkably other than changing the effective shear rate and the lubricant flow rate. For any application where rheometric measurements are made, or where the flow of lubricant affects transport conditions, for example in thermal mapping for shear stress measurements [22], the possibility of a deviation from the Reynold's equation solution should be considered, particularly for any polymeric lubricant that may become entangled due to the applied pressure.

5.2 The effect of normal pressure on EHD flow

The velocity profile obtained at the centre of a glass-glass EHD contact, shows slight deviation from the assumed Couette flow profile as discussed in section 5.1. The degree of such deviation is possibly related to the severity of the experimental conditions. Hence, the effect of normal stress on the velocity profile was investigated with a range of shear rates.

Photobleached-fluorescence imaging velocimetry was applied at two positions in a glass-glass EHD contact, lubricated by H-300. The applied load and speed were varied, to study potential effects caused by the variation in pressure and shear rate. Typical reconstructed velocity profiles, based on measurements performed at the centre of the contact, are shown in Fig. 66a. The results at four combinations of load and speed are all very similar. The mean flow of lubricant is larger than is expected by the Reynolds equation (shown by the dotted black line). The higher load and speed may have reduced the curvature of the profile, causing it to be more similar to Couette flow, although the effect is marginal

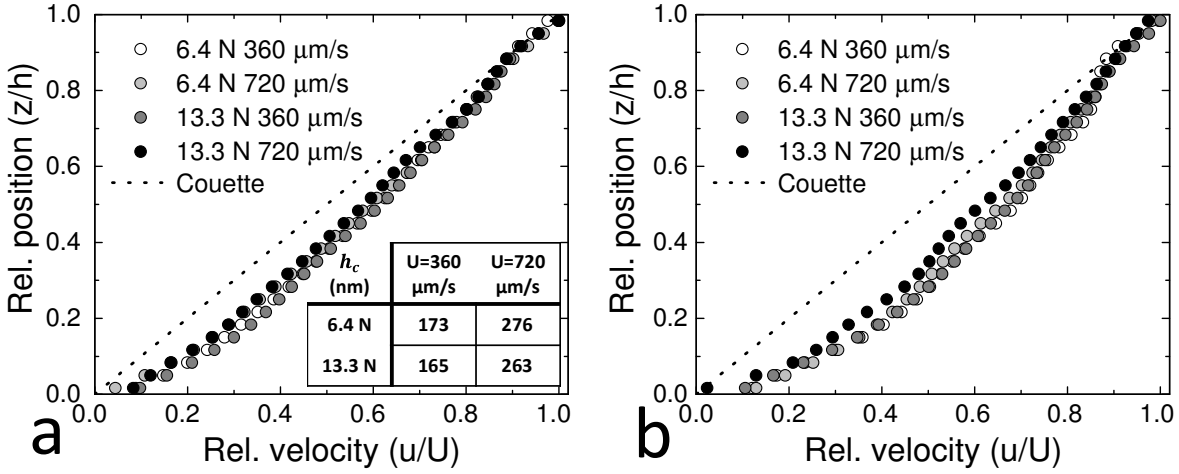


Fig. 66: Velocity profiles for H-300 at loads 6.4 N (263 MPa) and 13.3 N (335 MPa). a) Relative velocity profiles at position x/a = 0 (centre). The central film thicknesses are given in the table inset. b) Relative velocity profiles at approximate position x/a = -0.5 (near inlet).

Velocity profiles were also determined near the inlet of the contact, as seen in Fig. 66b. Compared to the results for the central position, the curvature of the velocity profile is larger resulting in an increase of the mean velocity. Again, the curvature reduces slightly at the highest load and speed.

In section 5.1, a potential cause for the curvature was proposed to be the pressure amplified entanglement of polymers [120], which in combination with large shear rates could result in a non-linear velocity profile. If this conjecture is accurate, the non-linear effects would be expected to increase with pressure. Such an dependency was not observed in Fig. 66, which further suggests that pressure induced entanglement is not the cause of the observed velocity profile.

The velocity profile has been shown to vary only moderately with pressure and speed, but it is clear that there are variations of the velocity profile with position in the contact. These variations were explored by measuring the profile at multiple positions in the contact.

5.3 Spatial variations

The velocity profile was determined at various positions in the contact, lubricated by H-300, along the centreline of the sphere in the sliding direction (at y = 0). Tests were repeated twice at each position for loads 6.4 (263 MPa), 13.3 N (335 MPa), and speeds 360, 720 µm/s. Observation of the velocity profiles in Fig. 66, suggests that the curvature of the velocity profile could be quantified by the mean velocity, with larger mean velocity corresponding to larger curvature, signifying more deviation from the assumed Couette flow profile. This quantity is plotted against position in Fig. 67a. The positions (red dots) at which the photobleaching imaging technique was applied are shown in Fig. 67b for a sample contact.

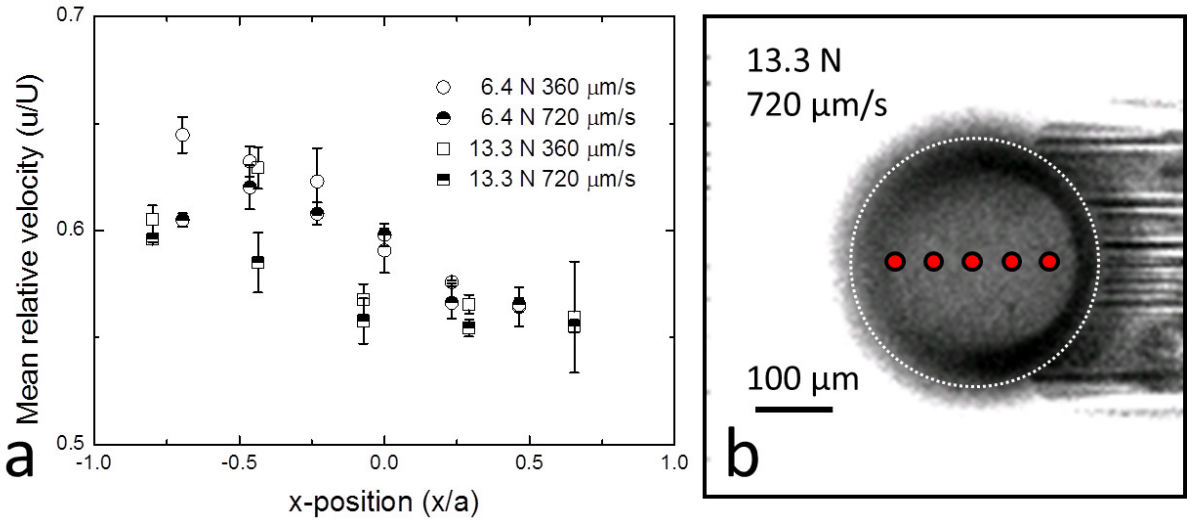


Fig. 67: a) Spatial variation of mean lubricant velocity of H-300 for various loads and speeds. Information on film thickness and pressure is given in Fig. 66. b) Fluorescence intensity map of a 13.3 N (335 MPa) EHD contact, indicating positions (red dots) where measurements are performed for the data in (a). The white circle shows the contact area.

There is a clear spatial variation (approximately 10 % between inlet and outlet) of the mean velocity of H-300 in an EHD contact. Given that no slip was observed, this variation is a result of the positive curvature of the velocity profile. When the lubricant enters the contact, the curvature is large (see Fig. 66) and increases with lower loads and speeds. As the lubricant passes through the contact, the mean velocity reduces and reaches a mostly constant value, which is relatively independent on the load and speed.

Two observations require explanations which needs particular attention. Firstly, what gives the profiles their shapes; secondly why does the mean velocity change as the lubricant travels within the contact? The spatially dependent decrease in mean velocity indicates that the observed effects are not related to the pressure driven flow of lubricant, as pressure driven flow would result in a negative curvature, giving rise to a lower mean velocity towards the inlet. Since the cause for the increased velocity is still unknown, no explanation for the spatial dependence can be given at this time. The observation of spatial dependence is of importance for properties which are affected by the velocity profile, such as thermal effects in EHD lubrication. The only other fluorescence measurement of flow in EHD lubrication showed an increase in mean velocity at the outlet of the contact [31], although that study was performed for a steel-glass contact in pure rolling conditions.

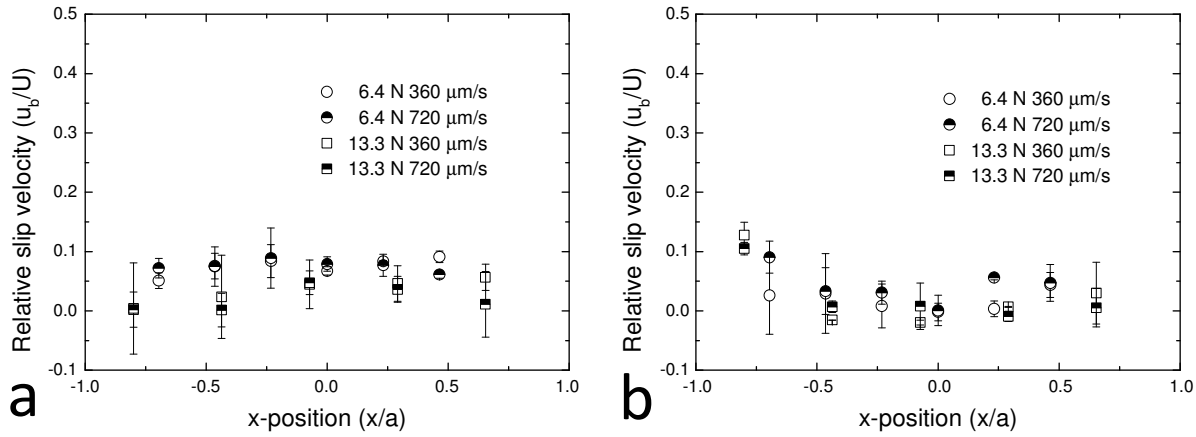


Fig. 68: Spatial variation of the relative slip velocity for H-300 at the lubricant-glass ball (a) and lubricant-glass slide (b) interfaces. Information on pressure and film thickness is given in Fig. 66.

To show that no slip was observed, the slip lengths at the interfaces were evaluated by extrapolating the velocity profile to the surfaces (z = 0 and z = h). The results are presented in Fig. 68a for the lubricant-glass ball interface, and in Fig. 68b for the lubricant-glass slide interface. It is clear that no significant slip could be observed in the EHD contact under the experimental conditions, given that the resolution of the boundary velocity was of the order of 5 % of the ball speed (see section 4.3).

5.4 Summary

Photobleached-fluorescence imaging velocimetry was applied to an EHD contact created by entraining polybutene between a glass sphere and a glass slide. It was shown that the determined velocity profile mostly agreed with the prediction made by Reynolds equation, which suggests a linear through-thickness velocity profile. The fluid was flowing slightly faster (~10 %) near the centre of the channel, and it was argued that neither pressure driven flow, pressure-induced entanglement nor a thermal gradient could be responsible. Currently the cause remains unknown.

The speed and load were varied to study their effects on the velocity profile. It was shown that although an increase in load and speed slightly supressed the curvature, their effects on the curvature were minimal. Profiles were acquired at various positions in the EHD contact. A spatial dependency could be found, which indicated that the curvature of the velocity profile, hence the mean velocity, increased with proximity to the inlet of the contact. This

again suggested that pressure driven flow did not cause the observed velocity profile. It was also shown that no significant boundary slip could be observed under the studied experimental conditions.

The results suggest that the theoretical description of the flow in an EHD contact can be somewhat accurate, although spatial heterogeneity was identified. To verify that this remained true for most experimental conditions, velocity profiles were obtained at high load, where the likelihood of polybutene undergoing a glass transition increased (see chapter 6).

6 The glassy (high pressure) regime

This chapter describes the flow of PB at high pressures ($P > 350$ MPa). At these pressures the PB can reach the glass transition viscosity. Squeeze film experiments (subsection 2.3.6) and film thickness measurements (subsection 3.2.5) for PB in an EHD contact were carried out. It was shown that the rheological behaviour of PB significantly changes at large pressures. The transition may affect the flow of PB. This phenomenon is expected to be significantly dependent on the applied pressure and shear rate. In this chapter, the effect of the pressure and shear rate on the flow of polybutene at such elevated pressures is studied. Spatial variations in the profile are also examined. Finally, the influence of molecular weight on the high pressure flow of PB in an EHD contact is evaluated.

6.1 Typical result

The response of the lubricant was measured in the centre of the contact, at a load of 28 N (430 MPa), to determine the effect of applying large pressure. This could potentially induce a glass transition of the lubricant, which could alter its rheological properties. Such an event may be observable in the flow of the lubricant.

The first discernable effect of high pressure on the properties of PB in an EHD contact is the resulting anomalous film thickness. LIF film thickness results (see section 3.2.5) showed that a region of increased film thickness, referred to as a dimple, appears in the contact at high pressure. As discussed in section 3.2, two types of dimples can form, depending on applied normal pressure. At high pressure, the primary dimple forms. It covers a large region, including the centre of the contact, and resembles a parallel plate geometry. At very high pressure and shear rate, a secondary, narrow, crescent shape dimple forms. The flow of PB at high pressure is investigated by studying the primary dimple region. In this region, the film thickness cannot be calculated using the Hamrock-Dowson equation. Instead it was determined using the LIF results. The result of applying photobleached-fluorescence imaging velocimetry at the centre of the contact is shown in Fig. 69, for PB2300 at a speed of 360 µm/s.

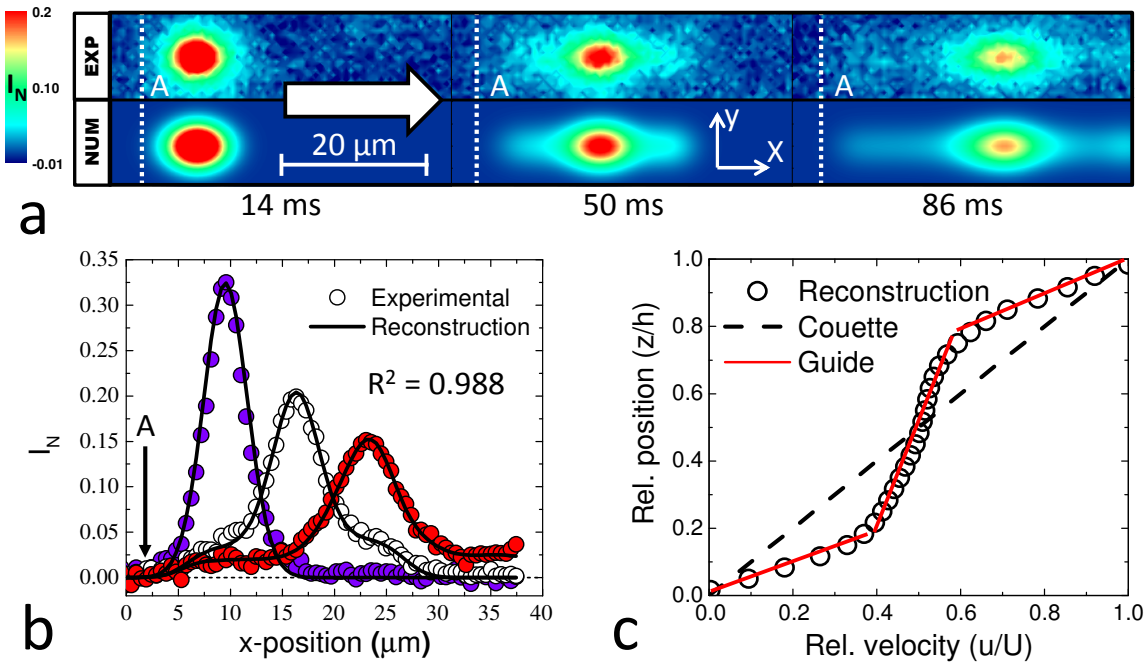


Fig. 69: a) Experimental (EXP) and numerical (NUM) spatiotemporal normalised relative intensity distributions at three times for PB2300 at speed 360 µm/s, load 28 N (430 MPa) and film thickness ~900 nm. The arrow indicates the direction of the flow. The dotted line A indicates the position of the back of the column. b) Averaged distributions from (a) with point A indicating the initial back position of the back of the column. c) Reconstructed velocity profile and theoretical Couette velocity profile. The red lines are a guide to the eyes, indicating three separate regions of varying shear rate.

There is good agreement between the experimental and reconstructed intensity distributions in Fig. 69a, as confirmed by the coefficient of determination of the distributions averaged in the y-direction, shown in Fig. 69b. The intensity distribution retains its Gaussian shape, unlike the previously presented responses for the low pressure (see Fig. 64) and soft (see Fig. 62) EHD contacts. The rheological response of the lubricant is studied further by observing the reconstructed velocity profile, shown in Fig. 69c. The profile, hence the lubricant, separates into three regions of varying shear rate, marked by red lines. This indicates that some rheological change has taken place due to the extreme pressure. The profile suggests that the two layers of lubricant next to the rubbing surfaces are experiencing higher shear rate, while the lubricant at the centre of the thickness is sheared at a lower rate. The velocity profile is an example of inhomogeneous shear, and the rheological state of the lubricant varies through the thickness of the film.

Inhomogeneous shear velocity profiles, similar to those in this work, have been observed for flows with large temperature gradients [48,121], and for molecular dynamics simulations of shear flows at high pressures [49,122] (comparable to EHD lubrication pressures). Molecular dynamics simulations of shear flows of amorphous phases [44] and experiments on flows of heterogeneous fluids [41] have also yielded similar profiles of inhomogeneous shear. However, no theoretical prediction for the presented profile exists in literature. Pressure-induced, partial or complete, solidification is suggested as a possible cause for the observed phenomena. The pressure effectively raises the glass transition temperature, T_g, [12] of the lubricant. The bulk Tg for PB is about -65 °C. Hence the transition temperature of PB could potentially reach the ambient temperature under the applied high pressure EHD conditions. For a lubricant transitioning into an glassy phase, sufficient shear stresses, induced by the shear flow, can cause yielding [123]. Yielding of lubricant at high pressure has been shown in [17], causing the formation of shear bands. The position of yielding may vary with experimental conditions, such that it can take place either at the surfaces (apparent slip), towards the centre of the contact (shear banding) or both. Such behaviour, dependent on load and shear rate, has been shown to occur [49] for a Leonard-Jones fluid at high pressure, using molecular dynamics, although very large velocities for a very thin film were required to achieve shear banding. In this work only pseudo-Couette and inhomogeneous shear flows were observed. The fact that there is a non-zero shear rate in the central region of the inhomogeneous shear flow in this work, suggests that the polybutene does not completely solidify under the experimental conditions. It is possible that this central shear rate varies with the applied pressure, and that complete solidification may be achieved. Therefore the transition into inhomogeneous shear and shear banding is not a first order transition. Second order phase transitions haves been observed for a Newtonian liquid at high pressure [124].

The observation of inhomogeneous shear has implications for the condition of lubricant in EHD lubrication. It can shed light on origins of other EHD anomalies, one of which is the appearance of dimples. Literature has suggested frictional heating [48], plug flow due to solidification [45], plastic yielding due to limiting shear stress [125] and slip [38] as causes of dimple formations in EHD contacts. The temperature rise due to frictional heating in this

work is negligible (see subsection 2.3.5). In [45] the appearance of a dimple was modelled by the plug flowing at a velocity different to the entrainment velocity. This effect is similar to interfacial slip, where the mean velocity of the lubricant changes, which is accommodated by a change in the film thickness due to conservation of mass. The result in Fig. 69c however does not show a sufficient acceleration or retardation of the mean velocity to explain the results observed in subsection 3.2.5, where the film thickness almost doubles. One should note that inhomogeneous shear, similar to plug flow, is observed (see Fig. 69) at conditions similar to those for which the dimple appears. Since inhomogeneous shear occurs at pressure similar to the pressure required for dimple formation, its appearance may be related to the pressure-induced transition of the flow into inhomogeneous shear. Further investigations into the cause for the dimple are required. Given that the formation of the primary dimple creates two regions of mostly uniform film thickness at high loads (see subsection 3.2.5), the photobleached-fluorescence imaging velocimetry technique should be applied to both regions in the same contact to determine if their flow conditions are different.

The existence of inhomogeneous shear (IS) complicates the measurement of a flow curve, which represents the rheology of the lubricant. This has an impact on predictions where rheological information of the EHD lubricant is required. The calculation of friction in an EHD contact is described in subsection 2.3.4, where an assumption of Couette flow is used to define the shear rate. Using this assumption and knowing the relationship between shear rate and shear stress, allow the determination of the friction. The calculation of the coefficient of friction in the case of IS is not trivial as the profile indicates local shear rate heterogeneity. Current EHD theory is incapable of accounting for the effects of IS. Yet the existence of IS in an EHD lubricant may be more prevalent than generally considered. IS may also enable the accommodation of peculiar effects such as the limiting shear stress. This invalidation of the general linear flow assumption would affect predictions of film thickness and the analysis and interpretation of results from methods such as infrared temperature measurements [86], used to estimate surface stresses. In regard to friction, it should be noted that the slope of the flow curve, $\partial\sigma/\partial\dot{\gamma}$, typically drops as the shear rate increases. Therefore, if the viscosity is constant through the film, a splitting of the velocity profile into lower and higher shear

rates would result in a reduction of the average shear stress, and thus the friction. The friction in the EHD contact should be measured for the various experimental conditions, and be compared with the results for the velocity profiles to support the postulation that inhomogeneous shear affects the friction coefficient (see section 8.2).

If the shear stress is constant through the film, rather than the viscosity, the relationship between friction and the velocity profiles could be used to enable in situ rheometry [126]. The shear rate as a function of position through the thickness of the film can be obtained if the local velocity profile is known. The stress can be estimated using the friction coefficient. Thus the flow curve, $\sigma = f(\dot{\gamma})$, can be constructed. If the stress is constant, and multiple shear rates exist due to inhomogeneous shear, this flow curve would be non-monotic, a condition which has been used to model inhomogeneous shear [43]. This potential application is complicated by the fact that the velocity profile is spatially heterogeneous. However, as photobleached-fluorescence imaging velocimetry enables local measurements, this complication can be accounted for.

If solidification of PB is the cause for the results in Fig. 69, a critical pressure and shear rate may exist, for which the effects of IS are observed. If a critical pressure is not reached, i.e. in a low pressure contact, the velocity profile should be linear. This is supported by the observations of nearly Couette flow profiles for PB in the low pressure EHD condition and in the soft-EHD condition. To investigate the possible existence of a critical pressure and shear rate, and their effects on the rheological behaviour of the lubricant, through-thickness velocity profiles are obtained at various conditions of pressure and shear rate.

6.2 The effect of load and speed

Photobleached-fluorescence imaging velocimetry was applied at the central position of a glass-glass EHD contact lubricated by PB2300, and the load and speed were varied to study pressure and shear rate induced effects on the flow. Each experiment was repeated twice.

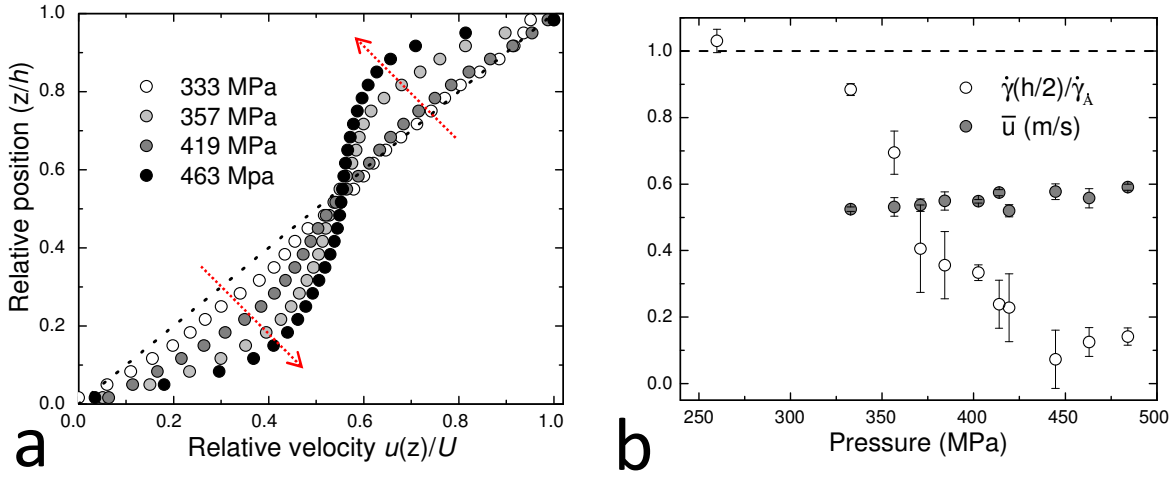


Fig. 70: a) Velocity profiles at various applied loads for PB2300 at speed 360 µm/s. The film thickness at the lowest pressure is 654 nm. At the highest pressure the dimple causes the thickness to increase to 980 nm. The dotted line indicates a linear velocity profile. The red arrows show how the plug grows with load. b) Central relative shear rate and mean velocity as a function of load. The dotted line shows the apparent shear rate for Couette flow. (Adapted from [127])

Sample velocity profiles are shown in Fig. 70a, measured at a speed of 360 µm/s for all loads. At a load of 13 N (335 MPa), the velocity profile is nearly linear, suggesting that the lubricant is still flowing as a liquid. As the pressure is increased, the profile assumes an increasingly sigmoidal shape, as the effects of IS progress. The thickness of the boundary layers of low viscosity (experiencing higher shear rate) reduces with the applied load, indicating the growth of a central solidified plug. The central relative shear rate was determined using a linear fit over five data points adjacent to the central z-position, $z = h/2$, and the result as a function of pressure is plotted in Fig. 70b, along with the mean velocity. Plateaus can be identified. At low pressure, the central relative shear rate is roughly 1. It then reduces gradually and plateaus, suggesting that the observed phase transition is of second order. The result clearly shows the progressive development of the plug. The critical pressure for the transition from high to low central relative shear rate is about 355 MPa. It is also shown that there is a small variation in the mean velocity of about 10 %. Given that the variation in mean velocity is small, the effect of elevated pressures on the anomalous film thickness observed for PB cannot be explained by retardation of the lubricant, which has been suggested as a potential cause for the appearance of the dimple [45].

The sigmoidal shape of the velocity profile is believed to be related to the formation of a solid plug, caused by a second order phase transition. This is supported by the identification of a critical pressure that necessitates the formation of the plug. The viscosity of PB2300, at approximate critical pressure of 355 MPa, identified in Fig. 70b, can be calculated by the Barus equation, and is found to be 19 MPa s. This is similar to the glass transition viscosity of polybutene of 10 MPa s [12], suggesting that a phase transition is a likely cause for the plug formation and that the plug is likely a glass. The pressure at which this transition occurs is very similar to the critical pressure observed in the squeeze film study (subsection 2.3.6). It would be of interest to investigate whether the critical pressure varies for the three available polybutenes of various molecular weights, as their critical glass transition pressure would be expected to vary (see section 6.4).

The shear rate is also expected to affect the flow of polybutene, as it has been suggested that the solidified lubricant yields through shearing at the interfaces. In subsection 3.2.5 it was shown that the formation of dimples in an EHD lubricant film was dependent on the applied shear rate (see Fig. 43). If the shape of the film was caused by the yielding of partially solidified lubricant at the interfaces, the shear rate would indeed be expected to affect the flow. It was also shown that the observed dimple could be completely removed by applying a low surface energy coating, which severely reduced the applied shear. The effects of shear rate should therefore be observable by studying the flow of the lubricant.

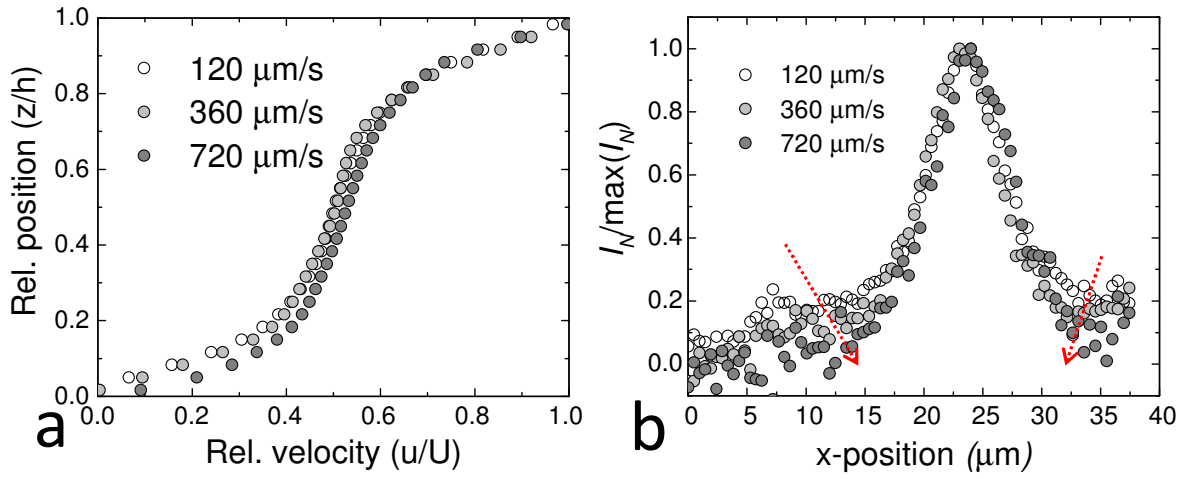


Fig. 71: a) Velocity profiles at various applied speeds for PB2300 at load 28 N (430 MPa). The approximate central film thicknesses in the dimple are 397, 829 and 1320 nm for the three speeds. b) Relative normalised intensity distributions for three speeds, at a fixed characteristic distance after photobleaching. The distributions have a significant Gaussian component with visible shoulders on either side of the peak intensity. The red dotted arrows indicate the decay of these shoulders with increased velocity.

Photobleached-fluorescence imaging velocimetry was applied at the centre of a glass-glass EHD contact lubricated by H-300, at a load of 28 N and various speeds. The reconstructed velocity profiles are shown in Fig. 71a. The apparent shear rates at the three increasing speeds are 303, 434 and 545 s^{-1}. Compared to the effect of load on flow, the effect of shear rate appears to be mostly negligible. This could be due to the small range of shear rate tested, which is limited by the experimental setup. The normalised relative intensity distribution at a fixed distance travelled by the ball is shown in Fig. 71b. The data has been normalised by the maximum value to enable a comparison between the intensity distributions. While the general Gaussian shape is similar for all speeds, shoulders can be seen, especially at the lowest speed. The decay of these shoulders, as the shear rate increases, is indicated by red arrows in Fig. 71b.

Suppose that yielding of the lubricant near the surfaces occurs within a band of fixed thickness. Such a conjecture is supported by the yielding of amorphous solids, where yielding typically occurs over a thickness of the order of 10 nm [128]. Assuming the yielding layer is always next to the rubbing wall and that its thickness is small and constant, the yielding layers would be more visible if the film thickness was comparatively small. If the film thickness increases, the relative intensity from thin yielding layers of constant thickness

would reduce, similar to the effect observed in Fig. 71b. This suggests that there may be a thin layer of PB near the surfaces which shears easily, facilitating the low shear rate flow in the centre of the film. The reconstruction scheme is limited in terms of resolvable relative shear rates (see section 4.4), such that the thickness of the high shear rate layers appear identical for all three speeds in Fig. 71a. It would be interesting to conduct experiments with even smaller film thicknesses to see if the shoulders in Fig. 71b become more pronounced. Unfortunately this is difficult due to limitations of the optical technique as well as due to the typical roughness of the surfaces involved in EHD contacts. Given that the appearance of the glassy flow is suggested to be related to yielding, it would also be beneficial to study the effect of shear rate on the velocity profile using a system where the slide-roll ratio can be varied. Indeed, it has been shown that the appearance of the dimple does not occur for pure rolling conditions [95]. Thus a critical shear rate may be found at which the glassy flow appears.

It is clear that the flow of polybutene is mostly affected by the applied pressure. The pressure in an EHD contact varies over the contact area however, suggesting that the characteristics of the glassy flow varies with position in the contact.

6.3 Spatial variations

When a non-classical film thickness was observed at elevated pressures (see subsection 3.2.5), it was shown that two regions of different but mostly constant film thickness were present. To accommodate such variations in the film, a drastic change in either the flow or the properties of the lubricant is required, for conservation of mass to apply. Measurements of the lubricant flow were performed at various positions along the centreline (y = 0), in a glass-glass EHD contact lubricated by H-300. The results for the central relative shear rate and the mean velocity are presented in Fig. 72a. Positions at which measurements were performed are indicated in Fig. 72b.

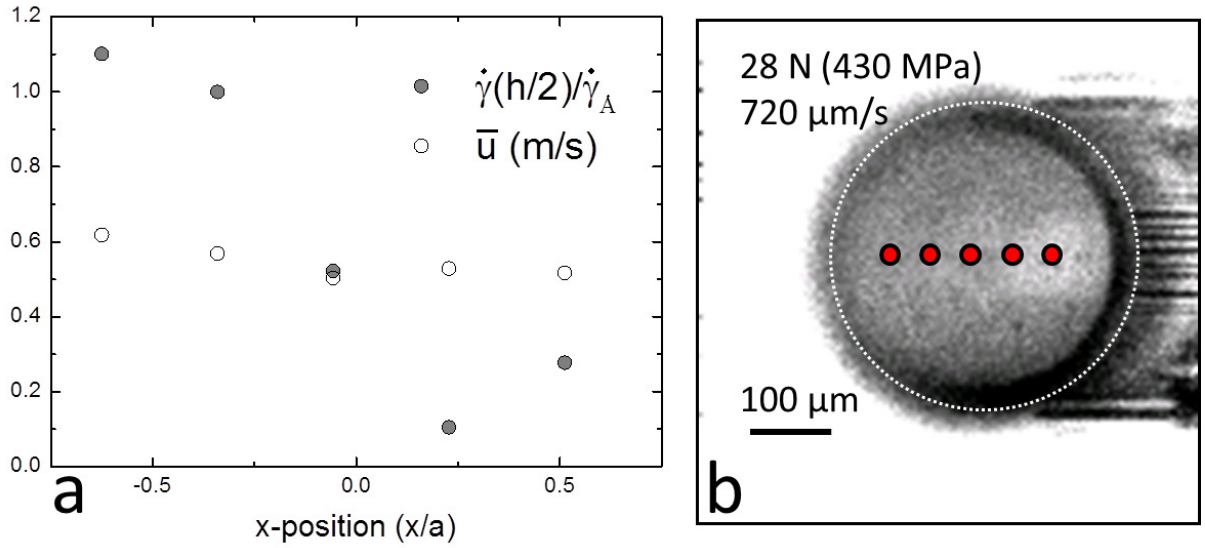


Fig. 72: a) Spatial variation of central relative shear rate and mean lubricant velocity for H-300 at load 28 N (430 MPa) and speed 720 µm/s. The film thickness varies between 249-398 nm depending on position. b) Fluorescence intensity map of a 28 N (430 MPa) EHD contact, indicating positions (red dots) where measurements were performed for the data in (a). The white circle shows the contact area.

There are only small variations in the mean velocity, similar to the variations present in the liquid regime (see Fig. 67a). The variations in the central relative shear rate are however substantial. Near the inlet, where the pressure is low, the relative shear rate approaches unity, showing that the flow is liquid and has that the velocity profile is mostly linear. As the lubricant travels through the contact it undergoes up to a tenfold reduction in the central shear rate, indicating a significant presence of solidified lubricant. This shows that the liquid and glassy regime can coexist in the contact, and that the degree of solidification varies with position, likely induced by the variation of pressure within the contact.

The mean velocity slightly drops with position in the contact. The drop is however not nearly sufficient to explain the dramatic increase in the film thickness observed in section 3.2.5. The occurrence of the dimple is therefore proposed to be caused by the glassy flow, as the drop in the central shear rate of the velocity profile coincides with the increase in film thickness. Therefore the dimple is suggested to be formed due to changes in the material properties of the lubricant to facilitate conservation of mass.

6.4 Critical transition pressure

The phase transition of the lubricant can be represented by the drop in the central relative shear rate of the velocity profile. This value describes the degree to which the velocity profile assumes a sigmoidal shape. By creating plots of the relative shear rate as a function of pressure (as done in Fig. 70b), the critical pressure at which the transition occurs can be determined. A second-order phase transition of polybutene was inferred to occur at a critical pressure in subsection 2.3.6, by studying the dynamics of squeeze film. The critical pressures required for the two observations are similar, suggesting that the flow transition is related to the phase transition of the lubricant. Since molecular weight is known to affect the glass transition temperature of polymer, the photobleached-fluorescence imaging velocimetry technique is applied to three polybutenes to study the effect of molecular weight on the critical pressure for flow transition.

Photobleached-fluorescence imaging velocimetry was applied to the central positions of glass-glass and sapphire-glass EHD contacts, lubricated by three polybutenes, to determine the critical pressure at which the lubricant starts showing glassy characteristics. The properties of the polybutenes are listed in Table 2. Since the effect of shear rate on the glassy flow was shown to be negligible in the previous subsection, the speed for each lubricant was selected to keep the film thickness approximately constant. The speeds used were 360 µm/s (PB2300) and 720 µm/s (H-300 and PB900).

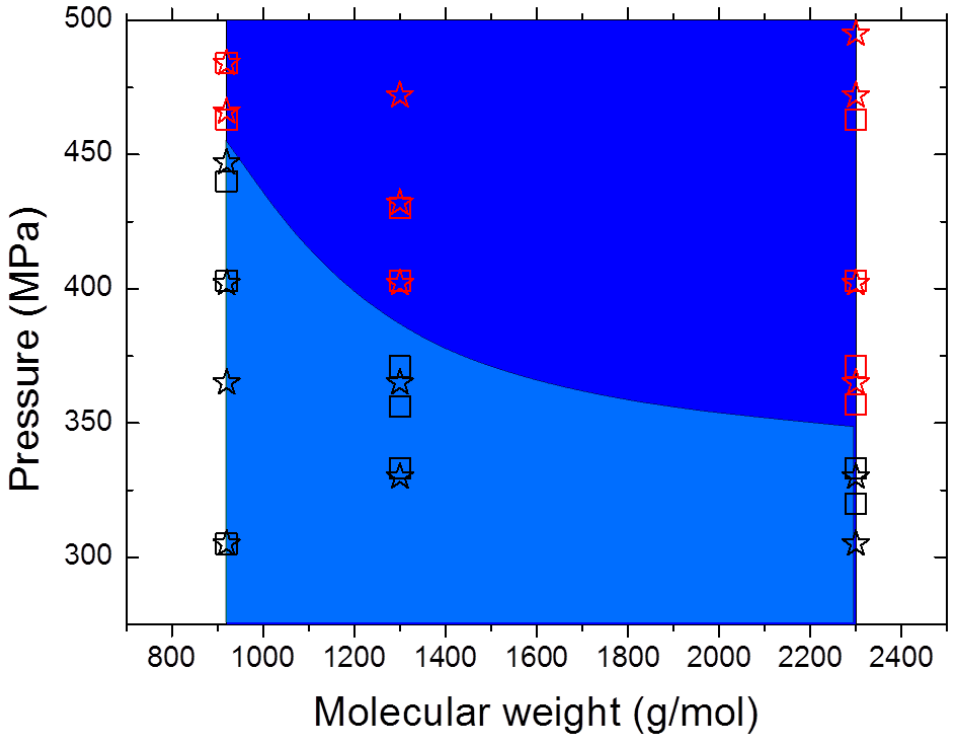


Fig. 73: Pressure-molecular weight phase diagram for polybutene. Black data points are in the liquid phase (nearly Couette flow) and red data points are glassy (sigmoidal velocity profile). Squares represent data for a glass-glass contact and stars represent data for a glass-sapphire contact. The coloured areas are a guide to the eye, indicating the author's interpretation of a possible glass transition boundary. Adapted from [127].

The experimental results are presented in Fig. 73, in the form of a phase diagram, where the data points indicate whether or not a phase transition has occurred. A critical value for the central relative shear rate was chosen as 0.7, to identify the glass transition of the lubricant. The effect of this value, in the range of 0.6-0.9, on the determination of the critical pressure was minimal. The critical pressure is similar for both the glass-glass and sapphire-glass contacts. This suggests that the solidification is dependent on pressure rather than confinement or thixotropy (referring to time dependent changes in the rheology) of the lubricant. Another observation that can be made is that the dependency of the critical pressure on molecular weight is non-linear. This would be expected based on the non-linear relationship between pressure, glass transition temperature and molecular weight [129]. This particular result is a good example of how the technique of photobleached-fluorescence imaging velocimetry can be applied to an EHD contact to study the rheology of lubricants. Furthermore, the estimated critical pressure of 350 MPa for PB2300 agrees with the approximate critical pressure of 330 MPa, determined by the squeeze film study (see

subsection 2.3.6). This agreement adds to the hypothesis that the pressure induces a phase transition of the lubricant.

There are a few potential improvements that could be made in the creation of the phase diagram. Smaller variations in load could be applied to more accurately find the transition pressure. Unfortunately the transition is not immediate, and at any given position the liquid and glassy regimes can coexist (over a small range of pressures), due to the chaotic nature of the phase transition and yielding, as well as instabilities in the experimental setup causing small variations in pressure over time. The more important improvement would be to increase the number of lubricants used which would allow the determination of whether or not the observed phenomenon is system dependent. Currently only three data points are available, which suggest that the relationship between molecular weight and critical pressure is non-linear.

6.5 Summary

The velocity profile in EHD contacts at high pressures (>350 MPa) was studied using the photobleached-imaging velocimetry technique. It was shown that the velocity profile assumes a sigmoidal shape, separating into a low shear rate thick (comprising a large proportion of the film) central plug and thin high shear rate layers next to the interfaces. This is indicative of inhomogeneous shear. Solidification by glass transition was proposed as the cause for the observed shape. This was suggested by the estimated PB viscosity in an EHD contact at high pressure, which surpasses the glass transition viscosity. Given that measurements at high pressures, showing inhomogeneous shear, were performed inside the primary dimple (thicker film thickness), it was believed that the appearance of the dimple is related to the sigmoidal plug flow velocity profile.

The speed and load were varied to determine the effect on the sigmoidal velocity profile. While only two speeds were tested, the effect was shown to be negligible. The load on the other hand strongly influenced the velocity profile. It was shown that a critical pressure was required for the observation of the sigmoidal plug flow. The viscosity of polybutene at the critical pressure was similar to the glass transition viscosity of polybutene determined by

others. The critical pressure for a transition in EHD flow behaviour also coincided with the critical pressure causing a change in the characteristic decay time of PB squeeze films. Furthermore, as the pressure was increased, the plug became more distinct. This was quantified by the central shear rate, which was shown to reduce with increasing pressure. This result further supports the postulation of a glass transition being responsible for the observed velocity profile. While the speed did not significantly affect the reconstructed velocity profile, studies of the resulting intensity distributions hinted at the fact that there may be a thin adsorbed PB layer, which possesses different properties to the bulk polybutene. This adsorbed layer would not be resolved by the reconstruction scheme due to limitations in terms of maximum resolvable shear rates.

The technique was applied to various positions in the contact, due to the spatial pressure distribution, which would be expected to affect the flow. It was shown that the plug flow only appeared in the high pressure region, and also that the locations of plug flow coincided with the appearance of the dimple, showing that liquid and glassy polybutene can coexist in the contact. Some material property of the polybutene would need to change drastically to accommodate conservation of mass, as the mean velocity was shown to be mostly constant with position.

The load was varied for all three polybutenes to study the effect of molecular weight on critical transition pressure. The study was carried out for glass-glass and sapphire-glass contacts to isolate the effect of pressure. It was shown that the critical pressure decreased with an increase in molecular weight, which is consistent with the existence of a glass transition viscosity for polybutene.

7 Boundary slip

A low surface energy coating (see subsection 2.3.8) was applied to the stationary surface to facilitate slip on one of the lubricant-solid interfaces. As the slip length is commonly assumed to be dependent on the shear stress [9], the effect of pressure and shear rate is expected to affect the degree of slip exhibited by the lubricant. In this chapter, velocity profiles for PB in a glass-Fusso EHD contact are presented at various loads and speeds. The velocity profile is also measured at different positions to confirm the existence of spatial variations of the slip length.

For all experiments in this chapter, each measurement was taken within one minute after moving to a new position on the coated glass slide. This was done to certify that no wear of the coating had taken place, ensuring repeatable and comparable results. The polynomial reconstruction scheme was applied rather than the previously used 'free' scheme. The argument for using the polynomial scheme is the improved accuracy in determining the slip length in the presence of noise when the slip length is large, as shown in section 4.3.

7.1 Typical result

In chapters 5 and 6, it was shown that the no-slip condition holds for polybutene in a glass-glass EHD contact. By lowering the interfacial energy between the lubricant and the solid interface, it is possible that this boundary condition no longer remains appropriate. The photobleached-fluorescence imaging velocimetry technique was applied to a glass-Fusso EHD contact, where the stationary glass slide was coated with a low surface energy (Fusso) coating (see 2.3.8). The result for H-300, in a glass-Fusso EHD contact, at a velocity of 720 µm/s and a load of 6.4 N (263 MPa), is shown in Fig. 74. The result was acquired within a minute, after moving the contact to a fresh position on the Fusso surface, to minimize the effects of wear of the low surface energy coating. The film thickness of ~120 nm was determined using laser-induced fluorescence (see subsection 3.2.6).

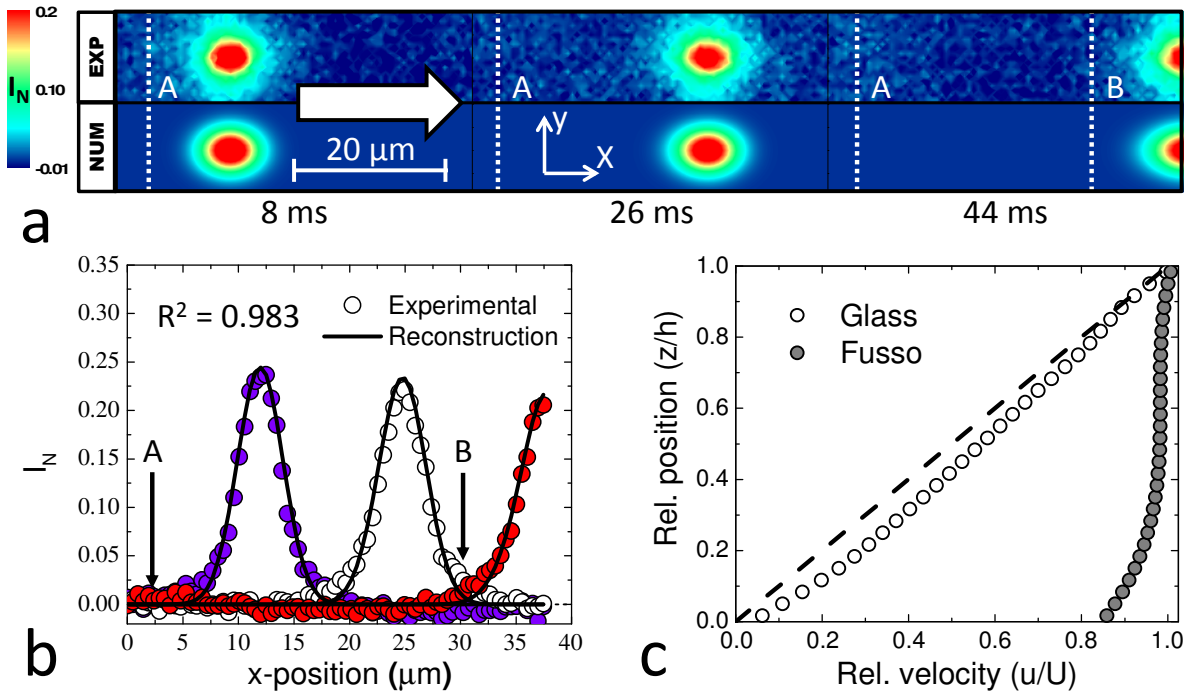


Fig. 74: a) Experimental (EXP) and numerical (NUM) spatiotemporal normalised relative intensity distributions at three times for H-300 at speed 720 µm/s, load 6.4 N (263 MPa) and film thickness ~120 nm. The arrow indicates the direction of the flow. The dotted line A indicates the initial position of the back of the column. The dotted line B shows the approximate measured back of the column, indicating interfacial slip. b) Averaged distributions from (a) where points 'A' and 'B' maintain the same definitions. c) Reconstructed velocity profiles and theoretical Couette velocity profile.

The experimental and reconstructed intensity distributions in Fig. 74a and Fig. 74b are well correlated, as shown by the coefficient of determination. They are also distinctly different from the result acquired for the glass-glass contacts (see Fig. 64). The back of the photobleached column now moves over time, as shown by the dotted line in Fig. 74a and the arrow in Fig. 74b labelled 'B', indicating that slip is taking place at the lubricant-Fusso interface. Given the significant amount of slip present, the polynomial velocity profile reconstruction scheme (see end of section 4.3), which is more suitable for slip length determination, was applied. The result acquired using this scheme is shown in Fig. 74c. Substantial slip at the bottom interface can clearly be observed. The slip velocity can be determined using the polynomial coefficients of the velocity profile. The relative slip velocity was found to be 0.84. The slip length could then be calculated using equation (32) and by assuming an approximate film thickness reduction of 40 % (see subsection 3.2.6). This results

in values $b_{rel} = b/h_c = 5.25$ and $b = 0.63$ µm, for an approximate film thickness of $h_c = 120$ nm.

In [130] it was shown, for a hydrodynamic point contact, that there is a significant reduction in friction when a glass interface is modified by a low surface tension coating. The authors in [130] explain the friction reduction by solving a modified Reynolds equation with slip boundary conditions measuring an approximate slip length of 6 µm, which is also accompanied by a significant reduction in film thickness. This compares well to the results found in this work. A large relative slip velocity of 0.84 was identified, which is of similar order to the slip velocity of 0.8 used to explain the film thickness reduction found in subsection 3.2.6, measured using laser-induced fluorescence. While this shows that the film thickness results could be used to determine the slip length, the velocimetry measurements enable the direct observation of the phenomenon.

A question that arises when studying questions of slip, especially at nanoscopic levels as in this work, is the nature of the slip, if it is real or apparent, occurring over a few molecular layers with significantly reduced viscosity. If slip were to take place over a single molecular layer, the technique would still show the existence of slip, or shear banding, but the reconstruction of the velocity profile would not be accurate, as nearly infinite relative shear rates would not be resolvable, especially using the polynomial reconstruction scheme. In section 4.3, it was shown that the reconstruction scheme is capable of resolving relative shear rates up to a value of 3. While molecular dynamics simulations have suggested that extreme gradients in the velocity profile are not present in thin films [49,131–133], these limitations however somewhat diminish the capabilities of the technique, in terms of solving the issue of apparent versus real slip. Having said that, the general observations of pressure-induced changes in the rheological response of PB in an EHD contact remain. There is also currently no other known technique which would be able to provide this information.

As it has been shown that slip can be measured directly, the effects of various parameters such as shear rate, pressure (see section 7.2) and position (see section 7.3) on slip were explored. The applied coating would reduce the effective shear rate, and thus the effective

shear stress and friction [130]. The effect of slip on friction was investigated (see section (8.2)). These studies shed new light on the existence of a critical shear stress for slip and the relationship between slip, pressure, shear rate and friction.

7.2 Dependency on shear rate and load

The shear rate and load was varied to study their effects on the slip at the lubricant-Fusso interface. Photobleached-fluorescence imaging velocimetry was applied to the centre of the glass-Fusso EHD contact, lubricated by H-300. Profiles and slip lengths were obtained as per section 7.1. Tests were performed three times for each experimental condition.

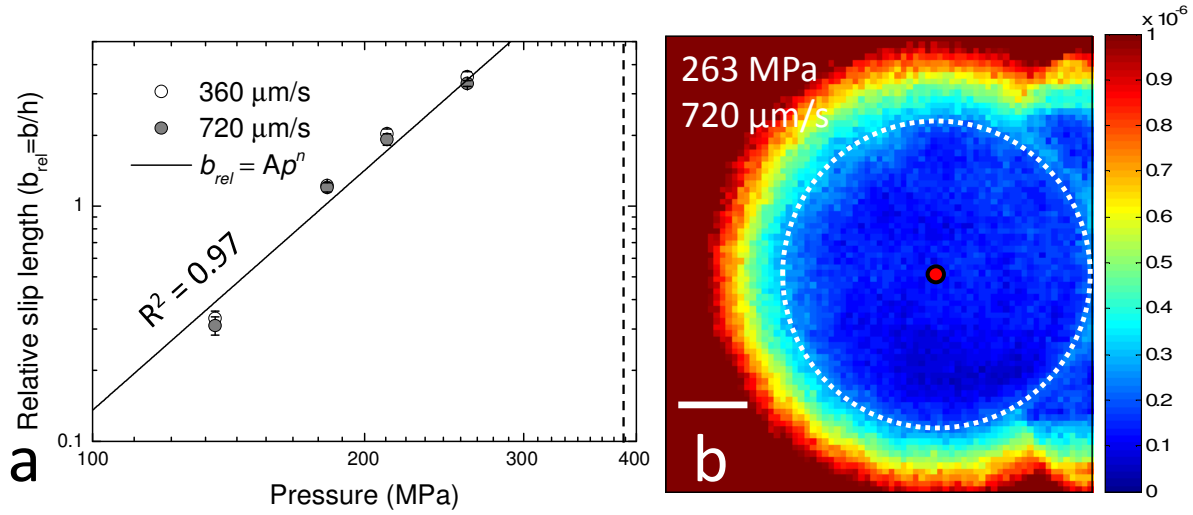


Fig. 75: a) Relative slip velocity as a function of load for two speeds for H-300. The dotted line indicates the critical pressure for phase transition of H-300. Note that the error bars are barely visible. b) Film thickness map of a 6.4 N (263 MPa) glass-Fusso EHD contact, indicating the position (red dot) where measurements were performed for the data in (a). The white circle shows the contact area and the scale bar is 50 µm.

The variation of the relative slip velocity with pressure is presented in Fig. 75a, and a film thickness map of the EHD contact is shown in Fig. 75b. The pressure clearly has a significant effect on the flow within the contact. Many models have been used to relate the shear stress and the slip length for polymers [9]. Unfortunately the shear stress is unknown in the contact. An estimate could be made, as shown in subsection 2.3.4, but the rheology of the polybutene used is also unknown. Similarly to the work in [134], the slip length is related to the pressure in this work by fitting a power law of the form $b = Ap^n$, where A and n are coefficients. The result of the fitting is shown in Fig. 75a, and the power law describes the

relationship well. The coefficients were found to be $A = 5 \cdot 10^{-9}$ and $n = 3.7$ for the two shear rates used. The shear rate on the other hand does not affect the slip length significantly, although only two speeds were investigated. The apparent shear rates at these speeds depend on the pressure due to slip but the approximate range tested was 2000-5000 s^{-1}.

The slip length was conjectured to depend on pressure, as there is a pressure-induced increase in the interfacial shear stress through viscosity, and because slip generally varies with shear stress [9,62,135]. In the case of an EHD contact, the relationship would be expected to be complicated, due the simultaneous occurrence of pressure enhanced viscosity and spatial pressure variation, requiring an acceleration of the flow to accommodate slip. Moreover, the relationship between slip length and shear stress in polymers has been shown to be non-linear [62]. Here a power law expression was chosen based on the analysis in [134], which was motivated by experimental studies on the influence of pressure on the boundary slip of polyisobutylene [136]. The exponent in [134] was 2.35 which is different to this work. This is not surprising given that the interfaces as well as the experimental conditions were different. The lubricant in [134] was also claimed to solidify, which was avoided here. It would be interesting to vary the surface energy and the roughness to study the effect on the slip length, as these quantities have been shown to have substantial effects [135]. The molecular weight would also be expected to affect the pressure-slip length relationship, and a study could easily be carried out in the future, given the polybutenes of various molecular weights available.

In this work only the low pressure region, where no glass transition occurred, was studied. This was done to avoid the complexity of the sigmoidal velocity profile which occurred after this transition. The sigmoidal velocity profile would not be compatible with the reconstruction scheme applied for slip velocity measurements. One should also note that in cases with sigmoidal velocity profile, film thickness measurements may not be sufficient for slip length measurements as flow assumptions have to be confirmed to be accurate.

Typically in EHD lubrication varying the speed has two effects: (1) The film thickness is increased and (2) the shear rate changes, causing a change in the shear stress depending on

the rheology of the lubricant. When slip occurs, its effect is complicated to predict as the film thickness, shear rate and slip length are all related, and their relationship depends on the rheology of the lubricant. Without knowledge of the rheology of the lubricant and the relationship between shear stress and the slip length, it is difficult to hypothesise how the slip length would be affected by speed in a pure sliding contact. Furthermore the explored test conditions are not sufficient to determine the effect of shear rate. Unfortunately the speed range is rather limited in the pure sliding setup, which constrains the accessible shear rates. By using another EHD setup capable of maintaining a slide-roll ratio, an improved study of the effect of the shear rate on wall slip could be performed.

In [130] friction data was fitted for a hydrodynamic contact, assuming a constant slip length at the glass-lubricant interface. In [25] the slip in EHD contacts was investigated using a dimple interferometry method. The lubricant in [25] was similar to this work. It was shown that the lubricant slips at the chromium-lubricant interface in a steel-chromium contact. Later work using the same method under similar conditions showed that the lubricant can also slip at the steel-lubricant interface [134] in a steel-glass contact. The slip length was shown to increase non-linearly with the shear rate and at some critical shear rate it would stagnate. At low shear rates, slip was not present. Similar slip lengths to this work were measured, although at significantly lower shear rates. This could be caused by the difference in boundary conditions as well as the different experimental conditions. In [134] lubricant was conjectured to slip on steel, while in this work it slipped on a fluoroalkyl coating. The fluoroalkyl coating would however be expected to promote slip more than steel. The fact that slip occurs at lower shear rates in [134] is thus surprising. It could potentially be caused by differences in techniques and experimental conditions.

The method in [134] and photobleached-fluorescence imaging velocimetry are somewhat different. It is likely that the presence of the thick (~ 1 micron) dimple in [134] affects the state of the lubricant, as the film thickness and shear rate are changed from the steady state EHD condition. In comparison, the method of photobleached-fluorescence imaging velocimetry enables the study of rheology of EHD lubricants in steady lubrication conditions similar to typical tribological applications. The technique also enables local measurements.

However, a main advantage of the work in [134] is that the effect of the shear rate was studied by varying the slide-roll ratio, which has not yet been performed in this work.

Given that the pressure significantly affects the amount of slip at the lubricant-solid interface, the slip length would be expected to vary with position in the contact.

7.3 Spatial variations

The pressure varies greatly with position in an EHD contact, and this variation is likely to affect the degree to which the lubricant slips. This spatial dependency is typically taken into account when relating slip to friction [36], although until now there has been no method of directly confirming the dependency. Therefore, spatial variations of the slip length in a glass-Fusso EHD contact was studied by applying the photobleached-fluorescence imaging velocimetry technique at various positions. Tests were repeated three times and two different loads were used.

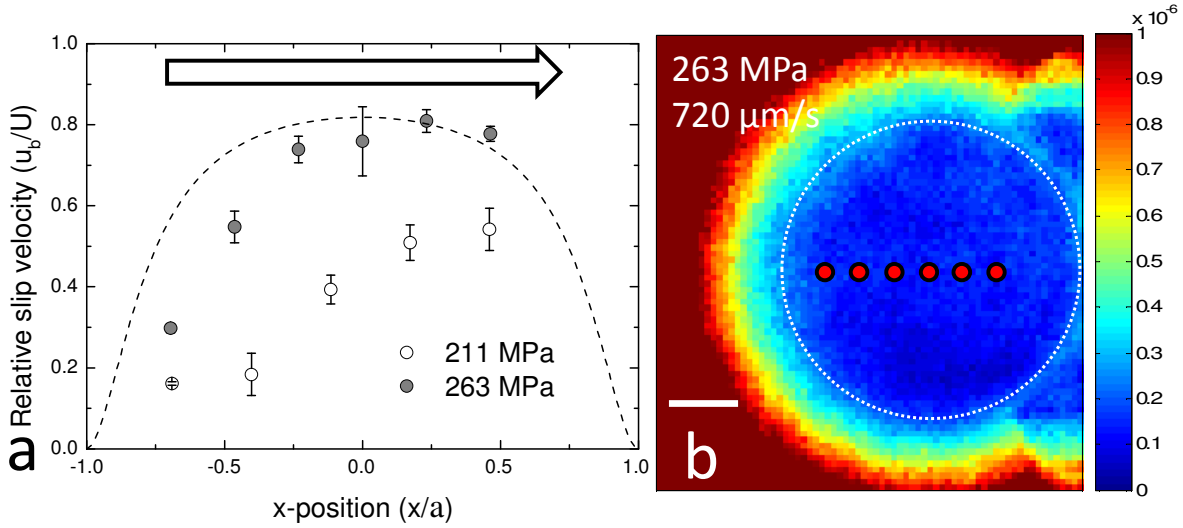


Fig. 76: a) Spatial variation of the relative slip velocity for various loads and speeds for H-300. The dotted line indicates the slip velocity predicted for 263 MPa by the power law fit in Fig. 75. The arrow shows the direction of the flow. b) Film thickness map of a 6.4 N (263 MPa) glass-Fusso EHD contact, indicating the positions (red dots) where measurements are performed with respect to the EHD contact for the data in (a). The white circle shows the contact area and the scale bar is 50 µm.

The result for the relative slip velocity as a function of position is shown in Fig. 76a for two different loads. The positions at which measurements were performed, for the higher load, are indicated in Fig. 76b. There are clear variations in the slip length with position in the

contact. Near the inlet, where the pressure is low, slip is minimal. As the pressure increases, the slip increases substantially and then plateaus. Measurements could not be performed close to the outlet due to cavitation. The result for the higher load is compared to a prediction based on the power law determined section 7.2. In this case the pressure was assumed to be Hertzian.

There is some agreement between the prediction and the results for the higher pressure, as the slip length is indeed expected to become mostly constant near the centre, and decrease with distance from the centre. Note that the prediction for the lower pressure would be worse, as the Hertzian pressure distribution is symmetric, while the slip distribution is not. The discrepancy could potentially be caused by the inappropriate choice of a Hertzian pressure distribution, which can be inaccurate depending on the experimental conditions. A more appropriate approach would be to somehow measure the pressure directly. Typically this is performed by determining the film thickness, which has been done in this work, and then relating the deformation to the pressure using theory [111]. This is commonly referred to as the inverse method.

The slip length was shown to vary significantly with position in the contact. This is an important discovery, which is contradictory to slip models commonly used to describe EHD contacts, where an average value is used for the slip length [130,137]. These models assume that slip only occurs after a critical shear stress is reached, after which the lubricant slips at a constant slip length. An average slip length may still describe friction reduction accurately, without correctly describing the flow. The spatial variation of the slip length complicates friction predictions. Therefore, the spatial heterogeneity should be mapped out more rigorously as the experimental technique is improved, especially once compatible fluorophores for other lubricants are found. This observation showcases one of the main advantages of photobleached-fluorescence imaging velocimetry for slip length determination, in comparison to the dimple method [38], where an average slip length is measured instead.

7.4 Summary

A low surface energy coating (Fusso) was applied to the stationary glass slide, to promote boundary slip in the EHD contact. The photobleached-fluorescence imaging velocimetry technique was applied to the centre of the contact, to study the effect of the applied coating. It was shown that the coating caused the polybutene to slip at the lubricant-Fusso interface. At a load of 6.4 N (263 MPa) and speed of 720 µm/s, the relative slip velocity was found to be 0.84, corresponding to a slip length of 0.63 µm. The measured relative slip velocity could successfully explain the reduction in film thickness in subsection 3.2.6. While the technique could be used to determine the slip velocity, it would be unable to determine the nature of slip (real or apparent), due to limitations in resolvable shear rates.

The speed and load were varied to study the effect on slip. Changing between the two speeds applied had a negligible effect on the slip length. The pressure on the other hand could be related to the slip length by a power law. At low pressures, no slip could be observed, while at large pressures, the effects were significant. The effect was explained in terms of the pressure-induced increase in viscosity and thus shear stress, as shear stress is known to be related to the slip length.

Similarly to how spatial variations were shown to exist for the high pressure plug flow, the spatial pressure distribution was shown to affect the slip length, by measuring velocity profiles at various positions in the contact. The results could be compared to a calculation made using the established power law relationship between pressure and slip length, and the comparison showed similarities in the distributions. The difference between the two distributions was explained by the incorrect assumption of a parabolic pressure distribution. In an actual contact the pressure distribution is more complex. The fact that the slip length varies with position is of importance, as this is typically not considered in experimental studies of slip length where film thickness or friction data are fitted to a constant slip length.

8 Friction measurements

Measurements have been made for the velocity profile of the lubricant and the film thickness in an EHD contact. This allows the local shear rate to be extracted, which provides information about the rheology of the lubricant. Experimental results in chapters 6 and 7 showed that the lubricant can exhibit inhomogeneous shear and interfacial slip, both of which depend on multiple experimental parameters. These phenomena may affect the tribological response of the EHD contact. In this section, the coefficient of friction is measured for the polybutene H-300 at various loads and speeds. This enables an estimation of the flow curve of polybutene in the EHD contact. Finally, the friction coefficient is measured for the low surface energy coating, and the reduction in the observed friction is compared to a calculated value, based on the slip lengths measured using photobleached-fluorescence imaging velocimetry in chapter 7.

8.1 Setup

A UMT-2 tribometer system (CETR) was used, with two load cells (5 and 100 N) and an ultra-low speed drive, to measure the coefficient of friction of polybutene in an EHD contact. The setup is shown in Fig. 77a. A glass ball was mounted onto the load cell and a glass disc was spun to entrain the lubricant. The ball was fastened onto a mount by a bolt, to stop it from rotating, creating the pure sliding contact. The ball could be rotated between tests to provide a fresh surface to minimize effects of wear. This was particularly important for friction tests with the Fusso coating. In this setup the disc is spun rather than the ball, compared to the setup used for fluorescence measurements, detailed in subsection 2.3.1. Although the apparent shear rate and sliding speed are the same, there might be slight differences in the two setups. At the time of this work, this was the only setup available. Naturally it would be preferable to measure the friction under the same exact conditions in future work. However, it has been shown that there are minimal differences between pure ball sliding and pure disc sliding for the lubricants used in this work [39], even for surfaces of different materials. Therefore general observations made should remain accurate.

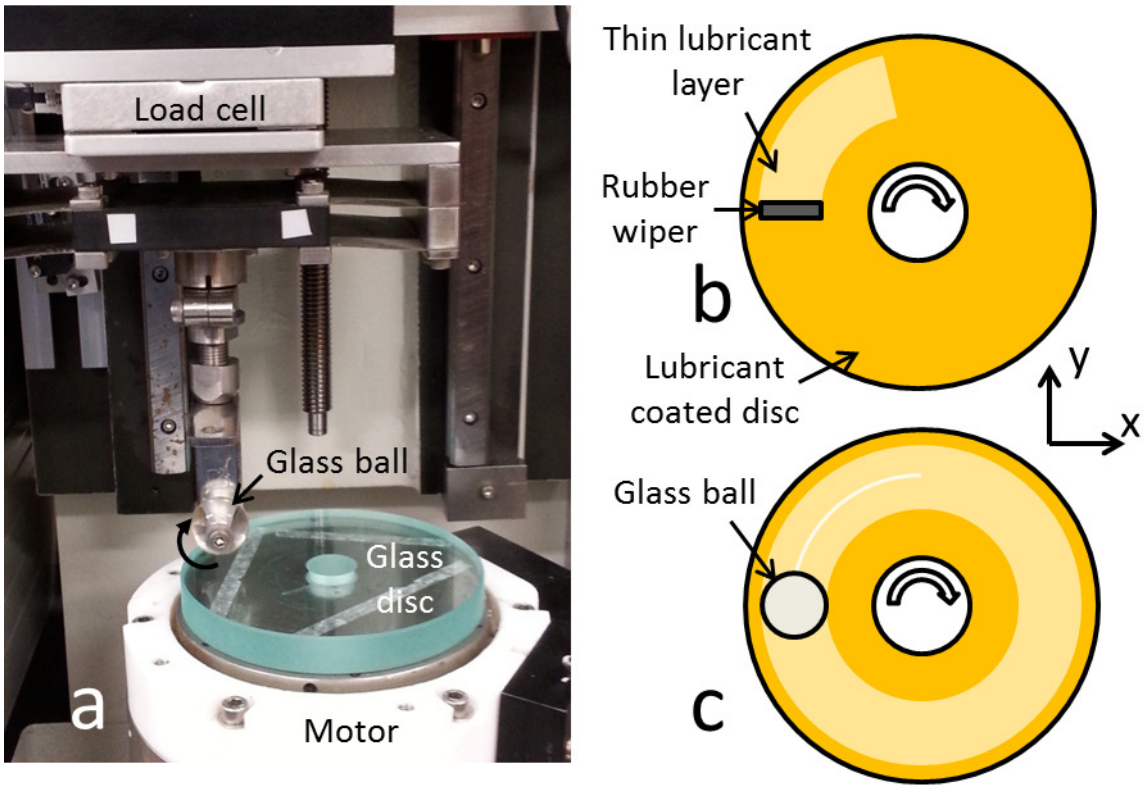


Fig. 77: a) UMT-2 tribometer setup. b) Schematic of thin film deposition using a wiper. c) Schematic of the setup used for the friction measurement.

An issue when measuring friction coefficients in EHD contacts, especially for lubricants of high viscosity, is the contribution of shear stresses outside of the contact to the coefficient of friction. To minimize this effect a wiper blade was employed, as seen in Fig. 77b. As the glass disc was rotated the blade was used to deposit a very thin layer of polybutene, on the track where the contact runs (see Fig. 77c). This ensured that most of the contribution to the coefficient of friction came from the EHD contact. Measurements were made for speeds in the range of 10-2000 µm/s. The ball was first run at 100 µm/s for 10 s to allow the load and speed to stabilize. Then each speed was run progressively, for 10 s at constant load, and the average value of the coefficient of friction for the 10 s was taken as the result for that speed. A sample friction curve for a speed ramp is shown in Fig. 78. It can be seen that the friction is stable over each test, and that the difference in friction coefficient for the various speeds is readily distinguishable.

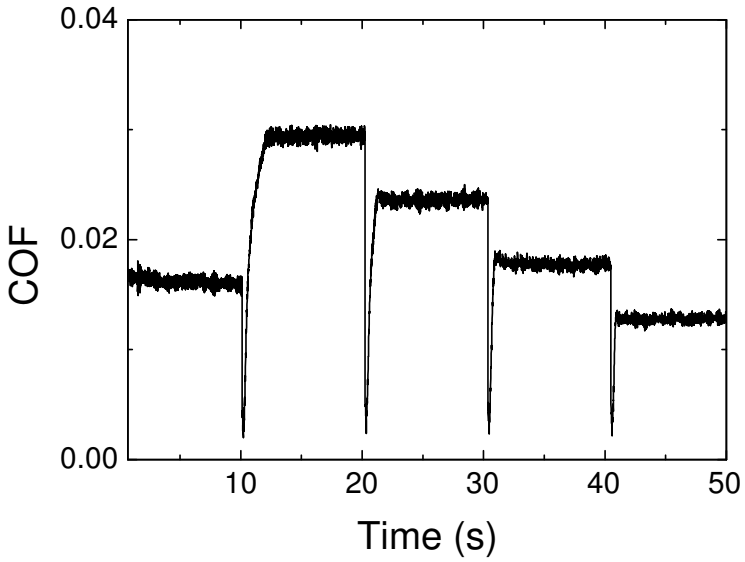


Fig. 78: Sample speed ramp for coefficient of friction (COF) measurements.

The total distance travelled by the ball for each experiment was less than the track length of one revolution of the disc, such that only fresh layers of the thin PB film were used for the friction measurements. Measurements were performed at a temperature of 25±1 °C and the applied loads were similar to the loads in the photobleached-fluorescence imaging experiments. To confirm that the deposited film was sufficiently thin, thin films were created at two various speeds and no significant difference in the measured coefficient of friction could be seen. This was not the case when a thick film was present, where the measured friction was significantly larger, especially at high speeds. The described setup was used in EHD conditions to measure flow curves for polybutene.

8.2 PB in a Glass-glass contact

The friction measurement of H-300 in a glass-glass contact at various loads and speeds is presented in Fig. 79a. Measurements were performed twice, and the glass ball was rotated to a new position for each load measured, to reduce effects of wear. No dramatic change in the friction could be observed when the critical load of approximately 20 N (384 MPa) for H-300 was reached. This suggests that the glass transition of polybutene has a minimal effect on the friction in the contact. The data in Fig. 79a was used to calculate the average shear stress and shear rate in the contact, as shown in Fig. 79b. The shear stress, σ, was calculated using $\sigma = F/(\pi a^2)$, where F is the frictional force and a is the contact radius. The shear rate

was determined using the estimate for the film thickness (see subsection 2.3.3). These flow curves were fitted with Johnson's constitutive relationship, described in subsection 2.3.4.

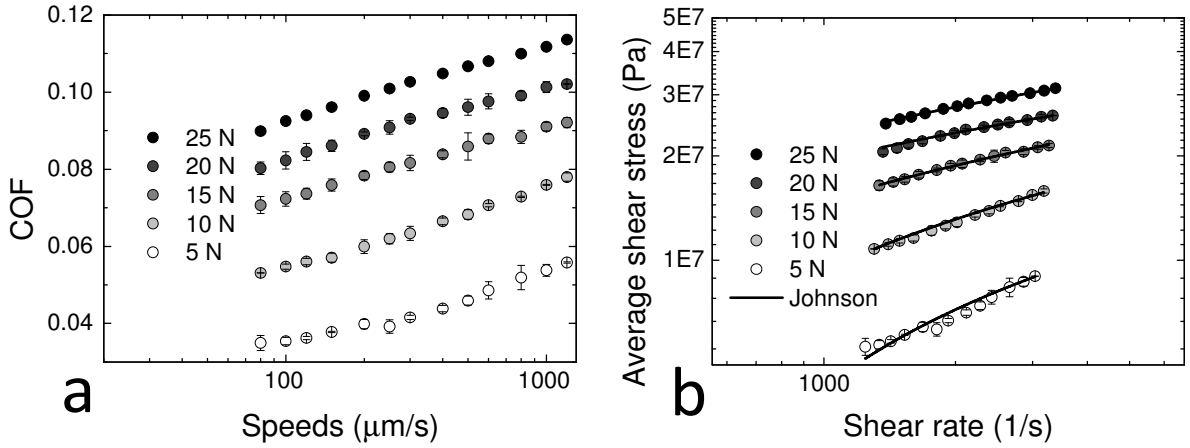


Fig. 79: a) Coefficient of friction as a function of speed for various loads for H-300. b) Estimated flow curves of polybutene. The black lines indicate a fit to Johnson's constitutive relationship. 5, 10, 15, 20 and 25 N correspond to 242, 305, 349 384 and 414 MPa respectively. Pressure-induced glass transition occurs at 390 MPa.

By fitting curves in Fig. 79b to equation (29), values for the Eyring stress and the viscosity, as a function of pressure, could be extracted. These values are shown in Fig. 80a and Fig. 80b. The variation of the Eyring stress with pressure was described using a linear fit, to enable estimation of the shear stress at any given pressure. The viscosity was fitted with the Barus equation, resulting in a pressure coefficient, α, of 26 GPa^{-1}.

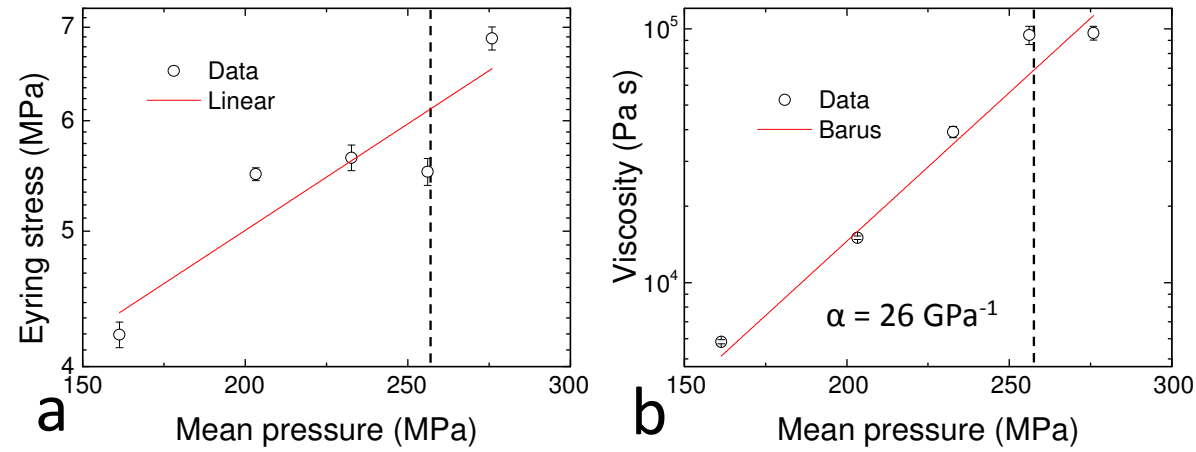


Fig. 80: a) The estimated Eyring stress as a function of mean contact pressure. The dotted line shows the critical transition pressure and the red line indicates a linear fit to the data. b) Variation of estimated viscosity with mean contact pressure. The dotted line shows the critical transition pressure and the red line indicates a fit to the Barus equation.

The ranges of shear rate and shear stress for the flow curves are not optimal. The ranges are limited due to the pure sliding condition. An improved study could be performed if a slide-roll ratio could be applied instead, as was done in the original work by Johnson and co-workers [15]. Thus, the variations of the Eyring stress and viscosity with mean pressure are not accurately determined which reduces the accuracy of resulting friction calculations. Nevertheless a calculation can still be performed. The value of the Eyring stress is similar to those of other lubricants under similar conditions and the viscosity compares fairly well with the value determined by interferometry in section 3.1.

While the friction coefficient increases with pressure, as shown in Fig. 79a, no particular effect on friction could be seen as the pressure reaches the critical pressure for glass transition, determined in subsection 6.4. This agrees with the results in [15], where no dramatic change occurs in either of the shear stress, viscosity or the Eyring stress at the glass transition pressure. The expected effect of the sigmoidal velocity profile on the friction is not trivial to predict. While the shear rate distribution is known, the shear stress distribution is unknown. The friction was unfortunately not considered in the numerical work on solidified plug flow in EHD [45], although it was suggested that the slip of the plug could be compared to boundary slip, which could tend to reduce the friction coefficient. This effect was not observed in this work, although the plug in this work is only partial and may therefore be unrelated to boundary slip. Given the small range of shear rates available (approximately 1000-4000 s^{-1}) no transition speed showing changes in friction could be found. Such a transition would provide a suitable comparison for the difference between Couette and plug flow, and would be possible given slide-roll ratio control. It is possible that the uniform shear thinning of the lubricant localizes at the boundaries without significantly affecting the overall shear stress. Indeed, if the observed velocity profile can be explained by a non-monotonic flow curve, the non-linear effect on the shear stress would be similar to that of shear thinning.

Although the friction coefficient seems unaltered by the solidification of the lubricant, the finding of the peculiar velocity profile remains important as the flow is significantly affected. This would affect lubricant transport, which is particularly important in thermal analyses for

example. Furthermore, the finding also implies that the commonly applied rheological models do not apply, as the linear velocity profile assumption is invalid. Finally, the velocity profile is important in determining the cause of the anomalous film thicknesses observed. Here, it was shown that the dimple is related to the sigmoidal velocity profile, excluding the possibility of boundary slip being the cause.

Given that the flow curve in Fig. 79b looks similar to typical flow curves for lubricants, it is possible that the glassy flow may occur in other systems. In this particular work however, the glassy flow has been shown to coincide with an anomalous film thickness. It would therefore not be expected to occur for lubricants which result in a classical EHD film thickness.

Having estimated the rheological parameters for the flow curve of polybutene by friction measurements, the effect of the low surface energy coating on the frictional force was studied.

8.3 The effect of interfacial slip on friction

Film thickness and velocity profile measurements both showed the existence of slip in a glass-Fusso EHD contact, at sufficient pressures. The effect of interfacial slip is a reduction in the effective shear rate exerted on the lubricant. Such a reduction would be expected to lead to a reduction in the shear stress, and thus friction. The friction coefficient of H-300, in a glass-Fusso EHD contact, was measured at various loads and speed. This enabled the study of apparent shear rates in the range of 1000-4000 s^{-1}. Before each speed ramp was performed, the Fusso coated glass ball was rotated, to ensure a fresh coating was used, minimizing the effects of wear. Measurements were repeated four times.

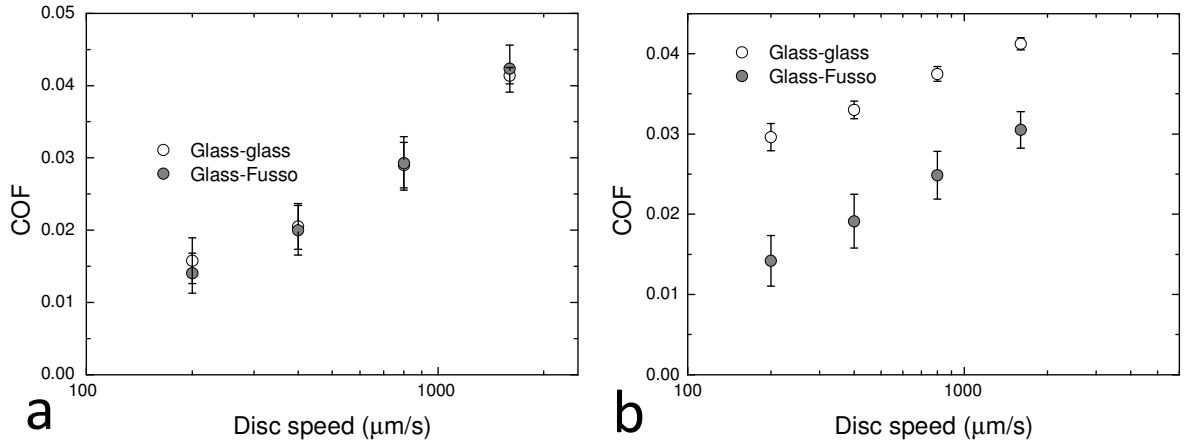


Fig. 81: Coefficients of friction (COF) at a load of 0.5 N (112 MPa) (a) and 5 N (242 MPa) (b) for the glass-glass and glass-Fusso contacts lubricated by H-300.

The results at a load of 0.5 N (112 MPa) are shown in Fig. 81a. Compared with the glass-glass results, it is clear that the coating had no significant effect on the friction coefficient at the low load of 0.5 N (112 MPa). The results for the load of 5 N (242 MPa) are shown in Fig. 81b. In this case the friction is reduced by up to 60 % at the lowest speed, for the low surface energy coating. This suggests that interfacial slip reduces friction. The relative reduction in the friction coefficient reduces as the speed is increased.

To further study the effect of pressure and shear rate, the ratio of the friction forces, F_F/F_G, for the glass and Fusso interfaces is plotted against speed for various loads in Fig. 82a. It is clear that the reduction in the friction coefficient due to the low surface energy coating increases with the applied pressure, and decreases with the applied shear rate.

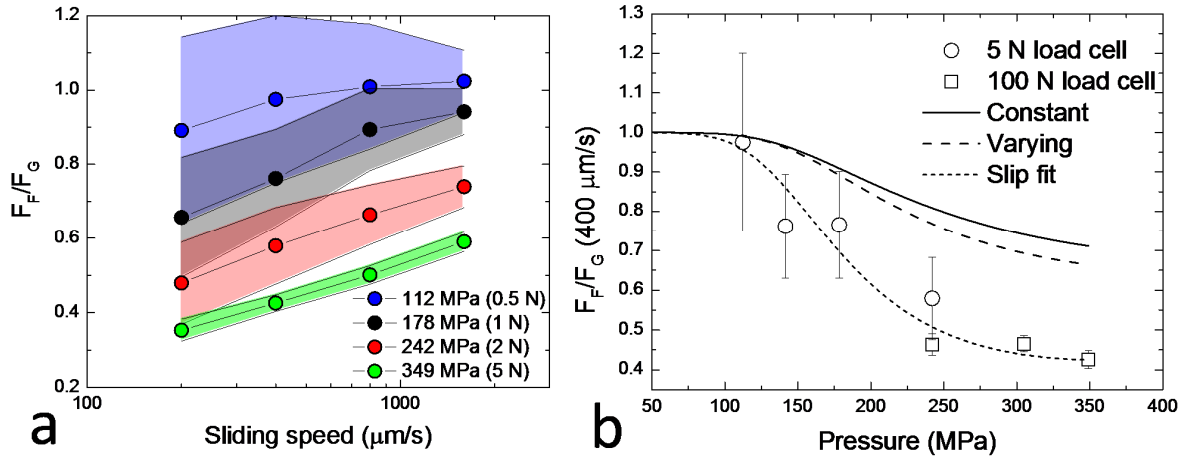


Fig. 82: a) Ratio of glass-Fusso friction, F_F, to glass-glass friction, F_G. The coloured areas represent the uncertainty. b) Friction ratio at the fixed velocity of 400 µm/s as a function of load. The solid line indicates a calculated relative friction determined by applying the determined pressure-slip length relationship based on Fig. 75a. The dashed line shows the calculation when the rheology was determined assuming spatially varying properties (see text). The dotted line shows a fit to the friction data used to determine an alternative pressure-slip length relationship.

The ratio of the friction forces is shown at $U = 400$ µm/s in Fig. 82b, as a function of load. The friction reduction was shown to decrease with speed. This can be explained by the fact that the relative slip length was constant, as observed using the photobleached-fluorescence imaging velocimetry technique. Therefore the only difference between the slip and no-slip cases, assuming a Hertzian pressure distribution, is a proportional reduction in the shear rate. Given the inverse hyperbolic relation for the shear stress (see subsection 2.3.4), the ratio of the friction coefficients is indeed expected to decrease with speed. The friction reduction was also shown to increase with pressure. This is explained by the increase relative slip length with pressure, which was shown in this work. The uncertainty in the friction measurements was relatively small, although the uncertainty of the friction ratio becomes large. It is still possible to distinguish the difference in friction at various loads except at the smallest loads. There were some differences in the results acquired using the two load cells which could be caused by the different resolutions. It would be necessary to investigate these differences for future work.

The friction force can be calculated using the flow curve parameters determined in the previous section. The shear rate can be estimated based on the calculated film thickness. For the glass-Fusso contact with slip, the film thickness is given by equation (41), where the slip

velocity is calculated by assuming a Hertzian pressure distribution and using the pressure-slip length relationship determined in subsection 7.2. Using the Hertzian pressure distribution, the viscosity can be obtained by the Barus equation and the shear stress can then be found using equation (29). Once the shear stress is determined, the friction can be obtained by integrating the shear stress over the contact area. This friction calculation was used to estimate the reduction in friction due to slip, shown by the black line Fig. 82b, based on the estimated relationship between pressure and slip length. Although the calculated friction drops with pressure, it does not agree well with the experimental results. This could be caused by the uncertainty in both of the slip length measurements, as well as the determination of the lubricant rheology. Recall that in all experiments, the apparent shear rate only varies between 1000-4000 s^{-1}. However, if slip occurs, depending on the load and speed the interfacial slip can cause the real shear rate to drop as low as 100 s^{-1}. As the rheology determination was only performed over a small range of shear rates (as shown in Fig. 79b), it may not be applicable once a large reduction in the shear rate, caused by slip, is applied. The uncertainty in the relationship between pressure and slip length particularly applies at the larger pressures. This was not considered in this work due to the possible solidification of polybutene at high pressure. Therefore the friction calculation uses an extrapolation for the slip length which may not be accurate. Nevertheless, even at low pressures, the calculated reduction in friction seems modest compared to the experimental results, indicating that the friction calculation used could potentially be flawed. It should be noted that a pressure-slip length relationship could easily be extracted from Fig. 82b (see dotted line). This fit was obtained for a power law exponent of $n = 3.9$. Recall that n = 3.7 was estimated based on profiles obtained from photobleached-fluorescence imaging velocimetry (Fig. 75a). The relationship between slip length and pressure based on Fig. 82b is significantly different from that measured using photobleached-fluorescence imaging velocimetry. This highlights the need to understand the origin and mechanisms of slip, which can only be accomplished by the accurate measurement of slip.

Due to the difference in experimental and calculated friction values, the appropriateness of the assumption of constant properties in the EHD contact, used for determining the rheology

of PB, was evaluated. A second fit to the data in Fig. 79 was made where a Hertzian pressure profile was used instead of mean pressure. The method used for friction calculation for slip, presented in this section, was used to calculate the no-slip friction at loads and speeds matching the data in Fig. 79. The Eyring stress and the pressure-viscosity coefficient were assumed to depend linearly on pressure. The 'lsqnonlin' function in Matlab could then be used to determine the pressure dependent Eyring stress and pressure-viscosity coefficient. The result using spatially varying properties can be seen in Fig. 82b. The difference between slip friction calculations performed using the newly evaluated parameters versus the old parameters was small (about 10 %). It was therefore determined that the assumption of constant parameters is not the cause for the discrepancy between the experimental and calculated friction.

The results obtained in this section cannot easily be compared with other data, as experimental measurements of wall slip in EHD conditions are fairly scarce. Examples of experimental results of friction measurements, claimed to be caused by interfacial slippage, includes various lubricants slipping on diamond-like-carbon (DLC) coatings [92,138] and polybutene slipping on chrome [119] and steel [139]. For these works, the friction reduction due to slip was of the order of 10-30 % and the reduction was load dependent, similarly to the results in this work. The reduction could not be directly shown to be caused by slip, as no method of slip length measurements in a steady EHD contact existed. However, as the only change between the slip and no-slip condition is the application of a coating, boundary slip is indeed implied. In this work, the slip was directly quantified using the photobleached-fluorescence imaging velocimetry technique, providing a unique insight into the interplay between the velocity profile, film thickness and friction generated at EHD conditions.

The occurrence of a limiting shear stress has been suggested to be facilitated by slip, either within the lubricant [14], or at the interface [139]. In this case the effective shear rate would remain constant while the apparent shear rate would increase, giving the appearance of a constant shear stress as a function of shear rate. Here, no such effect was observed. Firstly, no limiting shear stress was observed in any case, as the friction was shown to increase with speed. Secondly, the relative slip length was shown to be independent of speed, for the small

range of investigated shear rates. In the future, it would be of interest to investigate a lubricant dye system where the limiting shear stress is observed. This could involve lubricants such as 5P4E and Santotrac [15], but would require the development of a new technique, capable of studying EHD lubrication at higher speeds. Such a technique is developed in the subsequent chapter, for application to experimental conditions typical to practical tribology.

The results in this section highlight the complexity of boundary slip in EHD contacts. If slip is present, there is a significant effect on rheometric measurements. Such an occurrence deserves more consideration than is typically given in applications of EHD theory, due to the lack of knowledge and experimental data regarding the phenomenon. Ultimately the photobleached-fluorescence imaging velocimetry technique, combined with friction measurements, can enable the rheology of lubricants to be studied in the presence of anomalous flows. This can be done by extracting the effective shear rate through velocimetry measurements, and plotting this value against the calculated shear stress. Before standard methods, such as friction measurements, can be applied, it is necessary to confirm that the assumption of linear flow is accurate. This assumption has been shown to be non-universal, as various flows have been observed by changing experimental conditions. Given the abundance of anomalous film thicknesses and friction results observed in the literature, such flows are likely to occur even for more typical EHD conditions, relevant to practical applications in industry.

8.4 Summary

A tribometer was used to measure the friction caused by the shearing of polybutene in an EHD contact. Experiments were carried out at various shear rates and pressures for the glass-glass contact. The glass-Fusso contact was also studied, where glass balls had been coated with the Fusso coating.

The friction data was fitted using the rheological model by Johnson. This was used to determine the Eyring stress and viscosity as a function of pressure. The pressure-viscosity coefficient obtained (26 GPa^{-1}) was similar to the value obtained using interferometry (30

GPa^{-1}). These parameters were used to estimate the friction for a given shear rate and pressure.

No abrupt change in the friction curves could be observed at the critical pressure, despite the fact that a transition from Couette to plug flow of polybutene was expected. This suggests that the plug flow may not significantly affect the shear stress experienced by the lubricant. The finding of the plug flow velocity profile remains important for EHD theory however, as a change in the flow of lubricant affects the dynamics of transport phenomena which particularly concerns thermal EHD contacts. Furthermore it aids in explaining the observed anomalous film thickness and shows that the linear velocity profile assumption is not always appropriate.

The friction was measured for the Fusso-coated glass spheres at various shear rates and pressures. It was shown that there was a significant reduction in the friction coefficient (up to 60 %) compared to the uncoated sphere, at a pressure of 242 MPa. At a lower pressure of 112 MPa, the friction coefficients for the coated and uncoated surfaces were identical. This agrees with observations made for film thickness and velocity profile measurements, showing that high pressure is needed for significant boundary slip. The reduction in friction was shown to increase with pressure, in agreement with the power law relationship between slip length and pressure. The friction reduction was also shown to decrease with speed. The flow curve of polybutene was used to calculate the friction coefficient, and the calculated values were compared with the experimental data. While the general trend of increased friction reduction with pressure could be observed, the prediction was off by a factor of two. This discrepancy was suggested to potentially be attributed to the uncertainty in slip length determination or the inaccurate establishment of the flow curve for polybutene.

The complex relationship between film thickness, friction and velocity profile has been shown by their respective measurements. Clearly the typical fitting of film thickness of friction data to a slip length is insufficient in explaining the observed effects. The results in this chapter show that the mechanisms of slip are nontrivial and that a significant effort is required to achieve understanding of the phenomenon and its potential use in tribology.

9 Local rheometry in practical EHD lubrication

The main limitation of the photobleached-fluorescence imaging technique is the temporal resolution. It is shown in subsection 2.2.1, that the maximum speed for which acquisitions can be made accurately is 3.7 mm/s, requiring lubricants of very high viscosity to form an EHD contact. In this chapter fluorescence-lifetime imaging microscopy (FLIM) is presented for application to an EHD contact. Details of the technique are explained, and an experimental proof of concept is carried out.

9.1 Phosphorescence

When an excited molecule emits light, through the relaxation of excited electrons to the ground state, the relaxation can take multiple pathways. One pathway is the emission of a photon, of a wavelength equivalent to the excitation energy of the electron. This is a crude description of fluorescence. The process usually occurs on a timescale of nanoseconds to microseconds [140]. In certain cases, excited electrons can enter a triplet state, in which the emission of a photon to return to the ground state is forbidden. Instead, from the triplet state, a metastable state can be reached through vibrational relaxation, after which a photon can finally be emitted, returning the electron to the ground state. This is an example of phosphorescence. Transitions to other states can also cause phosphorescence, but the triplet state transition is the most common one. As the electron has relaxed through vibration, some energy has been released. This causes phosphorescence to commonly be significantly red shifted. More importantly, the vibrational relaxation is a relatively slow process. Therefore, phosphorescent compounds display emission lifetimes in the range of microseconds to seconds [140]. Following the excitation of a phosphorescent solution, after the nanosecond decay of the fluorescence, the phosphorescence intensity, I_{ph}, can be described by an exponential decay as

$$I_{ph}(t) = I_0 e^{-k_{ph}t} \tag{57}$$

where I_0 is the peak intensity, t is time and k_{ph} is the rate constant of phosphorescent de-excitation.

As the phosphorescent emission occurs over some time, the fluorophores remain observable, despite the lack of excitation. Thus, a volume of phosphorescent fluorophores in a fluid can be tagged, as was done using photobleached-fluorescence imaging, and the evolution of this volume can be tracked to infer the velocity of the fluid. The technique is commonly used to map two-dimensional flows such as that in an internal combustion engine [56], and it was recently employed to determine the velocity profile in a gas flow of acetone in a rectangular channel [141]. A main advantage of using another molecular tagging velocimetry technique is that the analysis remains mostly similar to the one developed in chapter 4. There are a few discrepancies between the techniques. Photobleached-fluorescence imaging shows a relative difference in intensity, such that the signal to noise ratio depends on the relative amount of photobleaching and the original signal. This relative intensity can never be larger than 1. In the case of FLIM, a positive phosphorescence intensity is monitored which does not have an upper bound. Another difference is that for photobleached-fluorescence imaging, the mean intensity remains constant after photobleaching, whereas for FLIM, there is an exponential decay of the intensity over time, which would need to be accounted for by the analysis. Lastly, the increased temporal resolution comes at a cost. Achieving sufficient signal in a thin EHD film, at exposure times of the order of 10 µs, is not trivial, even using synchronous averaging.

Similarly to the case of photobleached-fluorescence imaging, described in subsection 2.2.1, it is necessary to avoid blur, requiring the exposure time to be sufficiently small for the speed at which the phosphorescent volume is travelling. Using a typical distance of 30 µm and a typical minimum gating time, common for modern FLIM cameras, of 100 ns, giving a total acquisition period of 1.6 µs for 16 frames, the maximum resolvable speed is 18.8 m/s. It was shown in section 2.1.6, that a value of $\overline{B}$=4 is required for the assumption of instantaneous excitation to remain valid. FLIM is typically carried out using an Nd:YAG laser. Given a common excitation period for Nd:YAG lasers of 8 ns, for an excitation radius of 3 µm, the maximum speed is 1500 m/s for the assumption to be appropriate. Hence 18.8 m/s is the maximum resolvable speed. Finally, the Péclet number must remain above 100 as discussed in section 4.1. Combining equations (15) and (43), the Péclet number scales as $Pe_z \propto h_c \mu U$.

The film thickness scales as $h_c \propto (\mu U)^{0.67}$ such that $Pe_z \propto {h_c}^{2.49}$. Thus, if a lubricant is selected with a viscosity that creates a typical film thickness of 100 nm at the given velocity, the assumption of negligible diffusion remains appropriate. It is however likely that shear heating and shear thinning would take place at high speeds. The shear heating especially could further complicate the analysis, as the temperature distribution would be required to be known, or it would have to be approximately constant over the observation volume. Ultimately, these calculations show that FLIM exhibits a clear improvement compared to photobleached-fluorescence imaging in terms of temporal resolution, and could in theory probe the fastest of EHD contacts.

9.2 Fluorescence-lifetime imaging microscopy

Initially, a Guppy F-080 charge coupled device (CCD) was used (the author thanks Dr. Frank Beyrau for providing the Guppy CCD), which has a high speed electronic shutter capable of exposure times as low as 10 µs. The phosphorescent compound used was tris(dibenzoylmethane) mono(1,10-pheanthroline) europium(III), also labelled Eu(DBM)3Phen (Sigma-Aldrich UK). This phosphor is mainly excitable by UV light. A dye solution was formed by dissolving Eu(DBM)3Phen into acetone at a concentration of 0.1 mM and the solution was poured into a quartz cuvette. A green Orion (532 nm, 10 Hz, 5 ns pulse width) Nd:YAG laser (New Wave Research) was used to excite the fluorophore in the cuvette (see schematic in Fig. 83a), and the Guppy CCD was placed perpendicularly to observe the phosphorescent emission. The result for a power of 30 nJ and an exposure time of 20 µs, imaged at varying delays after excitation is shown in Fig. 83b-f. 10x synchronous averaging was used for the acquisition. It should be noted that the same experiment was repeated with rhodamine 6G, at a lower power and no significant emission was observed except for the case when the exposure time overlapped with the excitation. This shows that Eu(DBM)3Phen is indeed phosphorescent, and the intensity decays with time after excitation. It also confirms that the acquisition system is capable of FLIM. A closer study of the average intensity in the images showed that the decay could not be defined by a single exponential component as expected, but a double exponential fit was necessary. This could possibly be caused by the very high power used to excite the phosphors. The next step was

to carry out the same experiment with a focused laser beam through an objective. It was however quickly observed that when the excitation from the Nd:YAG laser was focused into the sample, using an objective, the fluid would consistently evaporate because of the increase in local power. This was recognized by the sound of bubbles bursting, coincidentally with the laser pulse. It was therefore decided that another excitation source should be used, due to the inefficient excitation of the UV-excitable dye using the green Nd:YAG laser.

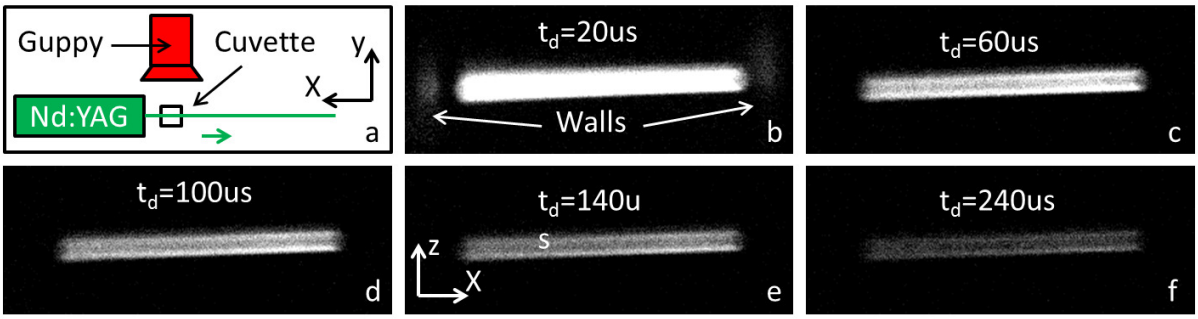


Fig. 83: a) Schematic of the optical setup. b-f) Intensity distributions of the fluorophore excited in the cuvette with varying delay times. White represents high intensity and black represents low intensity. The length scale is given by the distance between the cuvette walls indicated in (b), which is 10 mm.

A femtosecond laser (Spectra Physics Tsunami oscillator powered by a 5 W Millenia Pro laser) 800 nm source was frequency doubled to 400 nm using a beta barium borate (BBO) crystal. This created an effectively continuous beam of narrow UV-light, which could be used to efficiently excite the fluorophore. The power of the laser beam could be set in the range of 0.1-100 mw using density filters. An optical chopper system (Scitek 300CD with a custom made chopper disc) was used to control the duration of excitation in the range of 10-100 µs. The chopper used a photoelectric sensor to synchronize the acquisition system with the excitation. The chopped laser beam was directed into the microscope using a dichroic mirror, as described in subsection 2.1.3, with the exception of the EHD contact setup being replaced by a sample on top of the stage. The 10x objective was used in all cases. Using a maximum distance of 150 µm and a minimum cycle time of 10 µs, giving a total acquisition period of 160 µs, the maximum resolvable speed was about 1 m/s. The maximum speed for the assumption of instantaneous excitation to remain valid, for a beam radius of 3 µm, is $U = 1.2$ m/s. This shows that even without the Nd:YAG laser and an ICCD, FLIM still provides a major increase in temporal resolution.

Solutions of Eu-phen in dimethyl sulfoxide (DMSO) were prepared at a concentration of 1 mM. 100 µl of the solution was pipetted onto a glass slide and a cover slip was placed on top. The glass slide was placed on the microscope stage. The chopper was running at 27 Hz giving an excitation time of approximately 50 µs. Results for the temporal intensity response of Eu-phen, acquired with 50x synchronous averaging and excited with the 400 nm excitation at a power of 10 mW (on stage), are shown in Fig. 84a.

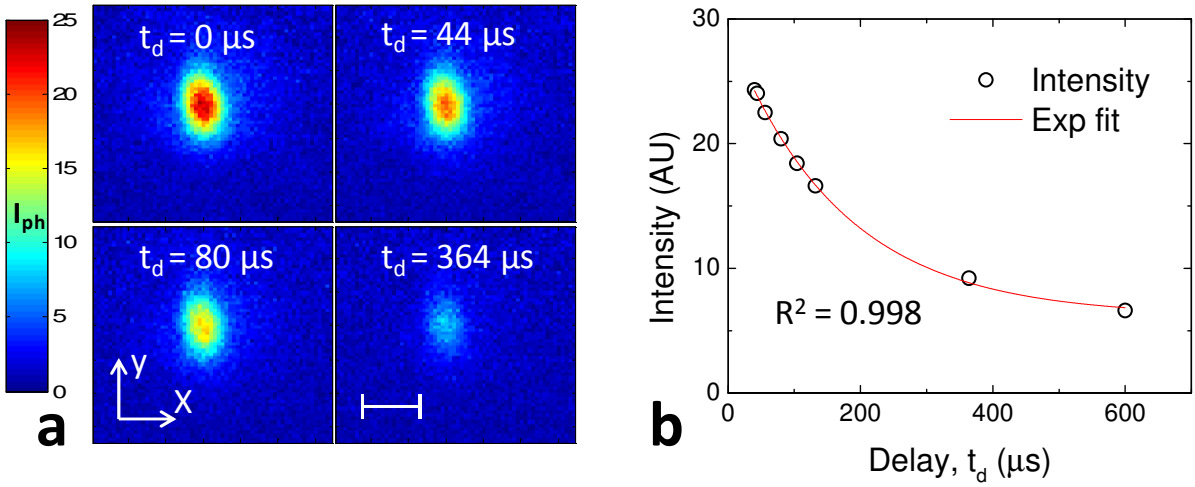


Fig. 84: a) Intensity distribution at various delay times, t_d, for phosphorescent solution between cover slip and glass slide. The scale bar is 20 µm in both directions. b) Mean intensity plotted against delay time for acquisition. The red line indicates a single component exponential fit to the data.

It is clear that the intensity decays with time. This is studied further by taking the mean intensity over a 3 pixel diameter circle, at the centre of the phosphorescent volume, presented in Fig. 84b. The fit shows that the temporal intensity response can be described by a single component exponential decay, with a lifetime, τ_{ph}, of 167 µs.

9.3 Proof of concept

Having shown that the acquisition system could be used for phosphorescence imaging, the technique was applied to a moving fluid, as a proof of concept, to show that high speed velocimetry could be performed using this system.

The Eu(DBM)3Phen/DMSO solution was placed in a plastic cylinder made of two petri dishes. This cylinder was attached to the shaft of the stepper motor and the bottom of the cylinder was situated on top of the stage, as shown in Fig. 85a. No surface adsorption of

Eu(DBM)3Phen on the petri dish could be observed. The use of the plastic cylinder as opposed to an EHD contact provides a substantial increase in signal due to the large volume of fluid and also eliminates issues of through-thickness diffusion, as the Péclet number increases with film thickness. The fluid was probed at a radial distance of 40 mm from the centre of the cylinder, and the thickness of fluid being probed was at least 5 mm. FLIM was applied as in the previous section, except for using synchronous averaging of 111x and a laser power of 100 mW. The excitation time remained 50 µs. The spatiotemporal intensity distribution at a frequency of 120 rpm (0.5 m/s), for various delay times, is displayed in Fig. 85b. In contrast to the results in Fig. 84a, the phosphorescent volume is now in motion, due to the rotation of the cylinder. The intensity drops drastically as the delay is increased, due to the phosphorescent decay of the phosphor. The intensity distribution is analysed by studying the distribution in the θ-direction (the direction of the flow), averaged in the r-direction, as shown in Fig. 85c. It is clear that the intensity distribution cannot be described well by a Gaussian fit (red line). This could possibly be caused by the invalidity of some of the assumptions made, such as the assumption of instantaneous excitation, which would break down at a velocity of 0.6 m/s. It could also be caused by the high power, which might induce photobleaching. Another contribution to the spread of the intensity distribution is the large thickness of fluid film (5 mm) being probed, as the excitation volume may no longer remain smaller than the depth of field.

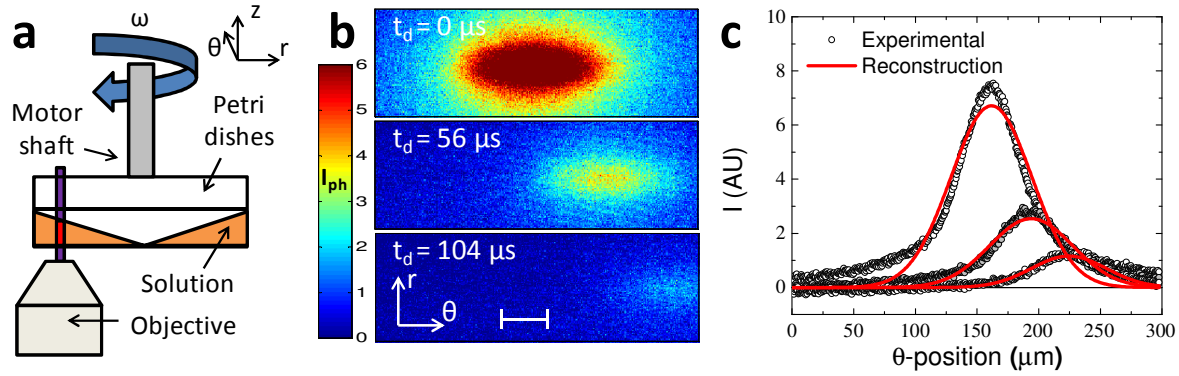


Fig. 85: a) Schematic of the system geometry. b) Intensity distribution of the phosphorescent volume at various delay times post excitation. The scale bar is 20 µm. c) Intensity distribution averaged in the y-direction for the three different delays. The red lines indicate Gaussian fits to the experimental data.

As the cylinder rotates at a constant velocity, the fluid velocity will reach an equilibrium at some point where the azimuthal velocity, $u_\theta = f(r, z)$, is approximately constant in the z direction. Thus the probed phosphorescent volume is expected to move as a plug. One property that can be extracted from the Gaussian fits in Fig. 85b is the central position of the intensity distribution, which for a plug flow can be used to determine the velocity of the fluid. The positions of the centres of the Gaussian fits are presented in Fig. 86a. The linear fits to the data show that the phosphorescent volume is moving at a constant average velocity. The initial position of the centres are different for the different speeds as the excitation time is too large, causing the Gaussian distribution to spread in the x-direction. The slopes of the data in Fig. 86a are compared to the theoretical value, assuming plug flow, in Fig. 86b. For the low speed the result is accurate, but this reduces as the speed is increased. This is not surprising, considering the non-instantaneous excitation and the non-Gaussian shape of the intensity distributions. Ultimately, this result demonstrates that phosphorescence imaging can be used for high speed velocity measurements, remarkably surpassing the temporal resolution of the photobleached-fluorescence imaging technique.

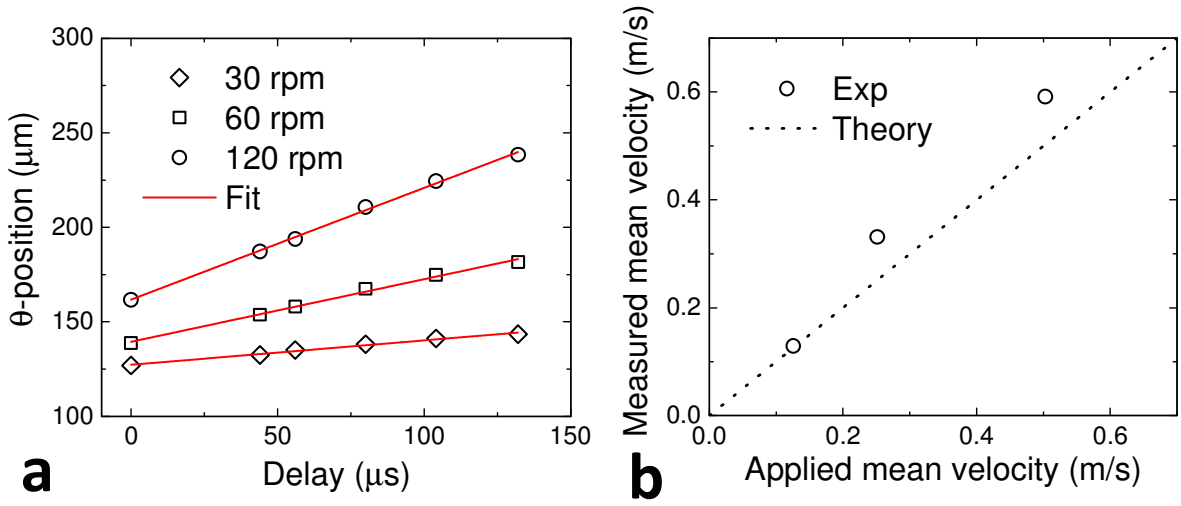


Fig. 86: a) Position of centre of the Gaussian fit plotted against delay time for three speeds. The red lines indicate linear fits to the data. b) The slope of the lines in (a) plotted against the theoretical value.

9.4 FLIM for practical EHD lubrication

Having confirmed that FLIM enables velocimetry with a temporal resolution superior to photobleached-fluorescence imaging for a macroscopic plug flow, the technique was applied

to a steel-glass EHD contact. Due to the reflective steel surface, interference will affect the experimental results. An Andor iStar 334T ICCD (Kindly lent by Amir Kadiric and Mourad Chennaoui from Imperial SKF university technology centre) was used for imaging. The ICCD works by using an image intensifier, which effectively multiplies photons through the use of advanced optics and electronics. The intensifier is placed in front of the CCD sensor, and it is turned on and off by circuitry, defining a gating period during which photons arrive at the CCD sensor. This enables extremely short exposure times, while still achieving acceptable signal. This device is capable of gating times in the nanosecond range. Furthermore, the gating enables thousands of sequences to be captured using one exposure (on chip integration), which greatly improves the signal to noise ratio, as shown in [141]. To provide a sufficient signal for the small EHD film, the concentration of the phosphor was increased. It was found that tetrahydrofuran (THF) was an excellent solvent for this purpose. 5 mM of Eu(DBM)3Phen was dissolved in THF. The THF solution was dissolved in polybutene H-300 at a volume ratio of 3:7, so that a sufficient EHD film would be created at speeds of the order of 100 mm/s.

The contact was observed using white light interferometry. At a speed of 10 mm/s the horseshoe region could be identified, indicating that the contact was in the EHD lubrication regime. This speed was however not sufficient to produce significant motion during the phosphorescent lifetime of the phosphorescent probe. At the higher speeds where FLIM was applied successfully the lubricant was in the transition between the EHD and the HD regime. In future work, the viscosity could be reduced to reach EHD conditions at higher speeds, by increasing the ratio of THF to H-300. Unfortunately the ICCD was only available for a single day so that this could not be performed. Another issue with the limited availability of the ICCD was that results were acquired prior to the consideration of the effects of interferometry (see subsection 2.3.7). Therefore the obtained results will not be completely representative of the lubricant flow, as interference is not taken into account. The effect of this should be minor however as the film is rather thick, given that the lubrication regime is close to hydrodynamic.

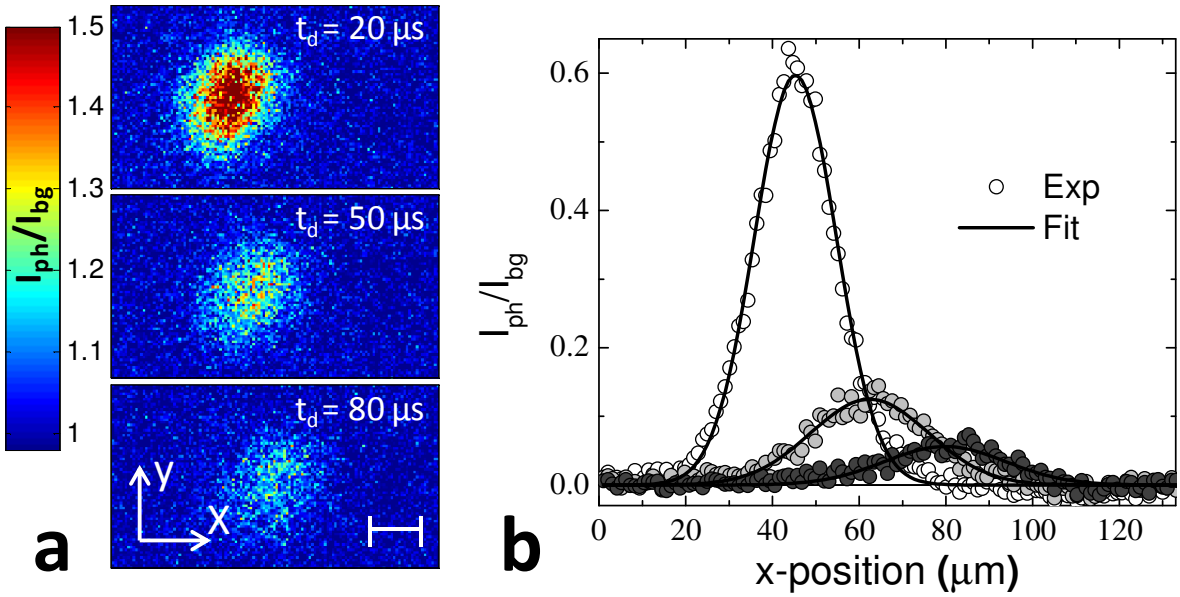


Fig. 87: a) Relative phosphorescence intensity distribution at three delay times. The scale bar is 20 µm in both directions. b) Intensity distributions averaged over 9 pixels in the y-direction (note that these are not the same times as in (a)). The solid lines indicate Gaussian fits to the data. Phosphorescent decay is not considered. The solution is 5 mM of Eu(DBM)3Phen dissolved in THF. The THF solution was then dissolved in polybutene H-300 at a volume ratio of 3:7. Load is 20 N (508 MPa). Speed is 360 mm/s. The film thickness is unknown.

The steel-glass EHD contact was imaged using the 20x objective with 2.5x optovar. The applied load was 20 N (508 MPa) and ball speeds of 120, 240 and 360 mm/s were used. The film thickness is unknown. The optical chopper was set to provide an excitation time of 20 µs using the 400 nm UV source (10 mW on stage). An exposure time of 0.5 s was used, resulting in approximately 100x on chip integration (similar to synchronous averaging). A sequence of 30 frames was captured where the delay was increased by 10 µs with each frame, starting from zero. A background image was taken at a delay of 1 ms, where the phosphorescence of the phosphor is negligible. The gating time was set to 10 µs, the intensifier gain was set to 600 and 4x4 binning was used. Results for the relative spatiotemporal intensity distribution, at a ball speed of 360 mm/s, are shown in Fig. 87a and the distribution averaged over 9 pixels in the y-direction is shown in Fig. 87b. It is clear that the excited volume is in motion. It is also clear that the flow is not Couette flow, as there is no uniform spreading of the intensity profile (see Fig. 57 for example). There could also possibly be slip as the back of the spot seems to move. The intensity drops with time due to the phosphorescence of the fluorophore as expected. As was done for the rotating cylinder,

the one-dimensional intensity distributions can be successfully fitted with a Gaussian distribution, as indicated by the solid lines in Fig. 87b, although the fit is now greatly improved.

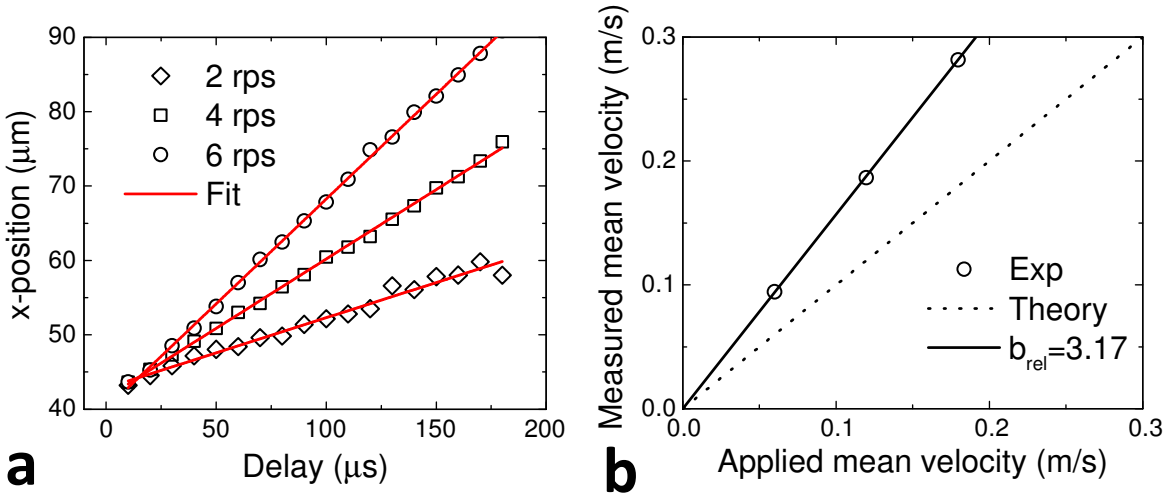


Fig. 88: a) Central position of Gaussian fit to the intensity distribution as a function of delay time for three different velocities. b) Measured average velocity plotted against the applied average velocity. The dotted line is the Couette solution and the solid line is a fit for Couette flow with a relative slip length of 3.17.

The displacement of the excited volume with time is shown in Fig. 88a. The linear fit (red line) to the data indicates that the volumes are moving at a constant velocity. This velocity can be compared with the applied velocity, as shown in Fig. 88b. It is clear that the lubricant is moving faster than Couette flow, as is seen directly in Fig. 87a. This could be caused by multiple reasons, such as slip, inhomogeneous shear, shear banding or temperature induced shear thinning. A fit of a constant relative slip of 3.17 can be made to the data, showing the potential inaccuracy involved when using mean velocity measurements to deduce the occurrence of slip.

The obtained data is not optimal for the velocity profile reconstruction scheme to be applied. The excited volume radius is large and the motion is relatively slow compared to the lifetime of the fluorophore. To account for the effect of the exponential decay of the intensity, the normalised relative intensity, I_N, for background ,I_{bg}, was defined as the ratio between the relative intensity, I_{ph}/I_{bg}, and the mean relative intensity, $\overline{I_{ph}/I_{bg}}$, given by

$$I_N(i,j,n) = {I_{ph}/I_{bg}}\Big/{\overline{I_{ph}/I_{bg}}} \tag{58}$$

This normalisation causes the total intensity to be constant for all frames. Naturally, the relative noise increases as the signal reduces in later frames.

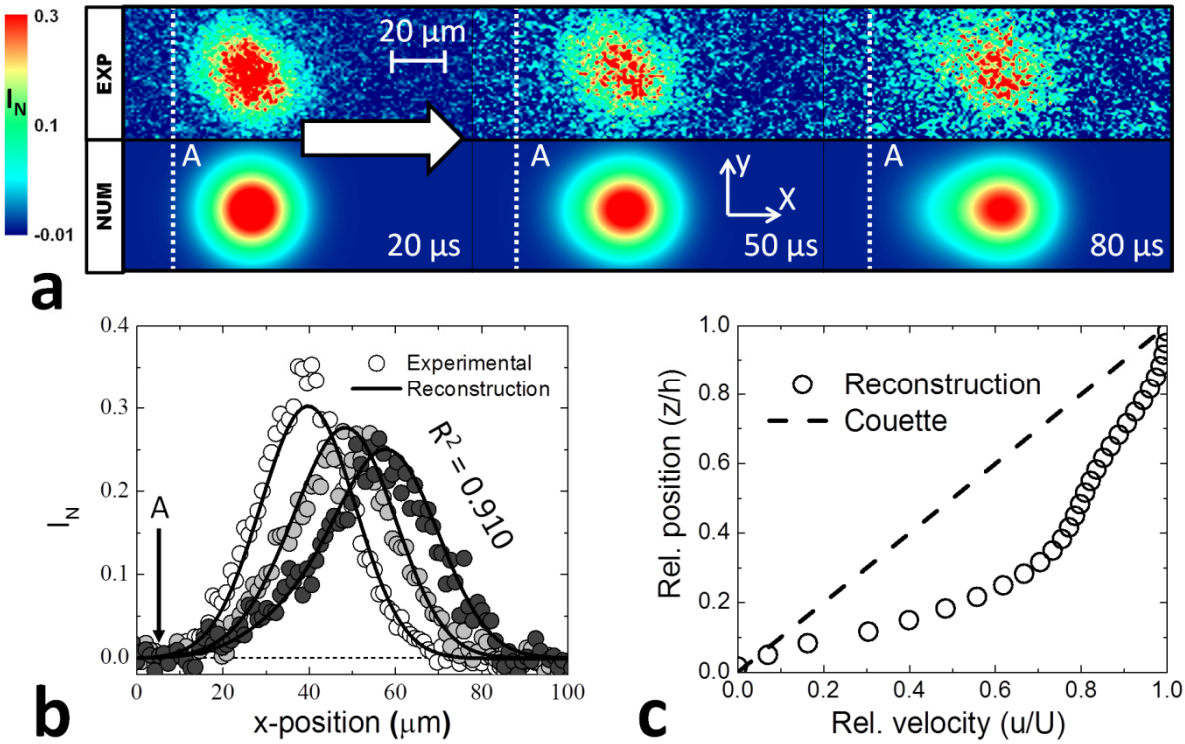


Fig. 89: a) Experimental (EXP) and numerical (NUM) spatiotemporal normalised relative intensity distributions at three times using data from Fig. 87a. The arrow indicates the direction of the flow. The dotted line A indicates the position of the back of the column. b) Averaged distributions from (a) with the point A indicating the back of the column. c) Reconstructed velocity profile and theoretical isothermal Couette velocity profile.

The experimental and reconstructed normalised relative intensity distribution for a ball speed of 0.36 m/s is shown in Fig. 89a. It is clear that the intensity distribution is fairly noisy compared to the results for photobleached-fluorescence imaging. This could be easily solved by optimizing the acquisition conditions such as gating time, exposure time and laser power. This becomes more important at larger delay times where the intensity drops significantly. The intensity distribution averaged in the y-direction is presented in Fig. 89b. There is agreement between the experimental and reconstructed data, although the noise is fairly large as indicated by the coefficient of determination. Despite the noise, a reconstruction of the velocity profile could be made, as shown in Fig. 89c. The inadequate

agreement between the reconstructed and the experimental data (shown in Fig. 89b) makes the accuracy of the reconstruction debatable, although it is apparent that the flow is not Couette flow (Fig. 89c). Furthermore, no significant interfacial slip can be observed. It does not seem as though the 20 N (508 MPa) contact in this chapter produces a plug flow. The difference could possibly be caused by an increase of the critical pressure for complete solidification, due to the reduction in viscosity of the lubricant, or by the significant increase in shear rate experienced by the lubricant. Furthermore, due to the significant noise, the velocity profile cannot currently be used to conclude if there is slip, or if there is a low viscosity layer near the lubricant-glass interface. Such a layer can appear if there is a significant temperature gradient in the lubricant [48], which could be induced by the different thermal properties of the bounding surfaces. A brief calculation using equation (33) shows that the temperature increase in the lubricant under the experimental conditions would be of the order of 20 °C, an increase which would significantly alter the viscosity of the lubricant. This effect could readily be investigated by altering the interfacial properties, and observing whether or not the velocity profile remains unaltered. The reconstructed velocity profile could also be produced if the Poiseuille component of the flow becomes significant [116], although this should not occur at the centre of the contact where the pressure gradient is small. It should be noted that the result for 0.24 m/s was similar, while the result for 0.12 m/s was difficult to analyse due to the limited motion.

A rudimentary implementation of FLIM was applied to a contact in the transition between the EHD and HD lubrication regimes. Due to the limited availability of the ICCD, only a few experiments could be performed, yielding initially inconclusive but promising results. It remains unknown whether shear banding and slip also exist in high speed-low viscosity contacts. It is consequently necessary to perform a study where the velocity, viscosity and load are varied for a low viscosity lubricant. Although a lower viscosity lubricant was used here, the viscosity modifier was still H-300, which was already studied using photobleached-fluorescence imaging. It would be interesting to explore other combinations of lubricants such as solutions phosphor solutions of THF or DMSO in alkanes, silicones and aqueous lubricants, to study the effects of chemistry on the velocity profile and lubricant rheology.

While the implementation of FLIM for EHD is far from extensive, it clearly shows the feasibility of the approach. The issues of low signal and a large excitation volume can be alleviated by careful choice and tuning of the optical setup and the acquisition system, making FLIM the optimal candidate for high speed velocimetry in EHD contacts. The greatest drawback of the photobleached-fluorescence imaging technique was the low temporal resolution and the restriction to a specific lubricant-fluorophore system. Ultimately, the application of FLIM to EHD contacts extends the developed method of velocity profile reconstruction by molecular tagging, to a greater range of lubricants and viscosities. This enables the direct study of phenomena such as limiting shear stress behaviour and slip of liquids at high pressures as well as the research of how these phenomena are related to the rheology and chemistry of lubricants.

9.5 Summary

The photobleached-fluorescence imaging velocimetry technique allows the through-thickness velocity profile of a lubricant in EHD lubrication to be obtained, by tagging the fluorescently doped lubricant with photobleaching. The requirement of a high relative photobleaching rate leads to the requirement of low entrainment speeds, which in turn demands high viscosity lubricants. While interesting phenomena have been observed for the model system of polybutene, only one system has been found so far, providing a sufficient photobleaching rate.

An alternative technique, which alleviates most of these issues, has been suggested. Fluorescence lifetime imaging (FLIM) involves the use of a short laser pulse to excite a dye. Emission of dyes occurs over time. Phosphors in particular have long-lifetime emission (order of µs). Hence, the laser pulse can be used to tag the fluid into which phosphors have been dissolved. Molecular tagging with FLIM is achieved simply by excitation of a phosphor, rather than photobleaching, which is an inefficient process. Therefore it is much more suited to high speed EHD experiments. A brief analysis was carried out to determine the applicability of the developed reconstruction scheme for much higher speeds than in this work. It was shown that the Péclet number is proportional to the square of the film

thickness, causing flows to remain advective even at high speeds. Not only does FLIM enable high speed velocimetry but a large range of phosphors are available so that lubricants other than polybutene could potentially be studied.

A model solution, consisting of the phosphor Eu(DBM)3Phen dissolved in acetone, was chosen to evaluate the potential of FLIM for velocimetry. It was initially shown that the long-lifetime phosphorescence of the phosphor could be imaged using the newly designed optical setup, and that the decay of the emission was exponential as expected. A proof of concept was carried out, by putting the solution in a transparent cylinder, which rotated at high speeds (0.1-0.5 m/s). It was shown that the flow of the model solution could be measured using FLIM.

A brief study of FLIM for EHD lubrication was then carried out. Eu(DBM)3Phen was dissolved in a mixture of polybutene and THF. The mixture had significantly lower viscosity than that of polybutene. FLIM measurements were performed at speeds up to 0.36 m/s in the centre of an EHD contact. The mean velocity of the solution could be determined by applying Gaussian fits to the intensity distribution and it was shown to be approximately 30 % larger than expected.

The FLIM data was used to determine the velocity profile of the solution by applying the previously developed reconstruction scheme. The profile did not appear to be Couette flow and no slip was observed. Rather, it had a similar but larger positive curvature to that observed for polybutene in the liquid regime. These results were only preliminary and more work would be necessary to accurately establish the velocity profile of the solution. Nevertheless, the results do show that high speed velocimetry in EHD lubrication is possible through the use of FLIM.

The use of FLIM in EHD velocimetry has great potential as the technique does not possess most of the limitations of photobleached-fluorescence imaging velocimetry. High speeds can be studied, the signal is not bound by relative fluorescence intensities, and a larger selection of dyes are available, enabling the study of more engineering relevant lower viscosity

lubricants. Clearly the availability of a tool to directly measure the flow of lubricant would be useful for future developments in EHD lubrication.

10 Conclusions

10.1 Summary of main findings

Lubricants in tribological contacts are exposed to severe stresses due to high shear rates and extreme viscosities induced by large pressures. Numerous models and experimental methods have been developed to describe and evaluate the physical properties of lubricants at these conditions, providing constitutive relationships for pressure, viscosity and shear stress. The flow of the lubricant, a property which is very much related to the lubricant rheology, has however mostly been neglected in these studies. The flow is typically considered to take the shape of a linear distribution between the velocities of two rubbing surfaces, as defined by the Reynolds equation. Given the lack of experimental data for this flow, a molecular tagging velocimetry technique using photobleached-fluorescence imaging was developed.

Photobleached-fluorescence imaging velocimetry relies on the fluorescence phenomenon of photobleaching, to selectively tag a small volume within the film of an elastohydrodynamic contact. The motion of the tagged volume is directly related to the flow of the lubricant, and can thus be used to deduce this flow. Optical and acquisition setups were designed to implement this technique, and the successful tagging of a photobleached volume was demonstrated. Nile red was chosen as the fluorescent dye and polybutene, a highly viscous oligomer, was chosen as the lubricant. The dye-lubricant system had a high photobleaching rate which was essential for the application of the technique. Polybutene was interesting as it was expected to undergo a glass transition once a critical pressure was reached, which could be induced by the pressure in a contact. Given the unique possibility of studying flows in elastohydrodynamic contacts, it was also decided to study the mechanisms of boundary slip, which was to be promoted using a low surface energy fluoroalkyl coating. A rig was designed to create the elastohydrodynamic contact, by loading a glass sphere onto a microscope glass slide, and entraining polybutene by the rotation of the sphere. The glass-glass contact was chosen due to the transparent surfaces, which avoided issues related to interference. The contact was shown to be stable in terms of position, fluorescence intensity and velocity, all of which were critical for the use of photobleached-fluorescence imaging

velocimetry. Fluorescence was used to study the dynamics of squeeze films formed by polybutene in the elastohydrodynamic contact. Results showed that the non-dimensional time constant for the decay of the squeeze film thickness increased once a sufficient pressure was reached, which indicated the potential glass transition of polybutene.

The film thickness in a steel-glass contact was studied using interferometry, enabling the determination of the pressure-viscosity coefficient of polybutene, which was shown to agree with values in literature. It was shown that anomalous film thicknesses would appear at high pressures and high speeds. The film thickness was also studied by laser-induced fluorescence for glass-glass-contacts. Again, at low pressure the commonly observed constant elastohydrodynamic film thickness with a horseshoe shape towards the outlet was observed, while anomalous film thicknesses appeared at higher pressures. For the low surface energy coated (Fusso) glass slide, no difference in film thickness obtained in a glass-glass and glass-Fusso contact could be observed at low pressures. However, at larger pressures a 40 % reduction in the film thickness could be observed in a glass-Fusso contact, indicating the existence of boundary slip. Furthermore, it was shown that the presence of the low surface energy coating prevented the appearance of an anomalous dimple at very large pressures, suggesting that (1) the observed dimple was not induced by a change in fluorescence of the dye due to the large pressures, and (2) the observed dimple for the uncoated case was likely caused by shearing of the lubricant. To shed light on these observed phenomena, the flow of polybutene was directly studied, which required the development of an analytical model to deduce the velocity profile using the motion of a tagged photobleached volume.

The Péclet number for flows in the elastohydrodynamic contact was evaluated, showing that a necessary assumption of pure advection was appropriate. This enabled the flow within the elastohydrodynamic contact to be modelled as the parallel flow of infinitesimal layers, which in turn enabled the simulation of the spatiotemporal intensity distribution based on a known velocity profile. Thus a reconstruction scheme was developed where the unknown velocity profile was continually iterated until the simulated spatiotemporal intensity distribution matched that of the experimental spatiotemporal intensity distribution, obtained from the photobleached-fluorescence imaging. Simulations showed that the reconstruction scheme was

able to accurately determine velocity profiles in the case of pressure driven (quadratic) and shear-driven (linear) flows. More exotic flows, which have been supported by some experimental evidence, such as inhomogeneous shear and shear banding, were also resolvable although with limitations on their maximum relative shear rates. The reconstruction of profiles with boundary slip was also shown to be accurate, although this necessitated the use of an alternative reconstruction scheme, which constrained the shape of the flow profiles.

The technique and reconstruction scheme were validated experimentally by studying the shear driven flow of polybutene between parallel glass slides and in a soft-elastohydrodynamic contact, where pressures were low. It was shown that the velocity profile was linear in both cases, as predicted by the Reynolds equation, confirming the validity of the developed technique and analytical model. This enabled the measurement of velocity profiles in elastohydrodynamic contacts. Four main flow types could be observed. In the soft-elastohydrodynamic contact, the flow profile was linear. In the glass-glass contact, at low pressure, the velocity profile was mostly linear, although the flow was slightly faster in the centre of the film thickness. At high pressures, it was shown that the velocity profile separated into three layers, comprised of a low shear rate plug in the centre of the film thickness, accompanied by two high shear rate layers adjacent to the interfaces. When the low surface energy coating was applied, the velocity profile was shown to exhibit substantial interfacial slip. The three anomalous flows were studied in more detail by varying experimental parameters.

Results at low pressure, where the polybutene was still expected to be a liquid, showed that a slight bump of accelerated flow appeared about the centre of the film thickness. Under no conditions could boundary slip be identified at either of the surfaces. By studying multiple combinations of load and speed, it was shown that minor variations in the bump could be observed, although no significant relationship could be established. Spatial mapping of the flow showed that the bump grew larger towards the inlet of the contact. The curvature of the velocity profile was unlikely to be caused by an increase in temperature, as thermal analysis showed that such a temperature rise due to shear heating or photobleaching was improbable. The idea of pressure driven flow was also rejected as the pressure gradient

would be negligible at the centre of the contact, and the bump should have been protruding in the opposite direction at the inlet of the contact. The relationship between viscosity and molecular weight showed that the polybutene was entangled, although this fact could not be used to explain the accelerated flow.

At high pressures, the velocity profile of polybutene separated into three regions of varying shear rates. In the centre of the film, a thick (comprising most of the film thickness) low shear rate plug formed, while thin layers of high shear rate appeared at the surfaces. This is an example of inhomogeneous shear which has been observed for heterogeneous fluids and glasses at ambient pressure. The relative shear rate of the plug was shown to decrease with pressure, indicating that the glass transition may be a second order phase transition, which was consistent with the squeeze film study. It was shown that the speed had a mostly negligible effect on the profile, although results indicated the possibility of a nanoscopic film adhering to the surfaces. It was shown that the central shear rate also varied with position. Comparison with film thickness measurements indicated that plug formation only occurred in the dimple zone, suggesting that the formations of plug and dimple were related. The critical pressure for plug flow was shown to be dependent on the molecular weight of the polybutene, in agreement with the concept of a glass transition viscosity.

Application of the low surface energy coating showed that boundary slip could be observed and that it was pressure dependent. This was explained in terms of a rise in shear stress due to the pressure-induced increase in viscosity. A power law was use to relate the pressure to the slip length, whereas speed was shown to have a negligible effect. Consistent with the relationship between pressure and slip length, the slip was shown to depend on position in the contact. The power law relationship could be used to predict the spatial distribution with some success. Discrepancies were believed to be caused by an incorrect description of the pressure distribution.

Friction measurements revealed no abrupt change in the friction coefficient when the critical pressure, corresponding to the initiation of plug flow, was reached. This suggested that the process does not influence the shear stress, which meant that the viscosity must vary

through the film thickness to accommodate variations in shear rate. The boundary slip observed for the low surface energy coating was shown to have a large effect on the friction coefficient, and the reduction in friction could be as large as 70 % depending on the applied load and speed. Using the determined rheology of polybutene, the reduction in friction due to boundary slip was estimated. While the general trend of an increase in friction reduction with pressure was observed, the calculation was underestimated by a factor of two, suggesting that the calculation of stress due to boundary slip is not straightforward.

An alternative molecular tagging velocimetry technique, fluorescence lifetime imaging, was suggested to potentially alleviate some of the limitations of photobleached-fluorescence imaging velocimetry. If successfully implemented, the technique would result in orders of magnitude increase in temporal resolution, enabling the study of practical lubricants for elastohydrodynamic lubrication. Furthermore the range of suitable dyes would be widened. A feasibility study was carried out showing that the temporal decay of the phosphorescence of the dye could be imaged. A model setup with phosphorescent solution rotating in a cylinder was used to show that the lifetime imaging could be used to determine the velocity of the solution. Finally, a proof of concept was performed in an EHD contact. While the initial results were limited in terms of accuracy, it was shown that it was indeed possible to use the technique to measure the velocity profile of a lower viscosity lubricant up to speeds of 0.36 m/s.

10.2 Limitations

The results presented in this thesis represent the first velocity profile measurements in elastohydrodynamic lubrication, acquired using a new implementation of photobleached-fluorescence imaging velocimetry. As the implementation of the technique is new, there are several limitations which could potentially be relaxed in future work.

The spatial (x-y) resolution was approximately 30 µm in the x-direction and about 3 µm in the y-direction. This limitation was imposed by the optical setup, such that these values could be reduced marginally with improved optics. The size of the polybutene molecules imposed an approximate through-thickness resolution of 4 nm, while the reconstruction

scheme resolved the velocity profile to within 10 % of the film thickness. The limited z-resolution makes it difficult to study nanoscopic high shear rate films adjacent to the rubbing surfaces, which have been suggested to exist in both plug and slip flows. The determination of slip lengths was fairly accurate (5 %). However, at high relative slip velocities, an uncertainty of 5 % is relatively large in terms of determining the shear rate, which complicates friction calculations for boundary slip.

Several restrictions are imposed by assumptions used for modelling of the flow, including constant film thickness and pure advection. This limits application of the technique to circumstances where the assumptions hold. The requirement of transparent surfaces also limits the application in terms of engineering relevance, as transparent materials are not typically used.

The main limitation of the developed technique is the temporal resolution, which at the fastest speed is limited to about 20 ms. This means that the technique is better suited for highly viscous lubricants. Furthermore, temporal variations in flow cannot be resolved due to the use of synchronous averaging, which occurs over a minimum of about 30 s. Not only does the temporal resolution limit applicable viscosities, it also imposes a minimum on the photobleaching rate of the model system tested. At the time of this research, only a single dye-lubricant system could be found with a sufficient photobleaching rate. Clearly, the ability to study multiple lubricants is essential in establishing the effects of flow on the tribology of EHD lubrication and to establish the universality of the phenomena observed in this work.

It should be mentioned that all experiments were carried out in pure sliding conditions, severely limiting the range of shear rates studied. For the friction measurements, this required an extrapolation for friction predictions in the presence of boundary slip.

It is apparent that the limitations of the current implementation of the photobleached-fluorescence imaging velocimetry provide an opportunity for future work to extend the applicability and accuracy of velocity measurements in elastohydrodynamic lubrication.

10.3 Future work

The optical setup used in this work can be optimized in a number of ways. Higher numerical aperture objectives can be used to improve the resolution of the technique. This could potentially be even further optimized by implementing sub-diffraction limit techniques such as stimulated emission depletion.

The modelling of the lubricant flow, used for reconstructing the velocity profile, could be enhanced. Assumptions of constant film thickness and pure advection were used to simplify the analysis, but by coupling the reconstruction scheme with finite element simulations, these assumptions could potentially be relaxed. This would enable the study of a larger range of geometries and systems, including the anomalous film thickness in the dimple and very thin films, where diffusion would be prevalent. Two-dimensional flow could also be considered, as it was shown to exist in the EHD contact. This would enable the three-dimensional mapping of flow in the contact.

The technique was validated using a parallel plate setup and a soft-EHD contact, where pressure-induced effects were expected to be minimal. It would be useful to use a second velocimetry technique to confirm the velocity profiles observed for EHD lubrication in this work. It was discussed that molecular tagging velocimetry was the optimal candidate for EHD lubrication velocimetry. While other techniques may not be able to completely resolve the through-thickness velocity profile, the distinct responses of plug flow and slip should still be observable. Thus it would be interesting to study the flow of small particles that can be tracked individually, such as quantum dots or fluorescent nanoparticles, in an EHD contact. The distribution of measured velocities would be related to the velocity profile of the lubricant, and would thus be useful for validating results measured using photobleached-fluorescence imaging velocimetry.

A key implementation required to improve the study of lubricant rheology in EHD lubrication is the ability to vary the slide-roll ratio. The glass slides used in this work could be replaced by a rotating glass disc. This would enable the fixing of the entrainment speed, and thus the film thickness, allowing the application of lower shear rates. A study where the

shear rate is varied for a constant film thickness would enable the determination of a critical combination of shear rate and pressure required for the formation of plug flow. It would also be helpful in studying the effect of shear rate on slip, which is likely to be pronounced due to the relationship between shear stress and slip length.

A natural progression of this work is the extension to velocimetry for EHD lubrication at conditions with engineering relevance, where it is necessary to identify if the phenomena observed in this work apply. The pathway to such a study has been laid by the application of FLIM for practical EHD lubrication. FLIM for velocity profile measurements in EHD lubrication should be applied to multiple phosphor-lubricant systems to determine the accuracy of EHD theory for a wide range of experimental conditions. It is likely that phenomena such as inhomogeneous shear, shear banding and slip can be identified. The determination of the correlation between film thickness, friction and flow measurements will be useful for elucidating a number of anomalous observations that have been made in EHD lubrication.

10.4 Implications of results

The main finding in this work is the invalidity of the assumptions of a linear velocity profile and spatial homogeneity, which are commonly used in the modelling of EHD lubrication. These assumptions are central in a number of methods used to predict film thickness and friction in tribological contacts, and thus their invalidation may affect the interpretation of data in tribological studies.

Experimental determination of lubricant rheology typically uses the assumption of a linear velocity profile. The invalidation of this assumption implies that the determined rheology is incorrect. While this does not necessarily affect friction prediction, due to the fact that the friction prediction is inherently based on friction measurements, descriptions of the state of lubricant, in terms of shear stress and shear rate, may potentially be inaccurate.

Rheological effects such as shear thinning and the limiting shear stress may very well be related to lubricant flow. It has been suggested that the lubricant may either slip or flow as a plug to accommodate the limiting shear stress, and slip and plug flows have been identified

in this work. Thus the application of the developed velocimetry technique may prove useful in seeking the origin of phenomena related to lubricant rheology.

In all of the identified flows, it was shown that spatial variations were present. Except in certain simulation studies, such spatial variations are commonly neglected. Any study involving the distribution or transport of physical properties would clearly be affected by the existence of spatial variations, indicating that spatial distributions may require more consideration than is generally given.

The technique of photobleached-fluorescence imaging velocimetry has been developed, which enables the study of flows in EHD lubrication. Particularly with the extension to general lubrication by FLIM, molecular tagging velocimetry provides a unique opportunity to verify and study a number of phenomena that have been proposed to exist in lubrication, such as the existence of inhomogeneous shear, shear banding and slip. Such studies would aid in the elucidation of the effect of lubricant rheology on film thickness and friction in EHD lubrication.

References

[1] Jacobson, B.: The Stribeck memorial lecture. Tribol. Int. 36, 781–789 (2003)

[2] Johnson, K. L.: Contact mechanics. Cambridge University Press (1985)

[3] Barus, C.: Isothermals, isopiestics and isometrics relative to viscosity. Am. J. Sci. 45, 87–96 (1893)

[4] Roelands, C.: Correlational aspects of the viscosity-temperature-pressure relationship of lubricating oils. PhD Thesis, Technische Hogeschool te Delft (1966)

[5] Bair, S., Kottke, P.: Pressure-Viscosity Relationships for Elastohydrodynamics. Tribol. Trans. 46, 289–295 (2003)

[6] Olver, A. V, Spikes, H. A.: Prediction of traction in elastohydrodynamic lubrication. Proc. Inst. Mech. Eng., Part J 212, 321–332 (1998)

[7] Echavarri Otero, J., Lafont Morgado, P., Chacon Tanarro, E., De la Guerra Ochoa, E., Diaz Lantada, a., Munoz-Guijosa, J. M., Munoz Sanz, J. L.: Analytical model for predicting the friction coefficient in point contacts with thermal elastohydrodynamic lubrication. Proc. Inst. Mech. Eng., Part J 225, 181–191 (2011)

[8] Bair, S.: The shear rheology of thin compressed liquid films. Proc. Inst. Mech. Eng., Part J 216, 1–17 (2002)

[9] Hatzikiriakos, S. G.: Wall slip of molten polymers. Prog. Polym. Sci. 37, 624–643 (2012)

[10] Cuenca, A., Bodiguel, H.: Submicron Flow of Polymer Solutions: Slippage Reduction due to Confinement. Phys. Rev. Lett. 110, 108304 (2013)

[11] Erdemir, A.: Rolling-contact fatigue and wear resistance of hard coatings on bearing-steel substrates. Surf. Coat. Technol. 54-55, 482–489 (1992)

[12] Bair, S.: The high-pressure, high-shear stress rheology of a polybutene. J. Non-Newtonian Fluid Mech. 97, 53–65 (2001)

[13] Spikes, H., Anghel, V., Glovnea, R.: Measurement of the rheology of lubricant films within elastohydrodynamic contacts. Tribol. Lett. 17 (2004)

[14] Bair, S., Qureshi, F., Winer, W. O.: Observations of Shear Localization in Liquid Lubricants Under Pressure. J. Tribol. 115, 507 (1993)

[15] Evans, C., Johnson, K.: The rheological properties of elastohydrodynamic lubricants. Proc. Inst. Mech. Eng., Part C 200, 303–312 (1986)

[16] Eyring, H.: Viscosity, Plasticity, and Diffusion as Examples of Absolute Reaction Rates. J. Chem. Phys. 4, 283 (1936)

[17] Bair, S., Qureshi, F., Khonsari, M.: Adiabatic Shear Localization in a Liquid Lubricant Under Pressure. J. Tribol. 116, 705 (1994)

[18] Bair, S.: Measurements of real non-Newtonian response for liquid lubricants under moderate pressures. Proc. Inst. Mech. Eng., Part J 215, 223–233 (2001)

[19] Bair, S.: Pressure-Viscosity Behavior of Lubricants to 1.4 GPa and Its Relation to EHD Traction. Tribol. Trans. 43, 91–99 (2000)

[20] Workel, M. F., Dowson, D., Ehret, P., Taylor, C. M.: Design and development of a ball impact apparatus for the direct measurement of lubricant friction under high pressures and shear rates. Proc. Inst. Mech. Eng., Part J 215, 211–222 (2001)

[21] Höglund, E.: The relationship between lubricant shear strength and chemical composition of the base oil. Wear 130, 213–224 (1989)

[22] Reddyhoff, T., Spikes, H. a, Olver, a V: Improved infrared temperature mapping of elastohydrodynamic contacts. Proc. Inst. Mech. Eng., Part J 223, 1165–1177 (2009)

[23] Klein, J., Kumacheva, E.: Simple liquids confined to molecularly thin layers. I. Confinement-induced liquid-to-solid phase transitions. J. Chem. Phys. 108, 6996 (1998)

[24] Wong, J. S. S., Hong, L., Bae, S. C., Granick, S.: Fluorescence recovery after photobleaching measurements of polymers in a surface forces apparatus. J. Polym. Sci. Part B: Polym. Phys. 48, 2582–2588 (2010)

[25] Guo, F., Wong, P. L., Geng, M., Kaneta, M.: Occurrence of Wall Slip in Elastohydrodynamic Lubrication Contacts. Tribol. Lett. 34, 103–111 (2009)

[26] Yamamoto, T., Sawa, K., Mori, K.: Velocity measurements for shear flows of CTAB/NaSal aqueous solutions between parallel plates. J. Rheol. 53, 1347 (2009)

[27] Bertola, V., Bertrand, F., Tabuteau, H., Bonn, D., Coussot, P.: Wall slip and yielding in pasty materials. J. Rheol. 47, 1211 (2003)

[28] Bécu, L., Manneville, S., Colin, A.: Yielding and Flow in Adhesive and Nonadhesive Concentrated Emulsions. Phys. Rev. Lett. 96, 138302 (2006)

[29] Ponjavic, A., Chennaoui, M., Wong, J. S. S.: Through-Thickness Velocity Profile Measurements in an Elastohydrodynamic Contact. Tribol. Lett. 50, 261–277 (2013)

[30] Gohar, R.: Elastohydrodynamics. World Scientific Publishing Company (2001)

[31] Reddyhoff, T., Choo, J. H., Spikes, H. a., Glovnea, R. P.: Lubricant Flow in an Elastohydrodynamic Contact Using Fluorescence. Tribol. Lett. 38, 207–215 (2010)

[32] Hartinger, M., Dumont, M.-L., Ioannides, S., Gosman, D., Spikes, H.: CFD Modeling of a Thermal and Shear-Thinning Elastohydrodynamic Line Contact. J. Tribol. 130, 041503 (2008)

[33] Larsson, R., Andersson, O.: Lubricant thermal conductivity and heat capacity under high pressure. Proc. Inst. Mech. Eng., Part J 214, 337–342 (2000)

[34] Ohno, N., Kuwano, N., Hirano, F.: Bulk Modulus of Solidified Oil at High Pressure as Predominant Factor Affecting Life of Thrust Ball Bearings. Tribol. Trans. 38, 285–292 (1995)

[35] Bair, S., Jarzynski, J., Winer, W. O.: The temperature, pressure and time dependence of lubricant viscosity. Tribol. Int. 34, 461–468 (2001)

[36] Choo, J. H., Spikes, H. a., Ratoi, M., Glovnea, R., Forrest, A.: Friction reduction in low-load hydrodynamic lubrication with a hydrophobic surface. Tribol. Int. 40, 154–159 (2007)

[37] Spikes, H. a: The half-wetted bearing. Part 1: extended Reynolds equation. Proc. Inst. Mech. Eng., Part J 217, 1–14 (2003)

[38] Guo, F., Li, X. M., Wong, P. L.: A novel approach to measure slip-length of thin lubricant films under high pressures. Tribol. Int. 46, 22–29 (2011)

[39] Fu, Z., Guo, F., Wong, P. L.: Friction-speed characteristics of elastohydrodynamically lubricated contacts with anomalous film shapes. Proc. Inst. Mech. Eng., Part J 226, 81–86 (2011)

[40] Guo, F., Wong, P. L.: An Anomalous Elastohydrodynamic Lubrication Film: Inlet Dimple. J. Tribol. 127, 425 (2005)

[41] Katgert, G., Möbius, M., Van Hecke, M.: Rate Dependence and Role of Disorder in Linearly Sheared Two-Dimensional Foams. Phys. Rev. Lett. 101, 3–6 (2008)

[42] Tapadia, P., Wang, S. Q.: Direct Visualization of Continuous Simple Shear in Non-Newtonian Polymeric Fluids. Phys. Rev. Lett. 96, 1–4 (2006)

[43] Picard, G., Ajdari, A., Bocquet, L., Lequeux, F.: Simple model for heterogeneous flows of yield stress fluids. Phys. Rev. E 66, 1–12 (2002)

[44] Mokshin, A. V., Barrat, J.-L.: Shear-induced crystallization of an amorphous system. Phys. Rev. E 77, 021505 (2008)

[45] Ehret, P., Dowson, D., Taylor, C. M.: On lubricant transport conditions in elastohydrodynamic conjuctions. Proc. R. Soc. Lond. A 454, 763–787 (1998)

[46] Meurisse, M.-H., Morales Espejel, G.: Reynolds equation, apparent slip, and viscous friction in a three-layered fluid film. Proc. Inst. Mech. Eng., Part J 222, 369–380 (2008)

[47] Chang, L.: On the Shear Bands and Shear Localizations in Elastohydrodynamic Lubrication Films. J. Tribol. 127, 245 (2005)

[48] Kaneta, M., Yang, P.: Effects of the thermal conductivity of contact materials on elastohydrodynamic lubrication characteristics. Proc. Inst. Mech. Eng., Part C 224, 2577–2587 (2010)

[49] Heyes, D. M., Smith, E. R., Dini, D., Spikes, H. a, Zaki, T. A.: Pressure dependence of confined liquid behavior subjected to boundary-driven shear. J. Chem. Phys. 136, 134705 (2012)

[50] Besseling, R., Isa, L., Ballesta, P., Petekidis, G., Cates, M. E., Poon, W. C. K.: Shear Banding and Flow-Concentration Coupling in Colloidal Glasses. Phys. Rev. Lett. 105, 268301 (2010)

[51] Boukany, P., Wang, S.: of particle-tracking velocimetry and flow birefringence to study nonlinear flow behavior of entangled wormlike micellar solution: From wall slip, bulk disentanglement to. Macromolecules , 1455–1464 (2008)

[52] Schall, P., Van Hecke, M.: Shear Bands in Matter with Granularity. Annu. Rev. Fluid Mech. 42, 67–88 (2010)

[53] Adams, J. M., Olmsted, P. D.: Nonmonotonic Models are Not Necessary to Obtain Shear Banding Phenomena in Entangled Polymer Solutions. Phys. Rev. Lett. 102, 067801 (2009)

[54] Lindken, R., Rossi, M., Grosse, S., Westerweel, J.: Micro-Particle Image Velocimetry (microPIV): recent developments, applications, and guidelines. Lab Chip 9, 2551–67 (2009)

[55] Mosier, B. P., Molho, J. I., Santiago, J. G.: Photobleached-fluorescence imaging of microflows. Exp. Fluids 33, 545–554 (2002)

[56] Stier, B., Koochesfahani, M. M.: Molecular Tagging Velocimetry (MTV) measurements in gas phase flows. Exp. Fluids 26, 297–304 (1999)

[57] Herr, A. E., Molho, J. I., Santiago, J. G., Mungal, M. G., Kenny, T. W., Garguilo, M. G.: Electroosmotic Capillary Flow with Nonuniform Zeta Potential. Anal. Chem. 72, 1053–1057 (2000)

[58] Mair, R. W., Callaghan, P. T.: Observation of shear banding in worm-like micelles by NMR velocity imaging. Europhys. Lett. 36, 719–724 (1996)

[59] Neto, C., Evans, D. R., Bonaccurso, E., Butt, H. J., Craig, V. S. J.: Boundary slip in Newtonian liquids: a review of experimental studies. Rep. Prog. Phys. 68, 2859 (2005)

[60] Zhu, Y., Granick, S.: Limits of the hydrodynamic no-slip boundary condition. Phys. Rev. Lett. 88, 106102 (2002)

[61] Bonaccurso, E., Kappl, M., Butt, H.-J.: Hydrodynamic Force Measurements: Boundary Slip of Water on Hydrophilic Surfaces and Electrokinetic Effects. Phys. Rev. Lett. 88, 1–4 (2002)

[62] Migler, K., Hervet, H., Leger, L.: Slip transition of a polymer melt under shear stress. Phys. Rev. Lett. 70, 287–290 (1993)

[63] Pit, R., Hervet, H., Léger, L.: Direct Experimental Evidence of Slip in Hexadecane : Solid Interfaces. Phys. Rev. Lett. (2000)

[64] Vinogradova, O. I., Koynov, K., Best, A., Feuillebois, F.: Direct measurements of hydrophobic slippage using double-focus fluorescence cross-correlation. Phys. Rev. Lett. 102, 118302 (2009)

[65] Cuenca, A., Bodiguel, H.: Fluorescence photobleaching to evaluate flow velocity and hydrodynamic dispersion in nanoslits. Lab Chip 12, 1672–9 (2012)

[66] Kuang, C., Wang, G.: A novel far-field nanoscopic velocimetry for nanofluidics. Lab Chip 10, 240–5 (2010)

[67] Eggeling, C., Widengren, J., Rigler, R., Seidel, C.: Photobleaching of fluorescent dyes under conditions used for single-molecule detection: evidence of two-step photolysis. Anal. Chem 70, 2651–2659 (1998)

[68] Curie, M.: Phosphorescent glasses. Decay of phosphorescence. Trans. Faraday Soc. 35, 114 (1939)

[69] Braun, S.: The synchronous (time domain) average revisited. Mech. Syst. Sig. Process. 25, 1087–1102 (2011)

[70] Song, L., Hennink, E. J., Young, I. T., Tanke, H. J.: Photobleaching kinetics of fluorescein in quantitative fluorescence microscopy. Biophys. J. 68, 2588–600 (1995)

[71] Fomina, N., McFearin, C., Sermsakdi, M., Edigin, O., Almutairi, A.: UV and near-IR triggered release from polymeric nanoparticles. JACS 132, 9540–2 (2010)

[72] Zhao, Z., Ding, Z., Wang, Z.: Fluorescence of Rhodamine 101 under High Pressures. Chin. J. High Pressure Phys. 20 (2006)

[73] Cox, W. P., Merz, E. H.: Correlation of dynamic and steady flow viscosities. J. Polym. Sci. 28, 619–622 (1958)

[74] Osa, M., Abe, F., Yoshizaki, T., Einaga, Y., Yamakawa, H.: Excluded-Volume Effects on the Hydrodynamic Radius of Oligo- and Polyisobutylenes in Dilute Solution. Macromolecules 29, 2302–2308 (1996)

[75] Sarkar, N., Das, K., Nath, D. N., Bhattacharyya, K.: Twisted charge transfer processes of nile red in homogeneous solutions and in faujasite zeolite. Langmuir 10, 326–329 (1994)

[76] Evans, C. R., Johnson, K. L.: Regimes of traction in elastohydrodynamic lubrication. Proc. Inst. Mech. Eng., Part C 200, 313–324 (1986)

[77] Nakamura, Y., Takimoto, A., Matsui, M.: Rheological study of solidified lubricant oils under very high pressure by observing microsphere deformation and viscosity prediction. Lubr. Sci. 22, 417–429 (2010)

[78] Wang, G. R., Fiedler, H. E.: On high spatial resolution scalar measurement with LIF. Exp. Fluids 29, 265–274 (2000)

[79] Axelrod, D.: Cell surface heating during fluorescence photobleaching recovery experiments. Biophys. J. 18, 129–31 (1977)

[80] Simon, J. R., Gough, A., Urbanik, E., Wang, F., Lanni, F., Ware, B. R., Taylor, D. L.: Analysis of rhodamine and fluorescein-labeled F-actin diffusion in vitro by fluorescence photobleaching recovery. Biophys. J. 54, 801–15 (1988)

[81] Boggs, J., Sibbitt, W.: Thermal Conductivity Measurements of Viscous Liquids. Ind. Eng. Chem. 47, 53–53 (1955)

[82] Scalettar, B. a, Selvin, P. R., Axelrod, D., Hearst, J. E., Klein, M. P.: A fluorescence photobleaching study of the microsecond reorientational motions of DNA. Biophys. J. 53, 215–26 (1988)

[83] Esfahanian, M., Hamrock, B. J.: Fluid-Film Lubrication Regimes Revisited. Tribol. Trans. 34, 628–632 (1991)

[84] Hamrock, B. J., Dowson, D.: Isothermal Elastohydrodynamic Lubrication of Point Contacts: Part III—Fully Flooded Results. J. Lubr. Technol. 99, 264 (1977)

[85] Jakobsen, B., Niss, K., Maggi, C., Olsen, N. B., Christensen, T., Dyre, J. C.: Beta relaxation in the shear mechanics of viscous liquids: Phenomenology and network modeling of the alpha-beta merging region. J. Non-Cryst. Solids 357, 267–273 (2011)

[86] Reddyhoff, T., Spikes, H. a., Olver, a. V.: Compression Heating and Cooling in Elastohydrodynamic Contacts. Tribol. Lett. 36, 69–80 (2009)

[87] Hardy, W., Bircumshaw, I.: Bakerian Lecture. Boundary Lubrication. Plane Surfaces and the Limitations of Amontons' Law. Proc. R. Soc. Lond. A 108, 1–27 (1925)

[88] Lu, R. F., Lin, J. R.: A theoretical study of combined effects of non-Newtonian rheology and viscosity-pressure dependence in the sphere-plate squeeze-film system. Tribol. Int. 40, 125–131 (2007)

[89] Sugimura, J., Hashimoto, M., Yamamoto, Y.: Study of elastohydrodynamic contacts with fluorescence microscope. Tribol. Ser. 38, 609–617 (2000)

[90] Hoang, A., Berteloot, G., Sharif-Kashani, P., Kavehpour, H. P.: Dynamic measurement of microfilms and nanofilms of fluids using fluorescence microscopy. Exp. Fluids 52, 1657–1662 (2012)

[91] Ren, S., Yang, S., Zhao, Y., Zhou, J., Xu, T., Liu, W.: Friction and wear studies of octadecyltrichlorosilane SAM on silicon. Tribol. Lett. 13, 233–239 (2002)

[92] Kalin, M., Velkavrh, I., Vižintin, J.: The Stribeck curve and lubrication design for non-fully wetted surfaces. Wear 267, 1232–1240 (2009)

[93] Stalder, A. F., Melchior, T., Müller, M., Sage, D., Blu, T., Unser, M.: Low-bond axisymmetric drop shape analysis for surface tension and contact angle measurements of sessile drops. Colloids Surf., A 364, 72–81 (2010)

[94] Glovnea, R., Forrest, A., Olver, A., Spikes, H.: Measurement of sub-nanometer lubricant films using ultra-thin film interferometry. Tribol. Lett. 15, 217–230 (2003)

[95] Guo, F., Wong, P. L.: Experimental observation of a dimple-wedge elastohydrodynamic lubricating film. Tribol. Int. 37, 119–127 (2004)

[96] Myant, C., Reddyhoff, T., Spikes, H. A.: Laser-induced fluorescence for film thickness mapping in pure sliding lubricated, compliant, contacts. Tribol. Int. 43, 1960–1969 (2010)

[97] Yang, P., Qu, S., Kaneta, M., Nishikawa, H.: Formation of Steady Dimples in Point TEHL Contacts. J. Tribol. 123, 42 (2001)

[98] Müller, J. D., Gratton, E.: High-pressure fluorescence correlation spectroscopy. Biophys. J. 85, 2711–9 (2003)

[99] Wedeven, L.: Optical measurements in elastohydrodynamic rolling-contact bearing. PhD Thesis, London University (1970)

[100] Yagi, K., Sugimura, J., Vergne, P.: Rheological response of fatty alcohols in sliding elastohydrodynamic contacts. Tribol. Int. 49, 58–66 (2012)

[101] Ehret, P., Bauget, F.: Observation of Kaneta's dimples in elastohydrodynamic lubrication contacts. Proc. Inst. Mech. Eng., Part J 215, 289–300 (2001)

[102] Molho, J. I., Herr, A. E., Mosier, B. P., Santiago, J. G., Kenny, T. W., Brennen, R. A., Gordon, G. B., Mohammadi, B.: Optimization of Turn Geometries for Microchip Electrophoresis. Anal. Chem. 73, 1350–1360 (2001)

[103] Schmatko, T., Hervet, H., Leger, L.: Friction and Slip at Simple Fluid-Solid Interfaces: The Roles of the Molecular Shape and the Solid-Liquid Interaction. Phys. Rev. Lett. 94, 244501 (2005)

[104] Ross, D., Johnson, T. J., Locascio, L. E.: Imaging of Electroosmotic Flow in Plastic Microchannels. Anal. Chem. 73, 2509–2515 (2001)

[105] Brunet, F., Cid, E., Bartoli, A.: Simultaneous Image Registration and Monocular Volumetric Reconstruction of a Fluid Flow. Proc. Br. Machine vis. conf., 83.1–83.11 (2011)

[106] Garbe, C.: Fluid flow estimation through integration of physical flow configurations. Pattern Recognit. LNCS 4713, 92–101 (2007)

[107] Ravindranath, S., Wang, S., Olechnowicz, M., Quirk, R. P.: Banding in Simple Steady Shear of Entangled Polymer Solutions. Stress: The International Journal on the Biology of Stress , 2663–2670 (2008)

[108] Tretheway, D. C., Meinhart, C. D.: Apparent fluid slip at hydrophobic microchannel walls. Phys. Fluids 14, L9 (2002)

[109] Leger, L., Hervet, H., Massey, G., Durliat, E.: Wall slip in polymer melts. J. Phys. Condens. Matter 9, 7719 (1997)

[110] Yagi, K., Vergne, P., Nakahara, T.: In situ pressure measurements in dimpled elastohydrodynamic sliding contacts by Raman microspectroscopy. Tribol. Int. 42, 724–730 (2009)

[111] Lee, R.-T., Chu, H.-M., Chiou, Y.-C.: Inverse approach for estimating pressure and viscosity in the elastohydrodynamic lubrication of circular contacts. Proc. Inst. Mech. Eng., Part J 217, 277–288 (2003)

[112] Hamrock, B. J., Dowson, D.: Elastohydrodynamic Lubrication of Elliptical Contacts for Materials of Low Elastic Modulus I—Fully Flooded Conjunction. J. Lubr. Technol. 100, 236 (1978)

[113] Toepke, M. W., Beebe, D. J.: PDMS absorption of small molecules and consequences in microfluidic applications. Lab Chip 6, 1484–6 (2006)

[114] Cole, S. J., Sayles, R. S.: A Numerical Model for the Contact of Layered Elastic Bodies With Real Rough Surfaces. J. Tribol. 114, 334 (1992)

[115] Walsh, C. B., Franses, E. I.: Ultrathin PMMA films spin-coated from toluene solutions. Thin Solid Films 429, 71–76 (2003)

[116] Flumerfelt, R. W., Pierick, M. W., Cooper, S. L., Bird, R. B.: Generalized Plane Couette Flow of a Non-Newtonian Fluid. Industrial & Engineering Chemistry Fundamentals 8, 354–357 (1969)

[117] Colby, R. H., Fetters, L. J., Graessley, W. W.: The melt viscosity-molecular weight relationship for linear polymers. Macromolecules 20, 2226–2237 (1987)

[118] Martin, J. D., Thomas Hu, Y.: Transient and steady-state shear banding in aging soft glassy materials. Soft Matter 8, 6940 (2012)

[119] Fu, Z., Wong, P. L., Guo, F.: Effect of Interfacial Properties on EHL Under Pure Sliding Conditions. Tribol. Lett. 49, 31–38 (2012)

[120] Floudas, G., Reisinger, T.: Pressure dependence of the local and global dynamics of polyisoprene. J. Chem. Phys. 111, 5201 (1999)

[121] Bruyere, V., Fillot, N., Morales-Espejel, G. E., Vergne, P.: Computational fluid dynamics and full elasticity model for sliding line thermal elastohydrodynamic contacts. Tribol. Int. 46, 3–13 (2012)

[122] Hu, Y.-Z., Wang, H., Guo, Y., Shen, Z.-J., Zheng, L.-Q.: Simulation of lubricant rheology in thin film lubrication Part 2: simulation of Couette flow. Wear 196, 249–253 (1996)

[123] Demirel, A. L., Granick, S.: Transition from static to kinetic friction in a model lubricated system. The Journal of Chemical Physics 109, 6889 (1998)

[124] Bair, S., Liu, Y., Wang, Q. J.: The Pressure-Viscosity Coefficient for Newtonian EHL Film Thickness With General Piezoviscous Response. J. Tribol. 128, 624 (2006)

[125] Iivonen, H., Hamrock, B. J.: A new non-newtonian fluid model for elastohydrodynamic lubrication of rectangular contacts. Wear 143, 297–305 (1991)

[126] Goyon, J., Colin, A., Bocquet, L.: How does a soft glassy material flow: finite size effects, non local rheology, and flow cooperativity. Soft Matter 6, 2668 (2010)

[127] Ponjavic, A., Di Mare, L., Wong, J. S. S.: Effect of pressure on the flow behavior of polybutene. J. Polym. Sci. Part B: Polym. Phys. (in press), doi: 10.1002/polb.23472 (2014)

[128] Zhang, Y., Greer, a. L.: Thickness of shear bands in metallic glasses. Appl. Phys. Lett. 89, 071907 (2006)

[129] Toratani, H., Takamizawa, K.: Effect of Pressure on the Relation between Glass Transition Temperature and Molecular Weight for Monodispersed Polystyrenes. Polym. J. 26, 797–803 (1994)

[130] Choo, J. H., Glovnea, R. P., Forrest, A. K., Spikes, H. A.: A Low Friction Bearing Based on Liquid Slip at the Wall. J. Tribol. 129, 611 (2007)

[131] Guo, Z., Zhao, T. S., Xu, C., Shi, Y.: Simulation of fluid flows in the nanometer: kinetic approach and molecular dynamic simulation. Int. J. Comp. Fluid Dyn. 20, 361–367 (2006)

[132] Fillot, N., Berro, H., Vergne, P.: From Continuous to Molecular Scale in Modelling Elastohydrodynamic Lubrication: Nanoscale Surface Slip Effects on Film Thickness and Friction. Tribol. Lett. 43, 257–266 (2011)

[133] Savio, D., Fillot, N., Vergne, P., Zaccheddu, M.: A Model for Wall Slip Prediction of Confined n-Alkanes: Effect of Wall-Fluid Interaction Versus Fluid Resistance. Tribol. Lett. 46, 11–22 (2012)

[134] Li, X. M., Guo, F., Wong, P. L.: Shear rate and pressure effects on boundary slippage in highly stressed contacts. Tribol. Int. (2012)

[135] Zhu, Y., Granick, S.: Rate-dependent slip of Newtonian liquid at smooth surfaces. Physical review letters 87, 096105 (2001)

[136] Koran, F., Dealy, J. M.: Wall slip of polyisobutylene: Interfacial and pressure effects. J. Rheol. 43, 1291 (1999)

[137] Spikes, H., Granick, S.: Equation for Slip of Simple Liquids at Smooth Solid Surfaces. Langmuir 19, 5065–5071 (2003)

[138] Kalin, M., Polajnar, M.: The Effect of Wetting and Surface Energy on the Friction and Slip in Oil-Lubricated Contacts. Tribol. Lett. 52, 185–194 (2013)

[139] Wong, P. L., Li, X. M., Guo, F.: Evidence of lubricant slip on steel surface in EHL contact. Tribol. Int. 61, 116–119 (2013)

[140] McGOWN, L. B., NITHIPATIKOM, K.: MOLECULAR FLUORESCENCE AND PHOSPHORESCENCE. Appl. Spectrosc. Rev. 35, 353–393 (2000)

[141] Samouda, F., Brandner, J. J., Barrot, C., Colin, S.: Velocity field measurements in gas phase internal flows by molecular tagging velocimetry. J. Phys. Conf. Ser. 362, 012026 (2012)

Appendix: Copyright permissions

SPRINGER LICENSE
TERMS AND CONDITIONS

Apr 06, 2014

This is a License Agreement between Aleks Ponjavic ("You") and Springer ("Springer") provided by Copyright Clearance Center ("CCC"). The license consists of your order details, the terms and conditions provided by Springer, and the payment terms and conditions.

All payments must be made in full to CCC. For payment instructions, please see information listed at the bottom of this form.

License Number	3363130893884
License date	Apr 06, 2014
Licensed content publisher	Springer
Licensed content publication	Tribology Letters
Licensed content title	Through-Thickness Velocity Profile Measurements in an Elastohydrodynamic Contact
Licensed content author	Aleks Ponjavic
Licensed content date	Jan 1, 2013
Volume number	50
Issue number	2
Type of Use	Thesis/Dissertation
Portion	Figures
Author of this Springer article	Yes and you are the sole author of the new work
Order reference number	
Original figure numbers	Figures 1, 4, 5, 6, 8
Title of your thesis / dissertation	Local rheology of lubricants in the elastohydrodynamic regime
Expected completion date	Apr 2014
Estimated size(pages)	217
Total	0.00 USD

JOHN WILEY AND SONS LICENSE TERMS AND CONDITIONS

Apr 06, 2014

This is a License Agreement between Aleks Ponjavic ("You") and John Wiley and Sons ("John Wiley and Sons") provided by Copyright Clearance Center ("CCC"). The license consists of your order details, the terms and conditions provided by John Wiley and Sons, and the payment terms and conditions.

All payments must be made in full to CCC. For payment instructions, please see information listed at the bottom of this form.

License Number	3363130362197
License date	Apr 06, 2014
Licensed content publisher	John Wiley and Sons
Licensed content publication	Journal of Polymer Science Part B: Polymer Physics
Licensed content title	Effect of pressure on the flow behavior of polybutene
Licensed copyright line	Copyright © 2014 Wiley Periodicals, Inc.
Licensed content author	Aleks Ponjavic,Luca Mare,Janet S. S. Wong
Licensed content date	Mar 17, 2014
Start page	n/a
End page	n/a
Type of use	Dissertation/Thesis
Requestor type	Author of this Wiley article
Format	Print and electronic
Portion	Figure/table
Number of figures/tables	2
Original Wiley figure/table number(s)	Figure 3 and Figure 6
Will you be translating?	No
Title of your thesis / dissertation	Local rheology of lubricants in the elastohydrodynamic regime
Expected completion date	Apr 2014
Expected size (number of pages)	217
Total	0.00 USD